LASER INDUCED PERIODIC SURFACES STRUCTURES: ADVANCES IN MODELLING, PROCESSING AND MONITORING

ALEKSANDRA MICHAŁEK

A thesis submitted to the University of Birmingham for the degree of

DOCTOR OF PHILOSOPHY

September 2021

Department of Mechanical Engineering

School of Engineering

University of Birmingham

UNIVERSITY OF
BIRMINGHAM

University of Birmingham Research Archive
e-theses repository

This unpublished thesis/dissertation is under a Creative Commons Attribution 4.0 International (CC BY 4.0) licence.

You are free to:

Share — copy and redistribute the material in any medium or format

Adapt — remix, transform, and build upon the material for any purpose, even commercially.

The licensor cannot revoke these freedoms as long as you follow the license terms.

Under the following terms:

Attribution — You must give appropriate credit, provide a link to the license, and indicate if changes were made. You may do so in any reasonable manner, but not in any way that suggests the licensor endorses you or your use.

No additional restrictions — You may not apply legal terms or technological measures that legally restrict others from doing anything the license permits.

Notices:

You do not have to comply with the license for elements of the material in the public domain or where your use is permitted by an applicable exception or limitation.

No warranties are given. The license may not give you all of the permissions necessary for your intended use. For example, other rights such as publicity, privacy, or moral rights may limit how you use the material.

Unless otherwise stated, any material in this thesis/dissertation that is cited to a third-party source is not included in the terms of this licence. Please refer to the original source(s) for licencing conditions of any quotes, images or other material cited to a third party.

ABSTRACT

Laser Induced Periodic Surface Structures (LIPSS) have been known to the scientific world for almost as long as the invention of first laser. The advantages of the ripples structures have been recognized soon after, which resulted in the development of many industrially fit applications because of the flexibility, environmental friendliness and robustness of the technology. Nonetheless, the important reason of the continuous growing interest in LIPSS is the great variety of functional responses that can be ‘imprinted’ on the surfaces, and thus be employed in many engineering fields. For the broader use of LIPSS treatments, specific industrial requirements and challenges still have to be addressed, especially associated with processing, modelling and monitoring. In this context, the research presented in this thesis focuses, firstly, on investigating the synergistic use of LIPSS with coatings for the purpose of combining the valuable surface properties without compromising on the functional performance. Next, the research addresses the issues of applying periodic structures on free form surfaces when the processing conditions vary. In particular, a predictive model is developed to account the effects from 3D processing disturbances hence minimizing the empirical research required to produce optimized structures for any given material and/or geometry. Subsequently, new approaches for ripples monitoring and process quality control are investigated. A light scattering method is proposed to satisfy the technical requirements of inline process monitoring with sufficient sensitivity to detect changes in LIPSS characteristics. Lastly, the use of artificial intelligence methods is considered for predicting the functional responses based on the topography data, also when the generation process is affected by the processing disturbances.

ACKNOWLEDGEMENTS

In the first lines of my thesis I would like to thank everyone that was involved in this journey over the last 4 years. Firstly, I would like to express my gratitude to my supervisor, Professor Stefan Dimov, for the guidance and support and helping me seeing the light in the tunnel. I would like to also thank my industrial supervisor, Dr Tian Long See, from The Manufacturing Technology Centre.

I would not be able to be to accomplish this work without the amazing colleagues from the Laser Manufacturing group that also became my friends. To Tony, who made my start at Birmingham much easier. To Tahseen for the help and long conversations. To Pavel for very helpful discussions and handy advice. Especially, my great appreciation goes to Afif and our fruitful conversations in Staff house - thanks for our lunches and coffee breaks and much more! I would also like to thank Shaojun for the assistance and support. And everyone else at Uni that helped me navigate through the research world.

I am forever grateful to Dario, who is always by my side, ready to put out fires and unconditionally caring at the times of doubt. Without you this whole journey would not be possible, thank you for being in my life.

My deepest appreciation is for my loving family who supported me on this path: Dzięki Mamo, Tato, Ewe, Maciej z Franiem i Hanią.

TABLE OF CONTENTS

LIST OF TABLES

LIST OF FIGURES

LIST OF ACRONYMS AND ABBREVIATIONS

2D	Two Dimensional
2D FFT	2D Fast Fourier Transformation
2D PSDF	2D Power Spectral Density Function
3D	Three Dimensional
A	Absorptivity
AFM	Atomic Force Microscope
ANN	Artificial Neural Network
ANNE	Artificial Neural Network Evolver
BIA	Beam Incident Angle
BP	Back-propagation
BP	Back Propagation
BWF	Breit-Wigner-Fano
CA	Contact Angle
CAN	Conditional Adversarial Network
CNN	Convolutional Neural Network
CoF	Coefficient of Friction
CW	Continuous Wave
DFM	Dynamic Focusing Module
DLC	Diamond-like Carbon
DLIP	Direct Laser Interference Patterning
EDS	Energy-Dispersive X-ray Spectroscopy
FDTD	Finite-Difference Time-Domain

FOD	Focal Offset Distance
FoV	Field of View
FWHM	Full Width at Half-Maximum
GAN	Generative Adversarial Network
GAXRD	Glancing Angle X-ray Diffraction
GC	Glassy Carbon
GISAXS	Grazing Incidence Small-Angle X-ray Scattering
GR	Graphitization
HAZ	Heat Affected Zone
HSFL	High Spatial Frequency LIPSS
HV	Vicker’s Hardness
HWP	Half-Wave Plate
ISO	International Organization for Standardization
LASER	Light Amplification by Stimulated Emission of Radiation
LBM	Laser Beam Machining
LIPSS	Laser Induced Periodic Surface Structures
LSFL	Low Spatial Frequency LIPSS
MLP	Multi-Layer Perceptron
NIR	Near infrared
PACVD	Plasma-Assisted Chemical Vapour Deposition
PSDF	Power Spectral Density Function
r.m.s.	root mean square
RSM	Response Surface Method
SEM	Scanning Electron Microscope

SERS	Surface Enhanced Raman Spectroscopy
SEW	Surface Electromagnetic Waves
SIM	Structured-Illumination-Microscopy
SPP	Surface Plasmon Polaritons

LIST OF SYMBOLS

Chapter 2

ε	Complex dielectric permittivity
Λ	Periodicity
λ	Laser source wavelength
ω_0	Smallest beam waist
ω	Beam waist
Au	Gold
CO_2	Carbon Dioxide
CoCr	Cobalt Chromium
He	Helium
k	Wave vector
Nd:YAG	Neodymium-doped Yttrium Aluminium Garnet
MoS_2	Molybdenum disulphide
Ne	Neon
Pt	Platinum
Ti	Titanium
TiN	Titanium Nitride
z	Propagation axis
z_0	Position of smallest beam waist

Chapter 3

F	Pulse fluence
f	Frequency

F_0	Peak fluence
h	Hatching distance
P_{avg}	Average Power
v	Scanning speed
Λ	Periodicity
λ	Laser source wavelength
ω	Beam waist

Chapter 4

λ	Laser source wavelength
Λ	Periodicity
d_b	Laser beam spot diameter
E	Polarization vector
f	Frequency
F_{acc}	Accumulated fluence
fs	Femtosecond
h	Hatch distance
MoS_2	Molybdenum disulphide
ns	Nanosecond
P	Average power
pps	Pulses per spot
pps_{total}	Total number of pulses per spot
ta-C	Tetra amorphous Carbon
v	Scanning speed

Chapter 5

$\Delta y'$	Distance between pulses on the surface if they are not compensated during laser scanning
Δz	Local focal offset
Δx	Distance between pulses along the x
Δy	Distance between pulses along the y
$\Lambda_{p\,\pm}$	Theoretical LIPSS Periodicity generated with P-type polarisation, calculated using ‘-‘ or ‘+’ sign in the equation
ε_1, ε_2	Complex dielectric constants of medium and the processed material
Λ	LIPSS periodicity
λ	Laser source wavelength
ω_{0i}	Smallest waist at z_{0i}
ω_x, ω_y	Beam waists of astigmatic beams
$\omega_{y\alpha}$	Beam waist value used for calculating F_{loc} when beam is not normal to the surface
ω_α	Beam radius measured at the $1/e^2$ of intensity drops on a tilted surface
A_c	Absorptivity for circular polarisation
A_p	Absorptivity for p-type polarisation
A_s	Absorptivity for s-type polarisation
E	Polarisation vector
f	Pulse repetition rate
F	Local fluence intensity distribution
$F_{acc\ th}$	Accumulated fluence threshold
F_0	Peak fluence

F_{01}	Peak fluence for the optimised laser setting for producing LIPSS
F_{02}	Peak fluence with still homogenous LIPSS but with higher reserve in regard to F_{th}
F_{acc}	Accumulated fluence
F_{loc}	Local fluence value on a surface when beam is not normal
F_{th}	Fluence threshold
$F_{th}(1)$	Fluence threshold for a single pulse
h	hatch offset
L_x, L_y	Lengths of the processing field
M_i^2	Beam quality factor
$N_{p\,eff}$	Effective number of pulses
N_p	Number of pulses
N_r	Number of passes over the area
N_x, N_y	Number of pulses along x and y
$(n+ik)$	Refractive index of materials
P	Average power
R	Local radius of the curvature
Rtm	Average distance between the highest peak and lowest valley in every sampling length
S	Incubation factor
v	Scanning speed
y'	Distance on the tilted surface from the beginning of the processing field and current pulse centre

x_c, y_c, z_c	Centre of the curvature
z	Laser propagation axis
z_{0i}	Smallest waists' position

Chapter 6

α	Processing incident angle (Beam Incident Angle)
ε_i	Complex dielectric function
θ_{in}	Incident angle of the pointer
θ_m	Diffraction angle
Λ	LIPSS periodicity
Λ_{theor}	LIPSS theoretical periodicity
Λ_{exp}	LIPSS measured periodicity
Λ_{p-}	Theoretical LIPSS Periodicity generated with P-type polarisation, calculated using '-' sign in the equation
Λ_{p+}	Theoretical LIPSS Periodicity generated with P-type polarisation, calculated using '+' sign in the equation
λ	Wavelength of the laser source
φ	Orientation of the laser pointer in regard to the LIPSS
F	Fluence
fs	Femtosecond
k_0	Propagation constant
m	Diffraction order
$x_{m=1}$	Distance from the laser pointer to the screen
$z_{m=1}$	Height of the first order diffracted pattern

Chapter 7

λ	Laser source wavelength
μ	mean
σ	standard deviation
$\lfloor \rho_{xy} \rfloor$	Correlation coefficient
F_n	Group of areal surface roughness parameters determined in feature selection analysis
F_p	Peak fluence
N	Class of samples that were produced with optimized laser settings
Q1, Q3	First and third quartile

Chapter 8

Λ_{p-}	Theoretical LIPSS Periodicity generated with P-type polarisation, calculated using ‘-‘ sign in the equation
Λ_{p+}	Theoretical LIPSS Periodicity generated with P-type polarisation, calculated using ‘+‘ sign in the equation
F_0	Peak fluence
F_{acc}	Accumulated Fluence

LIST OF PUBLICATIONS AND CONFERENCE PRESENTATIONS

The following Journal publications and conference presentations resulted from the research carried out within the scope of this thesis.

Journal articles accepted/submitted for publication:

1. **A. Michalek**, T. Jwad, P. Penchev, T.L. See, S. Dimov, Inline LIPSS Monitoring Method Employing Light Diffraction, J. Micro Nano-Manufacturing. 8 (2020). https://doi.org/10.1115/1.4045681.

2. **A. Michalek**, S. Qi, A. Batal, P. Penchev, H. Dong, T.L. See, S. Dimov, Sub-micron structuring/texturing of diamond-like carbon-coated replication masters with a femtosecond laser, Appl. Phys. A Mater. Sci. Process. 126 (2020). https://doi.org/10.1007/s00339-020-3303-4.

3. **A. Michalek**, A. Batal, S. Qi, P. Penchev, D. Bruneel, T.L. See, S. Dimov, Modelling ultrafast laser structuring/texturing of freeform surfaces, Appl. Surf. Sci. Adv. 2 (2020) 100036. https://doi.org/10.1016/j.apsadv.2020.100036.

4. L. Baronti, **A. Michalek**, M. Castellani, P. Penchev, T.L. See, S. Dimov, Artificial Neural Networks Tools for Predicting the Functional Response of Ultrafast Laser Textured/Structured Surfaces, International Journal of Advanced Manufacturing Technology (2021), Submitted on: 16th Sep 2021.

Conference presentations:

- Laser Precision Microfabrication 2018, Edinburgh, UK
- Industrial Laser Applications Symposium (ILAS) 2019, Crewe, UK
- World Congress on Micro and Nano Manufacturing (4M WCMNM) 2019, Raleigh, USA,
- Industrial Laser Applications Symposium (ILAS) 2020, virtual

Other publications as a co-author:

1. A. Batal, **A. Michalek**, P. Penchev, A. Kupisiewicz, S. Dimov, Laser processing of freeform surfaces: A new approach based on an efficient workpiece partitioning strategy, Int. J. Mach. Tools Manuf. (2020) 103593. https://doi.org/10.1016/j.ijmachtools.2020.103593.

2. A. Batal, **A. Michalek**, A. Garcia-Giron, V. Nasrollahi, P. Penchev, R. Sammons, S. Dimov, Effects of laser processing conditions on wettability and proliferation of Saos-2 cells on CoCrMo alloy surfaces, Adv. Opt. Technol. 9 (2020) 67–78. https://doi.org/10.1515/aot-2019-0051.

3. A. Garcia-Giron, J.M. Romano, A. Batal, **A. Michałek**, P. Penchev, S.S. Dimov, Experimental investigation of processing disturbances in laser surface patterning, Opt. Lasers Eng. 126 (2020). https://doi.org/10.1016/j.optlaseng.2019.105900.

CHAPTER 1: INTRODUCTION

1.1. Motivation

Laser Induced Periodic Surface Structures (LIPSS), often referred to as surface ripples, have been known to scientific world almost as long as the discovery of the first laser and since then have been studied thoroughly, especially in the last two decades when ultrafast laser systems became much more widely available [1]. Separately, industrial applications for LIPSS have started to emerge and thus to capitalise on flexibility of this technology to generate such surface structures almost on any material (metals, semiconductors, dielectrics, polymers, etc.) by employing relatively simple and at the same time sufficiently robust processing setups. Another, even more important reason for the constantly growing interests of researchers and industry in this technology is the great variety of functional responses that can be “imprinted” on surfaces, i.e. by modifying their physical, chemical or optical property, and thus LIPSS treatments for applications in medicine, optics, electronics or tribology, to name a few, are emerging.

Therefore, it is not surprising that the development of LIPSS treatments has become widespread as they benefit from the contactless application on almost any material and also from their environmentally friendly nature. Their main competing technologies are the conventional surface treatments that are not so environmentally friendly and might result in potential issues at the interface between the thin layer of engineered material and the substrate material. However, LIPSS treatments are not only an alternative but also, they can be applied synergistically with the coating technologies. It means that the coating directly can be laser structured and as a result the surface properties of the thin film can be combined with the added surface functionalities from the modified topography resulting from laser structuring. This synergistic use of both approaches can be achieved because of the ultrafast laser source’s “gentle” nature, i.e. the intrinsic laser-material interactions. Thus, by combining them, advantageous surface properties can be obtained, e.g. coatings can be applied as a wear resistant layer and/or solid lubricant while the additional surface properties can be varied through the use of LIPSS, for instance functional properties such as structural colouring, tribological, antibacterial or modified wettability. This combination of surface properties is particularly sought after in tool/master-making, medical, energy and other application areas. Hence, the synergistic use of LIPSS with coatings is another promising research direction for the development of new surface treatment applications, although also challenging considering potential undesirable side effects, such as coating’s structural and mechanical modifications which might lead to softening, delamination, cracking, excessive ablation, that can alternate the attractive properties of the deposited thin layer of material. Therefore, LIPSS processing domains have to be identified and validated to ensure that synergistic effects can be achieved on treated surfaces and that formulates the first research problem addressed in this thesis.

Particular application that can benefit from producing laser structures/textures on hard coatings is the injection moulding of polymers. This way, the structures/textures on the moulds during the replication process enable producing polymer replicas with functionalised surfaces at low cost per part. But also, having the advantage of coating’s properties will translate to extended tooling life and as well increased fidelity of the injection process. It is also important to consider that in the real-life applications the design of the polymer part might require to be of complex geometry and as well the surface functionalities to be present on them. As a result, the replication moulds also need to satisfy complex geometry requirement. This consideration is also important and applicable to generation of LIPSS not only on hard coatings for replication masters but, generally, on other materials for all ripples functionalities.

While an extensive research on LIPSS has been done, more attention has to be given to some practical issues, too, in generating specific functionality tailored LIPSS over large surface areas. It has been recently estimated that the cost of LIPSS treatments is approximately 0.04 £/cm^2 (0.046 €/cm^2) [2] and undoubtedly the processing cost will be reduced with the increase of processing speed and pulse repetition rates. There is still a significant research focus on developing LIPSS treatments for new novel applications, however there are many specific industrial requirements and challenges that have to be addressed in order to broaden the use of this technology. For example, it is required for LIPSS treatments to be applied on freeform surfaces for many real-life applications, however there are a number of open processing issues that can affect their targeted functional responses. Those include all factors that are not considered for planar surfaces but have an impact on the laser processing conditions of freeform surface, which are oblique laser incidence or changes in laser beam spot size due to defocusing. As a result, approaches for producing LIPSS on freeform surfaces typically require experimental studies for identifying the processing tolerances whereas tools related to modelling this process are not adapted yet for complex geometries that could enable reliability and efficiency in the industrial manufacturing process.

As mentioned above, the performance of LIPSS treatments can be affected by a number of processing disturbances, e.g. the varying beam incident angle and focal distance when processing freeform surfaces, and therefore their effects have to be investigated and controlled as otherwise the designed surface functionality may not be achieved or maintained within acceptable limits. Even though more advanced laser systems have already been developed, it will be very difficult and even impossible to maintain the processing conditions constant, i.e. control of spatial laser beam intensity while structuring complex geometry simultaneously in multi-axis laser processing platform, as it is the case when developing and characterising the LIPSS treatments on the planar surfaces. Therefore, predictive models that account for processing disturbances, e.g. beam incident angle and focal offset distance, have to be developed and thus to minimise the empirical research required to determine the LIPSS processing window and aid designing processing strategies for any given material and/or parts’ geometries. This formulates second research problem addressed in this thesis.

Another critical aspect preventing the broader use of LIPSS treatments is the availability of metrology/inspection tools for inline monitoring of the generation of sub-micron surface ripples and thus to ensure the presence of the desired functional response, indirectly. Therefore, as LIPSS are not visible with a naked eye and also hardly resolvable with optical metrology methods, new approaches for process monitoring and quality control are necessary and, in this way, to ensure the uniformity and functionality throughout the LIPSS treated areas, including those on freeform surfaces. There are techniques that can enable time-resolved LIPSS observations, however there is still lack of solutions that can be integrated into multi-axis laser processing systems that can satisfy the specific technical requirements for inline process monitoring. In particular, process monitoring solutions are required for fast data acquisition and simplified inline interpretation/analysis that are also suitable for integration in laser processing systems and offer the required level of automation. In addition, the use of artificial intelligence methods, e.g. Artificial Neural Network (ANN) tools should be considered for pre-processing and post-processing the acquired surface data and also for establishing the interdependences between the ripples' characteristics and their functional response. The problems for LIPSS monitoring and as well as functional prediction formulates third and fourth research problem.

1.2. Research aims and objectives

The overall aim of the PhD research reported in this thesis is to address four of current barriers preventing the LIPSS treatments to be used on a broader scale specifically associated with their generation on thin films, modelling on freeform surfaces and two related to their process monitoring. First, the suitability of LIPSS treatments for processing Diamond Like Carbon (DLC) coatings is investigated and thus to combine the capabilities of these two surface engineering technologies for producing durable and functional replication masters. The industrial use of this approaches might need the polymer replicas, replicated on the masters, to be applied on more complex geometries than just flat areas. Hence manufacturing challenges related to moving the LIPSS generation process to broader scale also need to be addressed. Therefore, and secondly, an ultrafast laser modelling approach is proposed for calculating accumulated fluence which can be used for predicting the resulting key LIPSS characteristics. The model implements the effects of varying laser conditions when processing freeform surfaces and can be employed in aiding the design of LIPSS treatment strategies on such surfaces. The material from now on that LIPSS are generated on is stainless steel in order to be more representative to metals with similar material properties and to more applications. Thirdly, a simple light scattering-based method is investigated for detecting changes in LIPSS characteristics with sufficient sensitivity that can be applied for monitoring the LIPSS generation. This approach can be employed with commercially available, compact light scattering sensors and provide a solution as an in-line process control tool that is unavailable with current metrology/inspection instruments due to ripple's sub-micron scale. Lastly, use of artificial intelligence based tools for pre- and post-processing the areal surface roughness parameters of LIPSS topographies are proposed. This combination of ANNs and laser structuring can be used for establishing interdependences with the processing conditions and ripples functional responses and also again for monitoring the LIPSS generation. The feasibility study is demonstrated on the prediction of wetting properties of LIPSS treated surfaces as an example of surface functionality.

The aims of this PhD research are achieved through the following objectives:

I. Investigate the effects of femtosecond laser processing as a potential treatment of replication masters with hard coatings. Especially, a LIPSS treatment of DLC coatings is investigated by varying the process settings, i.e. pulse fluence and number of pulses per spot. Mechanical properties together with the coating's structural modifications are studied after the ultrafast laser treatment.

II. Model the ultrafast laser irradiation process when treating freeform surfaces and thus to account for the actual beam distribution and local fluence threshold changes. The model is validated on the LIPSS treatment of stainless steel samples in the presence of two processing disturbances, i.e., focal offset distance (FOD) and beam incident angle (BIA). The modelling and experimental results, i.e. the predicted and actual LIPSS amplitudes and periodicity, are compared.

III. Develop a concept for an inline monitoring method based on the LIPSS optical response. Especially, the relative changes of light diffraction and reflectance of LIPSS produced in the presence of known processing disturbances are investigated. The sensitivity of the method that is defined based on the resolution of diffraction angle and reflectance measured values and is analysed to judge about its suitability for monitoring the LIPSS generation .

IV. Identify the processing conditions and establish interdependences with the functional responses, e.g. wettability by implementing ANNs tools, for pre- and post-processing the areal surface roughness parameters of LIPSS topographies. The suitability of those tools for monitoring the LIPSS performance is analysed and conclusions are made.

1.3. Thesis organization

This thesis is organized into eight chapters. This thesis presents nonlinear research. Each research question is formulated separately however the links between them are stated in the Chapter 2, as well as in preamble and concluding statements between the research Chapters. The general schematic highlighting the placement of the four research Chapters in LIPSS development areas is shown in Figure 1.1.

Chapter 1 introduces the motivation for the research reported in this thesis and then states its aims and objectives and also presents its structure.

Chapter 2 reviews the basic laser principles and introduces the system configurations and the beam delivery sub-system used in the research and also outlines the state-of-the-art and open research questions in developing and implementing LIPSS treatments.

Chapter 3 explains the experimental methodology and includes DOE of LIPSS generation on the materials considered in this thesis with listing laser parameters used as a preliminary sets and the ones chosen for the following studies.

Chapter 4 reports the effects of femtosecond laser processing and generating LIPSS on the DLC coated on stainless steel substrates. These two surface engineering methods are investigated as a means for achieving synergistic effects on the treated surfaces and thus to combine their capabilities. The resulting mechanical and structural changes of laser treated samples are compared to those on as-received ones.

Chapter 5 proposes a theoretical ultrafast irradiation model that accounts for the actual Gaussian beam distribution in the presence of processing disturbances, in particular those affecting the LIPSS generation on free form surfaces. The model is validated on stainless steel by using experimental results, i.e. samples that underwent LIPSS treatments with known processing disturbances.

Chapter 6 proposes a method for monitoring the LIPSS generation based on the light scattering of treated stainless steel surfaces. A simple optical setup is designed as a potential solution for in-line LIPSS monitoring, applicable to light scattering sensors placed in laser processing systems, based on their optical response, i.e. their light diffraction and reflectance. The capabilities and sensitivity of the proposed monitoring method are analysed and its suitability as a quality control tool is discussed.

Chapter 7 investigates the use of ANNs tools for pre- and post-processing the areal surface roughness parameters of LIPSS topographies, generated on stainless steel, as a means for establishing interdependences with LIPSS 3D processing disturbances and functional responses. Their pilot implementation is reported to demonstrate their capabilities as a method for monitoring the LIPSS generation.

Chapter 8 presents the main findings of the PhD research, summarizes the contributions to knowledge and outlines some directions for future research.

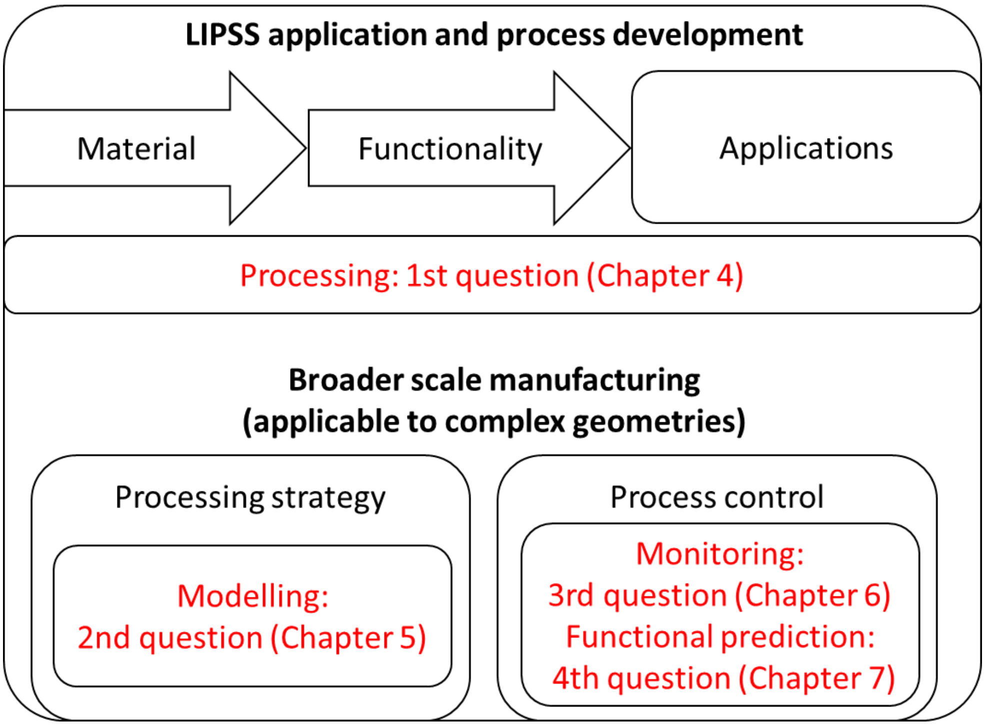

Figure 1.1 Schematic of the placement of each research Chapters into LIPSS development areas related to its processing, modelling and monitoring.

CHAPTER 2: LITERATURE REVIEW

2.1. Introduction to LASER

LASER is a source of light with very special properties and the acronym stands for “Light Amplification by Stimulated Emission of Radiation”. First commercially available was ruby laser invented by Theodore H. Maiman in 1960 [3]. Following this event, a boost in laser developments occurred following a construction of first generation of lasers with gas as a medium, such as CO_2 [4] or He-Ne [5], and soon after solid-state laser Nd:YAG [6]. Since then, the large potential of laser technology has been acknowledged by continuous growth and diversification into many fields of applications, i.e., industrial, medical, military and scientific, among others. Many types of lasers have been produced with not only advanced gain medium but also innovative optical elements or pumping techniques.

What makes laser unique is the specific properties of its beam. In particular, monochromaticity allows to emit central wavelength of the light with narrow optical bandwidth that is beneficial for processing of transparent materials and plays a role in absorbing laser energy in opaque ones [7]. Coherent laser beam has a fixed phase relationship between electric fields at different locations or at same location but different times, referred as spatial and temporal coherence, respectively. Another distinctive property is directionality of laser light that allows propagation of a narrow beam over long distances and ability to focus it in small spots of high intensity with relatively small divergence [8].

Lasers can operate in two different fashions: as continuous wave or by generating pulses. Depending on the pulse duration that can be partially dependent on active medium in the laser source that is either gas, liquid or solid-state, a further classification of lasers can be distinguished as ultrafast whose time duration is within femtoseconds or picoseconds (ultrashort pulses), sources generating short pulses in nanosecond regime or longer up to millisecond magnitude. Another sorting factor is the emitted wavelength from the laser source which ranges from ultraviolet (100 nm) through visible spectrum (400 – 700 nm), near-infrared (700 – 1400 nm) to far infrared (1400 nm – 1 mm) and the usability strongly influences the application as it is indicated in Figure 2.1.

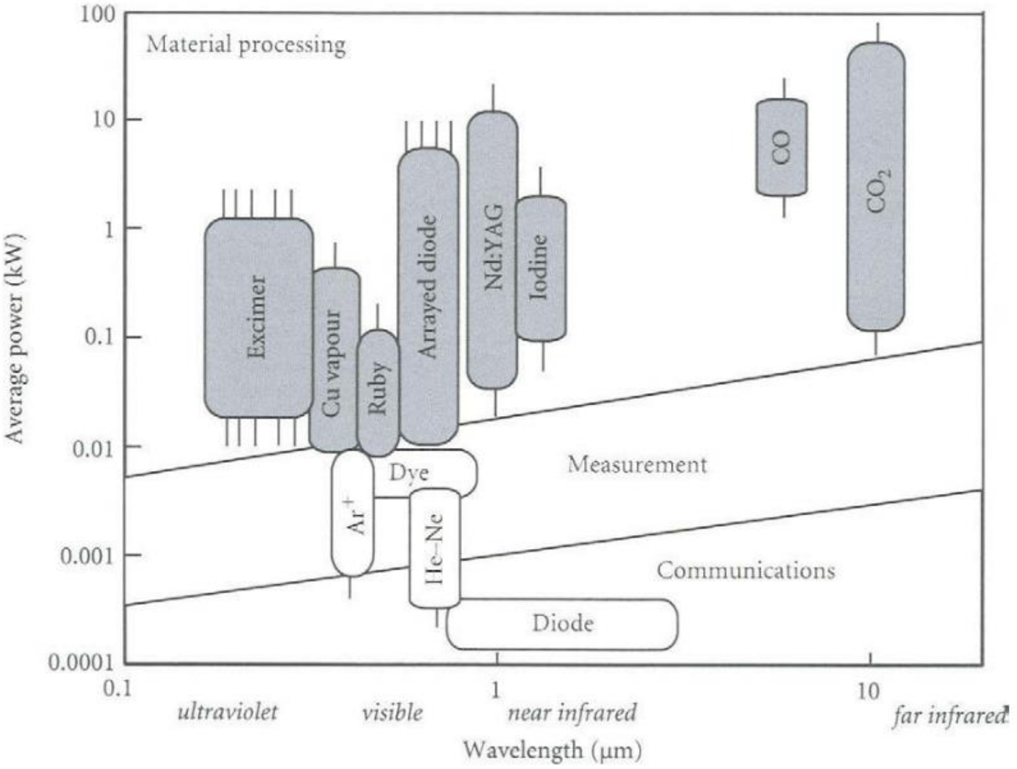

Figure 2.1 Commercially available lasers divided by emitted wavelength and offered average power with highlighted areas of application. Shaded laser sources are used for material processing [9].

Laser technology has become frequently employed in industry, especially in manufacturing, due to its exceptional advantages. Besides the unique feature of focusing the laser beam with high energy density, it can also be done in a controlled manner which makes the process flexible and accurate. For instance, compared to traditional machining, in non-conventional Laser Beam Machining (LBM) there is no contact between the tool and workpiece [10]. For this reason, LBM has lower maintenance costs and it is applicable to a wider range of materials, including ceramics, plywood or polymers [11]. As a result of the aforementioned benefits, material removal is possible with very narrow tolerances even below micron scale. For thermal processes, the heat affected zone (HAZ) is narrow and localised without microstructure changes in the bulk [12].

It does not come as a surprise that laser processes can surpass traditional approaches as single laser system can be effortlessly employed in more than one process, e.g. in drilling, cutting, engraving, welding, polishing, surface hardening or surface chemistry modifications to name a few. Particularly attracting researchers' attention in the recent decades is laser structuring which can be defined as creating simple geometries on material's surface such as small holes, trenches, cavities or generating periodic structures [13]. It enables obtaining additional or enhanced existing functionalities on the material's surface which is another significant benefit of laser processing.

2.2. Basic principles and laser-material interactions

Stimulated emission is the main phenomenon occurring in the laser source. Simply illustrated in Figure 2.2a, an incoming photon stimulates an excited atom or ion to undergo a transition from the excited to the ground state. After emission, the output photon has exact properties, i.e., wavelength, phase and direction as the original photon and, consequently, the power of the incoming radiation is amplified [9]. The atoms of the gain medium are put to the excited state by an external light source in a process called pumping by electric current, flash lamp or another laser. Third main component of laser source is optical resonator that consists of a pair of parallel mirrors, one highly reflective and second semi-transparent, located on ends of laser medium (Figure 2.2b). Light bounces back and forth between them, being amplified by the gain. Resulting output light is normally in a form of narrow beam that can be used for material processing [14].

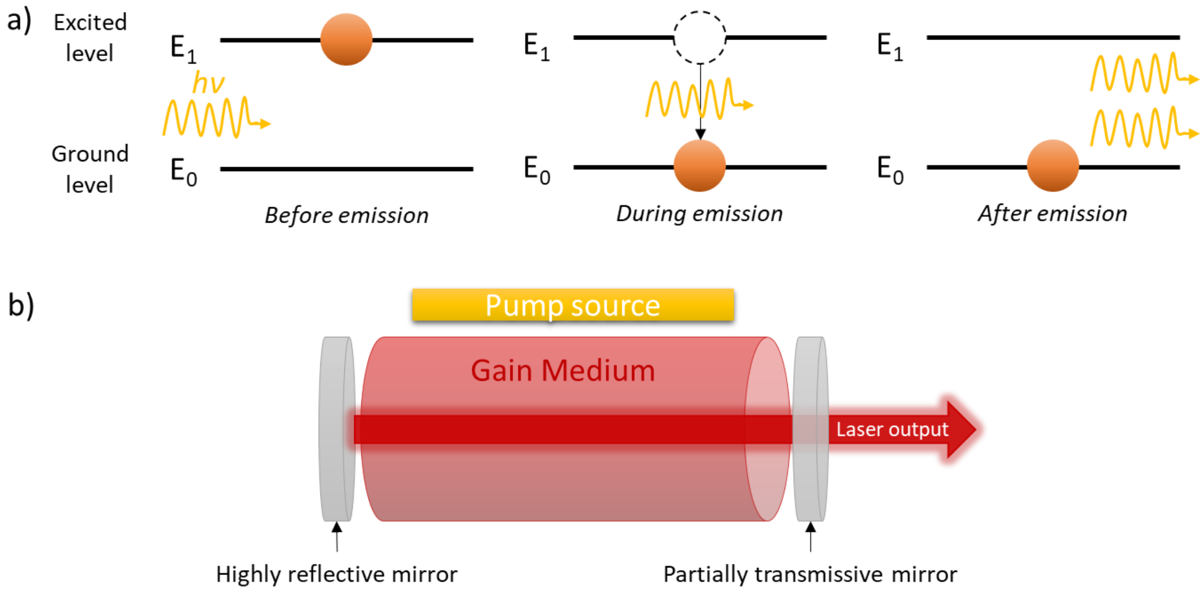

Figure 2.2 Schematic diagrams illustrating a) the process of stimulated emission and b) laser construction outlining major components.

The parameters of the laser beam determine the laser-matter interactions. The output beam’s wavelength, dependent on the gain medium, decide about the reflection, absorption and transmission of the light in the material. In fact, this feature becomes convenient when processing composite materials or welding two dissimilar ones where the laser light passes through one material to be absorbed by the other [15], [16].

Second important parameter is the mode of delivering laser beam. In continuous wave (CW) power is delivered constantly over time and is mostly used for cutting and welding applications [17]. Whereas pulses, characterized by high peak powers (with relatively low average power values), length and repetition rate, offer higher flexibility in controlling the way energy is distributed. Pulsed laser interactions with metals and semiconductors can be distinguished into two mechanisms: photothermal or photochemical [18]. The first occurs for short pulses, nanoseconds and longer, where linearly absorbed laser energy is transformed into heat, namely material initially melts and then evaporates. The photochemical mechanism, identified during ultrashort (femtosecond) laser pulses processing, results in non-thermal effects in the material mostly because the electron-lattice relaxation time is from 1 to 10 picosecond. Initially, electrons reach critical temperatures on the surface, and then, being in unstable nonequilibrium state, material is being ejected due to high pressure, while temperature of the system remains unchanged [19].

Nonlinear multiphoton absorption is the greatest advantage of femtosecond lasers that broadens the range of laser processing applications, i.e. corneal vision correction [20], 3D glass processing [21], but most of all, for material’s surface processing as well. Main resulting difference on the material is the absence of thermal effects, in particular negligible, residual HAZ, no presence of recast layer, damaged surface or micro cracks thus achieving very high quality of produced features [22], [23].

Another characteristic of the output beam is its polarization state described as oscillation of electric field in a certain direction perpendicular to the propagation of the laser beam. If this oscillation occurs in a single plane, polarization is linear, parallel or perpendicular to the incidence plane, referred as p and s type of polarization, respectively. The light can be circularly polarized if the electric field rotates around the direction of propagation (left- or right-hand). Described by Fresnel equations, polarization type strongly influences absorption mechanism of the laser energy with respect to the angle of incidence. For example, hot iron’s absorptivity of p-type is 10 times higher than s-type polarization for angles exceeding 80 degrees [24].

A parameter that describes the energy density delivered per unit area of laser pulse is fluence. Specifically, it is a position-dependent optical intensity of the laser beam. For laser processing the term peak fluence is commonly used representing the highest fluence value in the beam profile. In case of Gaussian laser beam distribution, peak fluence occurs in the middle of the beam axes.

2.3. Laser system and beam delivery

Laser as a source is not a standalone device and to benefit from its features, it has to be integrated into the system where the beam is guided, modified or transformed to desired shape and state. This kind of platforms can be constructed in a flexible configuration to be suited for the application or for the complex shape of the workpiece. Hence, main components included in laser systems consider beam delivery, workpiece manipulation and inspection, monitoring tools. The schematic diagrams of listed optical components and how they modify the beam are presented in Figure 2.3.

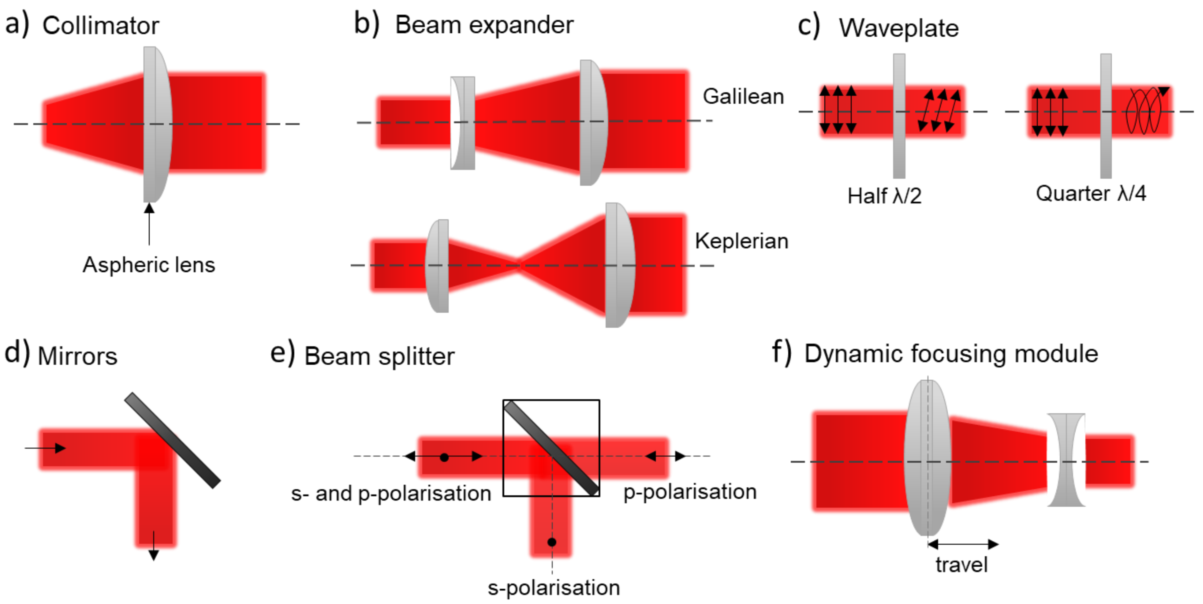

Figure 2.3 Schematic diagrams of optical components and their modification in laser beam: a) collimator, b) Galilean and Keplerian beam expander, c) half-wave and quarter-wave plates, d) mirror, e) beam splitting the polarization into p- and s- type, f) DFM with travelling and stationary lens.

Main function of collimator is to transform the divergent beam into a collimated one. Output beam after single aspherical lens is parallel and that makes the beam more manageable (Figure 2.3a). Adding one more lens enables change of beam size while still maintaining collimated beam. Beam expander, in Figure 2.3b, can have Galilean configuration that consist of convex and concave lenses while Keplerian type has two concave ones [25]. Polarization is controlled mostly by delaying or retarding the phase (half-wave or quarter-wave in Figure 2.3c) in the polarization direction which is achieved through birefringence phenomena in transmissive waveplates or functioning in reflective mode, based on nanostructured metallic surfaces [26]. For modification of spatial profiles of the laser beam, a beam shaper might be used that allows flat top-hat profile based on refractive, diffractive or absorptive elements [27]. Steering of the beam can be done by highly reflective mirrors (Figure 2.3d) which minimize the energy losses. They are covered with high performance multi-layered coating that has to be specifically chosen for optical intensity or wavelength [28]. Another type of mirror, used in laser systems, is a beam splitter where laser beam is divided into several components, for instance as shown in Figure 2.3e, two separate orthogonally polarized light beams [29].

After beam modifications, an important component on beam path delivery is the scan head. Demand for laser machining and processing of complex parts require to operate optical axes not only in X and Y directions but also Z with high dynamic capabilities. This is resolved in 3D scan heads by employing Dynamic Focusing Modules (DFM) which operation relies on two lenses, one moveable divergent or convergent and second stationary focusing lens (Figure 2.3f). This produces a change in the system's overall focal length, synchronized with the galvo scanner's mirror motion [30]. Changing distance between the optics during laser operation enables laser beam spot to be focused on different planes along propagation axis which allows to focus the beam within the volume [31]. Thanks to this faster processing speeds can be employed when compared to mechanical XYZ stages but there are limitation in the working volume in Z up to 10mm. The beam spatial intensity distribution should be maintained as for traditional XY galvo scanners as long as the processing settings are within the limits, e.g. DFM is not able to cope with scanning speeds higher than 1.5 m/s for dynamic repositioning [31]. Traditional galvo scanners rely on motorized mirrors that steer the beam in X and Y direction with remarkable accuracy and precision, e.g., about 5 μm and reaching scanning speeds up to 25 m/s [32]. Recently, with the growth of available laser power and increased pulsed repetition rates, polygon scanners are involved achieving twice the scan speed of galvo scanner [33] while their maximum capability is even at 1000 m/s [34].

Final optical component on the laser beam path delivery is the focusing lens. Two f-theta types are distinguished, normal and telecentric ones. In each case these focusing element consist of stack of optical lenses to allow movement of the focused beam on a working plane or, in case of 3D processing with DFM, within a volume. Telecentric lens has the advantage that the laser incident angle is always orthogonal to the surface and beam spot is not deflected while in a non-telecentric configuration this occurs only in the centre of the Field of View (FoV) [35].

For successful integration of laser into manufacturing process additional positioning and handling devices are needed. In order to scan area larger than lens’ FoV, workpiece movements should be resolved either simultaneously during laser scanning or as sample repositioning. The processing envelope is dictated by the complex geometry of the workpiece and scanning strategy. Typically, configuration of laser micro-manufacturing platform consists of X, Y and Z mechanical stages, on top of the optical three in scan head. With addition of rotary axis, a fully integrated system can be used for multi-process laser manufacturing. Recently, a system with simultaneous 7-axes was developed specifically for complex 3D geometries for structuring biomedical implants [36].

Inspection devices needed for quality control and monitoring of the process might consist of power meters, high resolution positioning cameras or optical probes. Those aid the preparation procedure, e.g., locating focal plane, and calibration of the lens and system coordinates prior laser processing and can be set up in automation techniques.

As those components help to reduce the preparation work, more advanced inline processing monitoring solutions are also being proposed recently. An example can be a measurement technique based on the frequency domain optical coherence tomography that allows its integration into the laser system based on beam splitting. The study proposed a measurement concept for a direct and accurate surface inspection during the structuring process [37]. This technique is based on low-coherence interferometry where the depth, up to 1.3 mm, can be acquired from analysed spectrum of the interferogram. The axial resolution of the measurement prototype was 4.5 µm and could have been reduced with image post-processing to sub-micron scale. This approach proved to be suitable for dimensional measurement of laser machined structures produced with ns laser source.

An example of an optical path in micro processing laser system is shown in Figure 2.4. The configuration can be used to scan the sample with polarized femtosecond laser beam and, hence, produce laser structures/textures, LIPSS included.

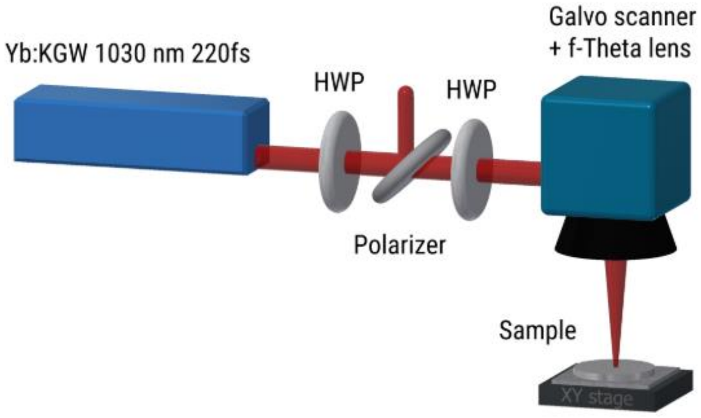

Figure 2.4 An example of optical setup for processing LIPSS consisting of fs laser source, HWP – half-wave plate, polarizer, galvo scanner and focusing f-theta lens [38].

2.4. Laser Induced Periodic Surface Structures (LIPSS)

2.4.1. Highlights and applications

Laser Induced Periodic Surface Structures (LIPSS) were first reported by Birnbaum in 1965 on germanium and described as "a regular system of parallel straight lines" [39] and since then they have been thoroughly studied by researchers. This interest spiked up even more two decades ago when ultrafast laser sources have become widely available. As can be seen in Figure 2.5, the results from the ISI Web of Science database show that the number of publications about LIPSS keeps increasing exponentially, and in 2020 year only, there were almost 150 records published.

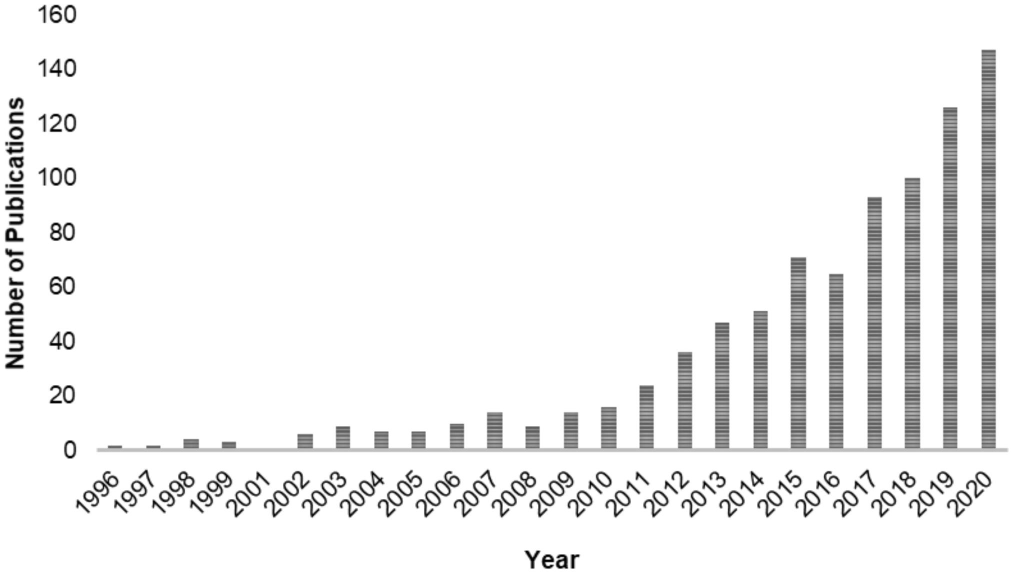

Figure 2.5 Number of publications with LIPSS as subject from year 1996 to 2020 from ISI Web of Science database, accessed on 23 Jan 2021.

LIPSS appear on the material's surface after laser irradiation as self-organized parallel ripples. Systematic studies on metals, semiconductors and dielectric revealed that main parameters affecting LIPSS morphology are material dependent constants, i.e., optical, thermal or surface properties, and laser beam settings such as fluence, wavelength, polarization type, pulse duration or angle of incidence. Ripples periodicity (Λ) is smaller than the focused beam spot size and usually depends on the laser source wavelength (λ). First theory on the LIPSS origin was based on the diffraction phenomenon of the laser beam and proposed that the ripples form by local ablation at the maximum of the intensity patterns [39] which then evolved into a variety of origin theories that are briefly explained in Section 2.4.4. Based on that two types of LIPSS can be distinguished: low spatial frequency LIPSS (LSFL) whose Λ is proportional to λ and high spatial frequency LIPSS (HSFL) that have smaller periods than λ. LSFL appear perpendicular to the linear polarization vector while HSFL can be orthogonal or parallel to polarization. LIPSS have been mostly observed after irradiation of fast and ultrafast pulse durations and these, i.e. femtosecond and picosecond, are mostly studied because of the simplicity of their producibility. The depth of LIPSS, measured as the average from peak-to-valley distance, was reported to be mostly influenced by the accumulated fluence used but also pulse duration [40], [41]. In the first study, the ripple depth was reported to be in the range from 130 nm to 220 nm and had a logarithmic dependency to the used accumulated fluence, which can be also referred as irradiation dose, in the range from 6.7 J/cm^2 to 29.5 J/cm^2. The accumulated fluence was calculated as the multiplication of peak fluence and number of pulses per spot. The parameters utilized for peak fluence were starting from 0.079 J/cm^2 to 0.35 J/cm^2 while the pulses per spot were varying from 19 to 374. It is worth noting that the laser source’s wavelength used for the experiment was 800 nm, pulse duration 300 fs and the structuring occurred on stainless steel sample [40]. For the same material, but with laser source’s wavelength and pulse duration of 532 nm and 100 ns, respectively, the reported depth of LIPSS was between 28 and 35 nm. The reported peak fluence was 3.3 J/cm^2 while, by varying the beam spot overlap, the accumulated fluence was in the range of 238 - 356 J/cm^2.

It is for the LIPSS physical characteristics and single processing step, that its potential for surface functionalization has been recognized. The benefit of adding new properties or improve the existing ones is integral in the modern engineering solutions with constantly increasing requirements for the materials and for surface engineering. Laser surface functionalization with micron/sub-micron structuring competes against conventional methods, such as etching [42], lithography [43], electrochemical anodization [44] or coating’s deposition methods with being more environmentally friendly and economically sustainable.

Highlights of the most common but also latest potential applications for LIPSS are presented below:

a) *Structural colouring*. As LIPSS periodicity is close or equal to the visible spectrum of light, first sign of LIPSS presence on the surface is the light diffraction. Therefore, ripples act as a diffraction grating and the angle-dependent colours are influenced by their periodicity and orientation. Additionally, due to display of selective patterns with good spatial resolution, this property found its application in anti-counterfeiting labelling, optical encryption or optical data storage [45], [46]. A promising approach was also presented in optical color marking to print images on metallic surfaces as shown in Figure 2.6.

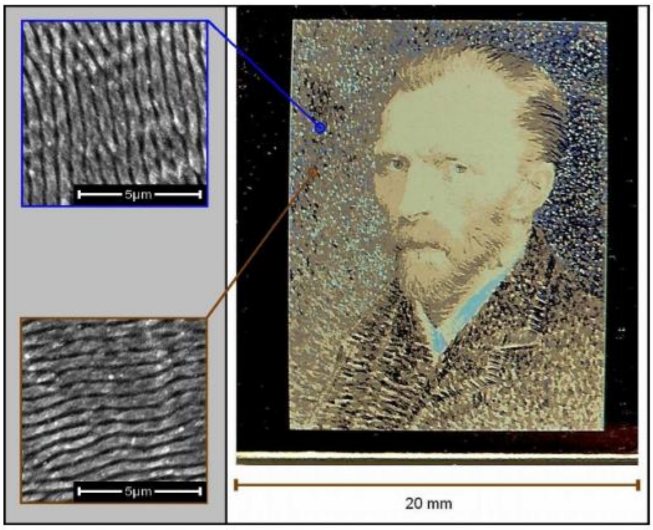

Figure 2.6 Color effects obtained by controlled nanostructures with a femtosecond laser on a 316L stainless steel sample, on the left, SEM images of controlled nanostructures marked with two different orientations [47].

b) *Light absorption modification*. Laser structures might increase the light absorption when compared to non-treated surface. LIPSS fabricated on Ti samples decrease the reflectivity by 10-30% and that can be reduced even more if additional nanogrooves, nanocavities are present on the surface which are controlled with varying laser settings [48]. Combining the hierarchical structuring (micron scale trenches + nanoripples) leads to anti-reflective surface with 2-4% reflection of incident broad spectrum light [49]–[51]. The phenomena is explained by increased surface roughness that enhance multiple reflections and absorptions. This surface modification finds applications in sensing, optoelectronic devices and solar cells.

c) *Tribology*. LIPSS have been widely recognized for the frictional properties, especially known to reduce coefficient of friction and wear. LIPSS covered on biomedical implant material resulted with friction coefficient 3 times smaller when compared to non-irradiated surface [52]. However, for different materials, it was reported that the reduction is negligible or significant only if certain lubrication is used [53], [54]. Creating femtosecond multi-scale periodic structures showed again more favourable case for friction reduction [55]. Proposing new direction of tribological improvements for reducing energy losses that contribute to CO_2 emissions, is vital in future manufacturing technologies and laser structuring is on this path [56].

d) *Antibacterial.* Laser structures have been studied for reducing bacterial adhesion and resisting the biofilm formation of various bacteria. LIPSS of Λ = 600 nm created on Au showed almost no E.coli bacteria after 24 hours [57]. Similar results were obtained on non-corrosive steel, presented in Figure 2.7, though reduction of bacterial colonization was not detected for materials that are prone to corrosion [58]. Testing of different bacteria, S. aureus, on LIPSS with around 700 nm periodicity on Ti revealed that area covered with the bacteria was only 7% and no significant biofilm formation was detected. It is explained by inhibited penetration of bacteria by reducing of the contact area for the attachment which proves suitability of laser structuring of dental and orthopaedic implants [59].

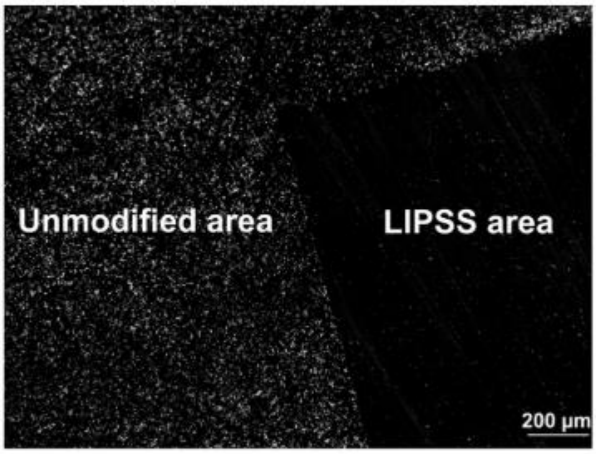

Figure 2.7 Fluorescence microscope images of samples colonized with E. coli on a corrosion resistant stainless steel [58].

e) *Cell proliferation.* Topographical features have an impact on cell adhesion and spreading next to the influence of surface chemistry. It was observed that different types of mammalian cells adhesion, orientation and proliferation can be improved and controlled on polystyrene surface covered with LIPSS. Their alignment axis is along the ripples orientation and cell density increases more than twice when compared to non-treated surface [60]. Similar trend was observed for CoCr material, even if LIPSS topographies are of relatively low surface roughness, sub-micron scale, it is sufficient for better cell anchoring effect [61]. This is highly applicable in bio-chip manufacturing, knee implants or general tissue engineering.

f) *Control of wetting properties.* LIPSS have been widely studied for wettability modifications after laser structuring. In general, contact angle (CA) values depend on surface chemistry and as well as on topography and both are modified after laser treatment. It was studied that CA values are not immediate stabilized after laser structuring of metals. It can take up to 15 - 30 days for surfaces to evolve from hydrophilic to superhydrophobic [62]. Applying laser structures for control of wettability is used on masters in polymer replications. The replicas, however, do not show such big changes in CA and only small differences have been reported [63]. Based on findings, it is concluded that mostly the laser-induced chemical variations affect the surface wettability rather than the topography of sub-micron LIPSS. Other than those mentioned, ripples can be fabricated for self-cleaning surfaces or for the purpose of directed fluid transport [64].

g) *Surface enhanced Raman spectroscopy (SERS)*. This analytical tool became important for broadening the quantitative determination in detecting molecular-specific chemical compounds or proteins from solutions. Nano structured surfaces substrates for SERS proved to substantially outperform commercially available ones in terms of sensitivity and reproducibility [65]. This method, when compared to other available ones, is simple in preparation, flexible for complex geometries and sample contamination can be eliminated. It might be applied in the fields of security, hazardous material detection or nanoelectronics [66].

h) *Other*. While a lot of publications focused on studying the LIPSS towards the further development of the aforementioned applications, some studies pointed out other promising areas where LIPSS can be applied. A research group demonstrated that a LIPSS covered surface of a tensile sample showed mechano-responsive change of colours which was associated to the sample’s deformation, as shown in Figure 2.8. This LIPSS implementation can be used for fabrication of safety devices or early detection of material failure where a change of color would indicate increasing deformation and this would be a warning before sudden rupture [67]. This phenomenon was possible to observe because the LIPSS periodicity would increase and therefore the wavelength diffracting from the ripples changed with fixed viewing angle. Another unique applications recently emerged are the LIPSS fabrication on reflective waveplates [26] or on a platinum electrodes in improving oxygen reduction catalysis process [68]. The latter study chose LIPSS structures to enhance the electrochemical activity of platinum by enlarging the number of active sites through increasing the surface area. Studies have been also carried out to produce ripples on the aerospace metal’s surface for reduction of the ice-accretion [69].

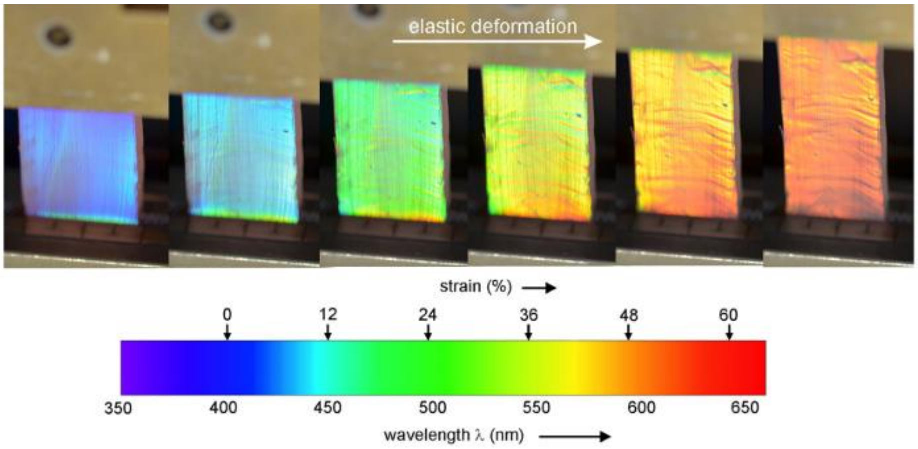

Figure 2.8 Structural colours resulting from LIPSS fabricated by replica casting using a stainless steel master. Elastic deformation results in a reversible mechano-responsive colour-change in the visible electromagnetic spectrum from blue to red [67].

2.4.2. LIPSS on coatings

The main purpose of applying coatings is to enhance product's performance. It can elevate the working surface strength or resistance. In particular, use of coatings can ensure low friction and non-sticky surface as well as to avoid chemical or abrasion alterations, improve corrosion prevention, electrical insulation among other specific functions [70]–[72]. Even though surface engineering through coatings competes with laser surface structuring, synergistic use of both techniques allows to benefit from chemical, mechanical properties of the coating and additional functionalization from laser structures [7], [73]. The combinations is worth considering especially for micro structuring of high hardness and brittle coatings because otherwise such effects are difficult to be achieved with conventional methods.

The processing window for LIPSS formation on bulk materials, particularly for larger areas, is achieved by overlapping scanning of laser beam and is obtained usually below material's ablation thresholds and with sufficient number of pulses on the surface. Additionally, in the case of thin films structuring, other factors have to be considered such as substrate effect, delamination and thin film's adhesion [74], [75]. It was shown that LIPSS produced on thin titanium nitrides (TiN) or on thinly deposited MoS_2 on cemented carbides, improved tribological and wetting performance when compared to non-structured samples [76], [77]. Hence, they represent a promising approach in industrial applications for tooling, bearings, moulds-making where low friction and high wear resistance is desired.

2.4.2.1. LIPSS on DLC

Diamond-like carbon (DLC) is an amorphous carbon material with majority of tetrahedral bonds (sp^3) that are responsible for its superior properties that also can be found in diamonds [78]. In particular, the coating is well known for its high hardness and low coefficient of friction. Additionally, good biocompatibility, chemical inertness and low surface roughness makes the DLC suitable as protective coatings in heart valves, inkjets printers and optoelectronic devices. Similarly, DLC proved to be valuable in automotive industry where increasing life cycle and minimizing energy consumption is prioritised by means of reducing wear and friction [79]–[81]. DLC coatings can be also used on tooling and masters in injection moulding as a solid lubricant to reduce demoulding forces, improve replication efficiency or increase the surface's durability which results in higher components life's span [80].

DLC's attractive physical and mechanical properties strongly depend on chemical and structural conditions. It is reflected in the ratio of sp^3 and sp^2 bonds, content of hydrogen [82] or other doping elements [80], [83]. Studies showed that DLC thin film's structure evolve into nanocrystalline graphite, also known as glassy carbon (GC), when the coating is exposed to higher temperatures between 200°C and 450°C [84] and similar thermal effects were observed when DLC is exposed to laser irradiation [85]. Laser energy from long and short pulses delivered to the surface causes transformation of sp^3 bonds into sp^2 and crystallization of the amorphous matrix. Therefore, with increased laser intensity and pulse duration the processes of graphitisation, spallation and evaporation take place [86]. Hence, for the purpose of fine DLC laser structuring, ultrafast laser sources are a favourable technique because the thermal effects can be minimized.

The effects and the potential for improved surface phenomena of ultrafast laser processing of DLC with observed LIPSS have been reported and the comparison of the findings is summarized in Table 2.1.

The listed studies aim was to show the change in functional response of LIPSS created on DLC compared to a non-structured coating and/or investigate structural modifications as the effects of ultrafast structuring. Each study utilized different ultrafast laser sources hence the range of fluence and number of pulses was varying. Most of the studies reported only the fact that LIPSS can be generated on the coating without presenting an optimization study of how to transfer from single spot irradiation to large area structuring. Yasumaru et al. [73] followed a traditional strategy of scanning laser beam along the surface with overlapping laser beams in X and Y over the area of 15 mm x 15 mm to achieve uniformly nanostructured surface. The authors also performed laser scanning of net-like patterning which means that laser beam overlapped only in one direction. From the periodicities reported in the Table 2.1 it can be concluded that both LSFL with Λ close to λ and second type HSFL (Λ ≈ 0.1-0.2λ) were created. The regularity of the ripples was never investigated in the mentioned studies. The LIPSS were categorized as regular or irregular in Table 2.1 based on the images provided whether the ripples showed straight lines with continuity within the irradiated single spot. It is worth noting that the studies reported one set of parameters for generating LIPSS without indicating the ranges in which the ripples do not change its morphological characteristics or the threshold of their transformations, e.g. from HSFL to LSFL. The functional tests that were carried out on laser structured DLC were checking mostly the tribological surface properties where the same beneficial low coefficient of friction could have been maintained when compared to non-structured sample. For example, Pfeiffer et al [87] reported decrease of CoF from 0.15 to 0.06 when the LIPSS are present on the DLC coated steel sample.

Most of the studies reported in Table 2.1 investigated the structural changes in the coating after the ultrafast laser irradiation based on the Raman spectra analysis of as-received and laser structured surface. Structural changes are possible to observe due to deconvolution of the spectra into two peaks D (1550 cm^{-1}) and G (1355 cm^{-1}) and analyse their ratios as well as peak positions. Shifts in the identified peaks indicate structural changes in carbonaceous materials (more details are provided in Section 4.3.2.1.).

Table 2.1 Summary of published studies of LIPSS produced with ultrafast laser on DLC. τ – pulse duration; λ – laser wavelength, nm; F – fluence, J/cm^2; N – number of pulses; Irradiated surface (SP – single spot, A – area, L – line); Λ – periodicity, nm; Functionality (CoF – coefficient of friction); Regularity (R – regular, IR – irregular); Structural changes (GR – graphitization, GC – glassy carbon); N/A – not studied, Ref. - references [73], [87]–[92].

τ	λ	F	N	Irr. sur.	Λ	Functionality	Reg.	Structural	Ref.
10 ps	532	0.3 - 0.76	100	SP	N/A	N/A	IR	GR, LIPSS on substrate	[88]
100 fs	800	0.05-0.15	30-1000	SP	75 - 170	N/A	IR	DLC → GC LIPSS on GC	[89]
120 fs	800	0.12-0.15	100-1000	SP	100	Decreased reflectivity, higher conductivity	IR	Non-thermal Partial DLC → GC	[90]
150 fs	800	0.3	20	SP	600	N/A	R	GR and ablation	[91]

100 fs	800	0.14	150	A	120	CoF: smaller or similar, decreased with MoS_2	IR	DLC → GC	[73]
320 fs	1030	Pulse energy = 2uJ	40	L	N/A	CoF increase with SS counterpart, decreased for Si_3N_4, modified wettability	IR	GR	[92]
150, 200 fs	387, 775	3.56, 14.19	2-10	SP, A	667, 330	CoF from 0.15 to 0.06	R	N/A	[87]

Yasumaru et al. [93] stated that ultrashort laser pulses led to creation of thin graphitization layer on top of DLC which structurally resemble of GC. The results were based using Raman spectroscopy and analysis of the shifts in the peak's position and widths. Glassy carbon is a carbon material with physical and chemical properties similar to DLC but having small graphite crystallites (~ 3 nm). It was shown that at fluences close to threshold, the spectral peaks are at $1355 cm^{-1}$ and $1590 cm^{-1}$ that are typical for GC. While when the fluence is increased the authors suggested the spectra consist of superposed GC and DLC. Other studies indicated that thin graphitized layer is formed after ultrafast laser irradiation of depths between 200 – 500 nm [91].

In conclusion, use of laser on DLC, even ultrafast one, might lead to undesirable mechanical and structural modifications such as changes in frictional properties or creation of thin laser-modified layers. Additionally, the studies reported focused only on reporting LIPSS generation within single spot irradiation of laser beam with a sufficient number of pulses without further examining the regularity of ripples and without exploring the influence of processing parameters. Additionally, most of the laser treated coatings were investigated for tribological performance and the CoF was reported to be similar or reduced when compared to non-treated surface, however a material used as a counterpart influenced the resulting CoF value.

Taking above into consideration, it is challenging to establish a processing window of laser settings where regular LIPSS are created on larger area without excessive ablation or delamination of DLC. Nonetheless, the synergistic approach of using both coating and laser structuring for enhancing surface properties is particularly desirable for producing durable replications masters since while the process benefits from higher wear resistance and lower demoulding forces due to low friction the ripples structures can also be passed on to polymer replicas in the injection moulding process.

This DLC coating is already used in this manufacturing process and the demoulding forces were reduced between 16% and 37% [94], [95]. The replication capabilities of this technology are constrained to the surface geometry and quality of the mould master. Especially for micro injection moulding the successful replication of micro and nano features is depending on the mould surface properties that contributes to high replication fidelity [80]. One way to achieve a mould surface with increased wear resistance, for increased tooling life, is applying the coating on the tooling. Then, a surface structuring method, such as laser structuring, which includes generation of LIPSS, can be performed to obtain micro, sub-micron or nano features on the coating’s surface. This way a mould master has the surface functionalities due to modified topography that through the replication process will be transferred to the polymer replicas. The combination of laser structuring and applying the coating on the mould substrate is to achieve a surface of the master that is durable and at the same time have the functional properties from LIPSS.

It is one possible scenario to produce replicas with functionalised surfaces. It might be worth mentioning that the combination of laser structuring on DLC coating can be used for other applications, too, wherever it is beneficial to have at the same time the advantageous DLC surface properties with LIPSS many added surface functionalities. The suitability of LIPSS treatments for processing DLC coatings should be investigated and thus to assess the capabilities of these two surface engineering technologies for the potential of producing durable and functional replication masters in injection moulding technology. This formulates the first open question answered in this thesis and corresponds to research Chapter 4 (also see Figure 1.1).

2.4.3. LIPSS and 3D processing disturbances

Implementing the laser structuring/texturing process on a large scale still has some limitations regardless the listed benefits of added surface functionalities summarized in Section 2.4.1. The best functional performance can be achieved when LIPSS topographical characteristics are considered as optimized. This means that for each functionality the requirements for LIPSS characteristic might vary. A good example is showed in the functional performance of LIPSS for display of structural colours and antibacterial properties. In the first case, the ripples regularity and alignment is important for the proper colour display [45], [46] while for the latter it was proven that it is the feature's size, i.e. depth and periodicity, that will inhibit bacterial growth is more vital and the regularity is not the criteria in this functional response [59]. There is no standardized measurement method for quantitatively assessing regularity of LIPSS but the most common procedure is through image processing of SEM and AFM topography images [96]. The 'recipe' for optimized ripples is normally defined in trials of varying the laser processing parameters most relevant to LIPSS generation, i.e. fluence, pulse overlap, wavelength, polarization etc, or aided by implementing modelling approaches (see Section 2.4.4). Another important factor influencing LIPSS uniformity is the surface condition, e.g. roughness and presence of defects [97], [98]. Overall, there are a lot of conditions that have to be satisfied to achieve desired ripples structures and those have been studied, so far, on flat small scale surfaces. It is important to understand the LIPSS behaviour also when they are produced on more complex geometries and how the processing strategies should be adapted for this case. This is also important to allow address the barriers in the implementation of LIPSS on 3D surfaces, e.g. in thin film sensors integration or fabrication of moulded interconnected devices [99], [100].

When a laser beam is directed to the 3D workpiece there are two main factors that have an impact on the processing conditions. In Figure 2.9 a simplified case of an output beam being focused on a curved surface by telecentric lens is presented. The ideal conditions of focused beam and normal to the surface exist only in the centre of the FoV. Further away from this point, the more the processing conditions are affected by the Beam Incident Angle (BIA) and Focal Offset Distance (FOD). These two factors can be identified as processing disturbances and they may influence quite significantly the LIPSS generation process. They can be classified as disturbances when they are undesirably present during structuring. In most cases the processing disturbances will be present when the surface is non-planar and there are no additional actions in the laser system to guide the beam always perpendicular to the surface with focused beam spot. They can also happen when the optical positioning system is not correctly calibrated and the beam is misaligned in X, Y and/or Z direction. The effects of BIA and FOD on the surface affect the laser beam spot size but also alter the reflectivity/absorptivity of the incident laser energy by the irradiated material hence the changes in the laser processing conditions (further details in Section 5.2).

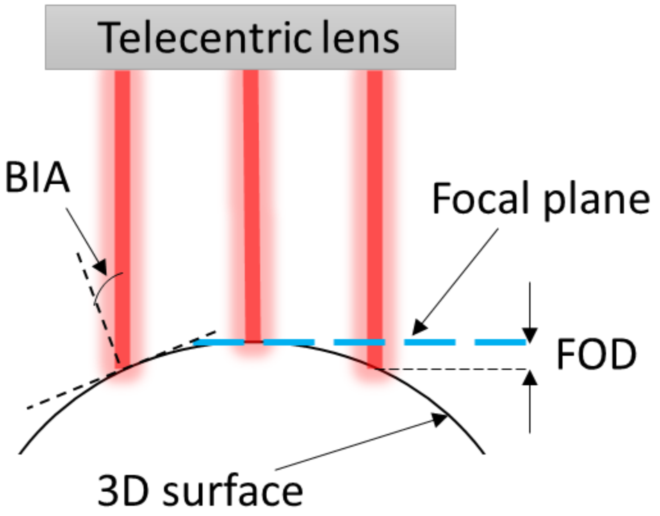

Figure 2.9 Graphic explaining the presence of processing disturbances on 3D surface.

The impact of the BIA on LIPSS have been studied and it has been observed that changing the angle of incidence, the period of ripples can be controlled [101]. Researchers focused on using this tendency for tuning the properties of periodic structures and still conducting the experiments on planar, tilted surfaces. At oblique incidence and with p-polarized beam, two types of ripple periods appear on the surface. Examples of LIPSS produced on steel at varied BIAs are presented in Figure 2.10.

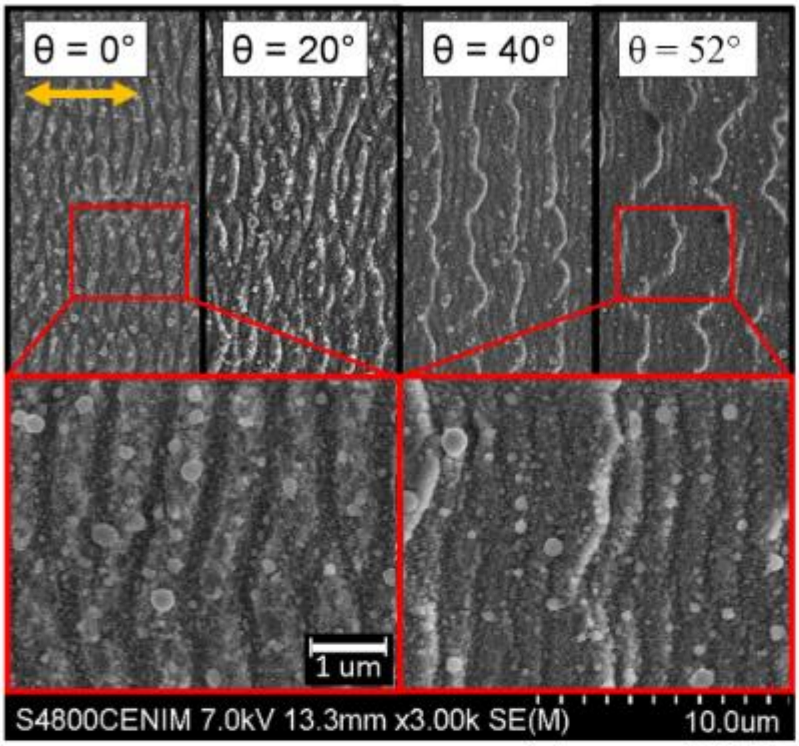

Figure 2.10 SEM images of LIPSS formed on steel at fluence 1.0 ± 0.1 J/cm^2. BIAs values are indicated in the top row on the pictures. Arrow indicates polarization direction [102].

This behaviour of ripples produced on tilted samples became a subject to study to understand more their generation process. LIPSS generated on metals with different optical constants showed that their orientation shifts with the increase of tilted angle, e.g. for stainless steel and Ti [103]. The presence of nanostructures covering the LIPSS on Au and Pt surface was acknowledged to have an impact on the angular dependence of ripples periods [104]. Same group of researchers also showed that with high BIAs of above 55°, the LIPSS profiles became more asymmetric and resembled blazed grating [105].

The influence of FOD on LIPSS is simpler to predict. Moving away from the focal plane, for Gaussian beams, the more the irradiated area increases and, since the energy delivered is constant, the fluence will be reduced. The beam waist, ω, evolution along the propagating axis (FOD $= z - z_0$) is well described by the equation [106]:

$$\omega(z) = \omega_0 \sqrt{\left[1 + \left(\frac{\lambda(z - z_0}{\pi {\omega_0}^2}\right)^2\right]} \qquad (2.1)$$

Where ω_0 is the smallest beam waist at z_0 position. The increased beam spot radius, and the consequently reduced peak fluence, leads to the conditions where LIPSS are not optimized. When the fluence drops below the fluence threshold, ripples cannot be longer generated on the surface. Laser structuring with defocused beam was proposed for upscaled manufacturing with higher laser powers where fluence was maintained within limits with increased beam spot size [107].

It should be stated that the Equation 2.1 is valid in case of ideal laser beam while, in reality, the fluence distribution on the surface may vary. Typically, one of the additional beam spot variations considered is the beam propagation comes from the limits of focusing lens, e.g. numerical aperture. On the other hand, the tolerance levels from calibration, beam instabilities or astigmatism are not considered in the processing parameters calculations. These factors might not be necessarily significant in laser machining, but could be critical for more sensitive processes, including LIPSS generation. A good solution would be to use an actual beam dimensions, e.g. measured by beam profiler.

One of the additional open issue on generating LIPSS on freeform surfaces is the inaccuracies in stitching, i.e. connecting the scanned paths/fields with the galvoscanner through laser beam repositioning on the surface. LIPSS discontinuities can be easily noticeable as a result of orientation mismatching or peak-to-valley misalignment. A method to reduce the stitching was proposed with changing the polarization direction during the process [108]. Another study recently showed that LIPSS can be also fabricated on freeform surfaces more efficiently with shaped femtosecond pulses in the propagation axis which helps to maintain stable energy distribution [109].

2.4.4. Origin and modelling of LIPSS

The phenomenon of LIPSS was firstly attributed to diffraction and the surface relief was explained by material removal at the maximum of intensity. However, with continued research interest in LIPSS and classification of LSFL and HSFL, different approaches for their explanation emerged. Up to now, ideas on LIPSS formation can be divided into (i) electromagnetic theories that assume the deposition of optical energy onto the solid and (ii) matter redistribution ones based on the rearrangement of surface near matter [110]. There is also analytical model based on the ultrafast laser irradiation to calculate the spatial fluence accumulation from the ultrafast laser pulses which is not included in the origin theories but was developed to empirically predict the ranges of laser processing parameters and to produce areas covered with homogenous LIPSS [111], [112]. The schematic of the theories are presented in Figure 2.11 and are discussed in the next paragraphs while their summary is later presented in Table 2.2.

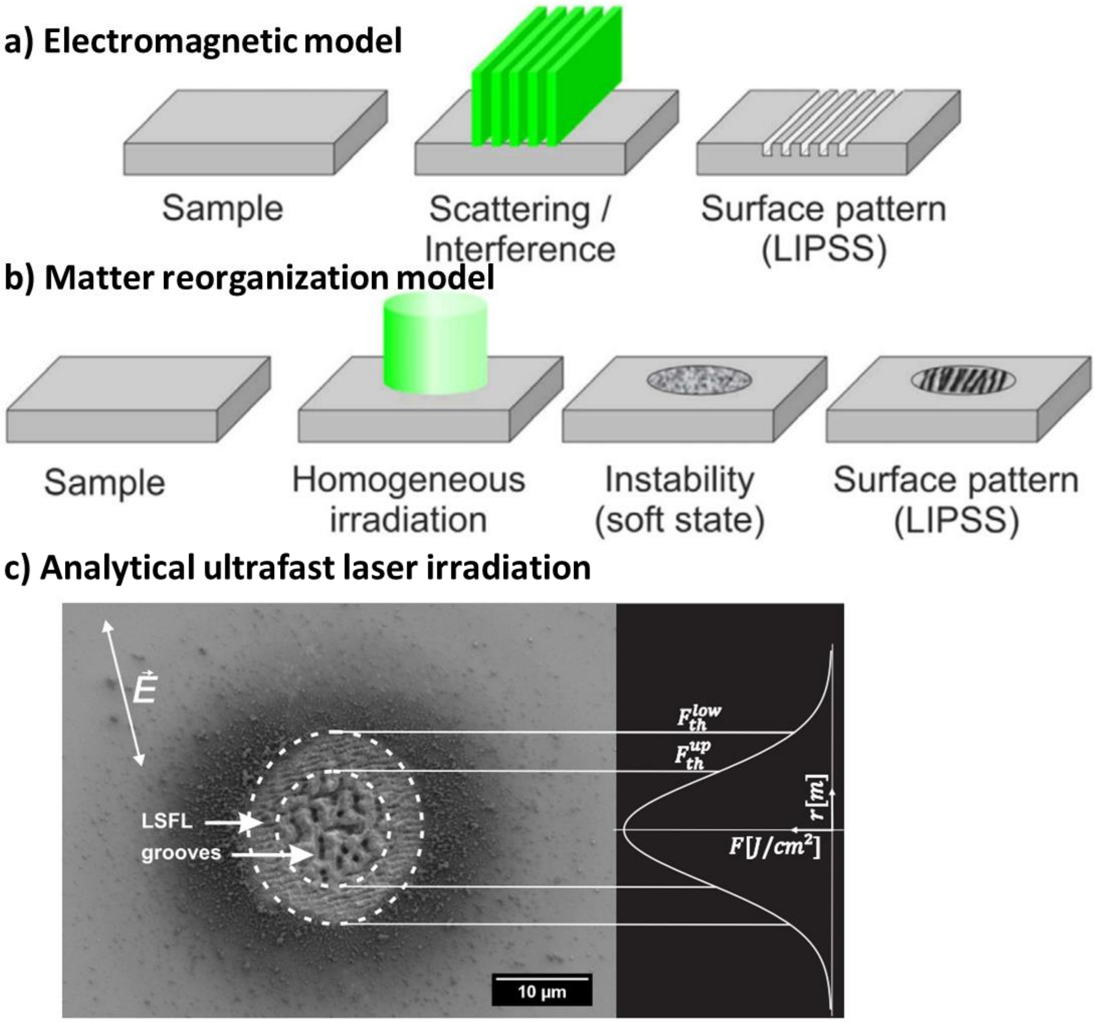

Figure 2.11 LIPSS origin theories on modelling into a) electromagnetic models b) matter reorganization models [110], [113] and with c) analytical approach of ultrafast laser irradiation model to calculate accumulated fluence based on the lower and upper fluence threshold requirements [111].

The main concepts on LIPSS origin are as follows:

- *Surface Electromagnetic Waves (SEW)*: Incident laser beam scatters on the rough surface and its interference may lead to excitation of surface plasmon polaritons (SPP) which results in a spatial intensity modulation that is imprinted on the surface via ablation [2]. This theory became commonly accepted for LIPSS with sub-wavelength periods (LSFL) calculated based on complex dielectric permittivity, ε, of the metal and the dielectric and is in good agreement with experimental evidences when low number of laser pulses is used [114]. Additionally, this theory can be extended to non-normal incidence based on s- or p- types of beam polarization.

- *Sipe's Theory*: Integral equation that describes dielectric polarization density for small roughness surface as a general scattered-field model. It predicts wave vectors, k, related to Λ as a function of surface parameters and laser irradiation parameters. The theory is based on efficacy factor that describes the moment where surface roughness can absorb optical radiation. It was shown to be relevant not only for metals and semiconductors but also transparent dielectrics [115], [116]. This theory was also combined with Drude model to acknowledge changes in ε for high intensity laser pulses and hence intra-pulse feedback is included [117].
- *Finite-Difference Time-Domain (FDTD) Simulations*: Numerically solving Maxwell's equations allowed to compute inhomogeneous energy absorption of fs pulses below the material's surface. The results were in good agreement with Sipe-Drude model [118] and with adding inter-pulse feedback, the FDTD could also include ablation conditions. The extended simulations could have predicted growth of other classes of LIPSS which process mechanism is based on hydrodynamic melt-flows [119].

- *Matter reorganization theories*: laser-excited material is reorganized into quasi-periodic group of surface protrusions through thermodynamic phase transitions, hydrodynamic effects (surface acoustic or capillary waves) of melted surface, material instabilities such as defects, erosion effects. These are relevant for long pulses, above few nanoseconds, or large number of pulses [110].

Ultrafast irradiation model was proposed in the past as a semi-empirical, analytical model for ultrafast micromachining predicting the depth and width of ablated craters or scanned lines [120]. The basis is to calculate initially the laser irradiation transmitted to the sample plane by spatial, but not temporal, laser intensity density of each laser pulse. Then, an ablated depth is obtained from one simple equation which is proportional to the logarithm of that laser intensity distribution and also a function of material dependent constants [121]. In particular, the calculated depth is dependent on the material's fluence threshold and optical absorption coefficient for lower fluences or thermal material properties for higher fluences. Additionally, the model includes the laser-material interactions also calculating the ratio of absorbed energy and the changes in fluence threshold due to incubation effect. With this few assumptions the ablation profile is predicted from irradiation the flat sample's surface with one single pulse, multiple pulses in one spot as well as multiple pulses scanned across area as trains of overlapping pulses.

More recent studies explored more the potential of the ultrafast irradiation model for micromachining. Cangueiro et al. [121] accommodated a standard model to predict the profile of ablated craters after every pulse in single spot irradiation. It was based on calculating the local surface angle in the crater profile point of a preceding pulse and the absorption depending on that angle. Additionally, the non-normal incidence of laser to the surface plane was also considered together with the fluence distribution calculated as a geometrical dependences of the flat surface, ablated profile and the fluence distribution. The proposed method obtained good match between experimental and modelled ablation profiles. Zemaitis et al. [122] used the same assumptions of the ultrafast irradiation model to propose the optimal point for highest ablation rate which can alleviate multi-level experiments. The authors extended the basic model by including spatial laser beam distribution along the propagation axis in x and y directions. Their model also included the prediction of ablation rate in a low and high number of pulses per spot regime. They proposed an analytical function with the soft saturation function. The experimental results proved to be aligned with modelled values based on ablation of rectangular cavities with 2.5D shape on copper flat surface samples.

Ultrafast irradiation model was also proposed for laser structuring. The reason that it could be applicable to this laser-based process is the accumulated fluence domain requirements for the spatial appearance of laser-induced structures [123]. It was observed that laser-induced structures appear on the surface in a conical arrangements, what can be observed on Figure 2.11c. That was due to the Gaussian fluence distribution which means there were structures appearing with higher fluence threshold in the centre of the irradiated spot and the structures with lower fluence threshold appeared on the periphery. Detailed studied revealed that different type of surface modification appear within ranges of material-specific threshold [2], [64]. Eichstadt et al. [112] suggested determining domain boundaries for the type of laser-induced structures by calculating the requirement of accumulated fluence needed to be delivered to the surface in order to obtain certain morphology. The main goal was to determine the laser processing parameters, i.e. peak fluence, number of pulses for generating uniformly covered LIPSS on the surface which could be achieved with delivering the fluence within the required domain, that is the lower threshold boundary and the upper fluence boundary which is highlighted also in Figure 2.12. They validated their model by producing areas with LIPSS by varying scanning speed and number of repetitions. They reported that the LIPSS were found to be with similar geometrical characteristics and it was argued that the accumulated fluence play an important role in spatial LIPSS emergence.

The same research group took the potential of modelling LIPSS even further by mathematically deriving the laser process parameters. Mezera and Romer [111] reported a non-iterative mathematical model to calculate optimal processing parameters to achieve areas on the surface homogenously covered with LIPSS. They proposed a calculation of accumulated fluence not as a summation of each pulse fluence intensity but they proposed a revision of the equation as Third Elliptic Theta function. With that approach the validation samples produced with different peak fluence and pulse overlap. The results were then classified based on the 2D FFT maps of their SEM images into no observed LIPSS, inhomogeneous or homogeneous and showed good agreement with the calculated accumulated fluence boundaries as presented in Figure 2.13.

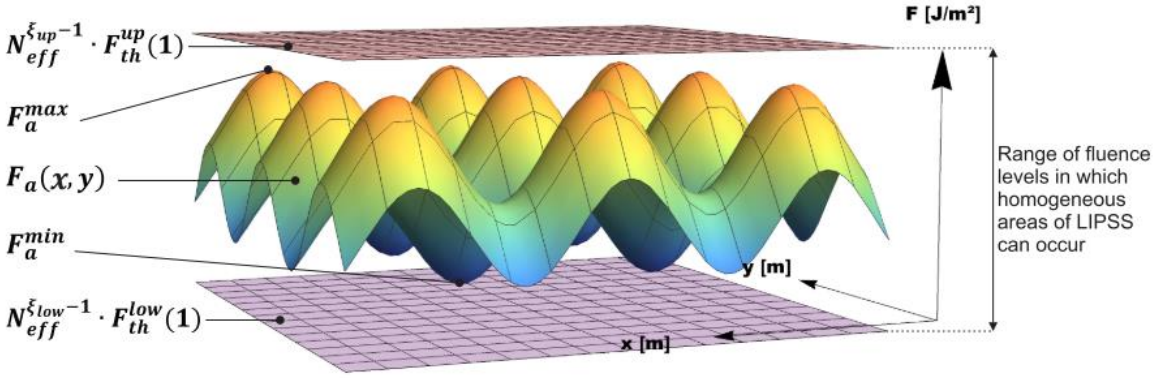

Figure 2.12 Accumulated fluence profile Fa(x,y) with highlighted minimum and its maximum together with the indication of the lower and higher fluence threshold for LIPSS occurrence [111].

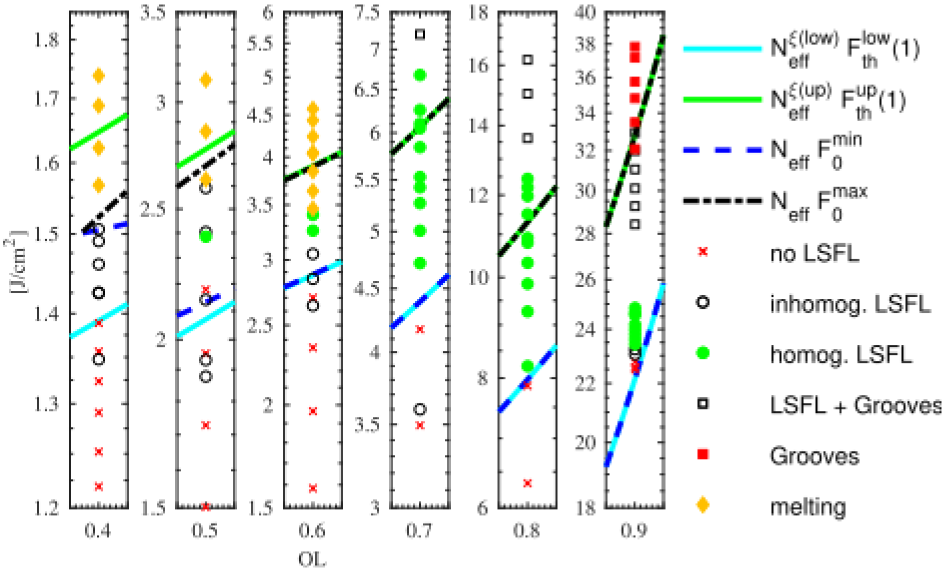

Figure 2.13 The validation of the analytical model for indicating the accumulated fluence ranges, by the upper and lower thresholds, for the LIPSS morphologies, and especially homogenous LSFL [111].

Table 2.2 Summary the modelling approaches for LIPSS and linking to the references.

Modelling Approach	Consideration	Output	Reference
Surface Electromagnetic Waves	Λ of LSFL prediction at oblique angles and includes beam polarization	Λ (2D)	[2], [114]
Sipe's Theory or Sipe-Drude model	Wave vector as a function of surface roughness and ε for Λ prediction, also relevant for transparent dielectrics, includes variations in ε	ε ,Λ (2D)	[115], [116]
Finite-Difference Time-Domain (FDTD) Simulations	Predicts the inhomogeneous absorption and the material ablation. Predicts other LIPSS with much higher fluence	Full 3D patterns	[118], [119], [124]
Matter reorganization theories	Includes all the effects is good in predicting LIPSS for longer pulse durations and high number of pulses	2D/3D topography, also LIPSS irregularity	[110]
Ultrafast irradiation model	Analytical model used for calculating accumulated fluence and correlate with spatial LIPSS appearance	Processing parameters	[111], [112], [123]

All the attempts for providing a reliable tool for a more general generation of LIPSS on the surface comes from the fact that the LIPSS generation is material and laser source specific. Often heavy simulations were not necessary to generate optimized structures as their formation was commonly established to be dependent on crucial laser parameters, i.e. pulse fluence and number of pulses, and those will vary for each material. It is worth mentioning that LIPSS optimisation always focused on carrying out iterative experiments and the determined processing windows for generating optimized structures are usually small. However, the main limitation of the proposed analytical model was always considering processing of flat surfaces and assuming constant processing conditions.

Even though the extensive research has been dedicated on explaining the mechanism of LIPSS generation (summarised in Table 2.2), there is still lack of developments of models for laser structuring of more complex geometries, including the variable laser processing conditions. As it was discussed in Section 2.4.3, LIPSS are very sensitive to any changes in the laser processing conditions, especially when affected by disturbances and produced on freeform surfaces. To structure such surfaces, the processing strategy would consist of division of the surface into fields with constraints of maintaining FOD and BIA within acceptable ranges [125]. Then this ranges can be applied into surface partitioning algorithms to define the processing field sizes [126]. It should be highlighted that the processing limits are tested empirically and long experimental campaigns are required to determine satisfactory LIPSS characteristic and even more testing is needed to ensure that the functional performance is preserved.

Modelling approach should be developed for predicting the resulting key LIPSS characteristics and implementing the effects of varying laser conditions when processing freeform surfaces and, hence, can be employed in aiding the design of LIPSS treatment strategies on such surfaces. This formulates the second question addressed in the research Chapter 5 (also see Figure 1.1).

2.4.5. LIPSS monitoring

2.4.5.1. LIPSS monitoring methods

The goal of process monitoring is the improvement of reproducibility and quality assurance during the process. In order to fulfil this criteria, the morphology of laser structures needs to be characterized in a robust manner and this has not been the prime focus of researchers while conducting study on LIPSS. In the review of laser monitoring approaches it was indicated that developments for laser structuring/texturing process are often neglected in this field [127].

LIPSS resolution is hardly resolved by standard metrology/inspection tools, like optical microscopes, due to their sub-micron scales and for this reason they are usually inspected by SEM or AFM microscopes. Methods were developed for in-situ LIPSS analysis through X-ray scattering [128], structured illumination microscopy (SIM) [124] to study their pulse-to-pulse development or detecting the appearance via backreflection imaging [129].

The first study used grazing incidence small-angle X-ray scattering (GISAXS) beam as in situ measurements of LIPSS creation on polymer material with an X-ray detector located 4 m away from the sample position. The laser beam and the GISAXS acquisition was activated simultaneously and the LIPSS patterns were recorded against time. As a result, LIPSS periodicity evolution over time dependence was captured as well as GISAXS intensity profiles for 4 different repetition rates. It was stated that a precise alignment of the laser beam and accurate sample positioning with attention to the ripples orientation is required for capturing the GISAXS pattern correctly [128].

The second study recorded the reflected laser beam from the sample which is referred as backreflection. The authors did not observe directly the LIPSS generation but the change in the secondary diffraction pattern around the laser beam spot. It was stated that a characteristic fringe pattern can be detected when ripples have been formed and therefore monitor only the LIPSS appearance during the structuring process [129].

In the third study, another technique for spatially-resolved LIPSS observations applying SIM which is super resolution optical method that is not observable in standard optical microscopy and suitable to LIPSS sub-micron scales. With this method LIPSS were observed during multi pulse formation with accuracy around 100 nm. The method allowed observing LIPSS formation in single spot irradiation and the range of peak fluence and number of pulses used were 0.09 J/cm2 to 0.31 J/cm2 and from 0 (non-irradiated surface) up to 100, respectively, with 1 kHz repetition rate [124].

The methods described above were not suitable for wider LIPSS production because either special instruments setup was required to characterized rather small areas with low repetition rates, as in the case of GISAXS, no LIPSS characteristics were possible to be obtained, as in backreflection imaging, or the technique was adjusted only to collect the feedback from planar surfaces in SIM.

Light scatterometry, as a contactless and non-destructive method, is a good candidate as an indirect periodic structures metrology method [130]. Especially, near-infrared LIPSS have features sizes that are close to the visible wavelengths hence it is easy and fast to analyse their reflective and diffraction patterns. Diffractometry was applied to evaluate the quality and morphology of reflected patterns from structures produced by Direct Laser Interference Patterning (DLIP) allowed to judge about the produced surface structures in a fast and responsive way [131]. The DLIP periodic structures spatial periods were higher than 4 μm and with depth up to 5 μm therefore not fitting into LSFL sub-micron scale. However, the developed method was able to detect the diffraction patterns from the periodic processing strategy which was a function of beam overlapping and hatch distances. The setup showed limitations in detecting spatial characteristic of the homogenous structures and only classification of morphological quality of structures was provided.

It is worth mentioning that by measuring the diffractive features, i.e. angular dependence of the structural colours displayed by surfaces with LIPSS, it additionally demonstrates indirectly the qualitative measurement of their functional response which is necessary, for instance, in imprinting images on metals in holography [132]. Recently, such colorimetric responses of omni- and unidirectional LIPSS on metal surfaces were successfully measured by spectrophotometer [133]. Even though this method was not considered by the authors as possible LIPSS monitoring method, it is worth highlighting that the colours observable on LIPSS covered surfaces were measured in a standardized way using CIELAB color space which can be a quantitative indicator of LIPSS functional response, that is structural colouring. On the other hand, the capabilities of any of the method for discussed applications were not analysed, in particular a sensitivity study to detect what is the smallest change in LIPSS homogeneity or dimensions was not presented.

The summary of abovementioned monitoring methods is provided in Table 2.3. Methods for LIPSS monitoring still should continue to be developed in order to provide a process control tool that is a fast and robust to be applicable to laser processing systems solution. That represents the third open question addressed in this thesis, specifically in Chapter 6 (also see Figure 1.1).

Table 2.3 Summary of current methods used for periodic structures monitoring highlighting the possibility of when in the LIPSS generation process can be applied, summarizing their main points and whether the periodicity or LIPSS amplitudes (Amp.) could be detected (Y – yes, N – no). Ref. – references.

Method	**When**	**Characteristics**	**Λ**	**Amp.**	**Ref.**
Grazing Incidence Small-Angle X-ray Scattering (GISAXS)	In-situ	Slow, special instrumentation required	Y	N	[128]
Structured Illumination Microscopy (SIM)	In-situ	High-resolution, implemented in same laser path, observation of LIPSS evolution	Y	Y	[124]
Backreflection imaging	In-situ	Simple, easy to implement	N	N	[129]
Scatterometry and/or diffractometry for DLIP	In-line	Fast, developed for DLIP structures, limitations for LSFL, only homogeneity or binary (OK/NOK) classification	Y	Y	[131], [134]
Frequency domain – optical coherence tomography	In-line	Developed for laser structuring and machining, coupled with the laser beam	N	N	[37]

Spectrophotometer	Not specified	Direct colorimetric measurement (structural colour indicator)	N	N	[133]

2.4.5.2. ANNs for LIPSS functional prediction

In the previous paragraphs, it was demonstrated that the scatterometry and diffraction methods are suitable for monitoring. The in-situ methods were focusing on observing the real-time LIPSS evolution and presence. All of the conclusions were indicating that the monitoring techniques are important for laser structuring to address industrial challenges. Moreover, Alleaume et.al. [134] clearly stated that more important than the LIPSS characteristics assessment is the need for rapid understanding whether the LIPSS covered surface area is suitable for the targeted functionality. For the authors, the end goal was to qualify the surface being hydrophobic or hydrophilic because that functional performance was the requirement in the final application. Therefore, there is a necessity for not only developing monitoring methods of LIPSS but also understanding from the acquired data whether they also fit for the targeted functional performance. This is particularly important to consider also in cases where not only the optimization of processing parameters is required but also when the process is affected by 3D processing disturbances, what will result in the changes of LIPSS topography and, possibly, in the functional response, too. It was mentioned that one of the promising solutions to link the optical responses from laser structured surfaces with their geometric features is through using neural networks [134].

Artificial Neural Networks (ANNs) are excellent tools for such applications as they can offer high accuracy of functional prediction or system modelling. Due to their generalisation capability they can be applied to many engineering tasks because the output and input data are dissociated from the complexity of the problem [135]. ANNs have been proven to be a good method for defects diagnosis [136] and have been used even as an on-line quality control assessment in laser welding [137]. Concerning other laser processes, neural networks have been successfully implemented in the prediction of ablation profiles or surface roughness based on the key laser machining parameters [138]–[141]. Those methods are summarised in Table 2.4 indicating the various input - output pairs that are used in the laser processes. Another takeaway is the efforts of matching the newer ANN algorithms with carefully chosen type of datasets which proves to very relevant to the application. For example, ANN technique of predictive surface topology visualisation was applied in laser structuring of dimples, especially the output of that modelling was actual 3D dimples depth representation [139].

Combining ANN methods with laser-based manufacturing processes is relatively new and novel approach. The key to successful ANN implementation is in the data preparation. Furthermore, a relatively big number of input-output experimental data pairs is required for achieving high prediction accuracy. Up to now there is no available study on linking the LIPSS topographical data to their functional responses using neural network approaches. It could surely set new grounds in development of monitoring solutions and faster data analysis. That formulates a fourth open question addressed in this thesis, specifically in Chapter 7 (also see Figure 1.1).

Table 2.4 Summary of neural network algorithms used in laser processes highlighting the various input-output pairs. (ANN methods: BP – back propagation, CNN -

Convolutional neural network, CAN – conditional adversarial network, RBFN - Radian Basis Function Network, RSM - Response surface method).

Laser process	ANN method	Input	Output	Ref.
Welding	BP	Audible sound signal	Weld defects	[136]
Welding	CNN	Thermal images	Weld defects	[137]
Machining	CNN, CAN	Laser spatial intensity profile	3D depth prediction	[138]
Structuring (dimples)	CNN, GAN	Pulse energy, Np, f	Dimple depth, crown height, 3D dimple profile	[139]
Machining	BP	Lamp current, f, pulse width, air pressure	Depth of groove, Height of recast layer	[140]
Cutting	RBFN, RSM	Cutting speed, power, tip distance	Surface roughness (Ra)	[141], [142]

2.5. Summary of open research questions

Throughout the carried-out literature review, the laser technology was introduced and the main topics in laser surface texturing/structuring were discussed, particularly relating to aspects of LIPSS processing, modelling and monitoring. The interest in research on LIPSS is growing exponentially and so are the industrial requirements for a broader applicability of the structures. The four open research questions are summarized below:

i. There is limited evidence of LIPSS created on amorphous diamond-like carbon coatings. It is crucial to study the synergistic approach of combining the advantageous DLC surface properties with LIPSS many added surface functionalities and at the same time maintain the benefits of both. This solution has the potential and is sought after in manufacturing laser structured masters for injection moulding technology of polymers.

ii. An extensive research has been done on the origin and modelling of LIPSS, but still a lot of focus is given to produce the structures on planar surfaces with ideal laser beams. The literature also showed that two main processing disturbances, i.e. FOD and BIA, that typically occur during processing complex 3D parts, can impact LIPSS significantly. Thus, for developing efficient processing strategies, a predictive method for assessing the laser conditions on the surface especially during the LIPSS generation is essential to alleviate the extensive experimental studies required for determining the design constraints.

iii. Efforts for developing methods and tools for in-line LIPSS monitoring are still necessary. The available methods can detect LIPSS evolution and geometric features but the setups and techniques are still not suitable to collect data from more complex parts and freeform surfaces. A fast qualitative assessment of LIPSS topography using light scattering is desired, especially when the generation process is affected by the 3D processing disturbances.

iv. Additional requirement in monitoring approaches of LIPSS is the functional performance assessment through data handling and interpretation. To address challenges for broader use of LIPSS in industry, the priority is to rapidly understand whether the LIPSS covered surface area is suitable for the targeted functionality rather than the LIPSS characteristics assessment. It is even more vital when LIPSS characteristic are affected by the 3D processing disturbances. ANNs tools have the potential to be a good fit for an accurate prediction of LIPSS functional responses with the preparation of relevant input - output values, and they have never been applied to ripples structures before.

CHAPTER 3: METHODOLOGY

In this Chapter methodology for conducting laser experiments is discussed. First a description of laser micro processing platform utilised for the experiments is given explaining which parameters were set in the software and which were obtained from calculations. Additionally, the laser and characterization equipment is also specifically described in relevant methodology section of each research Chapter. The next sections include Design of Experiments which is provided in Tables 3.1 to 3.12 where the levels for each set of produced samples as well as the constant parameters are listed. For each research Chapters new sets of samples were produced each time. The Tables are listing all the laser experiments performed including both preliminary experimental tests and the ones reported in Chapters 4, 5, 6 and 7. This information is included in Table’s captions for completeness.

3.1. Laser setup

Laser source utilised to produce LIPSS was ultrafast Ytterbium-doped laser source from Satsuma (Amplitude Systems, France) and it was integrated in the laser micro processing platform from LASEA. The beam delivery system is presented in Figure 3.1. Major components on the beam path guided from laser source included half waveplate, beam expander, z module (DFM), galvo scanner, and 100 mm telecentric lens to be delivered to the 5-axis stage. Parameters that were set in the KYLA software were scanning speed (v), pulse frequency (f), hatching distance (h) and average power level (P_{avg}). Based on those the pulse energy and hence pulse fluence (F) and peak fluence (F_0) was calculated as in the formula below [143]:

$$F = \frac{P_{avg}}{f\pi\omega^2}, \qquad F_0 = \frac{2P_{avg}}{f\pi\omega^2} \tag{3.1}$$

Where ω is beam waist. Pulse distance in one direction could be controlled through the function of speed and frequency (v/f) while the other direction was set by a hatching distance. The hatching orientation could be set horizontal, vertical, diagonal or specified by an angle. All the experiments were always done with horizontal or vertical hatching strategy which was specified in the experimental methodology sections within the research Chapters. The laser source maximum average power specification was 5W, however, due to losses on the optical path, the maximum average power when measured by power meter at the end of the optical path (after the focusing lens) was around 3W. The laser source power instability and the laser beam calibration routines affect the actual average power for chosen power levels in the software therefore these values were always measured on the day of experiments.

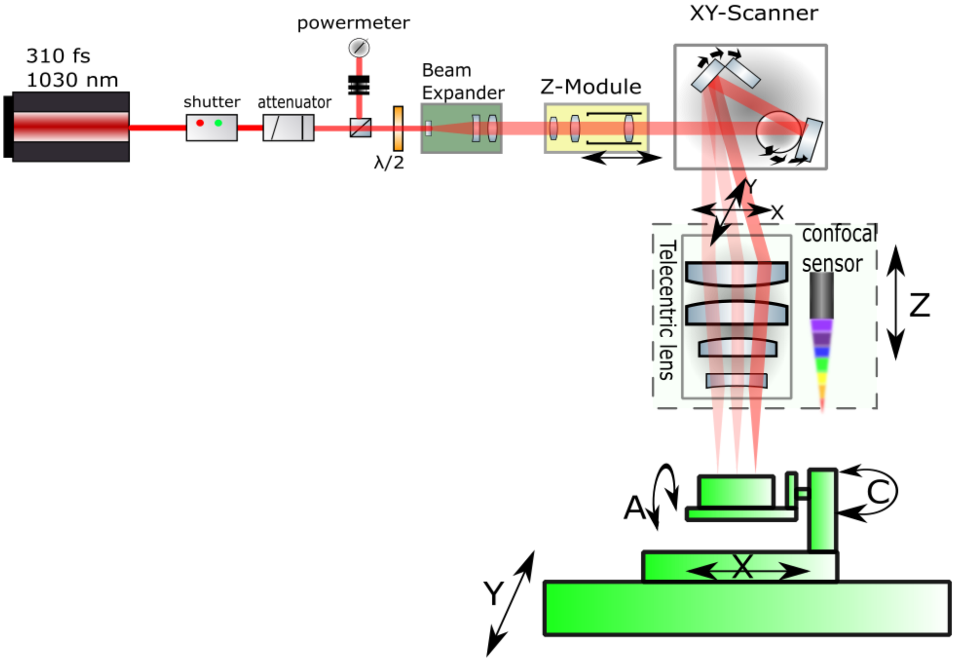

Figure 3.1 Beam delivery system on the laser micro processing platform utilised for the LIPSS studies (also in Chapter 6: Figure 6.1a).

For LIPSS appearing on the surface the two most decisive is the control the spatial and temporal flux of laser energy [123]. In other words, the influential parameters are pulse fluence and number of pulses per spot. The number of pulses delivered to the surface is defined - for single spot irradiation - as the set number of pulses hitting the same spot while, for the moving beam in lines over the area the defying parameter, it is defined as the number of pulses per spot. The same numbers is sometimes expressed as the percentage of overlapping pulses or as a pulse distance.

In the next sections laser processing parameters that were used to produce LIPSS are provided. The initial experiments that led to the definition of the final ranges of parameters used for reporting the results were done for Chapter 4 and Chapter 6.

3.2. Design of Experiments for Chapter 4

The initial experiments that lead to the definition of processing ranges of producing LIPSS on DLC was based, first, on exposing the surface to predetermined number of pulses, secondly on producing two-dimensional matrixes of squares with varying parameters. The laser beam in focus was around 40 µm, unless stated otherwise, while focused with 100 mm telecentric lens. The laser beam optical path was the same for all conducted experiments that includes the orientation of the polarization vector. During initial trials, the frequency was fixed at 100 kHz for single spot processing; for area processing, the fixed value was at 500 kHz as it yielded the fastest processing time while other parameters were varied. The tested levels are presented in Table 3.1, 3.2 and 3.3. Table 3.2 lists number of laser surfaces produced before that aided defining the final tested parameters ranges for Table 3.3 and later reported in Figure 4.3. In the tuning set from Table 3.2, pulse distance in x and y direction was varied together with average power. It is worth noting that other studies reported pulse fluence levels and numbers of pulses in the ranges of 0.05 – 3.5 J/cm^2 and 2-1000 [87], [89], as stated in Table 2.1, respectively, for laser sources with similar pulse durations and laser source wavelength.

Other details on experimental and characterisation methods are also provided in the Section 4.2.

Table 3.1 Laser processing parameters and its levels for single spot irradiation on DLC. Number of pulses is calculated as burst time multiplied by frequency (f). P_{avg} – average power, F – pulse fluence, F_0 – peak fluence. The 5 SEM imaged of irradiated spots from this Table are reported in Figure 4.2 (Pulse fluence of 0.1 J/cm^2 for 20 pulses, 0.9,0.1 and 0.18 J/cm^2 for 50 pulses, 0.18 J/cm^2 for 100 pulses).

f (kHz)	Burst time (μs)	P_{avg} (W)	Number of pulses	F (J/cm^2)	F_0 (J/cm^2)	Num. of surf.
100	10, 20, 100, 500, 1000 (5 levels)	0.08, 0.11, 0.13, 0.22 (4 levels)	1, 2, 10, 50, 100	0.06, 0.09, 0.1, 0.18	0.12, 0.18, 0.21, 0.35	20
100	50, 80, 120, 150, 200 (5 levels)	0.13, 0.22 (2 levels)	5, 8, 12, 15, 20	0.1, 0.18	0.21, 0.35	10

Table 3.2 Laser processing parameters sets for preliminary experiments that lead to the processing window of LIPSS on DLC. The scanning speed (v), frequency (f), hatching distance (h) and average power level (P_{avg}) were set in the KYLA software while pulse distances in x and y, pulse (F) and peak fluence (F_0) are calculated values based on the set parameters. Last column reports number of structured surfaces produced per matrix.

v (mm/s)	f (kHz)	h (μm)	P_{avg} (W)	P. dist. in x (μm)	P. dist. in y (μm)	F (J/cm^2)	F_0 (J/cm^2)	Num. of surf.
2000	500	3,5,7,9,11, 13 (6 levels)	0.44, 1.02, 1.74, 2.40, 2.83, 3.01, 3.04 (7 levels)	4	3,5,7,9,11, 13	0.07, 0.16, 0.28, 0.38, 0.45, 0.479, 0.484	0.14, 0.33, 0.55, 0.76, 0.90, 0.96, 0.97	42
1000	500	3,7,11 (3 levels)	0.44, 0.73, 1.02, 1.41 (4 levels)	2	3,7,11	0.07, 0.12, 0.16, 0.22	0.14, 0.23, 0.33, 0.45	12
1000	500	3,4,5 (3 levels)	0.66, 0.72, 0.78, 0.85, 0.91 (5 levels)	2	3,4,5	0.11, 0.115, 0.125, 0.13, 0.14	0.21, 0.23, 0.25, 0.27, 0.29	15

500	500	3,7,11 (3 levels)	0.44, 0.73, 1.02, 1.41, 1.74 (5 levels)	1	3,7,11	0.07, 0.116, 0.16, 0.22, 0.28	0.14, 0.23, 0.33, 0.45, 0.55	15
500	500	3,4,5,6 (4 levels)	0.66, 0.72, 0.78, 0.85, 0.91 (5 levels)	1	3,4,5,6	0.11, 0.115, 0.125, 0.13, 0.14	0.21, 0.23, 0.25, 0.27, 0.29	20
1000, 900, 800, 700, 600, 500 (6 levels)	500	3,4,5 (3 levels)	0.51	2, 1.8, 1.6, 1.4, 1.2, 1	3,4,5	0.08	0.16	18

Table 3.3 Laser processing parameters used for large area structuring of DLC. These parameters correspond to results in Figure 4.3. The scanning speed (v), frequency (f), hatching distance (h) and average power level (P_{avg}) were set in the KYLA software while pulse distances in x and y, pulse (F) and peak fluence (F_0) are calculated values based on the set parameters.

v (mm/s)	f (kHz)	h (μm)	P_{avg} (W)	P. dist. in x (μm)	P. dist. in y (μm)	F (J/cm^2)	F_0 (J/cm^2)	Num. of surf.
600, 800, 1000, 1200, 1400 (5 levels)	500	3	0.37, 0.46, 0.56, 0.63, 0.69, 0.75, 0.82 (7 levels)	1.2, 1.6, 2, 2.4, 2.8	3	0.06, 0.07, 0.09, 0.1, 0.11, 0.12, 0.13	0.12, 0.15, 0.18, 0.2, 0.22, 0.24, 0.26	35

3.3. Design of Experiments for Chapter 5

In Chapter 5 two sets of experiments were conducted. The material used for the LIPSS generation was mirror polished 304L stainless steel. Firstly, samples with fixed pulsed distances in x and y were produced and only peak fluence was varied starting from the level where LIPSS were still not appearing on the surface as the pulse fluence was still below the threshold. The levels of these experiments are shown in Table 3.4. The results were used to identify the LIPSS fluence threshold and correspond to Figure 5.6. Secondly, experimental samples produced for the validation of the analytical model is provided in Table 3.5. More detailed strategy for producing samples with two processing disturbances is provided in Section 5.3.3. For this material researchers were reporting producing LIPSS with pulse fluence 0.45 J/cm^2 [114] or in the range of 0.4 – 0.8 J/cm^2 [144] for similar laser sources but different beam scanning parameters.

More details about experimental and characterisation methods and setup is also provided in Section 5.3.

Table 3.4 Laser processing parameters used for LIPSS fluence threshold definition and correlation of LIPSS amplitudes and peak fluence. These parameters correspond to results in Figure 5.6. The scanning speed (v), frequency (f), hatching distance (h) and average power level (P_{avg}) were set in the KYLA software while pulse distances in x and y, pulse (F) and peak fluence (F_0) are calculated values based on the set parameters.

v (mm/s)	f (kHz)	h (μm)	P_{avg} (W)	P. dist. in x (μm)	P. dist. in y (μm)	F (J/cm^2)	F_0 (J/cm^2)	Num. of surf.
2000	500	6	0.27, 0.32, 0.36, 0.41, 0.47, 0.53, 0.59, 0.66, 0.73, 0.81, 0.88, 0.97, 1.04, 1.13, 1.22, 1.31, 1.4, 1.5, 1.6, 1.7, 1.8 (21 levels)	4	6	0.04, 0.05, 0.06, 0.066, 0.075, 0.08, 0.09, 0.1, 0.12, 0.13, 0.14, 0.15, 0.17, 0.18, 0.19, 0.21, 0.22, 0.24, 0.25, 0.27, 0.29	0.09, 0.1, 0.12, 0.13, 0.15, 0.17, 0.19, 0.21, 0.23, 0.26, 0.28, 0.31, 0.33, 0.36, 0.39, 0.42, 0.45, 0.48, 0.51, 0.54, 0.57	21

Table 3.5 Laser processing parameters used for validation the accumulated fluence modelling approach. The scanning speed (v), frequency (f), hatching distance (h), average power level (P_{avg}) and BIA on A rotary stage were set in the KYLA software while pulse distances in x and y, pulse (F) and peak fluence (F_0) are calculated values based on the set parameters. Please note the pulse distance reported was set in the KYLA software and not compensated on the inclined surfaces (details in Section 5.3.3.). Correspond to results reported in Figure 5.8 and 5.10.

v (mm/s)	f (kHz)	h (μm)	BIA (deg)	P_{avg} (W)	P. dist. in x (μm)	P. dist. in y (μm)	F (J/cm^2)	F_0 (J/cm^2)	Num. of surf.
2000	500	6	10, 20, 30, 40 (4 levels)	0.73, 1.31 (2 levels)	4	6	0.12, 0.22	0.25, 0.44	8

3.4. Design of Experiments for Chapter 6

In Chapter 6, the same mirror polished 304L stainless steel was also used. In this study the scanning speed and frequency, i.e. 2 m/s and 500 kHz, respectively, was always set as highest available, in the laser processing platform while average power and pulse distance in y was controlled. The first set in Table 3.6 tested the influence of the pulse distance in y, by choosing different hatching distances with also varying fluence. In this set, experiments were not progressed forward with the hatching distance where the diffraction from LIPSS was no longer visible on the laser structured surface. The structural colours were determined under white light through visual inspection. The next set provided in Table 3.7 correspond to initial results discussed in Section 6.3.1 in Figure 6.2 which started from first setting fluence where the diffracted colours started to be visible, that is F = 0.054 J/cm^2. Before final set of samples were produced for results in Section 6.3.2 a sensitivity to processing disturbances was studied for FOD at 3 fluence levels (Table 3.8) while for BIA for 5 fluence levels (Table 3.9). For samples with varying BIA always p-type polarization was used unless stated otherwise. Finally, the last Table 3.10 shows the laser parameters used for results reported in Figure 6.3 and Figure 6.5.

Each produced surface was characterised by reflectance and diffraction measurements. Experimental and characterisation methods for the Chapter 6 are also provided in Section 6.2.

Table 3.6 Laser parameters for fine tuning the hatching distance. Please note that the experiments for every line of fluence were terminated if light diffraction was no longer visible on the produced surface. The scanning speed (v), frequency (f), hatching distance (h) and average power level (P_{avg}) were set in the KYLA software while pulse distances in x and y, pulse (F) and peak fluence (F_0) are calculated values based on the set parameters.

v (mm/s)	f (kHz)	h (μm)	P_{avg} (W)	P. dist. in x (μm)	P. dist. in y (μm)	F (J/cm^2)	F_0 (J/cm^2)	Num. of surf.
2000	500	2,3,4,5	0.34	4	2,3,4,5	0.05	0.11	4
2000	500	2,3,4,5,6	0.44	4	2,3,4,5,6	0.07	0.14	5
2000	500	2,3,4,5,6,7	0.55	4	2,3,4,5,6,7	0.09	0.18	6
2000	500	2,3,4,5,6,7,8	0.68	4	2,3,4,5,6,7,8	0.11	0.22	7
2000	500	2,3,4,5,6,7,8,9	0.82	4	2,3,4,5,6,7,8, 9	0.13	0.26	8
2000	500	2,3,4,5,6,7,8,9,10,11,12	0.98	4	2,3,4,5,6,7,8, 9,10,11,12	0.16	0.31	11

Table 3.7 Laser parameters used for initial trials discussed in Section 6.3.2 whereas the results corresponding to this parameters are reported in Figure 6.2. The scanning speed (v), frequency (f), hatching distance (h) and average power level (P_{avg}) were set in the KYLA software while pulse distances in x and y, pulse (F) and peak fluence (F_0) are calculated values based on the set parameters.

v (mm/s)	f (kHz)	h (μm)	P_{avg} (W)	P. dist. in x (μm)	P. dist. in y (μm)	F (J/cm^2)	F_0 (J/cm^2)	Num. of surf.
2000	500	5	0.34,0.39, 0.44, 0.49, 0.55, 0.61, 0.68, 0.75, 0.82, 0.9, 0.98, 1.06, 1.14, 1.23, 1.32, 1.41, 1.49, 1.6, 1.68	4	5	0.054, 0.06, 0.07, 0.08, 0.09, 0.1, 0.11, 0.12, 0.13, 0.14, 0.16, 0.17, 0.18, 0.2, 0.21, 0.22, 0.24, 0.25, 0.27	0.11, 0.12, 0.14, 0.16, 0.18, 0.2, 0.22, 0.24, 0.26, 0.29, 0.31, 0.34, 0.36, 0.39, 0.42, 0.45, 0.48, 0.51, 0.54	19

Table 3.8 Laser parameters to study sensitivity of FOD to 3 fluence levels. The scanning speed (v), frequency (f), hatching distance (h) and average power level (P_{avg}), FOD with Z stage positioning were set in the KYLA software while pulse distances in x and y, pulse (F) and peak fluence (F_0) are calculated values based on the set parameters.

v (mm/s)	f (kHz)	h (μm)	FOD (mm)	P_{avg} (W)	P. dist. in x (μm)	P. dist. in y (μm)	F (J/cm^2)	F_0 (J/cm^2)	Num. of surf.
2000	500	5	0, -0.2, -0.4, -0.6, 0.2, 0.4, 0.6	0.34	4	5	0.054	0.11	7
2000	500	5	0, -0.2, -0.4, -0.6, -0.8, 0.2, 0.4, 0.6, 0.8	0.44	4	5	0.07	0.14	9
2000	500	5	0, -0.2, -0.4, -0.6, -0.8, -1, 0.2, 0.4, 0.6, 0.8, 1	0.55	4	5	0.088	0.18	11

Table 3.9 Laser parameters to study sensitivity of BIA to 5 fluence levels. The scanning speed (v), frequency (f), hatching distance (h) and average power level (P_{avg}) and BIA on A rotary stage were set in the KYLA software while pulse distances in x and y, pulse (F) and peak fluence (F_0) are calculated values based on the set parameters.

v (mm/s)	f (kHz)	h (μm)	BIA (deg)	P_{avg} (W)	P. dist. in x (μm)	P. dist. in y (μm)	F (J/cm^2)	F_0 (J/cm^2)	Num. of surf.
2000	500	5	0, 5, 10, 20, 30 (5 levels)	0.39, 0.44, 0.49, 0.55, 0.61 (5 levels)	4	5	0.06, 0.07, 0.08, 0.088, 0.1	0.12, 0.14, 0.16, 0.18, 0.2	25

Table 3.10 Laser parameters reported on Section 6.3.2. The first row corresponds to results in Figure 6.3 while the last two are reported in Figure 6.5. Please note that surfaces for FOD and BIA at fluence 0.088 J/cm2 were repeated from Table 3.8 and 3.9 but with decreased intervals. The last row S indicates s-type polarization. The scanning speed (v), frequency (f), hatching distance (h) and average power level (P_{avg}), FOD with Z stage positioning and BIA on A rotary stage were set in the KYLA software while pulse distances in x and y, pulse (F) and peak fluence (F_0) are calculated values based on the set parameters.

v (mm/s)	f (kHz)	h (μm)	BIA (deg)	FOD (mm)	P_{avg} (W)	P. dist. in x (μm)	P. dist. in y (μm)	F (J/cm^2)	F_0 (J/cm^2)	Num. of surf.
2000	500	5	0	0.1, 0.2, 0.3, 0.4, 0.5, 0.6, 0.7, 0.8, 0.9	0.55	4	5	0.088	0.18	9
2000	500	5	0,2,4,5,6,8,10,15,20	0	0.55	4	5	0.088	0.18	9
2000	500	5	0S, 5S, 10S, 15S, 20S, 25S	0	0.55	4	5	0.088	0.18	6

3.5. Design of Experiments for Chapter 7

Table 3.11 shows a list of parameters used as a supplementary set investigated in Chapter 7. The supplementary set included surfaces produced with range of F_0 from near-threshold 0.16 J/cm^2 to 0.54 J/cm^2 that were chosen based on the surfaces produced with parameters in Table 3.11. The fluence levels are similar to the parameters used in Chapter 5 however, the scanning speed had to be reduced in order to accommodate the limitations to the z-module (explained in Section 7.2) and frequency was scaled down to have the pulse distance of 4 μm. This meant that also the fluence levels were similar to the ones reported in Table 3.4. Table 3.12 reports the laser processing parameters used for producing surfaces with two processing disturbances that served as main input for the ANN tools. Those fields were produced three times with the parameters from Table 3.12 for the wettability measurements.

Topography of each laser structured field was acquired by AFM and from each produced field the static contact angle was measured 4 times. Each AFM image was cropped into 16 individual topographies and then fed into Alicona MeasureSuite software to calculate the areal surface roughness parameters. The experimental, characterisation methods are also explained in Section 7.2.

Table 3.11 Laser parameters used for generating supplementary set of LIPSS topographies. The scanning speed (v), frequency (f), hatching distance (h) and average power level (P_{avg}) were set in the KYLA software while pulse distances in x and y, pulse (F) and peak fluence (F_0) are calculated values based on the set parameters.

v (mm/s)	f (kHz)	h (µm)	P_{avg} (W)	P. dist. in x (µm)	P. dist. in y (µm)	F (J/cm^2)	F_0 (J/cm^2)	Num. of surf.
40	10	6	0.008, 0.009, 0.01, 0.011, 0.013, 0.015, 0.016, 0.017, 0.018, 0.02, 0.022, 0.023, 0.26, 0.027, 0.029, 0.031, 0.033, 0.036, 0.037, 0.039, 0.041, 0.042, 0.044	4	6	0.07, 0.08, 0.09, 0.1, 0.11, 0.13, 0.14, 0.15, 0.16, 0.18, 0.2, 0.2, 0.23, 0.24, 0.26, 0.27, 0.29, 0.31, 0.33, 0.34, 0.36, 0.37, 0.39	0.14, 0.16, 0.18, 0.19, 0.23, 0.26, 0.28, 0.3, 0.32, 0.35, 0.39, 0.41, 0.46, 0.48, 0.51, 0.54, 0.58, 0.63, 0.65, 0.69, 0.72, 0.74, 0.78	23

Table 3.12 Laser parameters used for producing samples with varied processing disturbances, BIA and FOD. The scanning speed (v), frequency (f), hatching distance (h) and average power level (P_{avg}), FOD with Z stage positioning and BIA on A rotary stage were set in the KYLA software while pulse distances in x and y, pulse (F) and peak fluence (F_0) are calculated values based on the set parameters.

v (mm/s)	f (kHz)	h (μm)	BIA (deg)	FOD (mm)	P_{avg} (W)	P. dist. in x (μm)	P. dist. in y (μm)	F (J/cm^2)	F_0 (J/cm^2)	Num. of surf.
40	10	6	0	0.1, 0.2, 0.3, 0.4, 0.5, 0.6, 0.7, 0.8, 0.9	0.016	4	6	0.14	0.28	10
40	10	6	2.5, 5, 7.5, 10, 12.5, 15, 17.5, 20, 22.5, 25, 27.5, 30, 32.5, 35	0	0.016	4	6	0.14	0.28	14

CHAPTER 4: SUB-MICRON STRUCTURING/TEXTURING OF DIAMOND-LIKE CARBON COATED REPLICATION MASTERS WITH A FEMTOSECOND LASER

This chapter answers the first research question formulated in Chapter 2. The objective is to investigate the effects of femtosecond laser processing parameters for generating LIPSS on DLC coating. First, a range of parameters is defined with where LIPSS are present and uniform on the surface and without visible damages to the coating. These processing parameters were derived from experiments presented in Tables 3.1-3.3. Then, a structural and mechanical characterisation is performed from representative laser structured surfaces. This study also aims to assess whether the synergistic approach of LIPSS treatments and use of DLC coating on steel substrates is suitable for the process of injection moulding, especially if the DLC’s advantageous properties can be maintained on the coated and femtosecond laser processed replication masters.

Aleksandra Michalek[1], Shaojun Qi[2], Afif Batal[1], Pavel Penchev[1], Hanshan Dong[2], Tian Long See[3], Stefan Dimov[1]

[1]School of Mechanical Engineering, University of Birmingham, Edgbaston, Birmingham, B15 2TT, UK

[2]School of Metallurgy and Materials, University of Birmingham, Edgbaston, Birmingham, B15 2TT, UK

[3]The Manufacturing Technology Centre Ltd, Pilot Way, Ansty Park, Coventry, CV7 9JU, UK

This research was published as a full-length article in *Applied Physics A: Materials Science and Processing (2020).*

Author's contributions:

A. Michalek	Main author, conceptualization and methodology, performing all LIPSS generation experiments, data analysis (Raman spectroscopy, nanoindentation, tribological, GAXRD), writing original draft
S. Qi	Supported with LIPSS AFM measurement and DLC characterisation
A. Batal	Supported with data analysis
P. Penchev	Assisted with laser setup
H. Dong	Co-supervisor
T.L. See	Industrial supervisor
S. Dimov	Supervisor, Revision of the manuscript

Abstract

Diamond-like carbon (DLC) coatings have very attractive mechanical and tribological properties, i.e. high hardness, low friction and high wear resistance. Therefore, DLC is often used as a solid lubricant in moulds for injection moulding. Laser processing of DLC with ultra-short lasers, i.e. femtosecond lasers, can be performed both at micro and sub-micron scales, namely by producing laser induced periodic surface structures (LIPSS). In this research, the effects of laser structuring/texturing on DLC properties are investigated. First, the laser processing parameters were optimised to produce uniform LIPSS without damaging a thin DLC film and then the properties of the textured DLC coated substrates were studied. It was determined that the tribological properties of the processed surfaces remained unchanged but the hardness of the structured/textured DLC layers was reduced significantly. Although, Glancing Angle X-ray Diffraction (GAXRD) and Raman spectroscopy did not show any significant crystallisation of the DLC coating after the laser irradiation, however, the analysis indicated that a thin graphitised layer had been formed on the surface as a result of the femtosecond laser processing.

Keywords: LIPSS, Diamond-like carbon (DLC), femtosecond laser, laser micro processing.

4.1. Introduction

Diamond-like carbon (DLC) coating is an amorphous form of carbon with a significant fraction of tetrahedral (sp^3) bonds [82]. The coating stands out among others for its high hardness, low friction coefficient, low adhesion, small surface roughness, optical transparency [83] and chemical inertness. Some of its properties are similar to those of diamond because of the presence of diamond-like bonds and also mostly because the isotropic disordered thin film does not possess any grain boundaries [145] (DLC is amorphous hence does not possess grain boundaries as a result of the deposition process). At the same time, they are cheaper to produce and therefore DLC coatings are widely used in various applications, i.e. as protective and wear resistant coatings in biomedical implants [81], microelectronic devices [78], as infrared optical windows and in magnetic storage discs [146].

DLC coatings also can be applied as solid lubricant to increase durability and reduce demoulding forces in injection moulding. The effectiveness of DLC coatings in this process was studied and it was found that the replication performance together with component's lifespan were improved [80]. In particular, it was possible to produce a higher number of replicas with acceptable quality while the tool wear was minimised, i.e. the sharp edges on the mould were preserved during a higher number of cycles without the need to clean or replace the mould. Another benefit associated with the use of DLC coatings in the micro injection moulding process is its lower thermal expansion compared with common steel moulds. This could increase the tool life by preventing delamination, cracking and coating failures. However, a good adhesion between the DLC coating and the mould is necessary and a proper selection of the tooling material, thermoplastics and moulding process parameters is required [147].

Additionally, due to DLC's lubricating properties and low surface roughness, the ejection forces in micro injection moulding of components with large area to volume ratios surfaces can be decreased significantly [95]. Also, the same effect was observed on DLC coated mould tools with sub-micron textures (nano bead-like features and nano pillars fabricated by photolithography) and this was explained with the low coefficient of friction (CoF) as a dominant factor in achieving low demoulding forces [94]. It is worth noting that these investigations were conducted using relatively thick DLC coatings up to 5 μm which were applied on completely machined moulds and thus their properties remained intact. However, if sub-micron structuring of the moulds is required this should be performed only after DLC is applied and it should be stressed that any processing, including laser, should not alter the coating's properties. In this way, DLC's advantageous properties could be combined with those of micro and nano patterned/textured surfaces. So far improving DLC's properties was achieved by either strengthening DLC with titanium or nitrogen doping [80] or by micro-scale patterning of the coating with a nanosecond laser, resulting in 30% CoF improvements [79]. Also, it was reported that the friction properties could be preserved or even improved after femtosecond (fs) laser sub-micron structuring, although this was dependent on the contact material and laser pulse energy [148], [149]. CoF as low as 0.02 was achieved when additional layer of MoS_2 was applied on top of the laser structured DLC [73].

Laser-induced periodic surface structures (LIPSS) are known for their optical [47], antibacterial, biological [61] and hydrophobic properties among their other surface functionalisation applications. Such surface responses had been achieved by optimising the process and thus to produce structures with specific geometric characteristics, e.g. to generate uniform and homogenous LIPSS by obtaining and maintaining the most effective light diffraction. LIPSS are formed on surfaces at process settings near the ablation threshold of a given material due to interference of incident laser light with excited surface electromagnetic wave [150]. Their sub-micron periodicity depends on the laser source wavelength and dielectric constants of the material while their orientation is normal to the beam polarisation vector and their amplitudes can be varied by controlling the laser fluence level [151].

Synergistic effects can be sought by fabricating LIPSS on replication masters with DLC films, especially to improve both their wear resistance, i.e. the tool durability with regards to the surfaces' functional response, and also the quality of replicas because of DLC lubricating properties. However, laser irradiation of amorphous materials, such as DLC, can lead to structural changes and thus alter their properties. Laser processing of DLC was already reported and pulse duration was identified as the most important factor governing the resulting coating's structure. Longer pulses and higher intensity led to graphitization, spallation and evaporation and thus creating swelling, delamination and removal of the DLC layer at the end. In addition, surface morphology changes were observed which is common in carbon based materials, for instance a structural transformation into glassy carbon (GC) [152]. This carbon material has sp^3 content close to 0% and benefits from higher conductivity, thermal resistance and similar frictional properties to DLC but inferior wear resistance [153]. Therefore, it was concluded that longer pulses, pico- and nanosecond, and higher ranges were not suitable for patterning/structuring of DLC films. At the same time, femtosecond laser processing has emerged as a promising technology for a very controllable generation of fine and precise structures both at micron and sub-micron scale with minimized thermal effects.

In this research, the effects of the femtosecond laser processing parameters in producing homogenous and uniform LIPSS on DLC coating were investigated with a special focus on their resulting properties. Especially, a LIPSS treatment of steel substrates with DLC films was studied as one-step approach for producing functional and, at the same time, durable surface structures/textures for replication masters.

4.2. Materials and methods

A thin DLC film was deposited on a 2.5 mm thick 316L stainless steel substrates by employing a plasma-assisted chemical vapour deposition (PACVD) to produce a coating with 2 – 5 μm thickness (2000 to 5000nm, range provided by the supplier, Oerlikon Balzers), 22 GPa hardness (equivalent of HV 2500) and 0.05 μm surface roughness. The coating process was carried out by Oerlikon Balzers, a company specialized in DLC coating, based in Milton Keynes (UK). The DLC film was irradiated with a femtosecond Ytterbium-doped fibre laser source with the following technical characteristics: a near infrared wavelength (λ) of 1030 nm, pulse duration of 310 fs and maximum pulse energy of 10 μJ. A linearly polarized laser beam was focused with 100 mm telecentric lens on the substrate surface to achieve a beam spot diameter (d_b) of 40 μm at $1/e^2$ of Gaussian profile intensity. The schematic scanning strategy of an area is illustrated in Figure 4.1 where fixed hatch distance (h) between scan lines was 3 μm that resulted in 92.5% pulse overlap in the Y direction while the pulse distance in the X direction was varied with scanning speed (v) and frequency (f) to control the LIPSS uniformity. The pulse fluence was calculated as follows [143]:

$$F = \frac{4P}{f\pi {d_b}^2} \tag{4.1}$$

where P is the average power (W).

The effects of accumulated fluence (F_{acc}) on the resulting LIPSS was identified in this research by varying the number of pulses for single spot irradiation and number of pulses per spot for large area structuring, which values were calculated as follows (adapted from [143]):

$$pps = \frac{f \cdot d_b}{v} \tag{4.2}$$

However, Eq. 3.2 defines only the number of pulses along one scan line. Processing of surfaces areas larger than the beam spot size requires multiple scan lines. Hence, the pulse overlap with h between the scan lines should be considered, especially when h < d_b, as follows:

$$pps_{total} = \frac{f \cdot d_b}{v} + \frac{d_b}{h} \tag{4.3}$$

Therefore for processing of surfaces with area bigger than d_b, pps_{total} was taken into account for F_{acc} calculations.

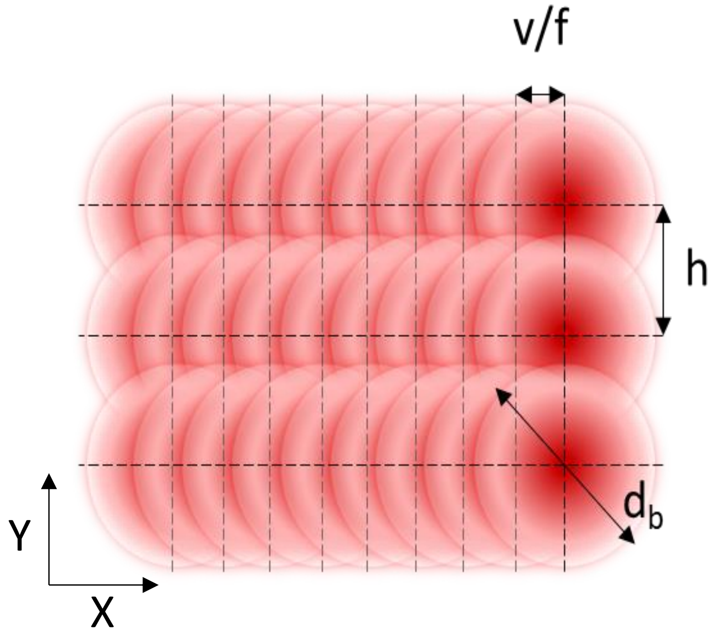

Figure 4.1 A schematic illustration of laser irradiation strategy for structuring of large area with pulse overlapping from scanning speed (v) and frequency (f) in X direction and hatch offset (h) between the lines in Y direction.

The topographies of processed surfaces were analysed with Atomic Force Microscope (AFM) and Scanning Electron Microscope (SEM) in order to study the LIPSS geometrical characteristics and at the same time to detect any damage (defined as cracks, excessive ablation or delamination) to the DLC coating, through Alicona optical microscope with a 100x magnification capabilities. LIPSS periodicity was determined by performing 2D Fast Fourier Transformation (2D FFT) of the images while their uniformity was assessed visually by indications of non-processed areas or highly irregular ripples.

CoF and wear resistance of textured DLC films were measured with a ball-on-plate tribometer at room temperature under dry condition. Linear reciprocating tests were performed using an Alumina ball of 8 mm diameter with a hardness of approximately 16 GPa (HV 1600). The distance of the lines was 4 mm per cycle and the reciprocating movements were executed with a speed of 2 mm/s. The load applied on the DLC film was 150 g (1.47 N).

Raman spectra was recorded from 100 cm^{-1} to 3200 cm^{-1} using a 633 nm laser source with a focused spot size of approximately 2 μm. Axial and lateral resolutions were less than 1 μm and 0.25 μm respectively. The resulted spectra were fitted with Lorentzian and Breit-Wigner-Fano (BWF) profiles for D and G peaks, respectively, with a linear baseline correction for the background. The peak position and the full width at half-maximum (FWHM) were calculated.

The DLC crystalline structure was analysed with Glancing Angle X-ray Diffraction (GAXRD) with a Cobalt source at an incident angle of 3 deg. The penetration of the X-ray beam was within the DLC film thickness and thus to easily detect any long-range crystallisation into the laser processed DLC.

The hardness of as-received (coating received from supplier defined as not structured surface) and laser processed DLC films were measured by conducting a nanoindentation test. A hard diamond indenter with a tip radius of 50 nm was used 10 times on each sample by applying a load with a loading rate of 0.3mN and with a depth control of 400 nm. In this way any periodic sub-micron structures present on the surface, that could have average peak-to-valley distance of 200nm, were less likely to affect the hardness measurements and also the indentation depth was within the recommended less than 10% thickness of the coating if assuming the coating was 5000 nm thick. In worst case scenario the indentation depth could have reached 20% of the coating thickness (when assuming thickness of 2000nm) and then there was a risk of the measurement to be affected by the substrate material. For this reason the indentations were repeated 10 times on each of the tested sample. For the clarity check further tests were also done with the depth control of 200 nm and 600 nm, and for comparison the 600nm results were also reported.

4.3. Results and discussion

4.3.1. LIPSS optimisation

4.3.1.1. Single spot irradiation

Two types of LIPSS can be distinguished when their periodicity (Λ) is considered, i.e. low spatial frequency LIPSS (LSFL) and high spatial frequency LIPSS (HSFL). LSFL has a Λ close to the laser source wavelength (λ) while the ripples are perpendicular to the beam polarisation vector. On the other hand, HSFL has a Λ much smaller than λ and their orientation can be either parallel or perpendicular to the beam polarisation vector [143].

Single spots were irradiated onto DLC with varied processing settings, i.e. the number of pulses and fluence, to study the LIPSS generation from their development onto the surface.

Five representative SEM images of LIPSS evolution as a result of the increasing pulse and accumulated fluence are provided in Figure 4.2. One pulse irradiation did not result in any surface damage and only after 20 pulses (see Figure 4.2 I) HSFL gradually appeared around the spot periphery with periodicity of approximately 140 nm (~ 0.1λ). At the same time, LSFL generation was observed at the spot centre where the intensity was much higher. A further increase of the number of pulses to 50 led to the generation of straight and uniform LSFL as depicted in Figure 4.2 III while there was a fraction of HSFL around the spot edge. Such observation is caused by the Gaussian distribution of the laser beam where the laser energy decreases at the peripheral of the beam spot. As can be seen in Figure 4.2 IV further increase of pulse fluence but same number of pulses lead to bigger area of uniform LSFL and reduced fraction of HSFL. Hence the threshold fluence for HSFL generation is lower than that for LSFL [154]. On the contrary, the same number of pulses but with a lower fluence resulted in formation of LSFL and HSFL across the spot area (Figure 4.2 II). Ablation of the DLC film at the spot centre can be observed at 100 number of pulses but with visible LSFL and HSFL around the spot edge together with some molten material (see Figure 4.2 V). Thus, the LIPSS evolution from HSFL to LSFL and the removal of the DLC film with the increase of pulse numbers clearly shows that optimal accumulated fluence with pulse fluence and number of pulses above respective thresholds are required for achieving homogenous LIPSS generation. In this research, the focus is on homogenous LSFL generation onto the DLC films (later referred as LIPSS only) as they are commonly investigated when LIPSS are employed to the functional response of surfaces.

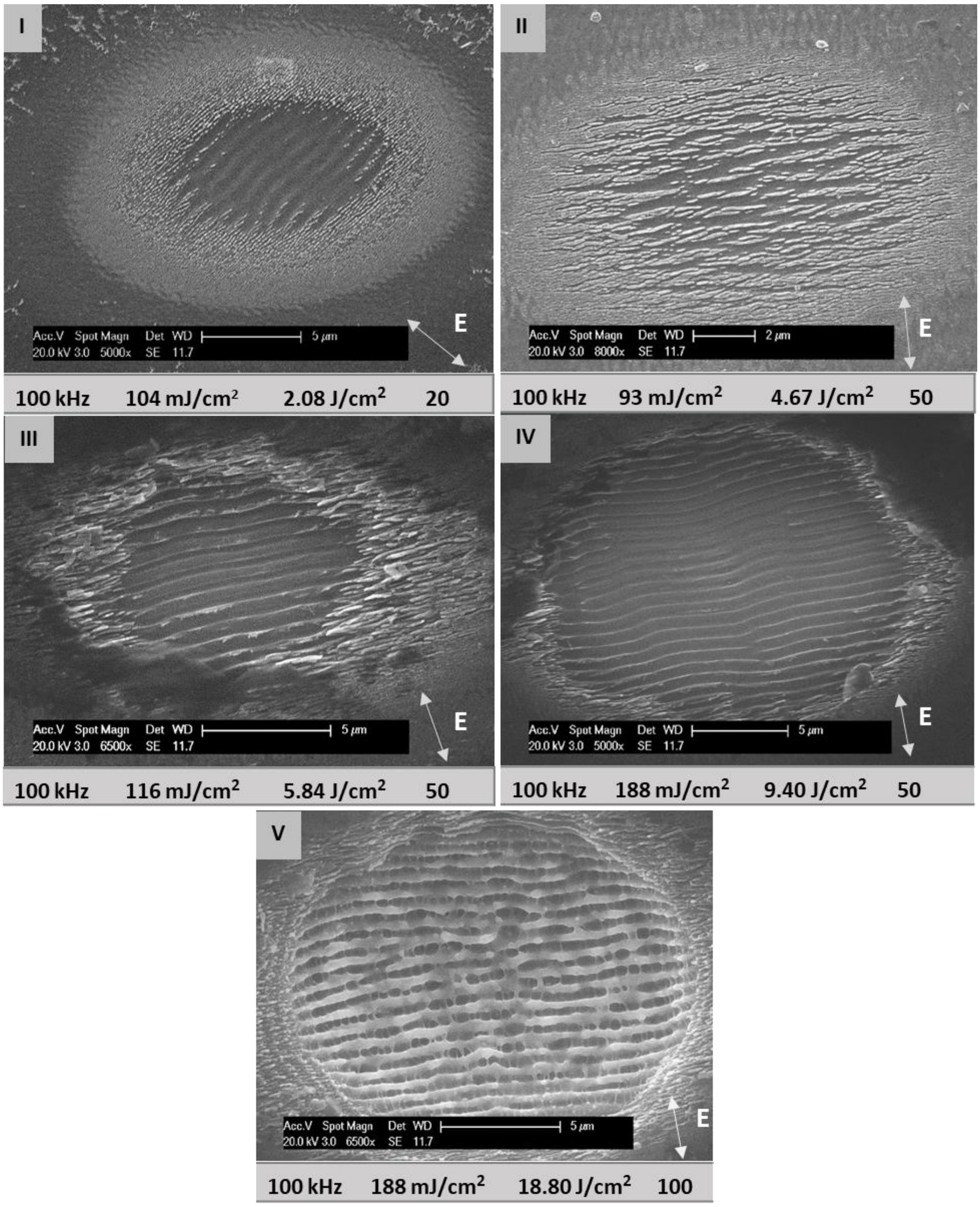

Figure 4.2 Single spots irradiated with a fs laser source and varying pulse numbers and fluence. Arrow indicates vector of polarization direction. Note: the processing parameters, i.e. frequency, pulse fluence, accumulated fluence and number of pulses,

used for the LIPSS generation are provided below the corresponding SEM images. Accumulated fluence equals the pulse fluence multiplied by number of pulses.

4.3.1.2. Large area structuring

A LIPSS treatment of replication masters with DLC films is the focus of this research and therefore the process settings should be optimised for large area structuring. Thus, a processing window to achieve uniform LIPSS coverage of large areas without damaging the DLC coating and any excessive ablation is identified. The parameter domain investigated has a fluence and pps of 58 to 130 mJ/cm^2 and 14 to 33 (levels of those ranges provided in Chapter 3), respectively as shown in Figure 4.3a. The scan lines' offset, h, was kept constant and thus pps$_{total}$ resulted in range from 28 to 47. The uniformity of the resulting LIPSS was assessed and any visible DLC damage was identified, especially when the stainless steel substrate underneath was revealed. It is worth noting that the use of process parameters outside the investigated parameter domain led to an ablation of the coating or the generation of non-uniform LIPSS over the processing area. The increase of fluence and pps$_{total}$ improves LIPSS uniformity. Therefore, the processing window investigated in this research (see Figure 4.3a) was defined by taking both, uniformity of LIPSS and damage of DLC, into consideration. The DLC characterisation work was performed on three representative samples, i.e. S1, S2 and S3, chosen at the window boundaries or just outside the tested parameters and one, S4, at its centre. The surface topographies of the four samples are depicted in Figure 4.3b with their respective laser processing parameters underneath the images. It should be noted that fluence used for sample S3 of 66 mJ/cm^2 was selected to be close to the processing window but not too similar to the laser intensity employed on other three samples.

Considering the results from the single pulse irradiation (see Section 4.3.1.1), it can be stated that LIPSS produced with a scanning beam over large areas are of similar characteristics where used F_{acc} is marginally lower when compared to the one applied for single pulse irradiation. A close look at the LIPSS morphologies in Figure 4.3b suggest that HSFL are still present on the samples but they are more pronounced on S3. The used pps_{total} and F for this sample was the lowest and as a result also low accumulated fluence (F_{acc}) and therefore the resulting ripples were similar to those depicted in Figure 4.2 I where LSFL are wavy and irregular. At the same time, the LIPSS straightness on S1 and S4 is better while HSFL are less visible due to higher F despite similar pps_{total} was applied. S2 was produced with the highest process settings, F and pps_{total}, which resulted in highest F_{acc}, and therefore LIPSS were well defined but at the same time there were some areas on the surface where the DLC film was much thinner and with beginning of delamination of the coating (not shown in Figure 4.3b).

It was observed that the LIPSS periodicity achieved with the optimised process setting was in the range of 700 to 800 nm (~ 0.7-0.8λ). This was lower than the commonly observed LIPSS periodicity range from 800 to 950 nm on steel substrates with the same laser wavelength and this could be partially attributed to the differences between steel and DLC optical constants, in particular refractive index and extinction coefficient. The height of the produced ripples was 200 nm on average and was consistently obtained across the studied processing domain.

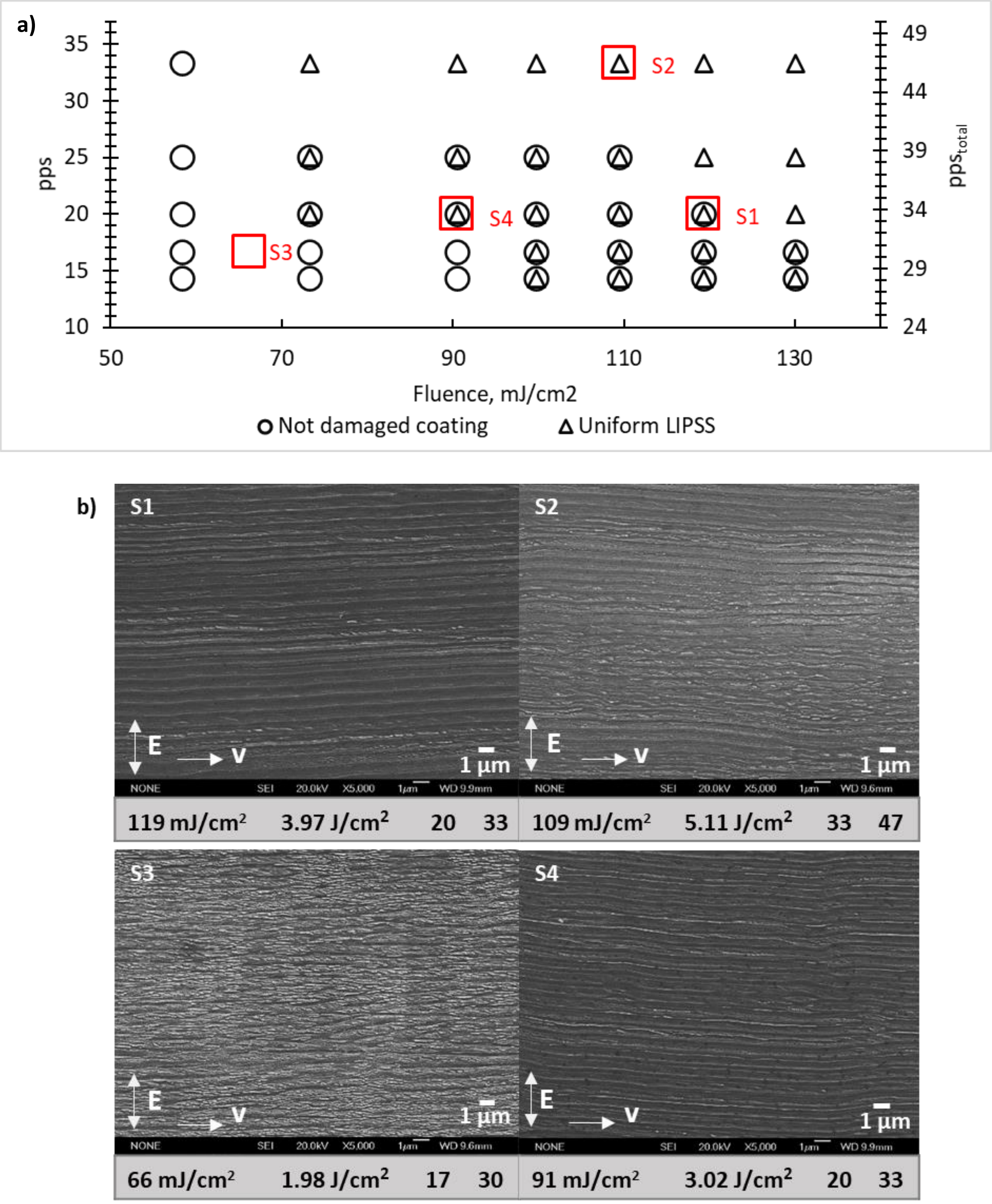

Figure 4.3 The results obtained with large area structuring: a) the effects of pulses per spot (*pps*) and fluence levels on LIPSS uniformity across the studied processing domain; b) SEM images of S1, S2, S3 and S4 samples (red squares in a). Arrow indicates direction of polarization vector (E) and scanning speed (v).

Note: the processing parameters: F, F_{acc}, pps and pps_{total}, are provided below the corresponding SEM images.

4.3.2. Characterisation

4.3.2.1. Raman spectroscopy

Laser treated and as-received DLC samples were analysed employing Raman spectroscopy that is considered a reliable way to obtain structural information and also to judge about the quality of carbon materials. The DLC specific spectrum shown in Figure 4.4 consists of two sp^2-carbon characteristic modes: D (‘disorder’ – ‘ring’ type bond) and G (‘graphite’ – both ‘ring’ and ‘chain’ types) with positions of 1268 cm^{-1} and 1509 cm^{-1}, respectively. The ratio between D and G peak, i.e. I(D)/I(G), can be used as an indication of the fraction of graphite-like (sp^2 aromatic rings) domains in a DLC thin film. Fitting results are provided in Table 4.1. The D and G peaks positions differ from the ones reported usually as 1355 cm^{-1} and 1550 cm^{-1} due to a higher Raman laser wavelength used in this study, which causes the peaks shift towards lower wavenumbers [145]. The spectrum is dominated by the sp^2 sites up to 230 times more when compared to sp^3 due to higher polarizability of π states, typical for this type of bonding [145]. The position of G peak is at 1570 cm^{-1} and intensity I(D)/I(G) ratio is close to 0 (for Raman data at 514 nm) in case of ideal ta-C DLC coatings with high fraction of sp^3 bonds (above 70%) [82]. It was reported for laser pattered DLC with ns laser pulses that the G position shifted to higher wavenumbers while D intensity increased with the increase of fluence, and this indicated a progressive laser-induced graphitisation of the amorphous DLC [85], [155]. After the femtosecond laser treatment of four samples which spectra are shown in Figure 4.5, it is visible that G peak shifted to 1590 cm^{-1}. The intensity ratio of two peaks I(D)/I(G) increased from 0.2 on the as-received DLC to above 1.0 for the laser patterned surface. Even though these changes in spectra could indicate an induced graphitisation of the thin film, there are no substantial changes between the four laser structured samples that have been produced with different laser processing parameters. This might be due to the ultrashort pulsed laser processing did not introduce ant heating into material and/or the differences of laser processing parameters between the samples were minor. Raman spectra were also obtained on the samples produced with a lower number of pps and higher fluence, and still there was no further shifts in the peaks or intensities. The similar spectra suggest that the increase of fluence did not initiate further changes in the DLC short ordering.

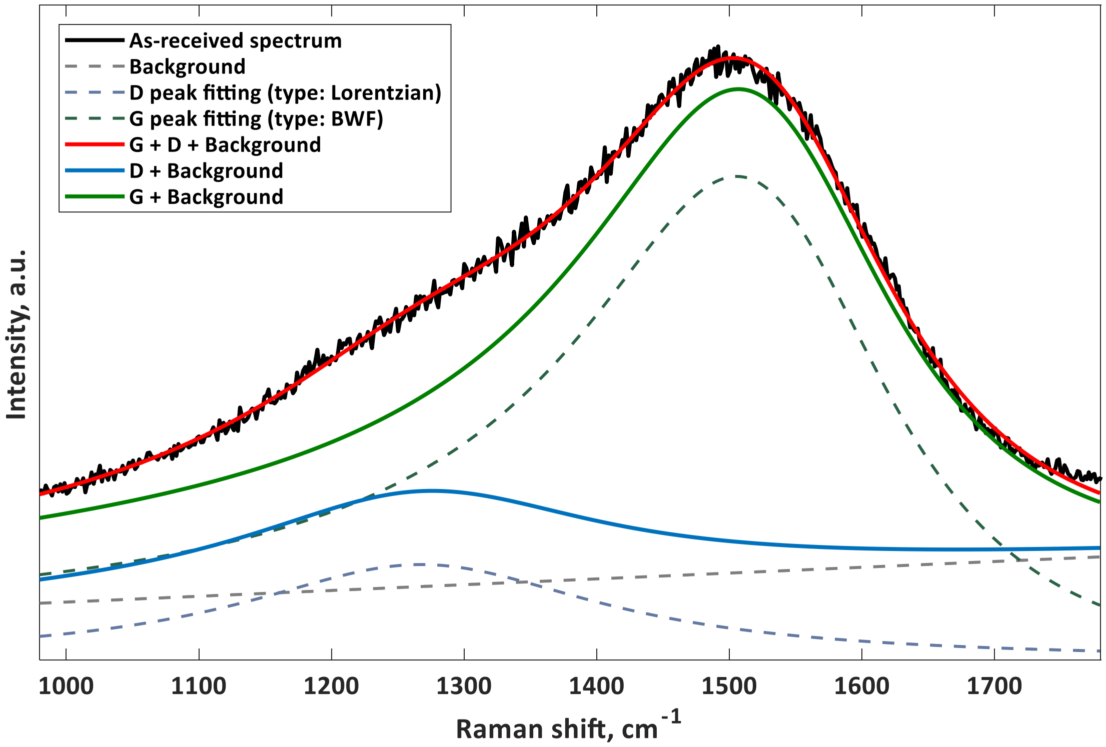

Figure 4.4 Raman spectra of as-received DLC and its deconvolution: linear background together with Lorentzian and Breit-Wigner-Fano fitting lines for D and G peaks, respectively.

Table 4.1. Results of G and D peaks' fitting for as-received and laser textured DLC samples.

Sample	G pos., cm^{-1}	G FWHM, cm^{-1}	D pos., cm^{-1}	D FWHM, cm^{-1}	I(D)/I(G)	Fitting error, %
S1	1590 ± 3	136 ± 42	1340 ± 6	294 ± 37	1.06	3.35
S2	1591 ± 5	132 ± 45	1338 ± 5	294 ± 46	1.12	2.95
S3	1587 ± 11	135 ± 136	1335 ± 7	293 ± 89	1.23	2.91
S4	1590 ± 6	133 ± 38	1335 ± 6	298 ± 67	1.16	2.30
As-received	1509 ± 3	286 ± 8	1268 ± 11	330 ± 49	0.20	1.26

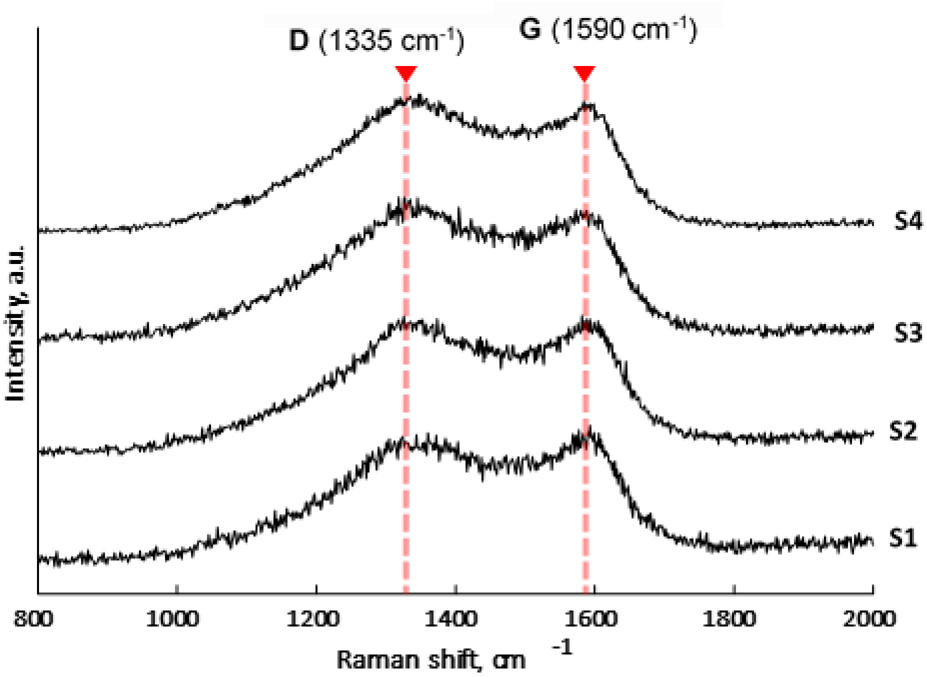

Figure 4.5 Raman spectra of four fs laser processed DLC samples. The D and G peaks positions of Raman spectra are highlighted by the red-dashed lines.

The interaction between ultrashort pulses and carbon phases should be properly explained to further understand the resulted change in Raman spectra. Studies reported that fs laser pulses induced non-equilibrium transition of sp^3 to sp^2 bonds [156]. Additionally, atomistic simulation of graphitization of the diamond involving electron system set to a very high temperature revealed that a layer-by-layer graphitisation could occur within the optical depth of diamond absorption [157] whereas for longer pulses graphitisation would propagate into the bulk due to heat dissipation and thus temperatures above the graphitisation threshold could be reached [152]. The thickness of such graphitised layers would be dependent on pulse numbers and fluence with a depth limitation of hundreds of nanometres (up to 200 nm). In addition, it was reported that the resulting Raman spectra of DLC processed with ns and fs pulses did not differ significantly, though it was stated that their graphitized layers led to structural distinctions [91]. Other researchers suggested that fs laser processed DLC would be modified into Glassy Carbon (GC), a form of carbon with 100% sp^2 and sp^3 content close to 0% with a hardness of 3 GPa [145], but with similar D and G peaks position [93]. A further increase of processing fluence would lead to Raman results similar to the spectra of superimposed GC, DLC and carbonaceous materials [158]. However, the penetration depth of Raman laser sources can be higher than modified layers and thus the laser can excite not only the modified layers but also non-modified DLC.

Overall, it can be stated that fs laser processing did not trigger significant changes in the bulk DLC structure and only a thin laser-modified surface layer was graphitised because, although the presence of graphitised surface layer was confirmed by Raman spectra analysis, it was not possible to identify the layer thickness. It is worth to remind that the Raman measurement axial resolution was 1μm and the reported thickness for femtosecond laser was from 90 to 200 nm [152]. Therefore, the LIPSS amplitude is of similar scale and therefore this fact cannot be neglected. Additionally, mechanical properties of such graphitised layers are quite different and inferior when comparing to as-received DLC.

4.3.2.2. Glancing angle X-ray diffraction

A further analysis was conducted with GAXRD to investigate the resulting structural changes in the laser treated DLC. The results obtained on as-received and laser modified DLC are shown in Figure 4.6. Samples S2 and S3 were chosen for this additional analysis as the laser settings used in their processing were the most distinct (see Figure 4.3), meaning S2 and S3 were produced respectively with the highest and lowest accumulated fluence. It was confirmed that the first and third peaks visible in Figure 4.6 come from the austenite in the substrate, i.e. the steel plates that were coated with DLC; that’s because GAXRD penetration capability was actually higher than the coating thickness itself thus detecting a signal also from the steel substrate. The second small peak could be attributed to either ferrite within the austenitic stainless steel or chromium coming from the buffer layer (which is standard layer applied during the PACVD process to improve adhesion) between the DLC and steel substrate as they have similar crystal structures. The difference in intensities or the small shifts could be explained with some misalignment on the surface level during the measurements that were more pronounced in GAXRD. No graphite crystallisation was detected by this GAXRD measurement implying the absence of DLC crystallisation or crystallites size changes after laser processing were too small to detect by X-ray. In addition, if the laser modified layer thickness is less than 200 nm (see Section 4.3.2.1), any signal coming from such a thin layer could be too weak to detect. If any substantial graphite crystallisation at micro or nano scale was present, a broad peak would have appeared at approximately 26 or 50 deg [159].

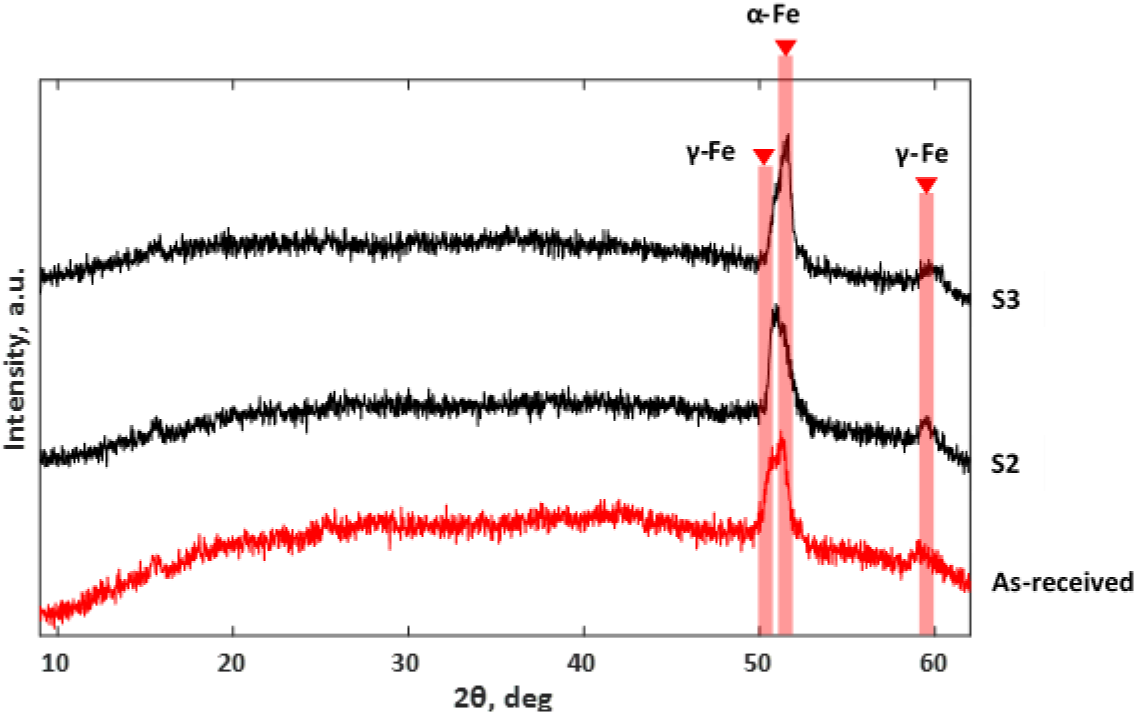

Figure 4.6 GAXRD spectra of DLC coatings on as-received and S2 and S3 samples after fs laser processing.

4.3.2.3. Nanoindentation

It is not easy to assess the actual hardness of LIPSS onto the DLC films due to the ripples influence on the surface and also the relatively soft substrate material. The results from the nanoindentation measurements are summarised in Figure 4.7 where a distinct hardness reduction of DLC coating can be seen after the fs laser processing. The main discussed results are the ones reported for the nanoindentation depth control of 400 nm but the results for 600 nm were also plotted in Figure 4.7 for comparison. The hardness has been reduced from 22 GPa to approximately 9 GPa for sample S3 which was a sample that was produced with lower fluence and less pps. These changes could be attributed more due to the presence of the laser-induced modifications in DLC, that is the presence of thin layer after the fs laser processing which affected its hardness (see Section 4.3.2.1) than to the presence of LIPSS. Another evidence for this effect is that the further increase of fluence and pps led to even bigger hardness reduction of approximately 4 GPa on sample S2. For comparison the hardness of the steel substrate is around 2.5 GPa which is highlighted with red dashed line in the Figure 4.7.

It is worth reminding that the as-received DLC coating thickness was from 2000 to 5000 nm meaning that the risk of the substrate influencing this measurement was reasonably low as the nanoindentation was depth controlled of 400 nm. The additional nanoindentation tests were also conducted with depth control of 200 nm and 600 nm but the repeatability was much lower in the first case because of the LIPSS presence on the surface. In the second case of the measurement control of 600 nm the results are also provided in Figure 4.7 and its can be stated that this measurement condition provided comparable results as to the 400nm depth controlled one. However, higher penetration depth during the measurement could have higher chances to be influenced by the substrate. Therefore, the measurements with depth control 400 nm were taken for consideration.

All these suggests that the DLC film is sensitive to the used laser processing parameters and even small changes can lead to substantial deviations of resulting nanohardness. The other reason for the distinct hardness reduction could be the wavy profile of LIPSS on the surface that could affect the indentation contact and thus the obtained hardness values.

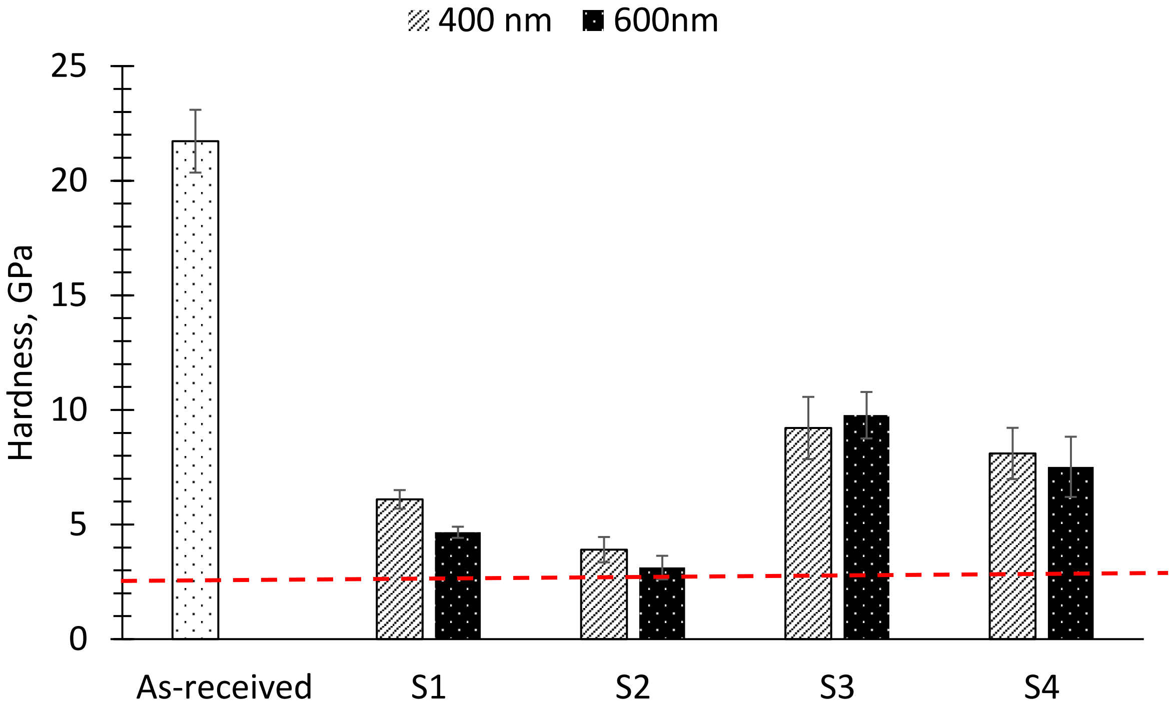

Figure 4.7 Nanoindentation results of as-received and laser textured DLC. Two sets of results for depth control of 400nm and 600 nm was provided. The red dashed line indicates the hardness of the steel substrate.

4.3.2.4. Ball-on-plate tests

The results from the CoF Measurements on fs laser processed and as-received DLC after 100 ball-on-plate cycles are provided in Figure 4.8. It can be seen that up to 50 cycles there were no visible changes in friction properties between as-received and laser processed samples. However, a slight CoF increase on processed samples was observed after 50 cycles. This can be explained with the increased contact area between the ball and the LIPSS treated plates as depicted in Figure 4.9. All four fs laser treated samples did not demonstrate significant CoF differences with the increase of the ball-on-plate cycles, in spite of the exhibited changes in their mechanical properties, e.g. their hardness. Taking into account the presence of the thin modified layer discussed in Section 4.3.2.1 that is structurally similar to GC, these results are expected because of the comparable tribological performance of both materials. In particular, it was reported that GC had CoF of around 0.2 when Alumina balls were used in the tests [160] while a mean CoF value of 0.12 was obtained in this research on as-received DLC. Interestingly, the same CoF trends were observed during reciprocating tests performed perpendicular and parallel to LIPSS, as can be seen in Figure 4.8a and 4.8b. In addition, the wear tracks had similar widths, too, and thus the orientation of periodic structures did not influence the CoF measurements but mostly the contact of the laser modified DLC with the ball.

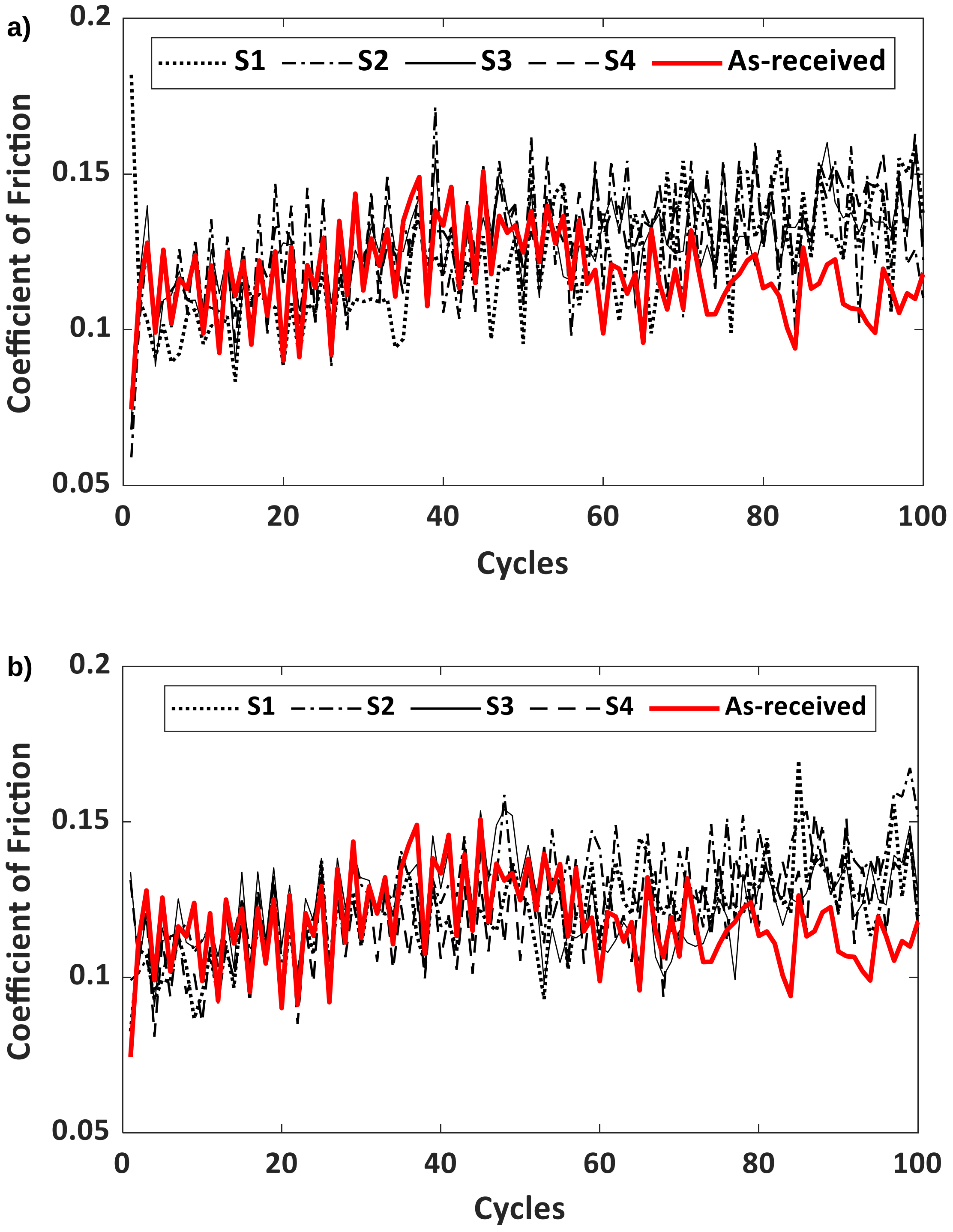

Figure 4.8 Measured COF for 100 cycles for as-received and laser patterned DLC samples with reciprocating direction perpendicular (a) and parallel (b) to LIPSS.

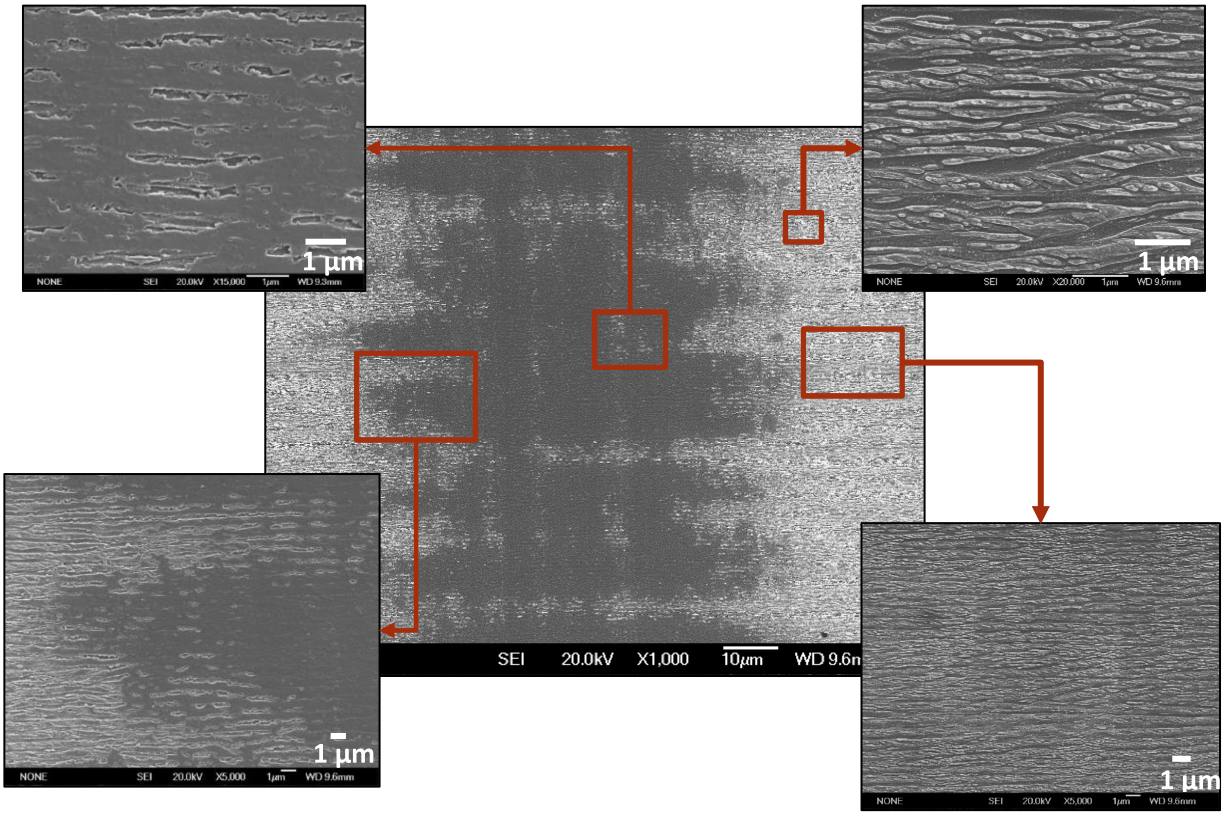

Figure 4.9 SEM images of wear tracks of sample S3 after 50 reciprocating cycles perpendicular to LIPSS.

After examining the wear track with the focus variation microscope, the track did not have any noticeable depth at macro scale or the material removal was too small to detect. Additional AFM measurements were conducted that revealed smudged LIPSS and the surface looked like have been polished as depicted in Figure 4.9 and 4.10. Further EDS inspections did not detect any Alumina traces in the wear track and thus to suggest that any debris came from the modified DLC. Apparently, the graphitised layer filled the valleys of the ripples during the ball reciprocating movements and as a result the LIPSS profiles became shallower (Figure 4.10). This cannot be considered unexpected as at this point the surface hardness was already lower than that of the alumina ball.

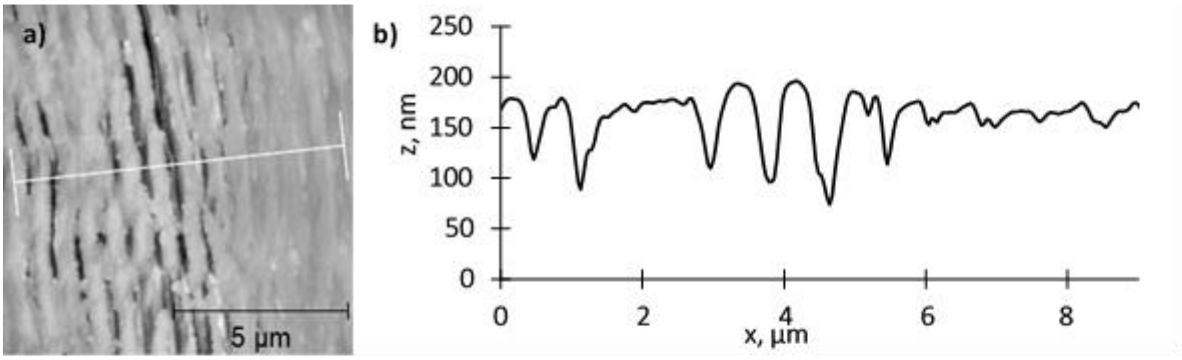

Figure 4.10 AFM measurements: a) sample S3 after 100 reciprocating cycles parallel to LIPSS with an Alumina ball; b) the LIPSS profile along the white line in a)

Note: the measurement was taken in the middle of the wear track.

The four samples were not investigated further because only the friction behaviour rather than long-term wear performance was of interest in this study. It is worth mentioning that maximum Hertzian contact pressure calculated as Alumina ball with flat DLC as a counterpart was around 620 MPa in this tests [161]. It is six to three times more than the contact/holding pressure in injection moulding processes [162]. Additionally, it can be stated that the measured CoF increase of 0.05 over the fs laser processed DLC should not make this surface treatment as not appropriate for producing replication masters but some additional micro tribology tests with tips smaller than nanostructures should be performed to validate this further.

4.4. Conclusions

The effects of fs laser processing of DLC, especially on its properties, were investigated in this research as a potential treatment for replication masters. It was demonstrated that highly uniform LIPSS can be generated on thin DLC films without any delamination when optimised process settings are used, i.e. pulse numbers and fluence. The effects of this fs laser treatment were studied on representative DLC coated samples and the following conclusions were made:

- Raman spectroscopy indicated that fs laser processing led to the formation of a thin graphitized surface layer that had changed properties to as-received DLC and could explain the reduced hardness of fs laser treated DLC samples.
- GAXRD showed that there were no appreciable changes in the DLC long-range ordering as a result of the fs laser processing, confirming that the change in crystallisation status, if any, should only occur within the thin laser-modified layer.
- The hardness of fs laser treated DLC samples was dependent on the used laser processing settings, i.e. it decreased with the increase of pulse number and fluence, and overall it was significantly reduced after the fs laser treatment.
- Fs laser processing of DLC had only a marginal effect on CoF. However, even small number of reciprocating cycles with an alumina ball led to flattening of sub-micron ripples on the fs laser treated DLC samples.

Based on the findings of this research, the fs laser treatment of DLC coatings can be considered suitable for producing replication masters because of its lubricating properties and with hardness still three times higher than the substrate material, i.e. stainless steel. Most of the DLC attractive properties can be maintained, especially relatively low CoF values and hence the low adhesive nature of DLC coatings even after their fs laser treatment. In other words, fs laser structuring/texturing of DLC coating for producing replication masters can benefit from functionalised sub-micron structures, i.e. LIPSS, incorporated on durable coatings' surface and with improved demoulding performance at the same time. This is very important for the broader use of fs laser technology in tool making that allows to combine advantageous properties of not only the material but also added functionality of structures/textures.

Chapter 4 demonstrated that uniform LIPSS can be generated on a larger area on the DLC without coating delamination when laser pulse numbers and fluence is controlled. The results confirmed structural changes in thin coating's layer of laser structured surface and indicated that frictional properties of DLC are maintained after femtosecond processing but with distinct reduction in hardness. Nevertheless, it was stated that combining femtosecond laser processing with DLC coating for manufacturing replication masters is still beneficial. The tested properties were inferior to as-received DLC but still superior to the substrate material, i.e. stainless steel.

In the previous Chapter, the experiments were conducted on a planar surface with normal laser incidence. However, the polymer replicas covered with LIPSS as functional surfaces might need to be of more complex shapes than just flat areas. The manufacturing of the replication masters and the laser structuring/texturing process could also be applicable to freeform surfaces. As explained in Chapter 2, the processing of non-planar surfaces affects the laser processing conditions and, without appropriate countermeasures, the LIPSS produced on such surfaces may degrade or lose their surface functionality. This is also a limitation for any industrial real-life application and it remains an open issue for LIPSS treatments. In the next chapters, LIPSS research questions are addressed that are related to their modelling and monitoring when laser processing conditions are disturbed which happens on freeform surfaces. The application is now not only restricted to injection moulding process but could have wider implications where functionalized freeform surfaces with LIPSS are required. For that reason, the material used for the following studies is stainless steel in order to be more representative to metals with similar material properties.

CHAPTER 5: MODELLING ULTRAFAST LASER STRUCTURING/TEXTURING OF FREEFORM SURFACES

In this Chapter, the second research question from Chapter 2 is addressed. The analytical model, based on ultrafast irradiation principles and previous works on predicting LIPSS parameters domains, is developed for assessing the accumulated fluence when treating freeform surfaces. For the first time, it acknowledges the impact of two main processing disturbances on the actual laser beam distribution and local fluence threshold changes. Afterwards, the model is validated on samples produced with controlled processing disturbances. The laser processing parameters for fluence threshold definition was provided in Table 3.4 while validation experiments correspond to the ones from Table 3.5. The research is proposing a basis for assessing laser conditions on freeform surfaces that is needed to understand the changes in LIPSS behaviour hence to define the limits of their functional responses. It is especially essential in determining the processing constraints for given laser parameters' domain which helps designing efficient strategies for laser structuring/texturing of non-planar surfaces.

Aleksandra Michalek[1], Afif Batal[1], Shaojun Qi[2], Pavel Penchev[1], David Bruneel[3], Tian Long See[4], Stefan Dimov[1]

[1]School of Mechanical Engineering, University of Birmingham, Edgbaston, Birmingham, B15 2TT, UK

[2]School of Metallurgy and Materials, University of Birmingham, Edgbaston, Birmingham, B15 2TT, UK

[3]LASEA, Rue des Chasseurs Ardennais, 10, 4031 Angleur, Belgium

[4]The Manufacturing Technology Centre Ltd, Pilot Way, Ansty Park, Coventry, CV7 9JU, UK

This research was published as a full-length article in *Applied Surface Science Advances (2020).*

Author’s contributions:

A. Michalek	Main author, conceived theory and methodology, software and code, performing all laser experiments, data analysis and writing original draft
A. Batal	Supported with data analysis
S. Qi	Supported with AFM measurements
P. Penchev	Supported with laser setup
D. Bruneel	Resources
T.L. See	Industrial supervisor
S. Dimov	Supervisor, Revision of the manuscript

Abstract

Laser structuring/texturing of freeform surfaces is attracting the attention of researchers and industry because it can enable high impact applications and also the technology can offer important advantages compared to alternative/conventional processes. So far, laser structuring/texturing has been applied mostly on planar surfaces, while employing it for 3D processing it introduces some disturbances that affect the processing conditions. In particular, Beam Incident Angle (BIA) and Focal Offset Distance (FOD) variations are two important processing disturbances that impact the resulting structures/textures on freeform surfaces and also their functional responses. Furthermore, those disturbances should be considered as constraints in planning the laser processing operations, i.e. when pre-processing 3D models by partitioning into laser processing fields, and also in designing the processing strategies. However, such constraints are always material specific for a given parameters' domain and can be time-consuming to determine empirically. In this research, a model for calculating the accumulated fluence for generating Laser Induced Periodic Surface Structures (LIPSS) throughout the processed freeform surfaces is proposed. It considers the actual spatial intensity distribution of a Gaussian beam when processing 3D surfaces in the presence of varying FOD and BIA. It was demonstrated that the 3D surface processing leads to variations in their processing conditions, in particular changes of beam spot size that affect local fluence thresholds. The comparison of simulation and experimental results has shown that LIPSS main characteristics, i.e. their amplitudes and periodicity, can be predicted with acceptable accuracy. Also, changes in processing conditions caused by disturbances that affect LIPSS performance can be identified. The results of this research can be used to determine the BIA and FOD limits/tolerances within which the LIPSS functional response on freeform surfaces can be maintained within acceptable levels for any given application.

Keywords: LIPSS, freeform surface, laser processing, femtosecond laser, astigmatic Gaussian beam

5.1. Introduction

Laser structuring/texturing is known as advanced manufacturing process that can enhance surface properties without compromising excessively the throughput or costs. It draws the attention of researchers and industry because it offers selectivity, relatively high accuracy and flexibility, e.g. for 3D processing, when compared to alternative/conventional processes.

Laser Induced Periodic Surface Structures (LIPSS) are a particular type of submicron surface structures produced by ultrashort lasers that stand out among others due to their vast applicability and the fact that they can be generated on almost any engineering material. Firstly, they were found on semiconductors [39] but with the constant advances of ultrashort laser sources they had become a viable alternative for surface processing of metals [163]–[165], ceramics [166], metallic glasses [167], glasses [168] and polymers [97]. Because of LIPSS specific geometrical characteristics, all these materials benefit from added surface functionalities, such as improved wetting properties for self-cleaning or anti-icing applications [169], [170], anti-bacterial surfaces for food industry [171], cell proliferation in medical implants [172], friction reduction [173], enhanced antireflection [40], [174] or they act as diffraction grating exhibiting structural angle-dependent colours utilised in hologram fabrication or counterfeiting applications [144].

LIPSS appear on the material’s surface as ripple-like structures after irradiation with a polarised ultrashort laser beam and their characteristic are dependent on wavelength and processing parameters. In particular, laser fluence affects ripples depth while wavelength and incidence angle have an impact on periodicity and polarisation vector influences their orientation [175]. Typically on metals, it has been observed that LIPSS emerge on a surface when the fluence is close to the ablation threshold of a given material and a relatively small number of pulses is required [96]. The evolution of LIPSS on processed surfaces is as follows. Firstly, random nanostructures are created with features like nano holes, nano cavities or nano protrusions. A further increase of accumulated fluence, e.g. by increasing the number of pulses and/or their fluence, leads first to High Spatial Frequency LIPSS (HSFL) that then evolve gradually from Low Spatial Frequency LIPSS (LSFL) into grooves/bumps and spikes [64]. Currently, LSFL attracts more attention as they can be easily controlled, optimised and homogenously produced on large areas and thus offer capabilities for functionalising surfaces with required repeatability for a range of applications.

So far, the LIPSS research was mostly focused on their generation and optimisation on planar surfaces because of the requirement to assess/characterise their functional response and also due to equipment related constraints. However, when the identified processing domains are applied onto non-planar surfaces, additional factors start affecting the LIPSS formation and also their functionality. These factors are disturbances that alter the processing conditions. The two most prominent ones are Beam Incident Angle (BIA) and Focal Offset Distance (FOD). Their influence on LIPSS formation was studied and it was reported that BIA mostly affects the LIPSS periodicity while FOD influences the average peak to valley amplitudes of generated ripples [176]. The presence of these disturbances can change laser processing conditions dramatically and result in an interrupted LIPSS generation that consequently can affect the surface functional response. One way to counteract these undesirable effects when processing non-planar surfaces is to process them with a focused laser beam and always with normal incidence. However, such approach requires the use of multi-axis laser processing systems with simultaneous control of optical and mechanical axes in the beam delivery sub-system. Therefore, a more common approach is to maintain BIA and FOD within some pre-defined limits that can be determined experimentally and thus to maintain the LIPSS functional response within acceptable limits [177]. Then, such “tolerances” can be used to partition freeform surfaces, e.g. by employing so-called “freeform surface layering” [178] or by applying tessellation/triangulation algorithms [126], [179], and thus to design and implement optimised processing techniques and strategies.

It is worth mentioning that the procedure for verifying the BIA and FOD tolerances is always material specific for a given laser processing domain and can be time-consuming. Therefore, when LIPSS surface treatments are employed in industrial applications, there are available simplified models that can be used to determine the laser processing domains for a given material and thus to produce areas covered consistently and homogenously with LIPSS [112]. However, the results are valid only for planar surfaces without taking into consideration dynamic changes in processing conditions. Therefore, there is a need for analytical methods that can determine reliably processing tolerances for producing functionalised surfaces on non-planar surfaces.

In this research, a model is proposed for assessing the accumulated fluence when processing non-planar surfaces that accounts for the disturbances affecting the processing conditions. It considers actual spatial pulse intensity distributions in the presence of varying FOD and BIA. Ultimately, by simulating the processing conditions considering the effects from these disturbances and material optical properties, the LIPSS characteristics can be predicted, i.e. their amplitudes and periodicity. Thus, it is possible to judge indirectly about LIPSS functional response on complex surfaces where otherwise their properties are difficult to measure.

5.2. Theory

5.2.1. Ultrashort laser irradiation with an astigmatic Gaussian beam

The existing models for ultrashort laser irradiation of materials usually assume an ideal Gaussian beam intensity distribution, i.e. a circular profile with symmetrical divergence above and below the focal plane, even when non-planar and inclined surfaces are processed [99], [100], [125]. This assumption can be acceptable in conditions where the effects of any processing disturbances can be simplified or even neglected. However, this is not the case anymore when a given laser structuring/texturing application is more sensitive to FOD and BIA variations. In addition, when laser sources are integrated into systems with relatively long beam paths incorporating several components, the beam reaching the substrate might be astigmatic. This type of Gaussian beams has two principal directions in the transversal planes. Its waists positions do not coincide and thus the beam is not always circular throughout the propagation axis and has elliptical cross-sections [180]. There are many applications where the presence of processing disturbances cannot be ignored and the actual Gaussian beam should be considered in the models. In this way, significant discrepancies in simulation results can be avoided, i.e. due to varying local fluence and pulse overlaps.

It could be assumed that the Gaussian beam is a simple astigmatic one where the ellipses of constant intensity and phase are aligned and their orientation stays constant at every point along the beam path [106]. The two-dimensional local fluence intensity distribution of such beam on a processed surface can be described using the following equation (derived from [106]):

$$F(x,y,z) = F_0\ exp\left(\frac{-2}{\omega_x^2(z)}x^2 + \frac{-2}{\omega_y^2(z)}y^2\right) \tag{5.1}$$

where F_0 is the peak fluence expressed as (derived from [106]):

$$F_0(z) = \frac{2P}{f\pi\omega_x(z)\omega_y(z)} \tag{5.2}$$

where: P is average power and f - pulse repetition rate. Beam waists ω_x and ω_y of astigmatic beams depend on the position along the laser propagation axis, z, and they can be calculated as follows [106]:

$$\omega_i(z) = \omega_{0i}\sqrt{1 + \left(\lambda\frac{z - z_{0i}}{\pi\omega_{0i}^2}M_i^2\right)^2}\ , i = x, y \tag{5.3}$$

where: ω_{0i} is the smallest waist at z_{0i}; λ – the laser wavelength, and M_i^2 – the beam quality factor for each principal direction. Astigmatism is defined as the difference between the smallest waists' position, i.e. $z_{0x} - z_{0y}$. If that distance is equal to zero, the beam is not astigmatic.

Processing of an area bigger than a beam spot size requires laser beam movements in a two-dimensional domain that is realised by employing x and y beam deflectors. The area processed with multiple pulse trains with different overlaps in x and y is depicted in Figure 5.1. For a given scanning speed v and f, the distance between pulses along the x equals to $\Delta x = \frac{v}{f}$ while along y is $\Delta y = h$, where h is the hatch offset between two consecutive y trains. Hence, the number of pulses along x and y when processing an area L_xx L_y can be calculated as follows (derived from [181]):

$$N_x = \frac{L_x - 2\omega_x}{\Delta x}, N_y = \frac{L_y - 2\omega_y}{\Delta y} \tag{5.4}$$

It is worth stressing that these equations are valid if an assumption is made that the beam waist is constant and the laser beam is always focused on the surface. However, due to the beam astigmatism and resulting ellipticity, the smallest beam waists might not always be at the same focal position.

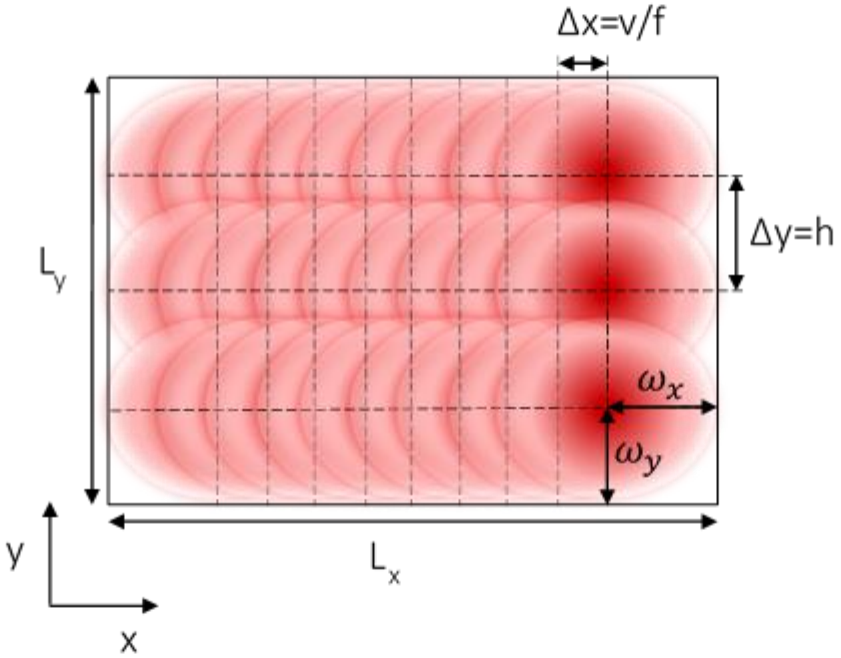

Figure 5.1. A schematic representation of an area L_x x L_y processed with elliptical beam spots with multiple pulse trains with pulse overlaps in x depended on the scanning speed (v) and frequency (f) while in y on hatch offset (h) between two consecutive pulse trains.

By combining Eq. 5.1 - 5.4, the accumulated fluence over a L_x x L_y area can be expressed by using the following equation (adapted from [181]):

$$F_{acc}(x,y,z) = N_r \frac{2P}{f\pi\omega_x(z)\omega_y(z)} \sum_i \sum_j exp\left(-2\left(\left(\frac{x-\Delta x\cdot i}{\omega_x(z)}\right)^2 + \left(\frac{y-\Delta y\cdot j}{\omega_y(z)}\right)^2\right)\right) \tag{5.5}$$

where: N_r is the number of passes over the area while i and j are integers in the ranges of $\left(\frac{-N_x}{2},\frac{N_x}{2}\right)$ and $\left(\frac{-N_y}{2},\frac{N_y}{2}\right)$, respectively, if the origin of the coordinate system is in the centre of the processed area.

5.2.2. The BIA effects on ultrashort laser irradiation model

As stated in Section 5.1, laser processing conditions vary when non-planar surfaces are processed, in particular due to BIA and FOD variations. BIA, α, is defined as the angle between the incident laser beam and the surface normal at a given point (x,y,z). For example, if an inclined planar surface is processed, BIA will be maintained the same throughout the area. In this case, to calculate the fluence intensity distribution of a single pulse, Eq. 5.1 - 5.3 should be revised. Figure 5.2 shows a schematic representation of a laser beam when processing an inclined surface. As can be seen, the beam ellipticity increases with the increase of BIA. The smaller ellipse in the figure depicts the spot size of the same beam but when it is focused on a surface normal to the beam. In this case, the BIA variations do not affect ω_x but ω_y varies and its value cannot be calculated anymore by using Eq. 5.3. In addition, the beam waist is now dependent on the local focal offset, Δz, and BIA, α, and this should be considered when calculating the local fluence (F_{loc} in Figure 5.2). As a result, $\omega_{y\alpha}$ increases with the distance from the pulse centre and thus Eq. 5.3 should be revised as follows:

$$\omega_{y\alpha}(y,z,\alpha) = \omega_{0y}\sqrt{1+\left(\lambda\frac{(z-\Delta z(y,\alpha)-z_{0y})}{\pi\omega_{0y}^2}M_y^2\right)^2} \tag{5.6}$$

where $\Delta z(y,\alpha) = \sin(\alpha)\cdot y$.

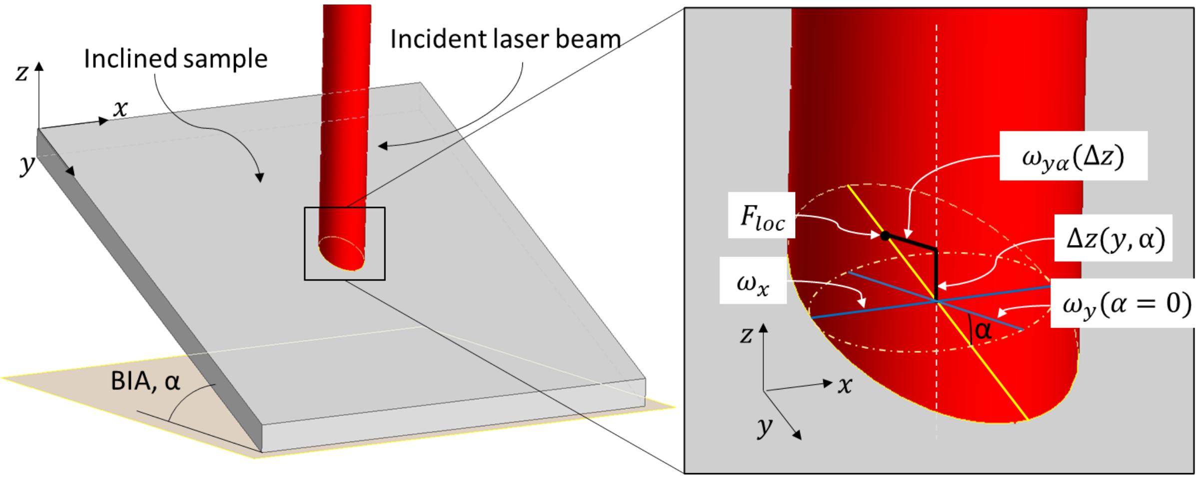

Figure 5.2. A schematic representation of an incident laser beam on an inclined surface. For comparison, the blue lines and smaller dash-dotted ellipse depicts the beam spot at the focal plane. The black lines represent beam waist $\omega_{y\alpha}$ and Δz necessary to calculate the local fluence F_{loc} at a given point. The bigger ellipse depicts the area where intensity is at $1/e^2$ of F_0 while the yellow line is the absolute beam diameter.

Considering Eq. 5.6, the fluence of a single pulse on an inclined surface can be calculated as follows:

$$F(x,y,z,\alpha) = \frac{2P\cos(\alpha)}{f\pi\omega_x(z)\omega_{y\alpha}(y,z,\alpha)}exp\left(-2\left(\left(\frac{x}{\omega_x(z)}\right)^2+\left(\frac{y\cos(\alpha)}{\omega_{y\alpha}(y,z,\alpha)}\right)^2\right)\right) \tag{5.7}$$

Examples of pulse intensity profiles are given in Figure 5.3a. The profiles were calculated based on Eq. 5.6 and 5.7 with $\omega_0 = 20\ \mu m$, $\lambda = 1.03\ \mu m$ and $M^2 = 1.2$ on planar and inclined surfaces, especially with BIA of 40, 60 and 80 degrees. The point at which the intensity drops to $1/e^2$ of also affected F_0 at given BIA determines ω_α on the processed surface. Figure 5.3b shows the relative changes of the same beam when varying BIA. It is apparent that the changes of the beam profile are less pronounced for BIA up to 40 deg while the difference increases up to around 30 % of ω_0. In addition, beams with different ω_0 will follow nearly the same trend for BIA changes. However, when processing a surface with a bigger BIA, ω_α increases more rapidly and for BIA = 80 deg the beam waists can be a few times bigger compared with that when it is normal to the surface. Therefore, when processing surfaces with a varying BIA, the irradiated area by each pulse increases together with the overlap between them.

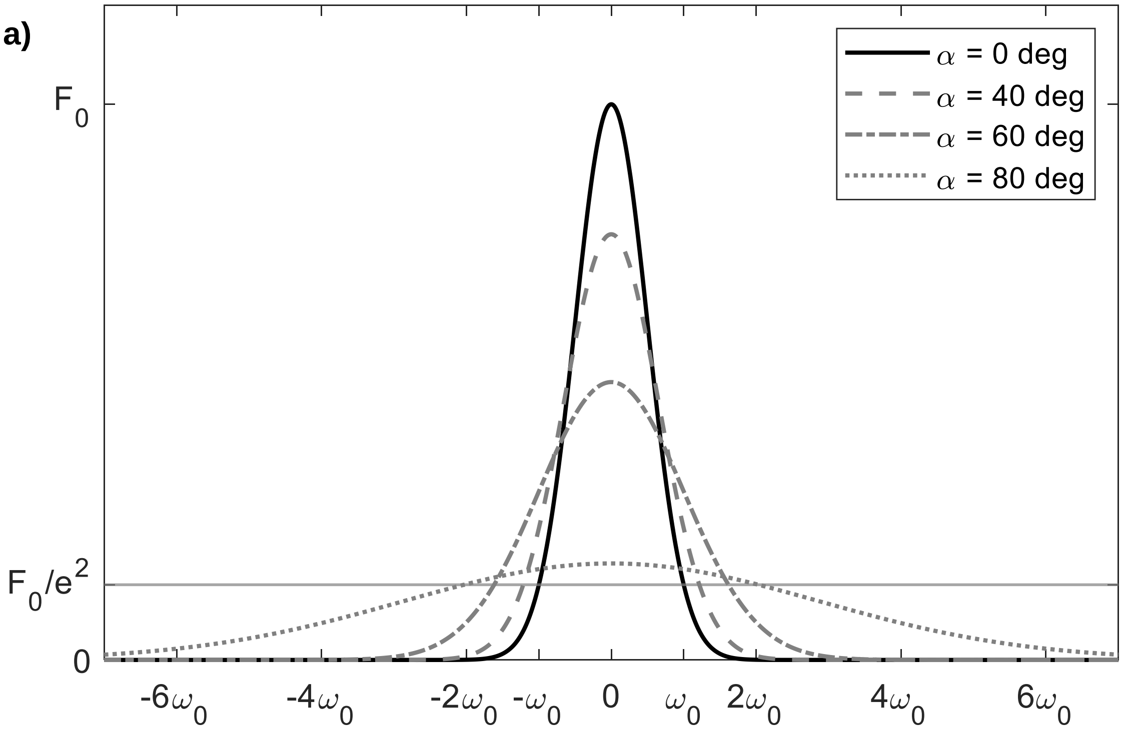

b)

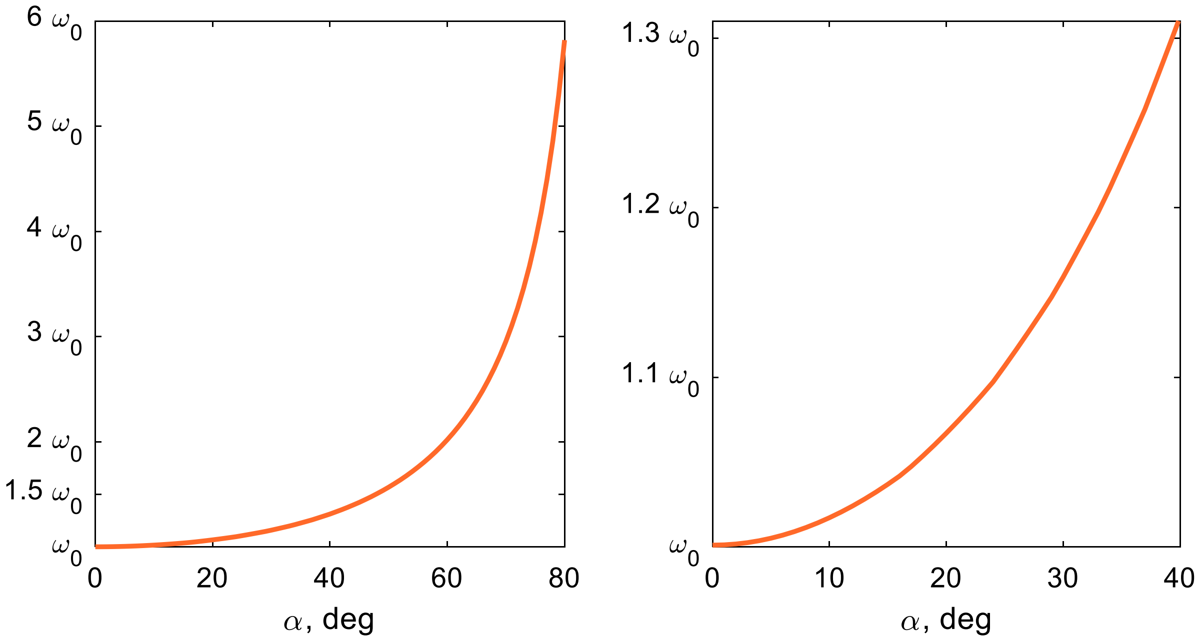

Figure 5.3. (a) The changes of pulse intensity profiles of a laser beam with ω_0 of 20 μm when varying BIA, calculated from Eq. 5.6 and 5.7 with $\omega_0 = 20\ \mu m$, $\lambda = 1.03\ \mu m$ and $M^2 = 1.2$ on planar and inclined surfaces (BIA = 0, 40, 60 and 80 deg). (b) The relative changes of same beam waist ($\omega_0 = 20\ \mu m$) when increasing BIA. The increased waist was measured at $1/e^2$ intensity from Eq. 5.6 and 5.7 as in examples shown in (a). BIA from 0 to 80 deg on the left; close up from 0 to 40 deg on the right. Curves plotted in MATLAB.

Depending on the substrate, fluence values might be altered with BIA because of the absorption changes. Absorptivity, A, of metals (stainless steel in this case) can be estimated based on the well-known Fresnel equations with the refractive index of materials $(n + ik)$ that is wavelength dependent [182]:

$$A_p = \frac{4n\ \cos\alpha}{(n^2+k^2)\cos^2\alpha + 2n\cos\alpha + 1}$$
$$A_s = \frac{4n\ \cos\alpha}{n^2+k^2+2n\cos\alpha+\cos^2\alpha} \qquad (5.8)$$

where: p and s denote linear p and s beam polarisations, respectively. If circular polarisation is used, absorption is an average of the two components $A_c = \frac{1}{2}(A_p + A_s)$. Taking all these into consideration, the absorbed accumulated fluence on an inclined surface of ultrashort laser simple astigmatic Gaussian beam can be calculated as follows:

$$F_{acc}(x,y,z,\alpha) = A\ N_r \sum_i \sum_j \frac{2P\cos(\alpha)}{f\pi\omega_x(z)\omega_{y\alpha}(y,z,\alpha)} exp\left(-2\left(\left(\frac{x-\Delta x\cdot i}{\omega_x(z)}\right)^2 + \left(\frac{(y-\Delta y'\cdot j)\cos(\alpha)}{\omega_{y\alpha}(y,z,\alpha)}\right)^2\right)\right) \qquad (4.9)$$

where: $\Delta y' = \Delta y/\cos(\alpha)$ is the distance between pulses on the surface if they are not compensated during laser scanning, in particular when the structuring strategy is based on projections [125]. Also, while calculating local distance Δz for each pulse, its displacement should be considered, thus $\Delta z(y) = \sin(\alpha)\cdot(y-\Delta y'\cdot j)$.

This model can be further generalised for processing of freeform surfaces. With the increase of surface complexity, its geometry plays a more important role in assessing the fluence distribution and accumulation. Surfaces can be clustered into developable and non-developable ones. In particular, the first are ruled surfaces, such as cylinders or cones, while the latter are compound curved surfaces, e.g. spheres, where the curvature is present in two or more directions [183]. When processing such surfaces, BIA varies in each direction and depends on the surface tangent at a given point (x,y,z) of the workpiece. Provided that the local radius of the curvature is significantly bigger than the beam waist (R>>ω), the fluence distribution of a single pulse on a freeform surface can be simplified to determine local BIA in both principal planes. Hence, BIA variations along x and y directions can be calculated as follows:

$$\alpha_k(k,z) = \frac{\pi}{2} - \tan^{-1}\left(\frac{z-z_c}{k-k_c}\right), \qquad k = x, y \tag{5.10}$$

where: x_c, y_c and z_c is the centre of the curvature, which radius is $R = \sqrt{(z-z_c)^2+(y-y_c)^2+(x-x_c)^2}$. Similar to Eq. 5.7, the fluence distribution of a single pulse on a spherical surface can be described as follows:

$$\begin{aligned} F(x,y,z,\alpha_x,\alpha_y) \\ = F_0(x,y,z,\alpha_x,\alpha_y)\, exp\left(-2\left(\left(\frac{x\cos(\alpha_x)}{\omega_{x\alpha}(x,z,\alpha_x)}\right)^2 + \left(\frac{y\cos(\alpha_y)}{\omega_{y\alpha}(y,z,\alpha_y)}\right)^2\right)\right) \end{aligned} \tag{5.11}$$

Regarding the accumulated fluence, analogous to inclined surface presented before, the contributions of all pulses delivered onto the processed area need to be considered. Hence, only an iterative model can be used that is adapted to the surface complex geometry and thus assess the influence of any processing disturbances, locally.

5.2.3. Fluence requirements in laser structuring/texturing

Models for ultrafast laser irradiation with Gaussian beams have already been used to simulate ablation [122] and laser structuring [111], [112]. One of their main assumptions is that ablation or structuring occurs when the processing fluence is above a certain threshold, F_{th}. Furthermore, different types of morphologies, i.e. laser induced structures, appear if processing is carried out within a predefined fluence range. Previous studies shows that, for multi-pulse structuring, with the increase of the pulse number, N_p, impinging a given spot the fluence thresholds can be reduced [184]. This phenomenon is called incubation and it is material dependent. Incubation is included ultrafast irradiation models and it is expressed in the equation for fluence threshold [181]:

$$F_{th}(N_p) = F_{th}(1)N_p^{S-1} \tag{5.12}$$

where: $S \in [0,1]$ is an incubation factor and $F_{th}(1)$ is the fluence threshold for a single pulse. The incubation model can also describe the relationship between the accumulated fluence threshold, $F_{acc\,th}$, and N_p as a requirement to achieve a certain morphology on the surface [181]:

$$F_{acc\,th}\left(N_p\right) = F_{th}\left(N_p\right)N_p = F_{th}(1)N_p^S \tag{5.13}$$

However, when beams are being scanned across a given surface area and pulses' overlap, assessing the number of pulses per spot have to be estimated and then used for threshold calculations. Thus, the effective number of pulses can be calculated as follows [111]:

$$N_{p\,eff} = \frac{\pi}{2}\,\frac{\omega_x\omega_y}{\Delta x\Delta y} \tag{5.14}$$

Please note that depending on the chosen scanning strategy and the complexity of workpiece geometry, the beam spot size is not constant anymore throughout the processed field, as has been shown in Section 5.2.2. This leads to increased impact of processing disturbances, i.e. BIA and FOD variations, and as a result, it will also influence the local fluence threshold variations that have to be accounted for when calculating F_{acc}.

5.3. Methodology

5.3.1. Experimental setup and materials

Experimental validation was performed using ultrafast Ytterbium-doped laser source with a pulse duration of 310 fs, maximum pulse energy of 10 μJ, a near-infrared wavelength (λ) of 1032 nm, and maximum average power of 5W. A linearly polarised laser beam was focused with a 100 mm telecentric lens which allows always normal incidence within the field of view. The laser processing of surfaces was realized by employing a 3D scan head. Additionally, a motorized rotational axis was employed to control BIA. The test workpiece on which LIPSS were created was 1.5 mm thick, mirror polished, 304 stainless steel plate. It was cleaned with acetone before the laser processing. The complex refractive index of this material for the employed laser source was (2.943 + 3.915i) [185] and this value was used in the calculations.

5.3.2. Beam characterisation

Beam waist measurements along the beam propagation axis were conducted using a scanning slit beam profiler. Each measurement was repeated three times with an increment of 100 μm along z. Results from beam waist measurements are provided in Figure 5.4. The values were fitted to Eq. 5.3 using least squares method assuming that z_{0i}, ω_{0i} and M_i^2 were variables and λ was constant. The peak fluence is the highest at the focal plane where the area the beam spot size is the smallest. The astigmatism of the used laser beam was 0.52 mm and the focal plane did not coincide with z_0 along x and y axis and were equal to -0.41 mm and 0.11 mm, respectively. The smallest waists, i.e. ω_{0x} and ω_{0y}, at these positions were 20.52 and 16.52 μm, respectively, while in the focal plane, ω_x and ω_y were equal to 22.33 μm and 16.82 μm, correspondingly. Beam propagation factor, M^2, that also characterizes the deviation of the ideal Gaussian beam in the fundamental mode was calculated to be 1.35 and 1.45 in x and y, respectively. That means that the beam's divergence half-angle differs in both directions and was 21.6 mrad and 28.8 mrad. It is worth mentioning that the beam spot size area, and thus peak fluence, along the propagation axis was not symmetrical and therefore this could lead to different processing conditions below and above the focal plane. Such initial characterization of the laser beam can be used in the model that also accounts for disturbances that occur during processing of free form surfaces, such as BIA and FOD variations.

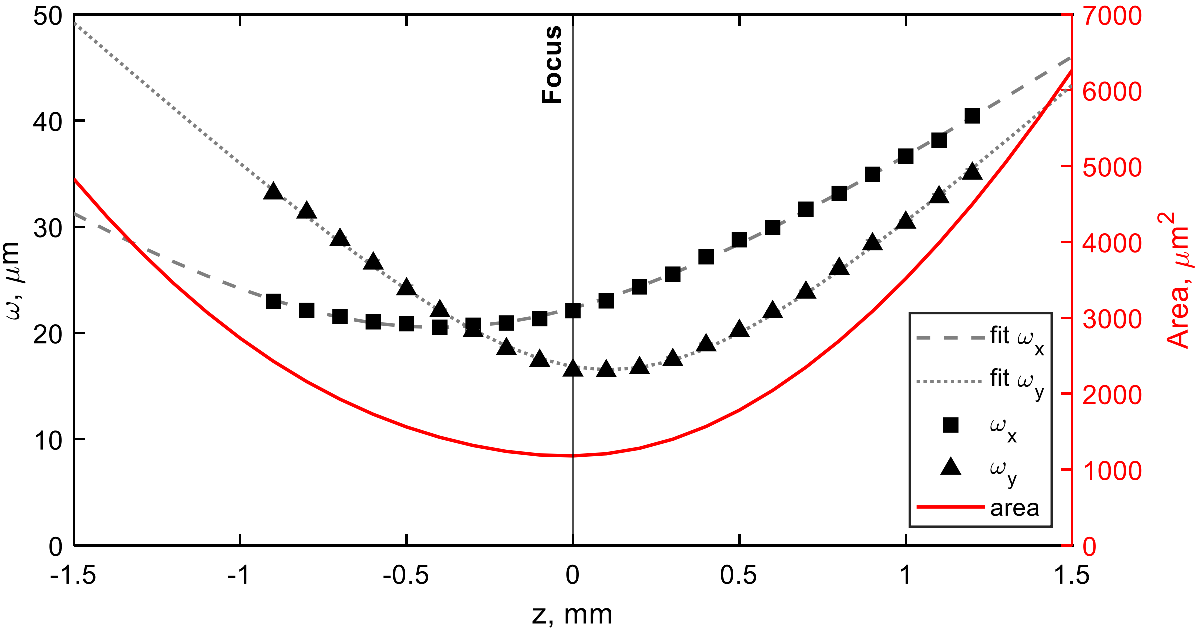

Figure 5.4. Beam waist measurements along the propagation axis, z, in two principal directions, i.e. x and y, and their fitted curves to Eq. 5.3. The red line represents the changes of beam spot area along z.

5.3.3. Experimental validation

A field of 4x4 mm was scanned with a linearly p-polarised laser beam in a way that both disturbances, i.e. BIA and FOD variations, were present and controlled as depicted in Figure 5.5. The laser beam was focused at one end of the square on the inclined sample and as the laser scanning progressed in y, FOD was increasing with each $\Delta y = 6\,\mu m$ displacement. As a result, actual Δy' on the sample was not compensated and differed for each BIA used in this experimental study, i.e. 10, 20, 30 and 40 deg. The repetition rate used was 500 kHz while the scanning speed was adjusted to 2000 mm/s and thus to maintain a pulse distance of $\Delta x = 4\,\mu m$. Initially, the LIPSS fluence threshold and the relation between fluence and LIPSS depth was determined when disturbances were not present, and this yielded constant $N_{p\,eff}$ of 24.6.

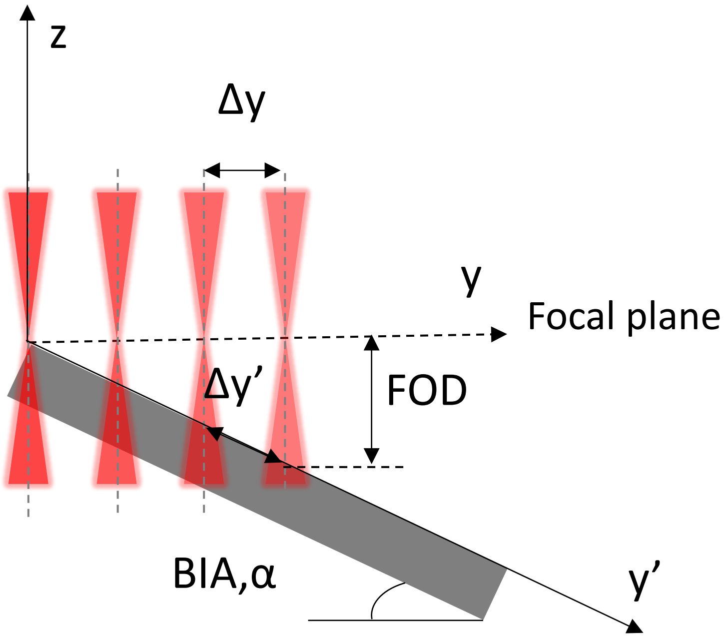

Figure 5.5. A schematic representation of the employed scanning strategy on test samples where both disturbances, i.e. BIA and FOD are present and controlled.

LIPSS were characterised with an Atomic Force Microscope (AFM). The samples produced without disturbances were measured three times in different locations while the validation samples were scanned along a straight line in y' every 250 μm, until LIPSS were still present. Ripples' geometric characteristics were obtained by using the open source software Gwyddion. From each 20 x 20 um (256 x 256 px) AFM scan, five lines, 2.3 μm (30 px) wide, were drawn perpendicular to LIPSS profiles. LIPSS amplitudes were expressed as standardised roughness parameter Rtm, that describes an average distance between the highest peak and lowest valley in every sampling length. Rtm was chosen because it was considered to give the best possible representation of LIPSS amplitude (average peak to valley distance) in a simple post processing operation. Additionally, for each scan 2D Power Spectral Density Function (2D PSDF) was performed based on 2D Fast Fourier Transformation (2D FFT) in order to evaluate characteristic spatial frequencies, occurring in LIPSS covered surface, from which periodicity was obtained.

LIPSS periodicities were calculated based on the theory of ripples generation with excitation of surface electromagnetic waves. In particular, this incorporates laser incidence on the surface, laser source wavelength (λ) as well as the polarisation type and complex dielectric constants of medium, ε_1, and the processed material, ε_2 [150]. Throughout the experiments the p-type polarisation was utilised, hence the theoretical LIPSS periodicity was determined as follows (derived from [186]):

$$\Lambda_{p\,\pm} = \frac{\lambda}{Re\sqrt{\dfrac{\varepsilon_1\varepsilon_2}{\varepsilon_1 + \varepsilon_2}} \pm \sin\alpha} \tag{5.15}$$

As the equation indicates, LIPSS produced with p-polarisation and with not normal incidence have two superimposed periodicities and are referred to + or – as for the sign used in the calculations. Dielectric constants employed in the calculations were ε_1 = (1+0i) and ε_2 = (-7.636 + 27.175i) for air and steel, respectively [187].

The theoretical model described in Section 5.2 was implemented in commercially available software MATLAB. The model was providing the calculation of accumulated fluence on the processing freeform surface. However, for the model input a laser beam dimensions were initially characterised and the fluence threshold needed to be determined as well. Therefore, before model validation an initial study was conducted to extract that information. Additionally, a correlation between LIPSS geometrical characteristics and the accumulated fluence was established. With this set inputs, the modelled values were directly compared to the measured experimental values of LIPSS amplitudes and hence the moment where ripples were no longer generated on the surface could be predicted.

5.4. Results and discussion

5.4.1. LIPSS characteristics vs. accumulated fluence

Initial experiments were conducted without the presence of any disturbances on the planar surface to study relations between LIPSS geometrical characteristics and the accumulated fluence. Only pulse energy was varied and thus, the accumulated fluence was affected by the changes in the peak fluence. As can be seen in Figure 5.6a, LIPSS amplitudes rapidly increase to 150 nm after the fluence threshold of approximately 0.11 J/cm^2, and then slowly continue to rise with the increase of the peak fluence. Above F_0 = 0.5 J/cm^2, LIPSS became noticeably irregular and were not considered homogenous anymore. Example of LIPSS produced with peak fluence 0.17 J/cm^2 and 0.5 J/cm^2 is presented in Figure 5.7.

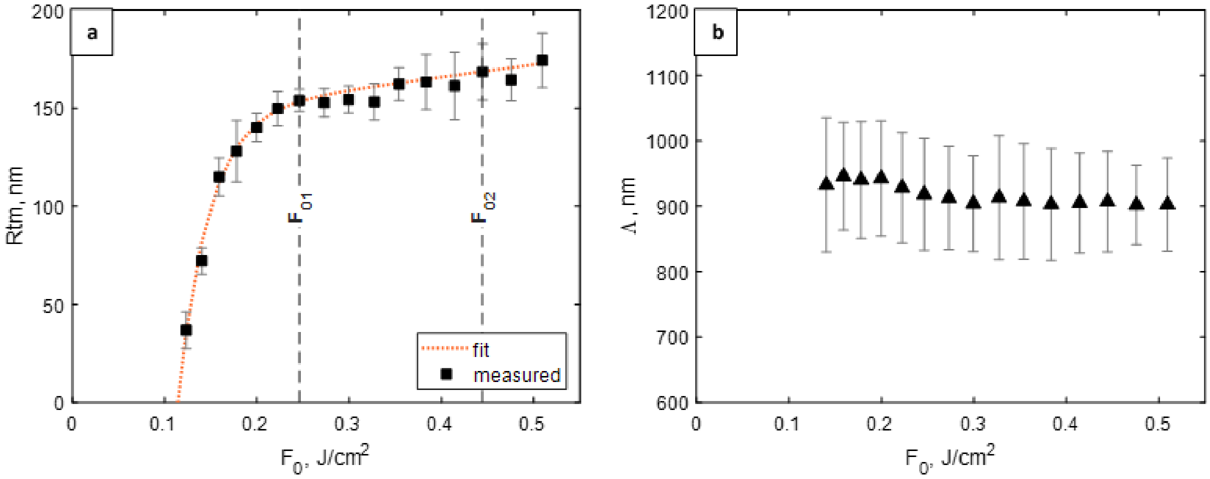

Figure 5.6. Dependence of LIPSS amplitudes **(a)** and periodicity **(b)** with F_0 increase. Two vertical lines in **(a)** indicate peak fluences used in validation samples fabrication.

With regard to the LIPSS periodicity, Λ, in Figure 5.6b, it was between 900 and 930 nm on average, which is proportional to the laser source wavelength, and it can be considered unaffected within the range of peak fluence studied in this research.

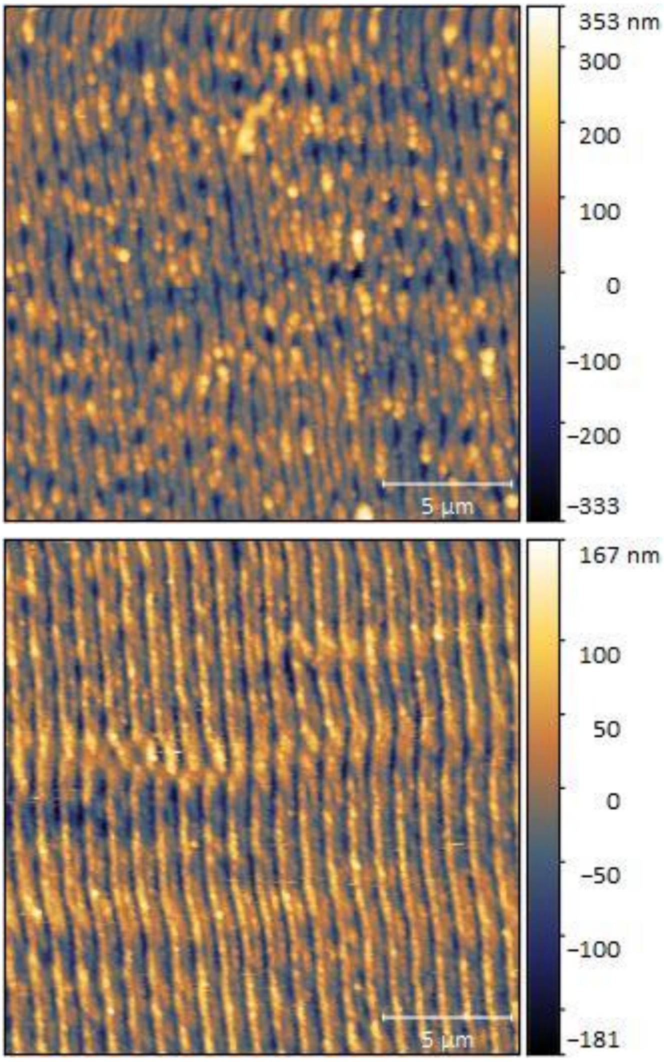

Figure 5.7 Examples of LIPSS topography, obtained by AFM, produced with peak fluence 0.5 J/cm^2 (top image) and 0.17 J/cm^2 (bottom image).

For the sake of simplicity, an empirical equation was fitted to the measured data in Figure 5.6a, that described the changes of LIPSS amplitudes with the increase of the peak fluence. Based on the same input data, the processing conditions were simulated and previously identified F_{th} was then used to assess F_{acc}. In the context of the freeform surface processing, this interdependence can be used to predict the processing settings that would lead to a significant decrease of F_{acc} and thus to the loss of LIPSS surface characteristics, i.e. a significant drop in the peak-to-valley distance. In particular, it is critical to identify the gradient between F_{th} and the fluence at which the surface structures can reach their optimum characteristics and ultimately functional response. By applying this approach, processing tolerances in regard to processing disturbances can be estimated and consequently the sizes of processed fields in freeform laser structuring/texturing can be optimized. To validate the model, two F_0 were used and they are highlighted in Figure 5.6a. In particular, F_{01} = 0.25 J/cm^2 was used for the optimised laser setting for producing LIPSS and F_{02} = 0.44 J/cm^2 where ripples are still homogenous and with a higher reserve of fluence in regard to F_{th}.

5.4.2. Model validation

As discussed in Section 5.2.3, the presence of disturbances leads to variations of the local beam waist and thus the local fluence threshold varies, too. Therefore, to assess F_{acc} only the local fluence from each pulse above the threshold was taken into account when simulating the process. Another reason for this was to avoid very small fluence values to affect final F_{acc} that do not have any physical effect on the laser structuring process. The incubation factor utilized in the process simulation was S = 0.86, with $F_{th}(1)$ = 0.179 J/cm^2, which is the typical value for 304 stainless steel if $N_{p\ eff}$ < 1000 is used [188].

Figure 5.8 shows the experimental results in regard to the resulting LIPSS amplitudes and their predicted values based on F_{acc} along y'. It can be stated that the ripples, especially at the upper end of the processed square field, where they were mostly influenced by the BIA deviation from normal and not as much by FOD, were typically deeper when compared to LIPSS produced with a beam normal to the surface. It should be noted that the LIPSS formation mechanism is more complex [189] and therefore some aspects were not taken into account in the relatively simple model presented in Section 5.2. However, in spite of this, it was possible to predict the location where the ripples are not anymore generated on the surface in all six cases depicted in Figure 5.8. In particular, this was done by calculating the LIPSS amplitudes that decreased with the drop of F_{acc} caused by processing disturbances. The area with LIPSS present on the processed fields decreased with the increase of the BIA while the FOD influence was more pronounced. The impact of the initial pulse energy was also visible. LIPSS of similar depth could be maintained onto a bigger area for F_{02} than F_{01}.

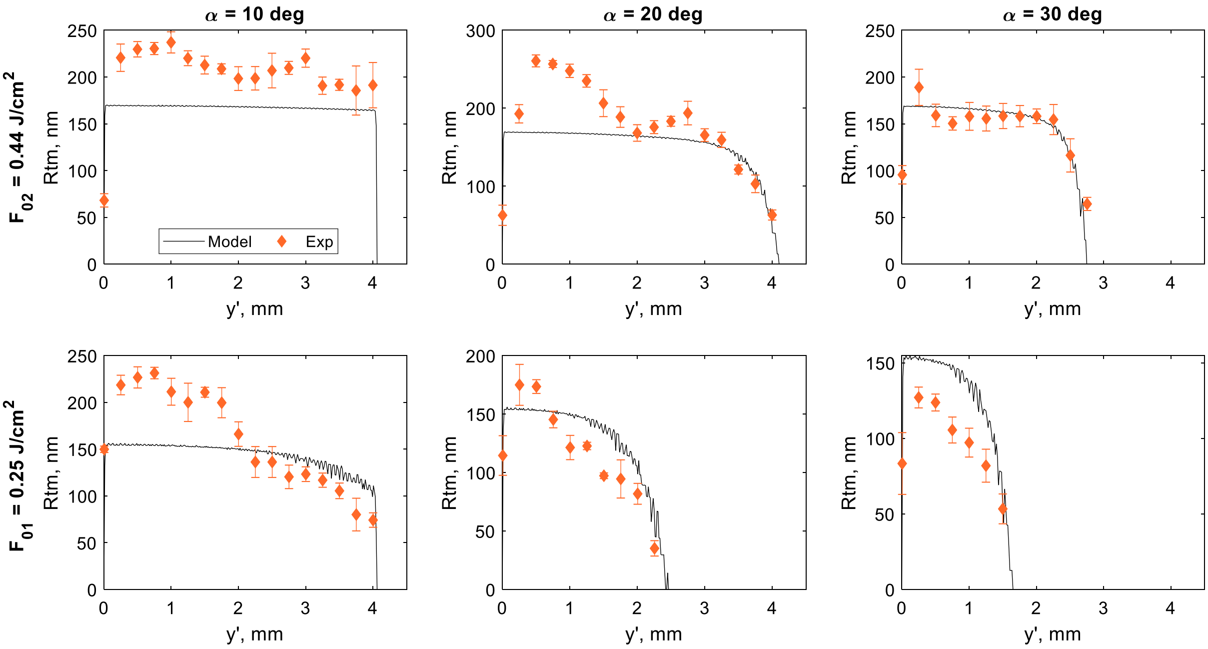

Figure 5.8. Experimental measurements of LIPSS amplitudes vs. their predicted values based on calculations of F_{acc} along y' for BIA of 10, 20 and 30 deg, and also for initial F_{01} of 0.25 J/cm^2 (bottom row) and F_{02} of 0.44 J/cm^2 (top row).

The percentage error between modelled LIPSS amplitudes along y' and experimentally measured ones was calculated for each of the initial peak fluence and BIA conditions and they are reported in Figure 5.9. The average error between all measured and modelled points was 20.2% and is also highlighted in the Figure 5.9. The prediction of location, that is the fit on the sample length (y') axis, where LIPSS where no longer generated was assessed to have the average error of 4%.

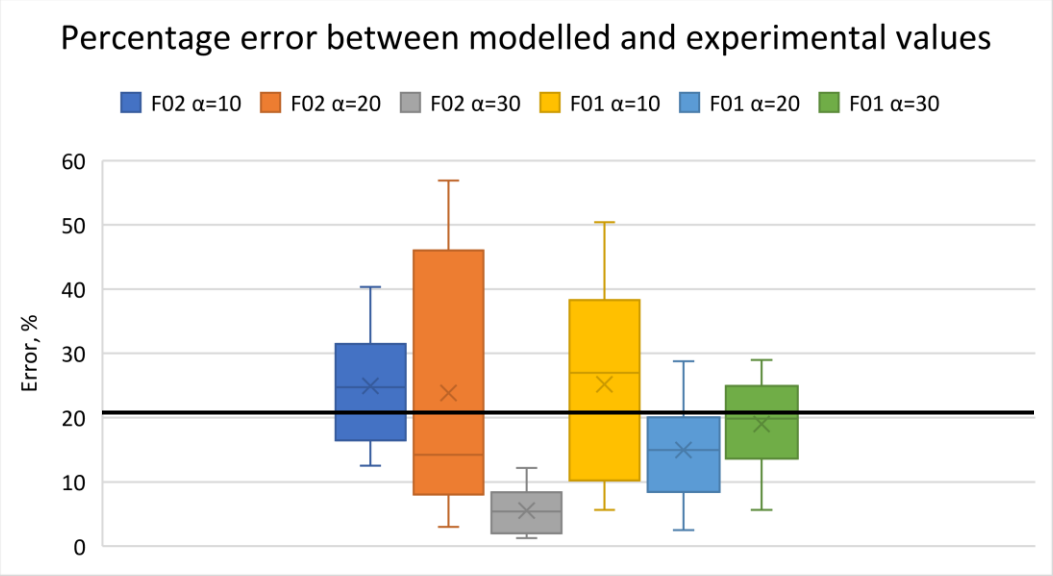

Figure 5.9 Box plot of percentage error between measured and modelled values from Figure 5.7 for BIA conditions of 10, 20 and 30 deg and with initial F_{01} and F_{02}. The horizontal black line shows the average percentage error of all the points.

Regarding the LIPSS periodicity, Figure 5.10 shows that mostly both Λ_{p-} and Λ_{p+} were present, as explained in Section 5.2.3. Despite the changes in processing conditions caused by the disturbances, i.e. increase of beam spot size and consequently the decrease of the peak fluence on the processed surface, no major Λ variations were observed. This could be attributed to the fact that the pulse energy was maintained constant. Moreover, the increase of BIA led to Λ_{p-} with lower values than the theoretical ones. This phenomena was already studied by researchers and it was explained with the increased influence of the surface roughness induced by the laser pulses that impacted the ripples periodicity [102]. In addition, Λ_{p+} was not always present on the processed fields, e.g. for F_{02} and BIA of 10 deg, smaller ripples emerged on the surface at y' = 2.5 mm, while at 20 deg, it was only at y' of 1.5 mm. Besides, at the upper end of the processed field where F_{acc} was higher, Λ_{p-} was always the more dominant periodicity than Λ_{p+} and with the decrease of F_{acc} along y' this tendency began to shift. The evolution of LIPSS Λ is depicted in Figure 5.11 that shows three AFM scans from the same field processed with F_{02} and at BIA of 20 deg. At y' of 0.75 mm, only a higher Λ_{p-} could be seen while at 1.5 mm a mix of both periodicities is detectable. The last image taken at y' = 3.5 mm shows only the presence of Λ_{p+}. This suggests that these periodicities are also sensitive to changes of F_{acc}. The 2D PSDF analysis of each AFM scans for this particular sample is presented in Figure 5.12 and now Λ magnitude in regard to F_{acc} can be analysed. Especially, there is a clear trend that with the increase of the distance from the top of the processed field, the significance of Λ_{p-} decreases. Furthermore, the processing conditions when Λ_{p-} becomes inferior to Λ_{p+} are reached when F_{acc} is approximately 6 J/cm^2 and below and they are the same for the rest of the tested samples produced with F_{02} while for F_{01} this value was above 2 J/cm^2. It can imply that different fluence thresholds need to be recognized for these LIPSS characteristics and further research should be conducted to confirm this.

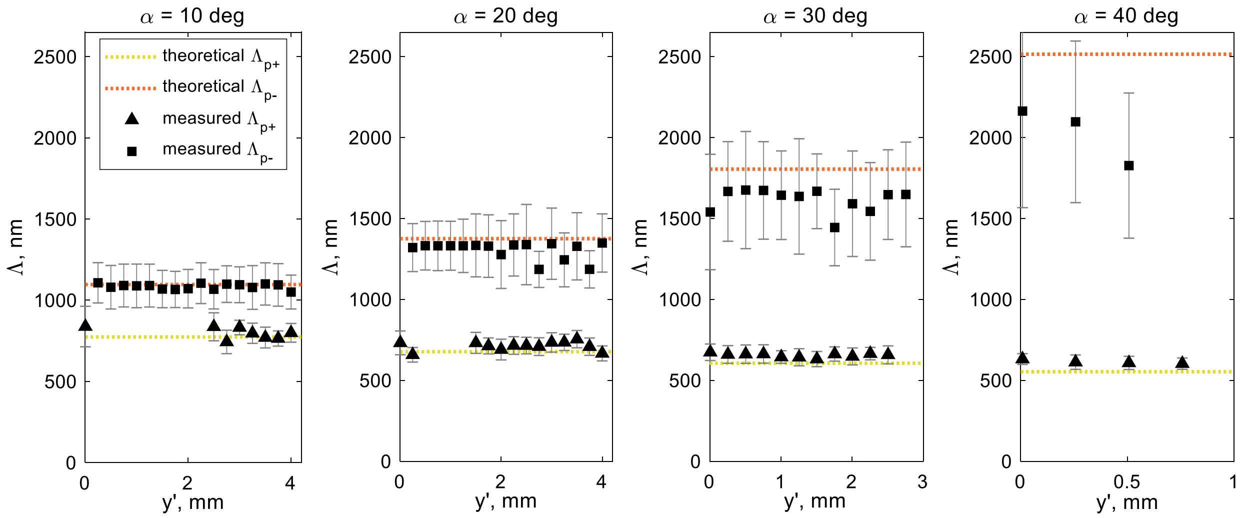

Figure 5.10. Measured LIPSS periodicities Λ_{p-} and Λ_{p+} and their theoretical values (from Eq. 5.15) for samples produced with F_{02} = 0.44 J/cm^2 and BIA of 10, 20, 30 and 40 deg.

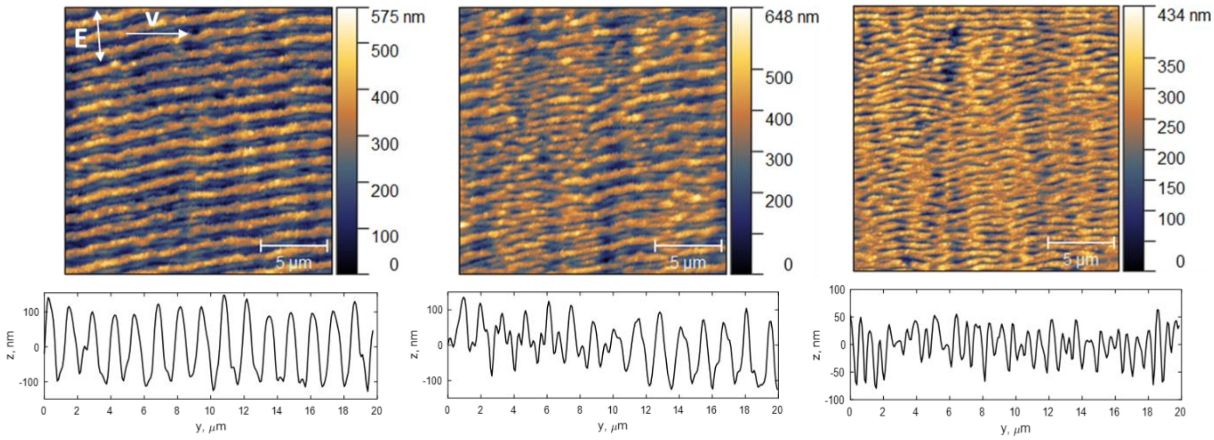

Figure 5.11. AFM scans of a sample produced with F_{02} = 0.44 J/cm^2 and BIA 20 deg along y' at 0.75 mm (left), 1.5 mm (middle) and 3.5 mm (right) with their respective profiles. White arrows indicate direction of polarisation vector (E) and scanning direction (v).

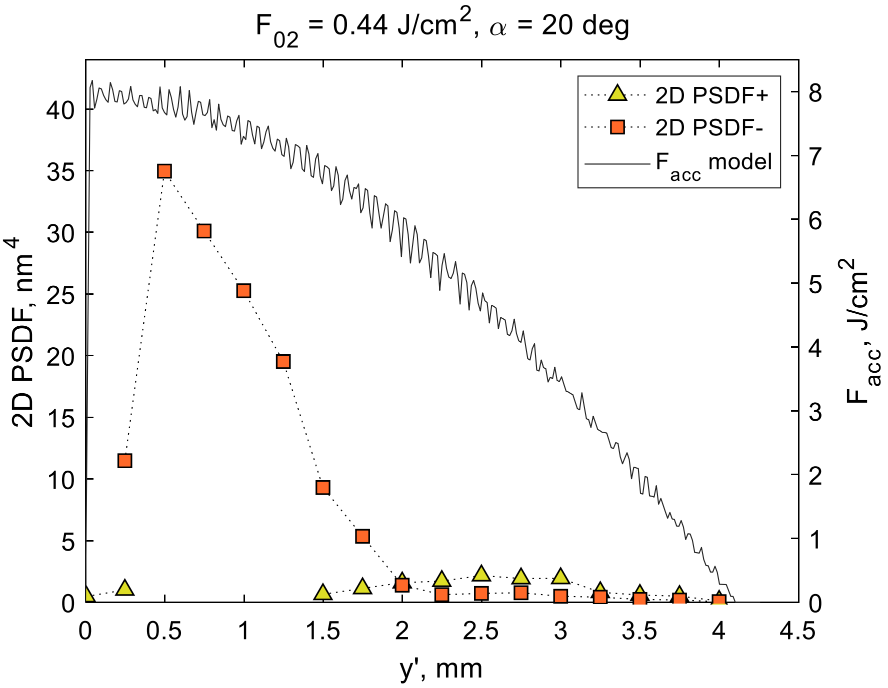

Figure 5.12. Measured PSDF values for sample produced with F_{02} = 0.44 J/cm^2 and BIA 20 deg along y' and calculated F_{acc} profile for this processing settings.

5.5. Conclusions

In this research, an ultrafast laser irradiation model for structuring free form surfaces was proposed. A simple astigmatic Gaussian beam was considered in assessing the accumulated fluence during structuring surfaces with varying BIA, i.e. inclined and curved ones. It was demonstrated that surfaces structured with processing disturbances, such as BIA and FOD, the pulse fluence distribution changes and results in modifications of laser processing conditions, in particular beam size variations that affect local fluence thresholds.

Validation samples were produced with varying BIA, i.e. on an inclined surface, where both disturbances were present and controlled. It was shown that the LIPSS characteristics, i.e. amplitudes and periodicity, can be predicted by modelling the accumulated fluence on a field processed with a characterised laser beam. Namely, the LIPSS disappearance or transformations due to the presence of BIA and FOD variations can be predicted. Furthermore, changes in LIPSS behaviour can be predicted, too, and thus to determine the processing constraints for a given laser parameters' domain without conducting the necessary empirical studies. Such information then can be used to drive the partitioning of freeform surfaces into laser processing fields and thus to achieve the required LIPSS homogeneity and consistency in their functional response.

For the first time, an ultrafast irradiation model was adapted to processing conditions when processing disturbances are present on the surface. The accumulated fluence was accurately assessed because the actual spatial beam intensity distribution and the effects of BIA and FOD were considered. It was also demonstrated that the effects from processing disturbances influences the beam spot sizes which leads to changes in local fluence thresholds. The initial analysis of LIPSS amplitudes with varied processing conditions, i.e. accumulated fluence, was used to validate results and to predict the changes in LIPSS behaviour. The model did not foresee precisely the LIPSS amplitudes along the sampling length. However, the moment when LIPSS started disappearing until no longer being present on the surface, because of reduction in accumulated fluence, could have been predicted with the proposed analytical model. A good agreement was also observed for LIPSS periodicities, where the transformation of dominant periodicity could also be linked to the calculated accumulated fluence. These findings are important for determining the processing constraints that are the basis for partitioning the freeform surface into laser processing fields. This way it is ensured that the functional responses are maintained on the laser structured freeform surface as long as the processing conditions are kept within the limits. The model was demonstrated on stainless steel, as an example, but it can be also applicable to metals with similar optical properties.

In the previous Chapter, an ultrafast irradiation model for freeform surfaces was proposed which addressed one of the open issue of broader LIPSS implementation for their many applications, as discussed in Chapter 2. After calculating the processing conditions required for maintaining the LIPSS functionality, another crucial aspect of laser structuring is to monitor the process. Especially, it is important to monitor the process and ensure that any shifts/deviations in LIPSS features can be detected as they can affect greatly the ripples functional response. During the design phase, the settings of the laser structuring strategy of the freeform surface can be chosen with narrower margins for the LIPSS treatments to be more flexible, although the process may not be the most efficient. Another challenge is that LIPSS sub-micron features are hardly resolved by the traditional optical metrology tools and other techniques proposed so far are not suitable to satisfy technical requirements for the process monitoring, i.e. fast and robust LIPSS data acquisition and analysis. The following studies will focus on proposing solution for LIPSS monitoring, when processing disturbances are present, based on their optical response and, ultimately, on using neural networks for the data post-processing aiming at direct prediction of their processing conditions and functional response.

CHAPTER 6: INLINE LIPSS MONITORING METHOD EMPLOYING LIGHT DIFFRACTION

This Chapter focuses on the third open question formulated in Chapter 2. A concept for inline monitoring of LIPSS is proposed; this is based on analysing the optical response from laser structured surface also when processing disturbances are present. The light diffraction angle and reflectance is measured to detect relative changes in LIPSS geometrical characteristics with respect to the given reference. The laser experiments related to this Chapter were provided in Tables 3.6-3.10, however only parameters from Table 3.7 and 3.10 are reported in this study. The sensitivity of the method is also analysed with its suitability for a process monitoring solution.

Aleksandra Michalek[1], Tahseen Jwad[1], Pavel Penchev[1], Tian Long See[2], Stefan Dimov[1]

[1]School of Mechanical Engineering, University of Birmingham, Edgbaston, Birmingham B15 2TT, UK

[2]The Manufacturing Technology Centre Ltd, Pilot Way, Ansty Park, Coventry, CV7 9JU, UK

This research was published as a full-length article in *Journal of Micro and Nano-Manufacturing (2020).*

Author’s contributions:

A. Michalek	Main author, conceptualization and methodology, performing all experiments and writing original draft
T. Jwad	Supported reflectance measurement and data analysis
P. Penchev	Supported with laser setup
T.L. See	Industrial supervisor
S. Dimov	Supervisor, Revision of the manuscript

Abstract

Laser induced ripples that are also known as Laser Induced Periodic Surface Structures (LIPSS) have gained a considerable attention by researchers and industry due to their surface functionalization applications. However, texturing large areas or batch manufacture of parts that incorporate LIPSS surfaces, require the development of tools for monitoring the LIPSS generation and potentially for controlling their main geometrical characteristics, i.e. spatial periodicity, orientation and amplitude. In this context, the focus of the research reported in this paper is on developing process monitoring and inspection methods for identifying shifts and changes in these characteristics. One of the well-known and widely used by industry method for characterising and inspecting surfaces is light scattering and this research investigates the capabilities of this method for inline monitoring of LIPSS optical response. A simple setup was designed and implemented for measuring the diffraction angle and intensity of the reflected light from LIPSS surfaces. The capabilities of this concept for determining relative shifts in the optical response on surfaces processed with known disturbances such as incident angle deviations and focus offset, were investigated. Sensitivity of the method proved to be sufficient to detect shifts/deviations from LIPSS reference and thus potentially to monitor their generation inline with a simple sensor, e.g. the LIPSS treatment of larger tool surfaces or serial manufacture of holograms.

Keywords: LIPSS, light diffraction, femtosecond laser.

6.1. Introduction

Laser-induced periodic surface structures (LIPSS) have attracted a significant interest from researchers and industry in the last decade due to their surface functionalisation capabilities. LIPSS are formed by irradiations with a polarised laser beam and appear as surface reliefs composed of periodic lines or ripples [190]. It has been widely reported that LIPSS surfaces exhibit super hydrophobic properties [191], improved tribological performance [173] and can be applied to control cell growth or bacteria adhesion [58]. Another prominent applications relate to the LIPSS periodicity that can act as a diffraction grating, in particular displaying structural colours that are dependent on the angles of incident light and observation. Such optical properties can be utilised in information storage, anti-counterfeiting or decoration applications [47]. The resulting optical properties of such textured surfaces could be controlled by controlling LIPSS geometrical characteristics, i.e. their spatial frequency, orientation and amplitude. The LIPSS periodicity is strongly dependent on wavelength of the laser source (λ), processing angle and fluence, while the laser beam polarisation determines the ripples' orientation. For most metals it is reported that LIPSS are orthogonal to the linear polarization vector [192]. Additionally, the ripples' height increases with the fluence increase and this affects surface reflectivity, i.e. leads to light trapping that is also called a 'blackening effect' [40], [174].

Femtosecond laser sources has been used for colouring metal surfaces not only by creating diffraction gratings but also by controlling surface's chemical compositions or morphology [165], [193]. The use of LIPSS as an angle-dependent colouring tool has been systematically studied, especially their dependence on laser wavelength (from 400 to 2200 nm) that affects the LIPSS spatial periodicity and in this way it is possible to exhibit desirable structural colours [194]. Furthermore, the LIPSS optical properties were utilised as a method for a selective display of colours, especially by encoding ripples with different orientations on metal surfaces [46], [195]. However, in spite of these promising technology advances there are still no qualitative method for controlling the angular-dependent, observable colours.

LIPSS monitoring approaches were already reported based on different methods, e.g. in-situ analysis of ripples' pulse-to-pulse variations by structured-illumination-microscopy (SIM) [124] or by recording LIPSS formation using small-angle X-ray scattering [128]. A common issue associated with these methods is that it is difficult or even impossible to implement them in any up-scaling LIPSS manufacturing solutions. Therefore, there is a need to develop process monitoring tools that could be implemented for fast in-line and cost-effective monitoring that could enable the development of tools for controlling the LIPSS formation process. One of the widely known method not only for characterising surfaces but also for detecting defects used by industry, e.g. in thin-film coatings, is light scattering [196], [197]. Especially, light scattering can be used as a non-destructive, non-tactile, accurate and robust real-time monitoring tool for inspecting surfaces [198]. In the case of laser induced ripples, it is possible to judge about their homogeneity, orientation and periodicity by analysing the diffracted light from them and thus to acquire indirectly information about their surface morphology [101], [199].

So far, most of the reported LIPSS research has been done on processing planar and not freeform surfaces. This is not surprising as it is much more difficult to maintain the LIPSS generation in control as other factors start affecting the process, i.e. the control 3D movements of the focused beam and also the beam incident angle. Additional possible disturbances occurring during 3D structuring could be the rotation of LIPSS orientation [200] or the insufficient 3D focusing for fast scanning speeds [31]. The factors affecting the LIPSS generation on tilted samples and their dependencies were already studied [104], [186] together with the effects of carrying out the processing with a defocused laser beam [201], [202], however not for the purpose of 3D structuring.

This research reports a concept for inline monitoring of LIPSS generation that can be realised by employing commercially available light scattering sensors. In particular, this work proposes a method for monitoring the LIPSS formation based on the diffracted light from textured surfaces that can be easily applied as in-line process monitoring tool. Its capabilities for determining relative shifts in the optical response on surfaces processed with known disturbances such as incident angle deviations and focus offset, were investigated. Then, the sensitivity of the method was analysed as a process monitoring solution for detecting shifts/deviations from reference LIPSS.

6.2. Methodology

The material used for all experiments was a mirror polished 304L stainless steel. The experimental investigation of the light diffraction response of LIPSS surfaces was conducted using ultrafast Ytterbium-doped laser source (Satsuma from Amplitude Systems), with a pulse duration of 310 fs, pulse maximum energy of 10 μJ, a near infrared (NIR) wavelength of 1030 nm and maximum average power of 5 W. The laser beam deliver system is depicted in Figure 6.1a. The spot size of Gaussian- linearly polarized beam was approximately 40 μm when a 100 mm telecentric lens was used and the laser processing of the surfaces was realized by employing a 3D scan head (the RhoThor system from Newson Engineering). Especially, the z-module of the scan head was deployed to process tilted samples and thus to keep the beam focused on the surface within a volume of ± 3 mm from the focal plane.

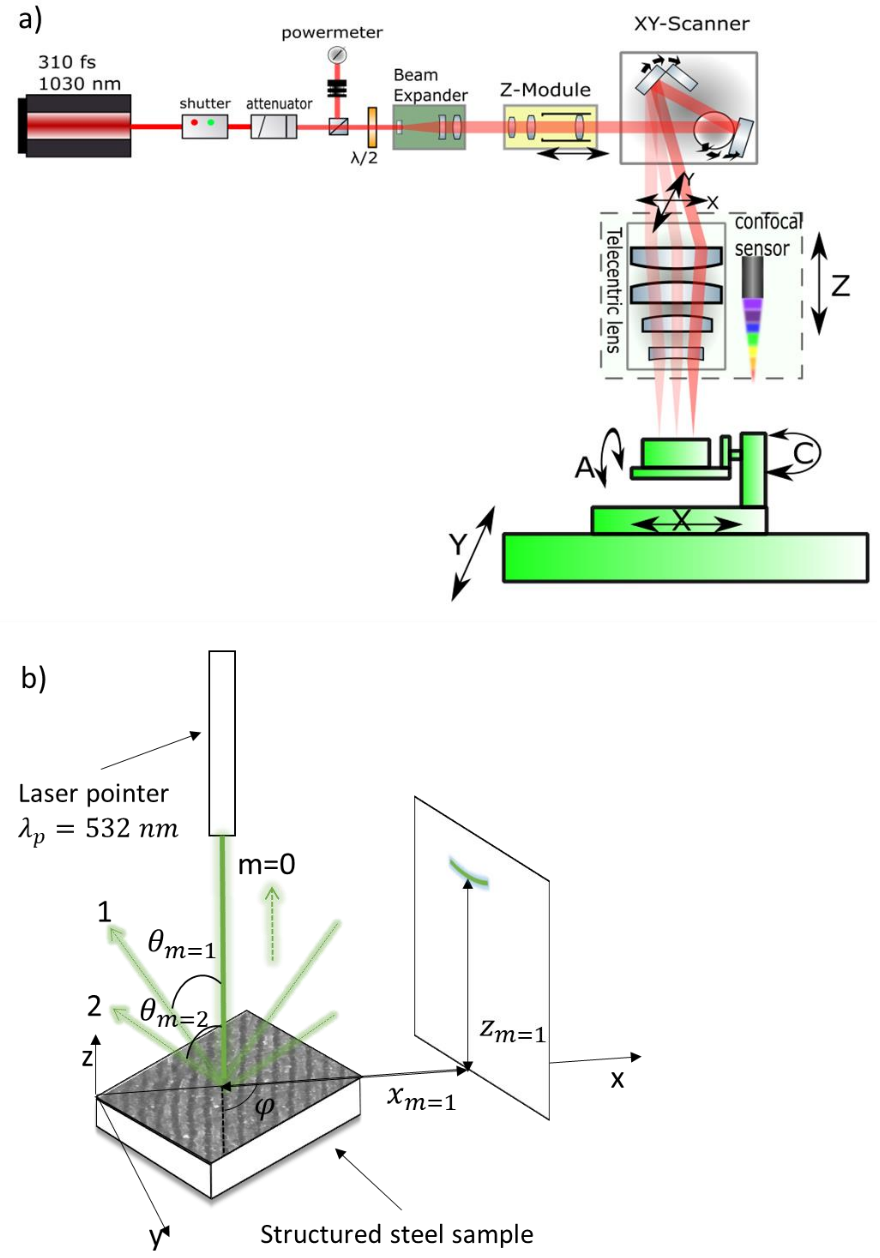

Figure 6.1 Experimental setups: a) the beam delivery sub-system of the laser processing setup; b) a schematic diagram of diffraction orders and their angles' measurements.

The experiments were conducted by using the highest possible processing settings in the available laser setup thus enabling fast LIPSS generation, keeping control over the fluence without affecting the surface integrity. In particular, scanning speed of 2 m/s and pulse frequency of 500 kHz were used to achieve 90% pulse overlap in the x scanning direction. The structures were produced on steel plates as 10 mm x 10 mm fields with 5 µm hatching distance what resulted in overlap of 75% in y direction (see Figure 6.1a). Taking into account the results from some preliminary trials and also results reported in literature for LIPSS processing of stainless steel samples [203] the pulse energy was set in the order to obtain fluence of 0.088 J/cm^2. With these laser settings textured samples were produced by varying the levels of the two processing disturbances considered in this research, i.e. the beam incident angle and focus offset. The variation of beam incident angles was achieved by tilting the A stage, as depicted in Figure 6.1a, from 0 to 25 degrees. It should be noted that in the experiments the polarisation vector was parallel (defined as p-type) or perpendicular (s-type) to the incident plane. Processing with a focus offset was realised by displacing the Z stage (Figure 6.1a) from focal point with a step of 100 µm until the light diffraction was still present.

The optical property of LIPSS was studied by employing the simple setup shown in Figure 6.1b. In particular, a monochromatic laser pointer with 1 mm diameter was shone on the surface and then the diffraction angle was measured at least three times for each sample. It was realised by analysing the diffraction patterns, projected on a flat, white screen and then by measuring the distance from the laser pointer to the screen ($x_{m=1}$) as well as the height of the first order diffracted pattern ($z_{m=1}$) with resolution of 1 mm, which are indicated in Figure 6.1b. Then, the LIPSS periodicity (Λ) was calculated by using the following equation [204]:

$$\Lambda = \frac{m \cdot \lambda_p}{(\sin\theta_m + \ \sin\theta_{in} \cdot \sin\varphi)} \tag{6.1}$$

where: m is the diffraction order; λ_p – the wavelength of the laser pointer, i.e. 532 nm in this research; $\theta_m = \tan^{-1}(\frac{x_{m=1}}{z_{m=1}})$ – the diffraction angle; θ_{in} – the incident angle of the pointer, i.e. 0 deg.; and φ – the orientation of the laser pointer in regards to the ripples, i.e. normal to the ripples as shown in Figure 6.1b.

By using the experimental setup in Figure 6.1b only the relative values of θ_m in regard to a set reference could be obtained. Therefore, the absolute value of Λ were determined by acquiring scanning electron microscope (SEM) images of the LIPSS surfaces and then by performing fast Fourier transformations (2D FFT) from three areas of the same sample. Also, Atomic Force Microscopy (AFM) measurements were performed to know the LIPSS amplitudes. One 20 μm x 20 μm area of per sample was inspected and the amplitudes were calculated as an average from four measurements. Then, in addition to diffraction angle measurements, the reflectance spectra from processed samples was acquired by using Ocean Optics USB2000+ Spectrometer with a tungsten-filament lighting and a Carl Zeiss Scope A1 optical microscope.

6.3. Results and discussion

6.3.1. Initial trials

An initial study was conducted to analyse the optical response of LIPSS samples produced by varying the fluence levels, in particular to study their first order light diffraction together with their zero-order reflectance. The relative differences were determined by using as a reference the sample produced with the LIPSS fluence threshold, i.e. the sample where the light diffraction became visible, as depicted in Figure 6.2a. The results showed that a fluence increase led to a periodicity decrease in line with what has been reported so far [48], [205]. However, not all researchers observed the same trend as some pointed out that the LIPSS periodicity could also increase with the increase of fluence [164].

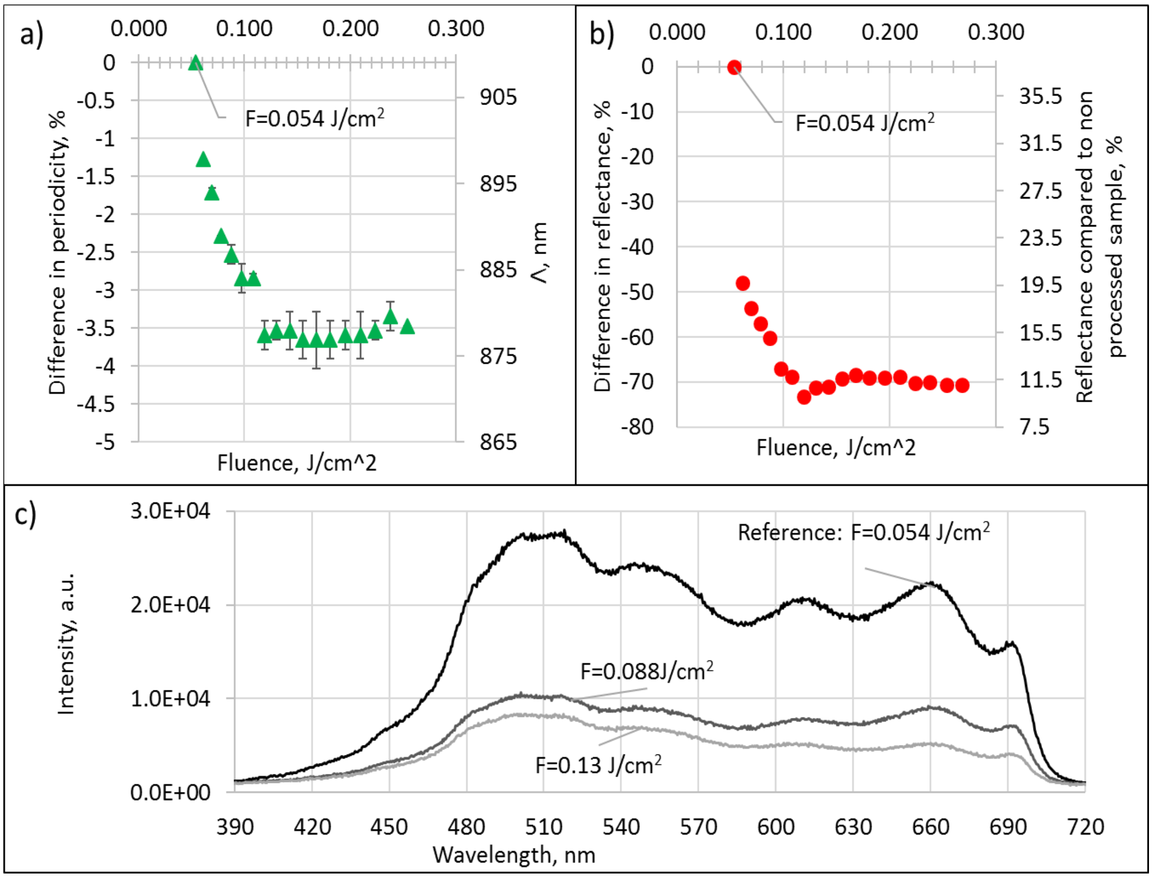

Figure 6.2. Relative changes in periodicity (a) and reflectance (b) with the increase of fluence with a reference to F=0.054 J/cm^2; (c) reflectance values for the wavelength range from 390 to 720 nm for fluence levels of 0.054 (reference), 0.088 and 0.13 J/cm^2.

Note: reflectance is expressed as the respective areas under the curves in (c), where F=0.054 J/cm^2 is the reference.

Furthermore, the fluence increase could lead to a significant decrease of zero order reflectance as shown in Figure 6.2b. This could be explained with the combined effects of ripples with a higher amplitude and surface oxidation that led to light entrapment [40]. The reflectance reduction could be up to 75%. It is important to note that the measurements were taken as intensity counts for the wavelength range from 390 to 720 nm. The resulted curves for fluence levels of 0.054 (reference), 0.088 and 0.13 J/cm^2 are depicted in Figure 6.2c. In particular, the reflectance in Figure 6.2b is represented as the respective areas under the curves defined for the considered wavelength range. It is apparent that both the periodicity and reflectance decrease initially with the fluence increase and then stabilise when fluence has reached approximately 0.12 J/cm^2. This indicates that above this fluence value there is only a negligible difference in the optical response of LIPSS samples. Therefore, the LIPSS samples produced with fluence equal to 0.088 J/cm^2 were considered as it was stated in Section 6.2. Especially, the samples produced with these laser processing settings were considered a good trade-off between fluence and reflectance, in particular the surface reflectance was sufficiently high. Then, these settings were used as a starting point to produce LIPSS samples without and with laser processing disturbances (see Section 6.2) in the follow up experiments while the same measurement approach was used to investigate their optical response.

6.3.2. The effects of beam focus offset on LIPSS light diffraction and reflectance

To judge whether the light diffraction could be used to monitor the LIPSS generation, first, the optical response of LIPSS samples produced with and without a focus offset was investigated where the fluence was set constant at 0.088 J/cm^2. In particular, the SEM image of the LIPSS sample processed in focus is shown in Figure 6.3a while the images of the LIPSS generated with the same laser settings but with offsets of 0.3 mm and 0.6 mm from focal plane are provided in Figure 6.3b and Figure 6.3c, respectively. As it can be seen in Figure 6.3, the increase of the focal offset led to less homogenous LIPSS and also to the appearance of some unstructured areas, especially as could be judged from Fourier transformation of the SEM images with the higher dispersion of spatial frequencies. Based on the SEM images, periodicity was measured and the results are provided in Figure 6.3d. In addition, AFM measurements were taken from the same structures as depicted in Figure 6.4a and they are also included in Figure 6.3d. However, at the same time the periodicity assessments based on the light diffraction measurements showed lower values. This could be attributed to the used indirect and simple measurement method that could be considered less accurate. Also, it should be noted that the reason for the slightly different periodicities obtained using SEM and AFM is that the measurements were not taken from the same areas. What is more important in this research is that the light diffraction measurements have shown the same trend as those obtained using both SEM images and AFM measurements. The periodicity increase with the increase of the focus offset can be explained with the increase of the laser beam spot that has led to a fluence decrease. For samples processed with a focal offset higher than 0.8 mm the light diffraction was no more visible and only the SEM images and the AFM measurements revealed areas with some LIPSS initiation.

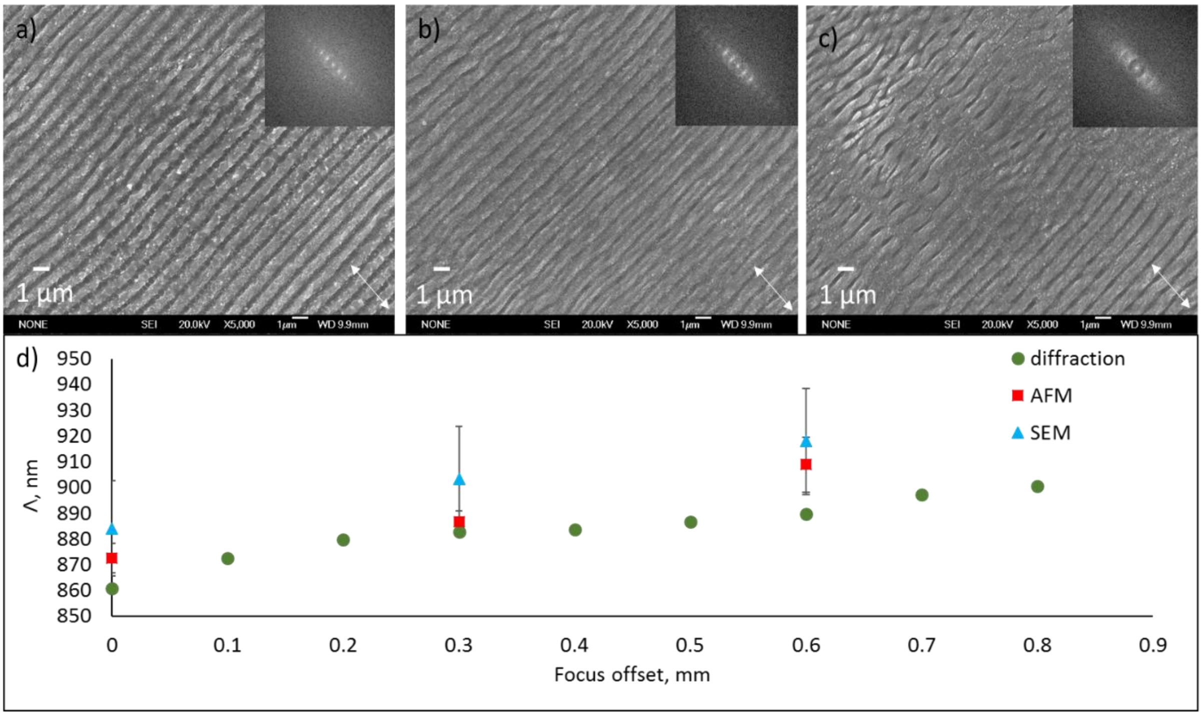

Figure 6.3 SEM images of LIPSS surfaces processed without and with a focus offset of 0.3 and 0.6 mm in (a), (b) and (c), respectively. Inlets are the Fourier transformation of these images while the white arrows indicate the polarisation direction. (d) provides periodicities' results obtained with the light diffraction measurements (green dots), SEM images (blue triangles) and AFM measurements (red squares).

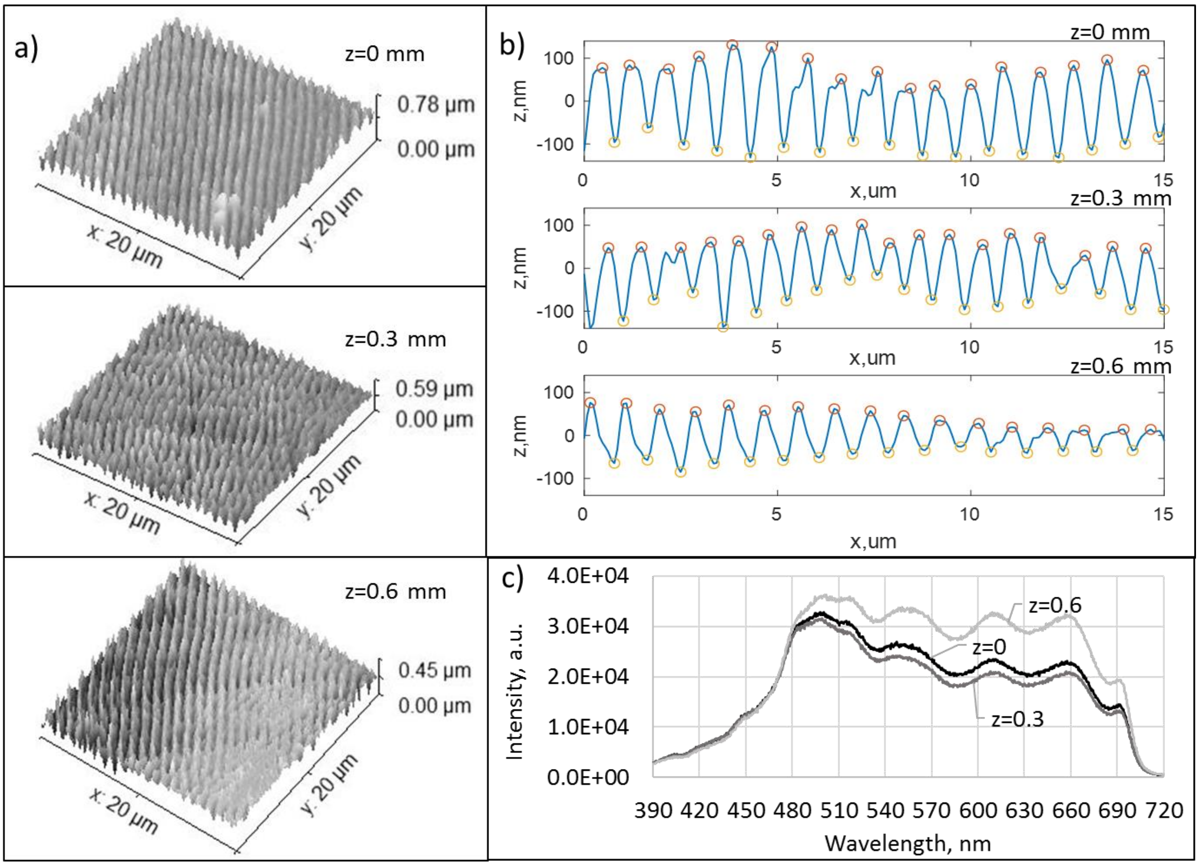

Figure 6.4 AFM measurements of samples produced within focus and with offset from focal plane (a) and their profile (b). Reflectance measurements of zero order of the same samples (c).

The LIPSS amplitudes were also measured, especially the average distance between peaks and valleys of the LIPSS profile, as shown in Figure 6.4b. When the laser processing was carried out in focus the average LIPSS amplitude was approximately 170 nm and then dropped to approximately 105 nm when a focus offset of 0.6 mm was introduced. The LIPSS amplitude decrease affected the zero order reflectance of the investigated LIPSS samples, too. In particular, the reflectance differences were insignificant up to a LIPSS amplitude of 0.3 mm and then there was an approximately

25% increase in the visible spectrum when an offset of 0.6 mm was used as shown in Figure 6.4c.

6.3.3. The effects of incident angle variations on LIPSS light diffraction and reflectance

The other laser processing disturbance and its effects on the LIPSS light diffraction and reflectance investigated in this research was the beam incident angle variations. It is widely accepted that the LIPSS formation is due to the interference of the incident laser wave with Surface Electromagnetic Waves (SEW) generated by the laser that results in periodic laser energy distribution and thus leads to periodic surface structures. According to the theory, the LIPSS periodicity can be calculated as follows [150]:

$$\Lambda = \frac{\lambda}{\sqrt{(\frac{k_0}{k})^2 - sin^2\alpha \, sin^2\beta} \pm cos\beta \, sin\alpha} \tag{6.2}$$

where: λ is the wavelength of the laser source; α - the processing incident angle; $k_0 = Re\sqrt{\varepsilon_1\varepsilon_2/(\varepsilon_1+\varepsilon_2)k}$ is known as propagation constant; $k = 2\pi/\lambda$; ε_i - complex dielectric functions of the photoexcited material and intact dielectric in which laser propagation occurs and as shown in the equation for k_0 their real part was taken into periodicity calculations; β is equal to 0 or $\pi/2$ in case of p and s linear polarisation of the laser beam, respectively. Thus, the periodicity equation could be simplified depending on the linear polarisation type as follows:

$$\Lambda_p = \frac{\lambda}{\sqrt{(\frac{k_0}{k})^2} \pm \, sin\alpha}, \qquad \Lambda_s = \frac{\lambda}{\sqrt{(\frac{k_0}{k})^2 - sin^2\alpha}} \tag{6.3}$$

According to Eq. 6.3, structures produced with p-polarised laser beam on non-planar surfaces can have two types of periods: Λ_{p-} and Λ_{p+} which coexist at the same time. This is attributed to the excitation of two types of SEW and their propagation throughout the surface at the angles $(\pi/2-\alpha)$ and $(\alpha-\pi/2)$ [150]. These two periods became noticeable on LIPSS samples produced with a beam incident angle deviation higher than 5 degrees and are also visible in the Fourier transformations of the SEM images as shown in Figure 6.5a-c. Taking into account the laser source wavelength, the ε_{steel} and ε_{air} values of the stainless steel samples utilised in the calculations were (-7.5032 + 27.002i) and (1+0i), respectively [151]. Thus, the theoretical interdependence between LIPSS periodicity and p- and s-polarisation can be calculated and is shown in Figure 5.5d. According to Eq. 6.3, the LIPSS theoretical periodicity, Λ_{theor} , should be approximately 1025 nm (the dash-dot curve in Figure 6.5d) when the incident beam is normal to the processed surface and thus should be very close to the laser source wavelength. However, the measured periodicity, Λ_{exp}, on produced LIPSS samples was approximately 870 nm (the dashed curve in Figure 6.5d) or approximately 0.85 of Λ_{theor}. This indicates that the LIPSS generation is affected by other factors such as changes of material optical constant during femtosecond laser processing and excitations of surface plasmons [104], [206] or the existence of additional nano- and microstructures on the surface [207]. For stainless steel it was reported that Λ_{exp} has varied in the range from 0.71 to 0.9 of Λ_{theor} [151].

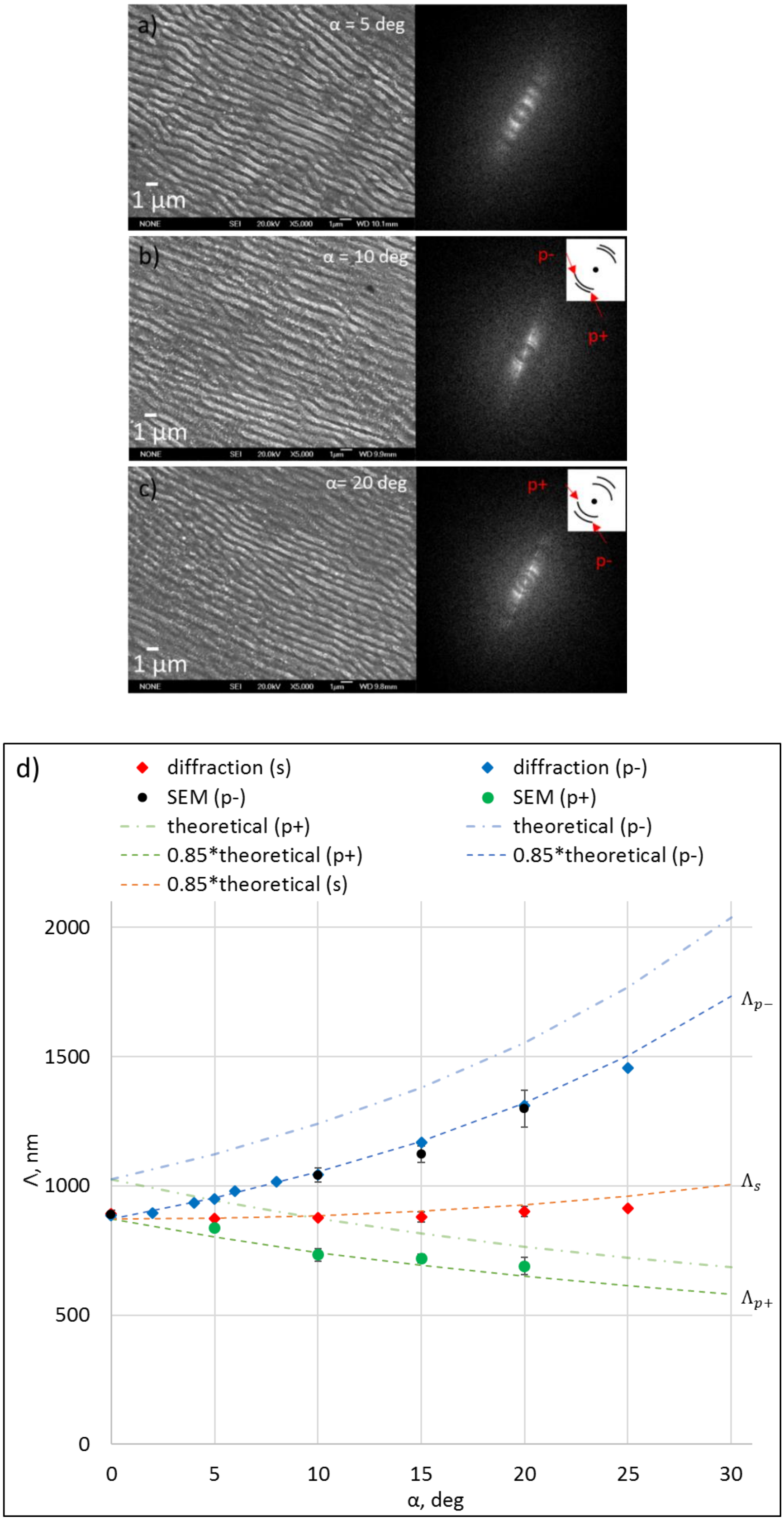

Figure 6.5 SEM images of samples processed with beam incident angle of 5 (a), 10 (b) and 20 degrees (c) with corresponding Fourier transformations; the periodicities

measured with light diffraction (diamonds), SEM (dots) and theoretical (dash and dash-dot lines) for beam incident angles up to 25 degrees and p+, p- and s linear polarisations (d).

As it was the case with the off focus processing it was possible to detect the effects of beam incident angle on the LIPSS formation while using a reference structures produced without any processing disturbances. In particular, the same light diffraction measurement setup was utilised to assess the optical response of LIPSS samples produced without and with beam incident angle deviations. As it was the case with the investigation of LIPSS generation when a focus offset was present (see Section 6.3.2) the periodicity assessment based on diffraction measurements were normalised to SEM results. The 2D FFT of SEM images showed two different periodicities when p-polarisation was applied while the light diffraction results detected only the “higher” Λ_{p-} periodicity. The “smaller” Λ_{p+} periodicity had much lower diffraction efficiency and as a result, the intensity variations of the diffracted light became undetectable.

Analysing the results in Figure 6.5d, it can be stated that the measurements from both, the light diffraction and SEM images, are in good agreement with theory and thus light diffraction could be deployed as a stand-alone method to detect and predict changes in the LIPSS generation. Regarding the reflectance changes as a result of beam incident angle variations, they were too small and could be considered negligible. In this case, it could be stated that the reflectance does not play an important role in tracking LIPSS changes while processing with varying beam incident angles. In addition, it should be noted that the differences in the NIR laser absorption of beam incident angles up to 25 degrees for p- and s-polarisations should be approximately only 6%, according to Fresnel equations [208], and were not compensated during processing.

6.3.4. Sensitivity analysis

The sensitivity of light diffraction as a mean to detect processing disturbances during LIPSS generation was analysed. In particular, the sensitivity of diffraction angle measurements was defined as the smallest absolute value of change, that was approximately 0.2 degrees considering the resolution of $x_{m=1}$ and $z_{m=1}$ measurements, what corresponds to 4 nm based on Eq. 6.1, which could be detected with the optical setup used in this research. Thus, it can be stated that by employing the proposed monitoring method LIPSS changes that are higher than the sensitivity value are possible to detect and then based on this data can be decided whether the LIPSS formation is in control. It is worth stressing that the proposed monitoring method, developed in the laboratory environment, could work only when LIPSS are covering all the surface with high regularity because of the limitations in method’s capability (high uncertainty due to data scatter). Hence, it was possible to identify disturbances affecting the laser processing only until the LIPSS morphology was not significantly affected.

When LIPSS have to be generated on freeform surfaces, a common approach is to divide the workpiece geometry into patches that reflects the capabilities of the laser system to perform processing within a volume [178] and thus to narrow down the 3D structuring to setting up tolerances for the maximum allowed incident angle deviation and focus offset. Therefore, it is very important to know to what extent the surface optical response will be reliable for detecting LIPSS changes and more importantly to judge indirectly if the surface desirable functional response is still present. For instance, if LIPSS are used for holograms production it is critical to assure that a given colour is visible with a fixed viewing angle. By utilising diffraction and reflectance measurements it is possible to detect changes in the LIPSS formation in regard to a reference structure produced without any processing disturbances. Specifically, when LIPSS generation were performed on planar surfaces with an increasing focus offset the periodicity changes detectable with the light diffraction were on average 0.5% per 100 µm offset within the depth of focus of the used beam delivery system, hence relatively minor, and then the property loss increased and became almost abrupt. At the same time when reflectance was considered, the detectable changes were even more pronounced, especially 4% per 100 µm offset. When the LIPSS generation was performed on tilted surfaces, the minimum detectable changes for p- and s-polarisations were 2% and 0.25% per one degree of beam incident angle deviation, respectively. Hence, the LIPSS formation with s-polarisation could be more practical due to the slower periodicity rise with the increase of the incident angle deviation and it allows to texture surfaces with a higher accuracy and flexibility.

6.3.5. Implementations for inline monitoring

The proposed light scattering method for monitoring the LIPSS generation is a simple and also fast approach for detecting changes in the structures above the respective sensitivity value. The experimental optical setup employed in this research is not automated and thus could be used only in a laboratory environment. However, there are existing light-scatter sensors that are compact and allow fast data acquisition with a measurement time less than 1s [209]; therefore such sensors can be easily deployed for inline measurements. In addition, they could overcome the limitations of the experimental setup used in this research, i.e. inability to analyse low reflectance structures, by employing laser pointers with higher power and/or different wavelength to improve the sensitivity of the proposed method and thus to broaden its application area. Such sensors can capture angle-resolved scattered light around the specular reflection and based on the acquired data to get intensity of captured light and calculate power spectral density and thus to determine dominant spatial frequencies of LIPSS. After some initial calibration with a reference LIPSS sample, such sensors can be placed at a safe distance from the workpiece within the laser processing system to capture diffraction data while avoiding capturing reflections from the laser source and/or being affected by any ablation debris. The proposed method should provide a cost-effective solution for monitoring the LIPSS generation without the need of constant SEM/AFM validations.

6.4. Conclusions

A simple and also fast light scattering based method for monitoring the LIPSS generation is proposed in this research. The method allows relative changes, in regard to a given LIPSS reference, to be detected. In particular, by employing this proposed method it is possible to track changes in the LIPSS optical response by performing diffraction angle and reflectance measurements. The method was developed and then validated by utilising planar LIPSS samples produced with known processing disturbances, i.e. beam incident angle variations and focus offsets, while LIPSS generated without disturbances were used as a reference. It was shown that LIPSS resulting from out-of-focus processing, can be determined by performing diffraction and reflectance measurements that are calibrated by using SEM images. Regarding the effects of laser processing with beam incident angle variations, it is possible by capturing the light diffraction to detect changes in LIPSS periodicity in regard to the reference LIPSS. The results showed that the sensitivity of the proposed method is sufficient to detect relative shifts/deviations and thus to monitor inline their generation by developing practical LIPSS inspection solutions. Such LIPSS generation monitoring tools are necessary for the broader use of LIPSS for surface functionalisation in a range of industrial applications.

The concept for an inline monitoring method based on the LIPSS optical response was developed. Relative changes in light diffraction and reflectance were tracked which indicated changes in LIPSS periodicities or amplitudes due to the presence of processing disturbances. The results obtained from this method were also compared to traditional surface topography characterisation methods. This simple approach proved to be sensitive enough to be suitable for inline monitoring/inspection of LIPSS treated surfaces that could be used with commercially-available, compact and light sensors.

The method focused on detecting any shift/deviations from LIPSS geometric characteristics which can be indication of changes in surface functional response. However, it does not directly indicate the effects on the specific functionality, e.g. wettability, display of structural colours, tribological or others mentioned in Section 2.4.1. In order to quantitively assess how the changes in LIPSS characteristics influence each individual functionality, an extensive experimental campaign with specific setups and instruments would be required. Establishing correlations between the LIPSS surface information and their functional response could also require knowledge of other physical phenomena related to the application. Therefore, a tool enabling prediction of LIPSS functionality based on standardized topography data is needed, also to avoid the extensive experimental campaigns. A very promising method to create such tool can be the use of neural networks that are known to address such problems. Therefore, the next and last study will focus on using artificial intelligence tools for pre and post-processing surface topography data in order to identify the processing conditions and also demonstrate the interdependences with LIPSS functional responses.

CHAPTER 7: ARTIFICIAL NEURAL NETWORKS TOOLS FOR PREDICTING THE FUNCTIONAL RESPONSE OF ULTRAFAST LASER TEXTURED/STRUCTURED SURFACES

In the next Chapter, the last research question from Chapter 2 is addressed. Artificial Neural Network tools are used for pre and post-processing the areal surface roughness parameters obtained from LIPSS treated surfaces. The objective is to classify the processing conditions that the surfaces were produced with and to demonstrate that a relation with LIPSS functional response can be determined, with wettability as an example. The LIPSS used in this study were produced both, with and without the presence of the processing disturbances, and correspond to the laser parameters reported in Table 3.11 and 3.12. The outcome of this study proves that after the data collection from inspection tools the indication of whether the LIPSS generation process is in control, can be determined.

Luca Baronti[1], Aleksandra Michalek[2], Marco Castellani[2], Pavel Penchev[2], Tian Long See[3] , Stefan Dimov[2]

[1]School of Computer Science, University of Birmingham, Edgbaston, Birmingham, B15 2TT, UK

[2]School of Mechanical Engineering, University of Birmingham, Edgbaston, Birmingham, B15 2TT, UK

[3]The Manufacturing Technology Centre Ltd, Pilot Way, Ansty Park, Coventry, CV7 9JU, UK

This research is published as a full-length article in *International Journal of Advanced Manufacturing Technology (2021)*.

Author’s contributions:

L. Baronti	Co-author, conceptualization, neural networks, use of GAN algorithms
A. Michalek	Co-author, conceptualization, application, experimental methodology, laser experiments, surface characterization, data acquisition, results analysis, writing original draft
M. Castellani	Neural networks, use of Feature Selection and ANNE algorithms, results analysis, contributing to writing original draft
P. Penchev	Supported data acquisition and laser setup
TL. See	Industrial supervisor
S. Dimov	Supervisor, conceptualization, revision of the manuscript

Abstract

Artificial Neural Networks (ANNs) are well-established knowledge acquisition systems with proven capacity for learning and generalisation. Therefore, ANNs are widely applied to solve engineering problems and are often used in laser-based manufacturing applications. There are different pattern recognition and control problems where ANNs can be effectively applied and one of them is laser structuring/texturing for surface functionalization, e.g. in generating Laser Induced Periodic Surface Structures (LIPSS). They are a particular type of sub-micron structures that are very sensitive to changes in laser processing conditions due to processing disturbances like varying Focal Offset Distance (FOD) and/or Beam Incident Angle (BIA) during the laser processing of 3D surfaces. As a result, the functional response of LIPSS treated surfaces might be affected, too, and typically needs to be analysed with time-consuming experimental tests. Also, there is a lack of sufficient process monitoring and quality control tools available for LIPSS treated surfaces that could identify processing patterns and interdependences. These tools are needed to determine whether the LIPSS generation process is in control and consequently whether the surface's functional performance is still retained. In this research, an ANN-based approach is proposed for predicting the functional response of ultrafast laser structured/textured surfaces. It was demonstrated that the processing disturbances affecting the LIPSS treatments can be classified and then the surface response, namely wettability, of processed surfaces can be predicted with a very high accuracy using the developed ANN tools for pre- and post-processing of LIPSS topography data, i.e. their areal surface roughness parameters. A Generative Adversarial Network (GAN) was applied as a pre-processing tool to significantly reduce the number of required experimental data. The number of areal surface roughness parameters needed to fully characterise the functional response of a surface was minimised using a combination of feature selection methods. Based on statistical analysis and evolutionary optimisation, these methods narrowed down the initial set of 21 elements to a group of 10 and 6 elements, according to redundancy and relevance criteria respectively. The validation of ANN tools, using the salient surface parameters, yielded accuracy close to 85% when applied for identification of processing disturbances, while the wettability was predicted within an r.m.s. error of 11 degrees, equivalent to the static water contact angle (CA) measurement uncertainty.

Keywords: multilayer perceptron; artificial neural network; general adversarial network; feature selection; laser induced periodic surface structures; laser surface texturing; surface functionalization.

7.1. Introduction

Artificial Neural Networks (ANNs) are popular and well-established learning systems that employ the principles of biological nervous systems. They are typically composed of several layers of simple nonlinear processing units called neurons. The first layer buffers the input data, after which the signal is processed by a variable number of interconnected hidden layers. Lastly, an output layer provides the ANN’s response [210]. Given ANNs’ ability to approximate any given function, they are a proven tool with applications onto a wide range of industrial problems such as functional prediction or system modelling. Thanks to their learning and generalisation capabilities, ANNs are particularly useful in cases where physical processes are unknown or too complex to be described analytically [135]. ANN development and applications are not limited to specific areas: they can be successfully employed not only in engineering and manufacturing but also in finance, medicine and many other fields [211].

In recent years, ANN developments applicable to laser-based manufacturing processes gained considerable research interest as a novel alternative to physics based analytical and numerical methods. Most commonly, machine learning algorithms were employed to predict the dimensions of laser ablated profiles [212]–[214], along with forecasting surface quality and material removal rates based on the input of the key laser processing parameters [215], [216]. ANNs were also used to identify the optimum laser pulse energy needed to obtain the desired craters’ depth and diameter for different materials [217]. Furthermore, ANNs were effectively applied to monitor and control laser processes, and to identify defects by non-destructive detection methods. This was achieved by building a system that identifies defects based on the extracted significant measurement data by employing only image processing [137]. Other methods focused on the analysis of acoustic emissions from the laser-induced plasma [136] or through in-situ speckle pattern observations [218]. In all of the various tasks, where the input/output dataset pairs differed significantly, trained neural networks were able to achieve very high prediction accuracy.

The key to obtain good results when applying ANN tools into manufacturing processes is to select an appropriate ANN topology and learning method, and suitable data preparation techniques [135]. In addition, a high amount of experimental data is required to train ANNs for optimal performance. Ideally, they should obtain all the relevant information to successfully carry out the desired task. However, building a system from sufficiently big data sets is time-consuming, problematic and in most cases not viable. A common solution to this issue is to augment the available training data, and such approach was already successfully applied in simulating complex systems based only on small experimental datasets [138], [219]. One of the novel augmentation techniques is Generative Adversarial Networks (GANs). They are composed of two Convolutional Neural Networks (CNN) and were originally designed to generate artificial images that are indistinguishable from the real ones [220]. GANs were already utilised as a predictive visualisation method in laser machining. Laser ablated topographies were recreated based on spatial laser intensity profiles [221] or by transforming the key laser parameters into predicted 3D surface profiles [139].

Another area where ANNs can be effectively applied is laser structuring/texturing for surface functionalization. A particular type of sub-micron structures, generated by ultrafast lasers, are Laser Induced Periodic Surface Structures (LIPSS). Low Spatial Frequency LIPSS (LSFL) are especially attractive to researchers due to their vast applicability and the wide range of achievable surface functionalities, e.g. modifying wettability, enhancing cell proliferation or structural colouring, to name a few [2]. The functional response of LIPSS surfaces is mostly dictated by their topological characteristics, i.e. periodicity, amplitudes and regularity of ripples. LIPSS are all sensitive to changes in laser processing conditions. In particular, in cases where processing disturbances affect the laser structuring process, e.g. when LIPSS are generated on 3D and freeform surfaces. The most common disturbances are variations of the Beam Incident Angle (BIA) and Focal Offset Distance (FOD). The relationship between disturbances and their influence on LIPSS topographies has been studied, and it was shown that BIA affects their periodicity while FOD mostly influences ripples amplitudes [176], [222]. Thus, any variations of processing conditions due to structuring disturbances during the LIPSS generation affect the surface functionality, too. Typically, the surface responses are analysed experimentally to confirm whether the functional performance is still within acceptable limits [177], [223]. However, obtaining functional performance data from the laser treated surfaces is often time-consuming, limited to specific processing settings, and requires special instruments and measurement setups. Another issue related to LIPSS generation in the presence of processing disturbances, is the lack of adequate process monitoring and quality control tools to maintain the process in control. ANNs can offer promising solutions for condition monitoring during the laser structuring process, and consequently indirectly to judge whether the surface’s functional performance is still within some predefined limits.

In this research, ANN tools were developed for pre- and post-processing of LIPSS topography data, i.e. their areal surface roughness parameters, for two main tasks. The first is the identification of whether any processing disturbances are present during the laser structuring process. The second is the mapping of the LIPSS topographies to their functional responses, here wettability. For both tasks, a small representative experimental dataset augmented with GAN-generated LIPSS topographies was used to develop and train ANN classifiers, while the validation was performed on a larger unseen dataset. The pre-processing step involved the application of feature selection methods to minimise the number of data attributes based on their relevance and redundancy. The next section outlines the experimental methods used to create representative data sets of LIPSS topographies. These data sets are required to develop and validate the proposed ANN tools. Then, the pre-processing methods (GAN and feature selection), and the ANN structure optimisation tools are described, together with the ANN tools developed for the two tasks. Subsequently, the experimental results of the implementation of the proposed methods are presented and discussed. Finally, conclusions are made about the effectiveness of the investigated feature extraction methods and ANN tools, and their applicability to the two classification and prediction tasks associated with the use of LIPSS treatments.

7.2. Experimental methods

Laser structuring was performed using an ultrafast Ytterbium-doped laser source with a near-infrared wavelength (λ) of 1032 nm, pulse duration of 310 fs, maximum average power and pulse energy of 5W and 10 μJ, respectively. A linearly polarised Gaussian laser beam was focused with a 100 mm telecentric lens on workpieces to deliver a beam spot size of 40 μm. The laser processing of surfaces was realised by employing a 3D scan head. A motorised rotational stage was employed and a dynamic focusing module with a working range of ± 3mm from the focal plane was used to control the laser focusing for the samples produced with varied BIA. The LIPSS treatments were performed on 1.5 mm thick, mirror polished, 304 stainless steel plates.

Optimised laser settings and strategy for generating regular and uniform LIPSS obtained from initial trials were used, in particular: peak fluence of 0.28 J/cm^2, pulse repetition rate of 10 kHz, 40 mm/s scanning speed and 6 µm hatching distance between the pulse trains that yielded the pulse distance of 4 µm and 6 µm in x and y direction, respectively. The relatively low scanning speed was chosen due to the limitations of the dynamic focusing module. The schematic representation of the described laser processing strategy is presented in Figure 7.1a. The laser processing settings were set constant, while structuring disturbances were present and controlled as shown in Figure 7.1b. Square fields of 8x8 cm were produced with varying disturbances, i.e. from 0 to + 900 µm with an increment of 100 µm for FOD, and separately from 0 to 35 deg with an increment of 2.5 deg for BIA. Each field with different set of disturbances was produced three times. Additionally, 15 supplementary LIPSS topographies were produced with the same scanning strategy, without disturbances but with varied peak fluence in the range from near-threshold 0.16 J/cm^2 to 0.54 J/cm^2.

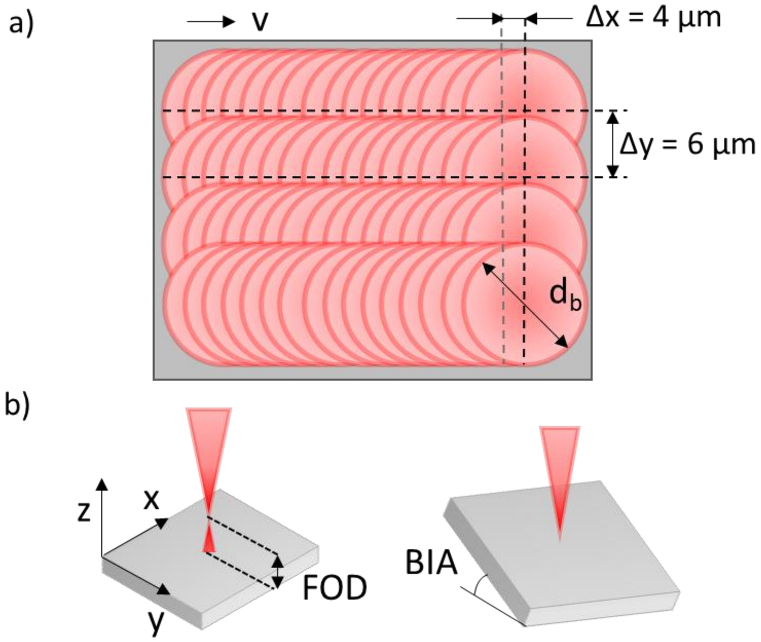

Disturbance	FOD	BIA
Range, increment	0 – +900 µm, every +100 µm	0 – 35 deg, every 2.5 deg

Figure 7.1 Schematic representation of processing strategy for LIPSS generation with (a) optimised processing settings and (b) when processing disturbances, i.e. FOD and BIA, are present during the laser structuring.

The topographies of the LIPSS-treated surfaces were analysed by using an Atomic Force Microscopy (AFM). In total, 87 scans of 20 µm x 20 µm (256 px x 256 px) fields were analysed, and all necessary topography data was acquired. Then, each surface sample was used to extract 16 reference images (100 px x 100 px) by using an overlapping sliding window every 50 px. Pre-processed images were fed into the Alicona MeasureSuite software to calculate 21 standardised areal surface roughness parameters according to ISO 25178. The roughness parameters are the most commonly used to characterise surfaces, i.e. sets of height, spatial, hybrid and functional parameters and they are listed in Table 7.1.

Table 7.1 The list of areal surface roughness parameters calculated based on LIPSS surface topography data according to ISO 25178 standard and considered as input data for ANN training.

Types of Parameters	**Height**	**Spatial**	**Hybrid**	**Functional**
Symbol	Sq, Ssk, Sku, Sp, Sv, Sz, S10z, Sa	Sal, Str	Sdq, Sdr	Smr1, Smr2, Sk, Spk, Svk, Vvv, Vvc, Vmp, Vmc

The static contact angle (CA) on each laser processed surface was measured 4 times employing the sessile drop arrangement for optical measurement of CA by using a drop shape analysis. Droplets of de-ionised water were deposited with 1 µl/s speed to form a droplet of 4µl and then they were carefully placed on the laser processed field. Prior to CA measurement, each test sample was carefully cleaned in an ultrasonic bath, first in acetone and then in 99.8% ethanol solution for 3 min. Next, the analysed surfaces were rinsed with deionised water and dried with compressed air after each bath. The reason for such rigorous sample preparation procedure was the necessity to minimise the effects of varying surface chemistry, and the presence of organic residuals after laser irradiation, which affect the resulting wettability of LIPSS treated surfaces [224]. All CA tests were repeated more than 6 months after the laser processing while the samples were stored in ambient conditions. The CA of as-received steel substrates was 73.3 ± 10 degrees.

The produced samples were split into a small experimental subset, i.e. Set A, and a much larger validation set - Set B. Set A consisted of 18 surface samples, where 5 were produced with varying FOD and another 7 with varying BIA. The remaining 6 samples were chosen from the supplementary set produced with optimised laser settings but varying laser fluence. From each sample 16 topography images were extracted, for a total of 288 created topographies. Set B comprised the remaining 69 surfaces from the conducted 87 AFM scans. Again, from each scan of the validation set, 16 topography images were created, for a total of 1104 LIPSS topographies.

7.3. Artificial Neural Networks tools

7.3.1. General Adversarial Networks for Data Augmentation

In this research, GAN, as a novel data augmentation technique, was used to generate additional realistic artificial LIPSS topographies based on Set A. The extracted LIPSS topographies were treated as height maps/depth images. The respective AFM data were converted into 16-bit grayscale height maps that contain the coordinates of each point on the surface in a three dimensional Cartesian system, i.e. the known Z resolution (nm per grayscale value) and pixel size value for X and Y [225].

One GAN was trained separately for each laser structured surface sample, using the 16 extracted height maps as reference images. The schematic representation of a GAN is shown in Figure 7.2. The main role of the Generator is to produce artificial images that are indistinguishable from the reference images for the Discriminator, and this is the basis for the training procedure. That is, the Generator aim is to learn to create images of progressively higher similarity to the reference ones. The aim of the Discriminator is to learn to distinguish the reference images from the artificial ones. After completing the training, the Discriminator was discarded and only the Generator was used to create 20 artificial images. The 100 px x 100 px height maps created by the generator were imported into the Alicona software, and the areal surface roughness parameters were calculated for each of them.

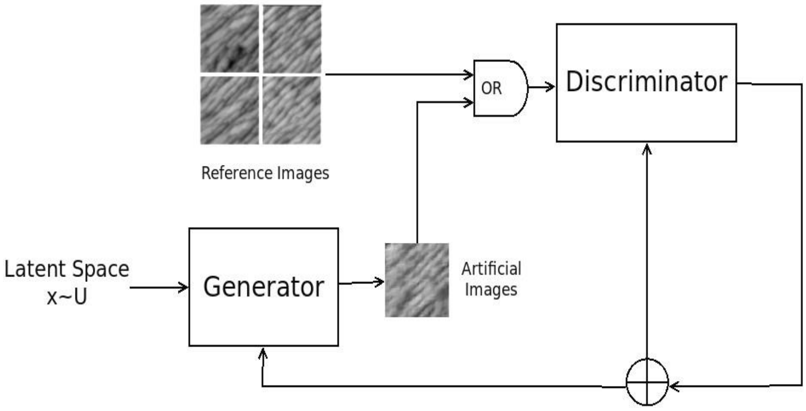

Figure 7.2 Schematic representation of GAN used to generate artificial height maps/depth images based on experimental LIPSS topography data. The loss signal of the Generator is the opposite of the loss signal of the Discriminator, which allowed the height maps, created by the Generator, to become progressively more realistic and similar to the real/reference surfaces.

The GAN architecture was determined by trial-and-error during a preliminary process of parameters fine tuning. The detailed learning process is described hereafter. Each artificial image created by the Generator, whose architecture is presented in Table 7.2, was based on a vector of 100 random scalar values fed as input to the network. Using a sequence of upscaling and convolutional layers, a matrix of 100x100 elements (normalised in [-1,1]) was produced. The final image was generated by re-scaling the matrix elements to 16-bits unsigned integers. The Discriminator architecture, described in Table 7.3, was composed of an alternate stack of convolutional and dropout layers. Both the Generator and Discriminator were trained together using the Adam optimiser, albeit with different learning rates. For each epoch, an equal number of real images (sampled with replacement from the reference images) and artificial images, created by the Generator, were fed to the Discriminator that was trained against a binary label (i.e. real=1, fake=0). The Generator was trained on a complemented value of the Discriminator loss, in a zero-sum fashion. The training parameters are given in Table 7.4. To improve the early convergence of the Generator, a measure of noise has been added to the data used by the Discriminator. Each time a reference (i.e. real) image was fed to the Discriminator, the associated label was randomly flipped (with p=0.5). This was not performed in the case of the artificial images. This regularisation procedure limited the Discriminator potential of greatly outperforming the Generator in the early stage of the learning process, to the point of hindering its ability to learn to generate good quality images.

Table 7.2 Description of the main layers that compose the Generator (with initial size S=10).

Layer	Parameters

Dense	# units = 128*S^2
	activation = ReLu

Reshape	size = (S, S, 128)
Batch Normalization	momentum = 0.8
Upsampling (2D)	factor = 5
Convolutional	# filters = 128 kernel size = 3 activation = ReLu
Batch Normalization	momentum = 0.8
Upsampling (2D)	factor = 2

Convolutional	# filters = 64 kernel size = 3 activation = ReLu
Batch Normalization	momentum = 0.8
Convolutional	# filters = 1 kernel size = 3 activation = tanh

Table 7.3 Description of the main layers that compose the Discriminator.

Layer	Parameters
Convolutional	# filters = 16 kernel size = 3 strides = 2 activation = Leaky ReLu (alpha=0.2)
Dropout	rate = 0.25
Convolutional	# filters = 32 kernel size = 3 strides = 2 activation = Leaky ReLu (alpha=0.2)
Dropout	rate = 0.25
Batch Normalization	momentum = 0.8
Convolutional	# filters = 128 kernel size = 3 strides = 1 activation = Leaky ReLu (alpha=0.2)
Dropout	rate = 0.25

Dense	# units = 1
	activation = sigmoid

Table 7.4 Parameters used for the GAN optimisers and learning process.

Parameter	Value
epochs	3*10^3
batch size	32
discriminator learning rate	5*10^-5
generator learning rate	2*10^-4
loss	binary cross-entropy

Overall, the set of GAN-generated images (henceforth Set GAN) consisted of 360 artificial topographies (18 x 20), each was described by 21 areal surface roughness parameters and one CA value. The procedure of assigning the CA to the GAN topographies (as well as to Set A and Set B) was as follows: the mean (μ) and standard deviation (σ) were calculated for the obtained CA values for each surface sample. Then, one CA value was assigned randomly to each topography from a uniform CA distribution within the interval $(\mu - \sigma, \mu + \sigma)$.

7.3.2. Feature Selection and ANN structure optimisation

The feature selection analysis, ANN optimisation and validation procedure were run three times in parallel to assess the usefulness of the GAN generated artificial LIPSS topographies. By using only the small Set A, it was intended to test the feasibility of performing the whole study using a limited amount of experimental data. Then, the quality of the GAN-generated topographies was assessed based on tests run only on the Set GAN. Finally, the benefits of augmenting the available experimental data with the artificially generated ones were evaluated on the merged Sets A and GAN. All three cases were also validated on Set B.

Feature selection methods were applied to the datasets to filter out redundant and irrelevant attributes among the ISO areal surface parameters, and jointly perform ANN structure optimisation [221]. A parameter/feature is considered relevant when it conveys useful information for a given task, and redundant when it does not add additional information that has not been already provided by other parameters. The purpose of feature selection was to find the smallest number of most related areal surface roughness parameters, without significantly reduce the ANN’s accuracy for the two specific tasks. The first task was a classification problem, where the ANN had to be trained to detect either the presence of processing disturbances (FOD or BIA in this research), or the use of optimised laser settings during the structuring process (labelled as class N). Then, the same group of surface parameters was applied to the second task. The second task amounted to a regression problem, where the ANN had to learn the relationship between the identified group of areal surface roughness parameters, and the static water CA of the laser-treated surfaces. It is important to state that the ability to detect alterations in LIPSS topographies due to any processing disturbances might also help to foresee potential variations in the surface performance. Therefore, the results from the classification task can indicate potential changes in the surface functional response and can be used to trigger some corrective processing routines to keep it within predefined limits.

7.3.2.1. Feature Redundancy Analysis

Data feature (attribute) redundancy was assessed by using the well-known Pearson correlation coefficient [226]. In this study, two data attributes (areal surface parameters) were considered highly correlated and hence redundant if their correlation coefficient $\lfloor \rho_{xy} \rfloor$ was higher than 0.8. After the analysis, redundant parameters were removed sequentially, starting with the one that showed significant similarities with the largest number of other parameters. Once this surface parameter had been removed, the one amongst the remaining that had the largest number of significant similarities with the others was eliminated, and so forth until no redundant parameters were left.

7.3.2.2. Feature Relevance Analysis and ANN Structure Optimisation

Feature relevance is usually assessed by some measure of correlation between the feature and the target variable. The analysis of relevance is complicated by the fact that analysing one feature on its own, as done in univariate feature selection approaches [227], may lead to the removal of elements that are not significantly correlated to the target variable, but that might become highly informative in combination with other features. For this reason, a multivariate method based on the evolutionary ANN Evolver (ANNE) algorithm was used. ANNE is specially designed for the optimisation of ANN classifiers [228], [229], and can be regarded as an embedded feature selection method that simultaneously performs feature selection, ANN structure optimisation and weight training [230].

ANN optimisation and feature selection were carried out for the processing disturbances classification task, and then the results were re-used for the wettability prediction task. A Multi-Layer Perceptron (MLP) ANN [231] was used as classifier in the first task, and predictor in the second. Preliminary tests revealed that one hidden layer of units was enough to attain a very high accuracy.

ANNE was run using the group of surface parameters obtained after redundancy analysis, and thus was employed only for relevance-based feature selection. The feature relevance selection and ANN optimisation procedure consisted of two stages as shown in Figure 7.3. In the first stage, ANNE was used to optimise the MLP structure, that is to define the size of its hidden layer, and to evolve minimal sets of relevant areal parameters. In the second stage, the MLP structure was set to the optimal configuration evolved by ANNE. Exploiting the feature selection results from ANNE, a number of candidate groups of surface parameters were formed, and their suitability was evaluated on the MLP ability to learn the classification task. The MLP was trained using the standard back-propagation (BP) procedure [232]. The main parameters of the MLP, and the learning parameters of the ANNE and BP algorithms were experimentally optimised and are listed in Table 7.5. The remaining parameters were set as in [228].

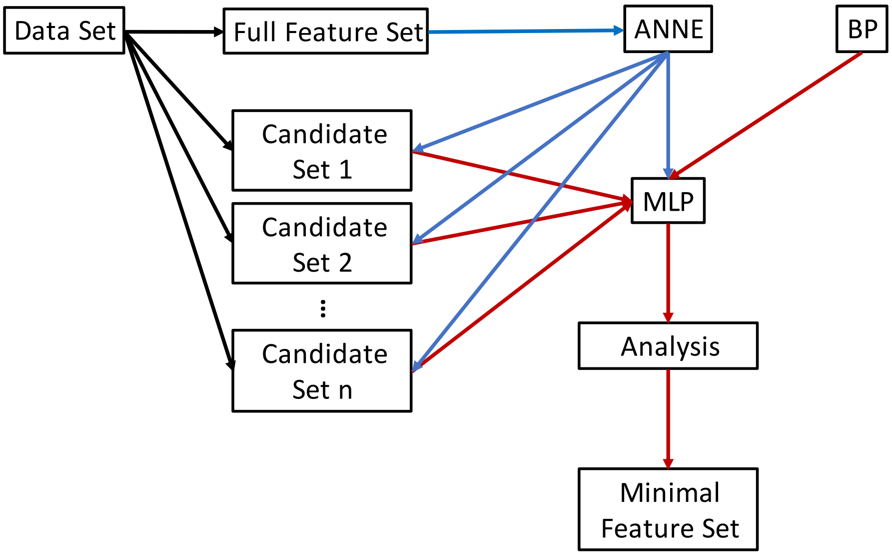

Figure 7.3 Steps of feature relevance analysis split into two stages. In the first stage (blue lines), the ANNE procedure was used to optimise the MLP structure and generate candidate groups of surface parameters. In the second stage (red lines), the parameter groups were evaluated on the learning results of MLP (using BP training) and a final minimal group of relevant areal surface parameters is generated.

A final tuning step was performed to adjust the number of iterations required for the BP procedure because of the different nature of the final learning task. The learning curves were analysed and the duration of the learning procedure was set in order to avoid overfitting. Training data overfitting occurred in both classification and regression tasks. Hence, the learning procedure had to be restricted to respectively 100 and 200 iterations, as stated in Table 7.5.

Table 7.5 MLP architecture and parameterisation of the ANNE and BP algorithms.

MLP	
Input nodes	*
Hidden nodes	*
Output nodes	3
Transfer function hidden nodes	hypertangent
Transfer function output nodes	sigmoidal
ANNE	
Population size	200
Iterations	5,000
Crossover rate on binary mask	1
Crossover rate on real-valued string	No crossover
Mutation rate on binary mask	0.1
Mutation rate on real-valued string	0.1
BP rate (problem-specific operator)	1
Cycles of BP learning per iteration	1
Selection scheme	Adaptive [233]
BP RULE	
Iterations (Feature Selection)	3000
Iterations (Classification Task 1)	100
Iterations (Regression Task 2)	200
Learning rate	0.01
Momentum term	0.1
*** Evolved by ANNE**	

Following a common practice, a pre-processing step was performed where the areal surface roughness data were normalised using the mean-variance procedure. Due to the stochastic variability of the learning procedure, 10 independent runs of the ANNE algorithm were performed for each experiment, and the results were statistically analysed. For each learning trial, the data set (Set A, Set GAN, or Set A+GAN) was randomly divided into a training set containing 80% of the samples, and a validation set containing the remaining 20%. For the BP algorithm, 100 independent runs of the procedure were performed for each experiment. The reason for the different number of repetitions is the computational cost associated with the two algorithms, in detail about 16 minutes for ANNE and 3 seconds for the BP algorithm.

7.4. Results and discussion

7.4.1. Datasets

Examples of LIPSS topographies from Set A and artificially generated topographies from Set GAN with and without the presence of processing disturbances are presented in Figure 7.4. The influence of FOD and BIA on the LIPSS characteristics is clearly visible. The FOD increase entailed a decrease in LIPSS amplitudes that eventually led to spots where LIPSS were no longer generated, e.g. when FOD = 0.8 mm. In regards to the influence of BIA, two types of ripple periodicities were present on the surface, which is typical for LIPSS generated with a p-type polarized beam that is not normal to the surface [101]. Samples produced with lower BIA resulted in a dominant periodicity above the one achieved with optimised laser settings, while higher BIAs led to only smaller periods. Generally, the LIPSS topographies selected for the representative Set A, and consequently the ones generated by the GAN, had widely varied dimensional characteristics, which led to diverse areal surface parameters values and altered their wettability. All of the laser-treated surfaces showed hydrophilic behaviour and the obtained CA values ranged from 26 to 80 deg, with a measurement uncertainty of approximately 10 deg. In Table 7.6, the number of input topographies in each Set, the distributions of the classes and the range of output CA values are summarised.

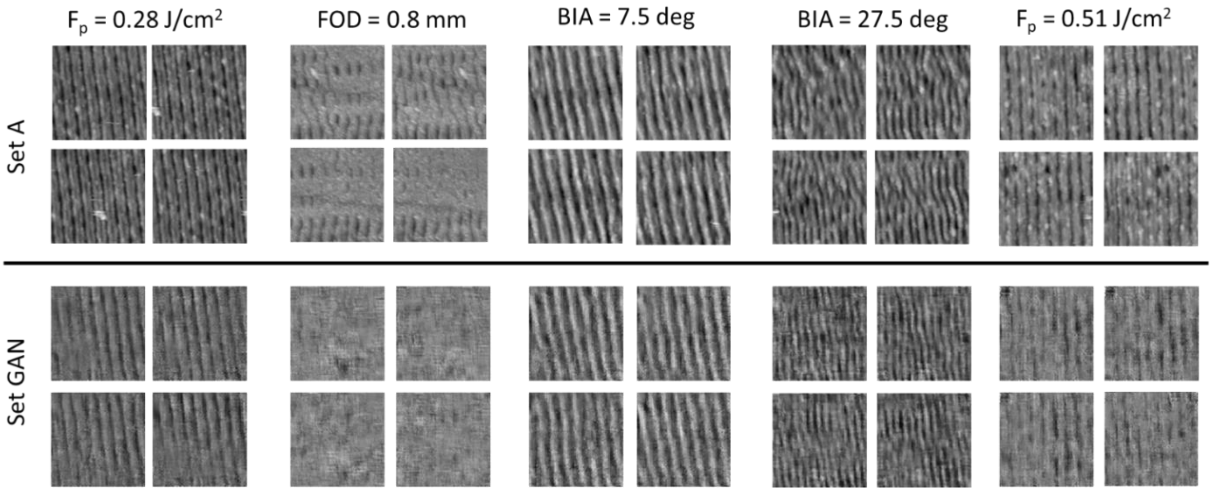

Figure 7.4 Examples of 7.8 μm x 7.8 μm LIPSS topographies with and without processing disturbances from Set A together with the respective artificially generated ones from Set GAN. Peak fluence of $F_p = 0.28$ J/cm^2 was used to produce the surfaces with varying FOD and BIA.

Table 7.6 Summary of LIPSS topographies within Sets A, GAN and B that was used to classify laser processing disturbances (the first task). Class N refers to samples produced without processing disturbances but with varying peak fluence. The output values of minimum and maximum CAs are also provided for the regression task, i.e. the wettability prediction.

	Set A	GAN	Set B
Total topographies	288	360	1104
ISO parameters		21	
Task 1: Processing Disturbance Classification (3 classes)			
Class FOD	80	100	384
Class BIA	112	140	560
Class N	96	120	160

Task 2: Wettability Prediction			
Min CA, deg	30.2	29.5	25.7
Max CA, deg	81.1	80.6	79.5

7.4.2. Feature Redundancy analysis

The correlation analysis revealed that several features, i.e. aerial surface roughness parameters, were redundant in all Sets, i.e. Set A, Set GAN and the largest Set B. The analysis of Set B was done only for reference purposes and kept for validation only. The redundancy analysis performed on the small Set A differs from that conducted on Set B. Out of 210 pairwise feature redundancy checks, 23 (11%) were different. Overall, despite some discrepancies, the analysis performed on Set A was in good agreement with the one performed on Set B. Thus, it can be judged that Set A is a representative example of the larger population of Set B. The analysis performed on Set GAN also differed from the distribution of Set B. It should be noted that Set GAN was created using the samples of Set A, and thus ‘inherited’ the inaccuracies of the latter. Out of 210 pairwise feature redundancy results, the analyses on Set A and Set GAN differed in 30 cases (14%). The results show a satisfactory agreement between the two sets, indicating that the GAN technique of generating artificial topographies captured reasonably well the statistics of Set A.

Table 7.7 shows the results of the elimination procedure for the three data sets. Redundancy elimination gave the same results for Set A and Set A+GAN, leading to a reduction of their attributes, i.e. ISO parameters, from 21 to only 10. On Set GAN, redundancy elimination reduced the set attributes to 9, 6 of them shared with the other two sets.

Table 7.7 Redundancy analysis of the feature selection procedure. Retained ISO parameters (attributes) of the three sets are depicted with '✓'.

Set	**Sa**	**Sq**	**Sp**	**Sv**	**Sz**	**S10z**	**Ssk**	**Sku**	**Sdq**	**Sdr**	**Sk**	**Spk**	**Svk**	**Smr1**	**Smr2**	**Vmp**	**Vmc**	**Vvc**	**Vvv**	**Sal**	**Str**	**Total**
A			✓	✓				✓						✓	✓	✓		✓	✓	✓	✓	10
GAN					✓		✓	✓					✓	✓	✓			✓		✓	✓	9
A + GAN			✓	✓				✓						✓	✓	✓		✓	✓	✓	✓	10

7.4.3. Feature Relevance analysis based on ANNE algorithm

The averages of the feature selection and structure optimisation results, and the classification accuracies obtained for the validation set (20% of examples of the data set in consideration) are reported in Table 7.8. For reference, the results obtained using the full set of the ISO parameters are also included in the table. The frequency of each data attribute that was selected in the 10 runs of ANNE is shown in Table 7.9 for the three data sets.

Table 7.8 Feature selection and structure optimisation results (ANN hidden nodes) obtained by the ANNE algorithm for the three sets. A summary of the classification accuracies achieved for Task 1 on the validation set (20% of examples of the data set in consideration) is included in the table, too. The results are calculated over 10 runs of the algorithm. In the table, 'all' refers to the trials run using the full 21 surface parameters, 'reduced' refers to the parameters group obtained after the redundancy analysis. The significance of the differences in the classification accuracies obtained using the full and reduced ISO parameters is analysed using Mann-Whitney tests and the p-values are provided in the table.

	Set A		**Set GAN**		**Set A+GAN**	
	all	reduced	all	reduced	all	reduced
Selected Features	6.20	5.30	6.90	5.40	9.00	8.10
Hidden nodes	3.40	2.9	3.10	2.70	4.00	4.50
Min	79.31	46.55	86.11	84.72	87.60	89.15
Q1	83.19	50.86	90.63	93.06	89.34	90.12
Median	85.34	55.17	93.06	94.44	94.57	91.86
Q3	86.21	58.62	95.83	95.83	96.51	93.02
Max	89.66	68.97	98.61	100.00	97.67	98.45
$\boldsymbol{p-value}$	1.7×10^{-4}		0.73		0.65	

Table 7.9 The selection frequency of each areal surface roughness parameter in the 10 runs of the ANNE algorithm obtained for Sets A, GAN and A+GAN.

Parameter	**Set A**	**Set GAN**	**Set A+GAN**
Sa	0	0	0
Sq	0	0	0
Sp	0.1	0	0.6
Sv	0.3	0	1
Sz	0	0.3	0
S10z	0	0	0
Ssk	0	0.2	0
Sku	0.9	0.6	0.8
Sdq	0	0	0
Sdr	0	0	0
Sk	0	0	0
Spk	0	0	0
Svk	0	1	0
Smr1	0.3	1	1
Smr2	0.4	0.5	0.8

Vmp	0.5	0	0.5
Vmc	0	0	0
Vvc	0.2	0.7	0.7
Vvv	1	0	0.7
Sal	0.7	0.1	1
Str	0.9	1	1
Total Selected	5.3	5.40	8.10

The results, presented in Table 7.8, obtained using the three data sets indicated that some ISO parameters might be further discarded due to being less relevant. However, it is important to note that the actual ISO parameters selected differed from set to set. Though, there was a considerable agreement in the size of the surface parameters group using the full 21 ISO parameters and the reduced group after redundancy analysis. In general, when all surface parameters were considered, ANNE tended to select slightly more relevant attributes. In terms of the selected ISO parameters and their selection frequency, the results obtained considering all or a reduced group of parameters, as in Table 7.9, cannot be compared. This is due to the fact that redundant attributes are equally likely to be selected, and the selected frequency is not necessarily an indication of their relevance.

Regarding the classification accuracy, the most evident result is the poor accuracies on Set A attained by ANNE. The analysis of the learning curves did not indicate significant overfitting of the training data. The most plausible explanation is the small size of Set A, which affected ANNE’s ability to evolve to high performing solutions. For Sets GAN and A+GAN, the results suggest that MLP could be trained to identify the processing disturbances with high accuracy. There was no distinguishable difference in the accuracy between the results obtained using all or only a smaller subset of attributes, i.e. ISO parameters.

7.4.4. Evaluation of candidate surface parameters subsets

Based on the results obtained using ANNE, the MLP structure was fixed to one hidden layer of 5 nodes even though it was slightly larger than proposed in Table 7.8. The reason for this was that the smaller Set A alone might under-represent the complexity of LIPSS topographies.

Using the results in Table 7.9, a number of candidate ISO parameter groups was created for each of the three sets as shown in Table 7.10. These candidate groups were based on the selection frequencies, starting with a minimal subset of most frequently selected ISO parameters, and successively adding more attributes. These candidate sets were evaluated on the learning results of the MLP after it was trained using BP using only the selected ISO parameters. The results are shown for each ISO parameters' group and data set in Table 7.11. For the sake of comparison, the results include those obtained using the full set and the set generated after redundancy analysis.

Table 7.10 Candidate surface parameters groups tested on data Sets A, GAN and A+GAN. Their size is indicated by their group coding in the first column (e.g. F_6 has six ISO parameters). Selected parameters in the group are indicated by '✓'.

Group	Sa	Sq	Sp	Sv	Sz	S10z	Ssk	Sku	Sdq	Sdr	Sk	Spk	Svk	Smr1	Smr2	Vmp	Vmc	Vvc	Vvv	Sal	Str
Set A																					
F_3								✓											✓		✓
F_4								✓											✓	✓	✓
F_5								✓								✓			✓	✓	✓
F_6								✓							✓	✓			✓	✓	✓
F_{10}			✓	✓				✓						✓	✓	✓		✓	✓	✓	✓
Set GAN																					
F_3													✓	✓							✓
F_4													✓	✓				✓			✓
F_5								✓					✓	✓				✓			✓
F_6								✓					✓	✓	✓			✓			✓
F_9					✓		✓	✓					✓	✓	✓			✓		✓	✓
Set A + GAN																					
F_4				✓										✓						✓	✓
F_6				✓				✓						✓	✓					✓	✓
F_8				✓				✓						✓	✓			✓	✓	✓	✓
F_9			✓	✓				✓						✓	✓			✓	✓	✓	✓
F_{10}			✓	✓				✓						✓	✓	✓		✓	✓	✓	✓

Table 7.11 A summary of the MLP classification accuracies obtained on the validation set (20% of the whole data set) using the parameter groups in Table 7.10. For each data set, the statistics refer to 100 learning trials using the BP algorithm. For reference, also the results of training the MLP using all ISO surface parameters are given. The significance of the differences in the classification accuracies obtained using the all and candidate attribute sets is analysed using pairwise Mann-Whitney tests and reported by the p-values.

Set A						
	F_3	F_4	F_5	F_6	F_{10}	F_{All}
Min	70.69	70.69	70.69	72.41	77.59	81.03
Q1	77.59	77.59	79.31	84.48	87.93	91.38
Median	81.03	81.03	82.76	86.21	89.66	93.10
Q3	83.19	84.48	86.21	89.66	93.10	94.83
Max	89.66	93.10	91.38	96.55	96.55	100.00
p-value	0	0	0	0	0	
Set GAN						
	F_3	F_4	F_5	F_6	F_9	F_{All}
Min	75.00	84.72	84.72	83.33	83.33	84.72
Q1	83.33	90.28	91.67	93.06	94.44	95.49
Median	86.11	94.44	95.83	95.83	96.53	97.22
Q3	88.89	95.83	97.22	97.22	97.22	98.61
Max	94.44	100.00	100.00	100.00	100.00	100.00
p-value	0	0	0.0065	0.0767	0.1721	
Set A+GAN						
	F_4	F_6	F_8	F_9	F_{10}	F_{All}
Min	70.54	78.29	83.72	86.05	84.50	82.95
Q1	75.97	88.37	89.92	89.92	91.47	92.05
Median	79.07	90.70	91.47	92.25	93.02	93.80
Q3	82.17	93.02	93.80	93.80	94.57	96.12

Max	88.37	96.90	98.45	97.67	99.22	99.22
p-value	0	0	0	0	0.0338	

In terms of classification accuracy, the results reported in Table 7.11 are in good agreement with those obtained using ANNE and confirm again that high accuracy results can be obtained with a significantly reduced number of surface parameters. The classification accuracies obtained using Set A are lower than those obtained using the other two data sets, although the differences are significantly smaller than those recorded for ANNE.

Table 7.11 shows that the removal of redundant features had marginal to no effect on the learning accuracy of the classifier for the data sets that included the artificial topographies. On Set A, the differences are more marked although still moderate. The same effect was observed after the elimination of irrelevant ISO parameters on the learning results of the classifier. The resulting classification accuracies were most sensitive for removing irrelevant surface parameters for Set A. This was likely due to the small size of the data set, which made accurate MLP learning and evaluation more difficult.

The results in Table 7.11 suggest that the feature selection affects the classifier performance mostly for Set A. The most conservative choice would be to use the group of non-redundant ISO parameters F_{10}, or if some further reduction in performance is acceptable, the parameter group F_6 could be adopted. If Set GAN is used, the surface parameters can be trimmed down to the six data attributes of F_6 without significantly affecting the performance. If Set A+GAN is utilised, the tests show that the classifier accuracy will suffer only a very modest deterioration (less than 1%) using group F_{10} of non-redundant ISO parameters and only modest (around 2%) using F_8 data attributes.

These final choices are validated in the last step, where the MLP is tested against the previously unseen Set B.

7.4.5. Task 1: Classification of laser processing disturbances

Figure 7.5 reports the results on accuracies achieved in identifying the processing disturbances when applying on Set B the classifiers obtained after 100 independent runs of the BP algorithm on Sets A, GAN, and A+GAN. In general, the accuracy results were inferior to those obtained in the feature selection steps (as in Table 7.11). The deterioration of the performance was most dramatic in the learning trials performed using only Set GAN, and least severe when only Set A was used. Set A+GAN achieved only slightly worse accuracy compared to Set A. It is worth stating that the learning tasks in the feature selection and classification stages were different, i.e. the first requiring generalisation to unseen samples of already introduced surfaces, and the second generalisation to different samples of previously unseen surfaces. The lower classification accuracies achieved in the latter experiments are likely to reflect the more challenging nature of the task.

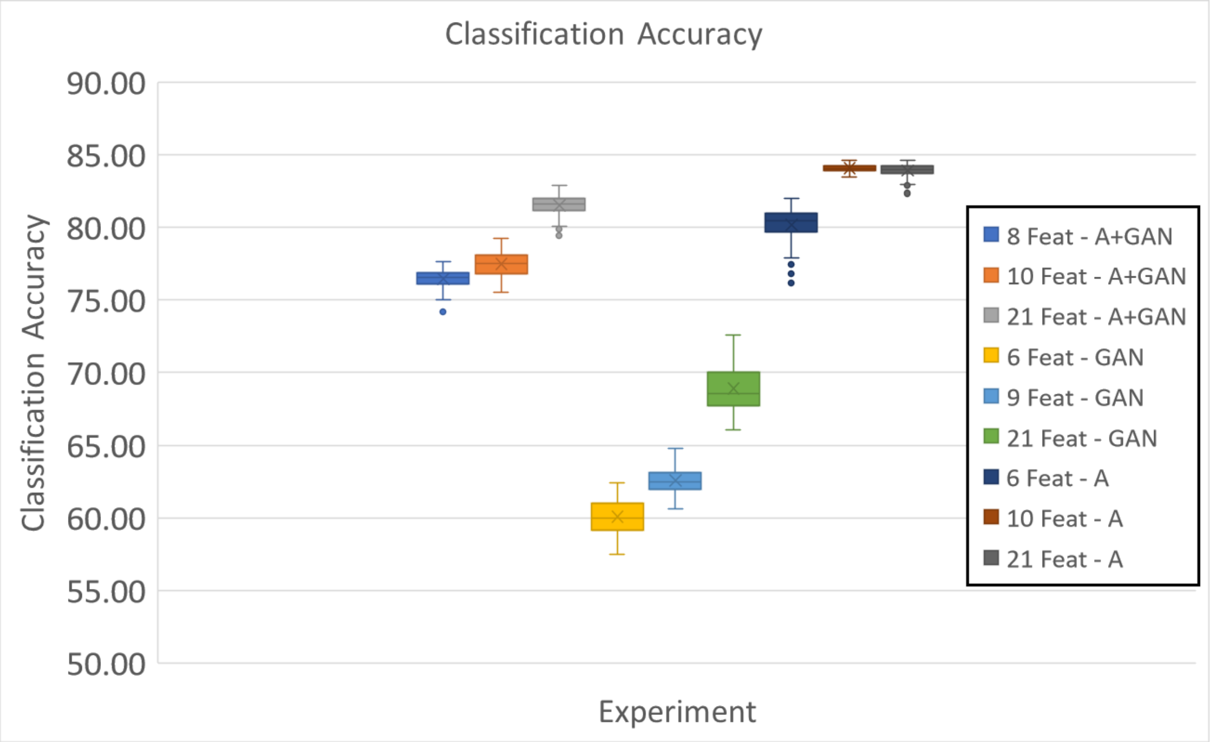

Figure 7.5 The results achieved on classification of laser processing disturbances. Accuracies obtained in three experiments where feature selection and BP training were performed respectively on Sets A, GAN, and A+GAN. The MLP learning procedure was validated on previously unseen Set B. Three surface parameters groups were tested per each data set.

The artificial LIPSS topographies generated applying GAN appeared to capture at least partly the overall characteristics of Set A. However, MLPs trained on Set GAN were very poor at generalising the learning results when applied on Set B. This result shows that the GAN-generated data were not representative of the full distribution of Set B. Given that MLPs trained using Set A did generalise well, the results seem to indicate that the problem lies within the GAN procedure itself, rather than the poor quality of the scans that were fed to GAN. One reason for this result may be that the GAN learning process had been interrupted too early. At present, the duration of the GAN learning reflected a trade-off between the computational cost and the visual appearance. Further tests could investigate whether it is worth the GAN learning time to be extended.

Since the use of data samples from real surface scans produced the best learning results, the next step was to use Set A to re-train the MLP using the ISO parameters groups selected using Set GAN and Set A+GAN. This experiment aimed at evaluating the goodness of the feature selection results obtained using artificial data samples. The results, shown in Figure 7.6, are very similar, with average classification accuracies mostly ranging between 82-84%. The only exception was the learning trials performed using the minimal parameter group F_6 that was selected using Set A, where the average accuracy was 80.4%.

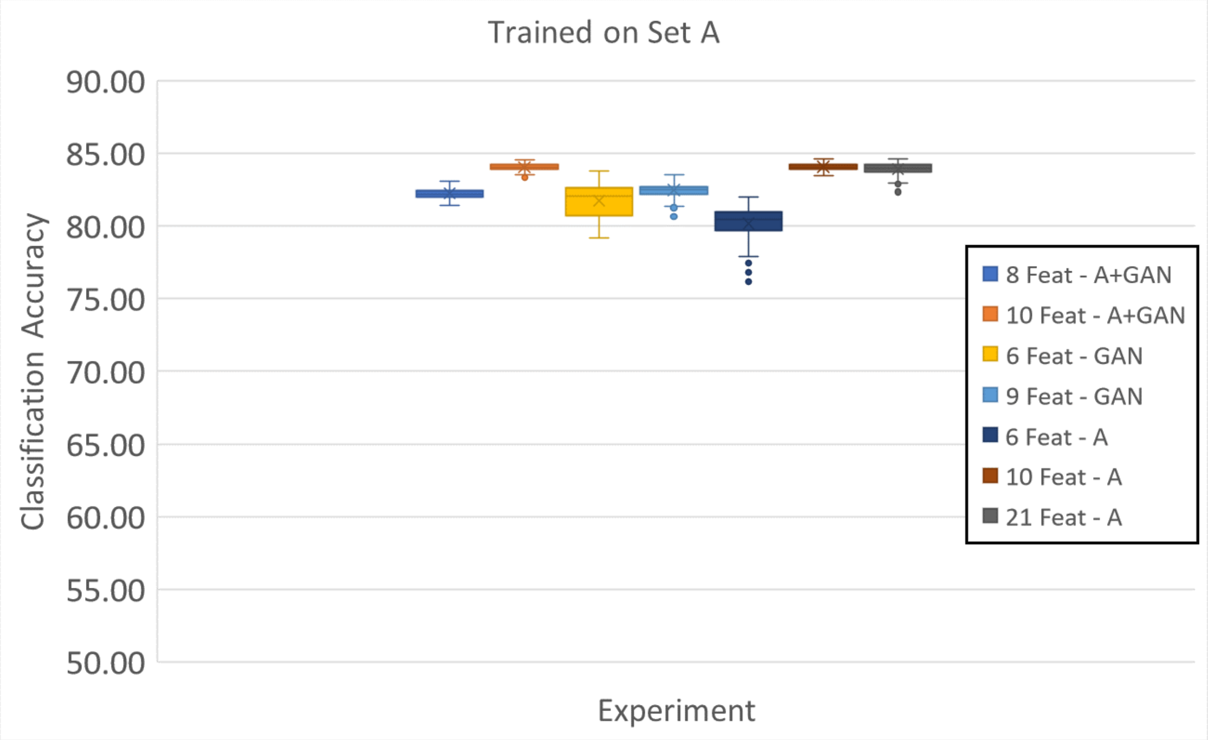

Figure 7.6 The results of the classification task with MLPs being trained only on Set A using the parameter groups identified for Sets GAN and A+GAN and the validation performed on previously unseen Set B. Two surface parameters groups were tested

per each dataset and the results compared to those obtained using all 21 surface parameters.

Note: Sets A and A+GAN had the same parameter group F_{10}, as indicated in Table 7.10.

The best learning results were obtained using surface parameter group F_{10}, i.e. the non-redundant data attributes selected after analysing Sets A and A+GAN. The removal of irrelevant surface parameters had instead a statistically significant negative effect on the accuracy results, although in practical terms this was very modest.

Table 7.12 reports the confusion matrices for the classification results on Set B presented in Figure 7.6, using MLPs trained on Set A by using the minimal parameter groups F_6 (selected on Set A), F_6 (selected on Set GAN), and F_8 (selected on Set A+GAN). The largest source of misclassifications was due to FOD topographies being identified as BIA. In proportion to the number of examples per class, the largest sources of incorrect classifications were samples from class N identified as BIA in the case of the surface parameters F_6 of Sets A and A+GAN, and FOD identified as BIA for F_8 obtained using Set GAN. It was also observed that for three tested cases a similar number of samples from class FOD were identified as class N. This could be attributed to the supplementary LIPSS samples produced with laser peak fluence close to the ripples' threshold, which had similar topographies to the ones obtained with higher FOD. Hence, those samples were more prone to be misclassified.

Table 7.12 Confusion matrices of processing disturbances classification results presented in Figure 7.6. The MLP classifier was trained only on Set A using the surface parameter group with minimal number of attributes selected respectively for Sets A, GAN, and A+GAN while the validation was performed on Set B.

a) Parameters selected using Set A

$\boldsymbol{F_6}$		**Classified as**		
		FOD	BIA	N
class	FOD	281.68	75.5	26.82
	BIA	47.65	505.9	6.45
	N	21.2	41.34	97.46

b) Parameters selected using Set GAN

$\boldsymbol{F_6}$		**Classified as**		
		FOD	BIA	N
class	FOD	260.96	95.7	27.34
	BIA	13.85	540.03	6.12
	N	30.73	27.98	101.29

c) Parameters selected using Set A+GAN

$\boldsymbol{F_8}$		**Classified as**		
		FOD	BIA	N
class	FOD	278.33	80.64	25.03
	BIA	22.5	531.79	5.71
	N	22.94	39.39	97.67

7.4.6. Task 2: Contact Angle Prediction

Figure 7.7 shows the root mean square (r.m.s.) values of the CA predictions from the validation step performed on Set B. Similar to the processing disturbance classification task, a further experiment was run employing Set A to train MLP by using the ISO parameter groups selected using Sets GAN and Set A+GAN. The results of this last experiment are given in Figure 7.8.

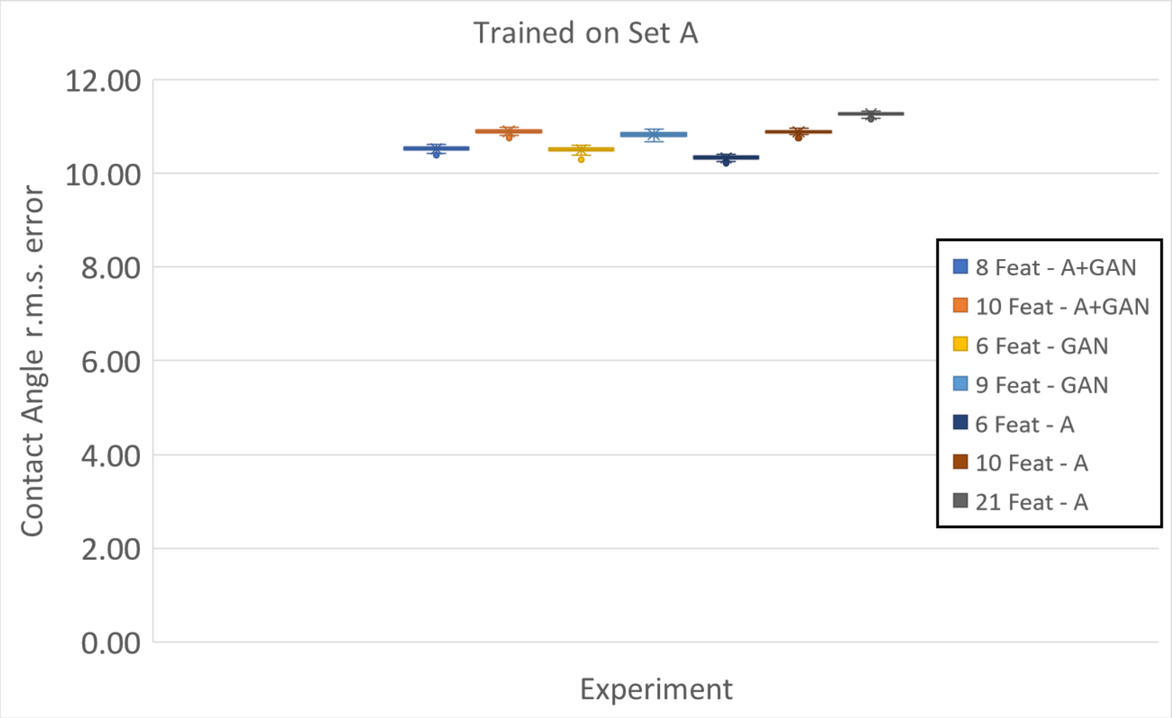

Figure 7.7 Root mean square (r.m.s.) accuracy results for the CA prediction task from three experiments where feature selection and BP training were performed respectively on data sets A, GAN, and A+GAN, while the learning results were validated on previously unseen Set B.

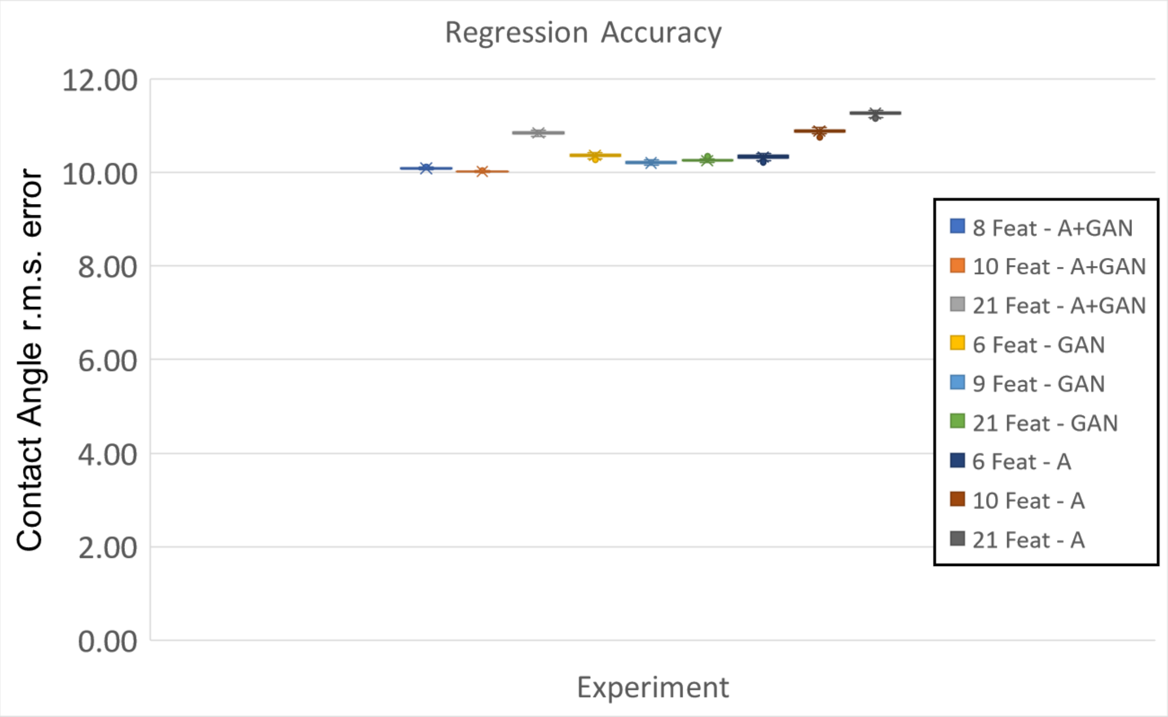

Figure 7.8 Accuracy results for the CA prediction task with MLPs being trained on Set A using the parameter groups identified for Sets GAN and A+GAN and validated on Set B. Two surface parameters groups were tested per each dataset and the results compared to those obtained using all 21 surface parameters.

The results presented in Figure 7.8 are fairly similar with the average (r.m.s.) error of around 11 degrees for all combinations of training data sets and ISO parameter groups. In general, feature selection helped the MLPs to learn the CA prediction with marginally better results. Data augmentation appeared also to play a beneficial role, since the best accuracy results were obtained by training the MLPs using Set A+GAN. Although statistically significant, it should be noted that the measured differences in accuracy were always within 1.5 degrees. The best results were obtained when training the MLPs on the augmented Set A+GAN of examples and using ISO parameter groups F_8 or F_{10} to describe the samples. In general, it can be stated that the average r.m.s.

values obtained in the experiments are comparable with the CA measurement uncertainty, and most probably this limited the MLP learning abilities. Obtaining a more accurate CA measurements might improve the MLP training and allow the MLP to differentiate better the usefulness of different data sets and ISO parameter groups.

7.5. Conclusions

In this research, an approach is presented for applying ANNs to classification and prediction tasks when ultrafast laser surface structuring/texturing is performed. ANN tools were developed and validated for pre- and post-processing of laser surface treatment data, especially areal surface roughness parameters of LIPSS topographies, that proved to be sufficiently effective. In particular, high prediction accuracies were achieved by MLP classifiers on the detection of laser processing disturbances that affect the LIPSS generation. MLPs were also used to predict with high accuracy the functional response, i.e. wettability, of LIPSS treated surfaces.

Regarding the applied ANN tools, using a small experimental dataset augmented with GAN-created artificial topographies proved to be beneficial for the tool’s development. GAN generated data were especially valuable when utilised for feature relevance analysis employing the evolutionary ANNE algorithm. Even if GAN-based artificial data reproduced well the statistics of real samples, the GAN generated topographies were less useful in supporting the MLP generalisation capabilities on the laser processing disturbances classification task. That was attributed to the GAN insufficient learning process, especially its premature interruption.

A range of feature selection methods were applied. By combining their capabilities, it was possible to reduce the number of salient aerial roughness parameters needed to characterise the surfaces, without any significant negative effect on the MLP performance. Specifically, feature redundancy analysis revealed that the initial 21 ISO parameters can be narrowed down to only 10, and such a small subset of data attributes was enough to achieve a high MLP prediction accuracy, especially in the laser processing disturbances classification task. Further trimming of irrelevant attributes down to an even smaller subsets of 6 or 8 surface parameters led to fairly similar prediction accuracies. Such substantial scale downs of data attributes can have a valuable impact on the practical aspects of data acquisition procedures, because it can reduce the number of costly, time-consuming, and sometimes complex measurements.

Finally, the ANN validation part on a larger unseen dataset showed that identification of processing disturbances could be accomplished with accuracy close to 85%. The wettability of LIPSS treated surfaces was predicted within the static water CA measurement uncertainty of approximately 10 degrees. Considering those encouraging findings, it can be concluded that the developed ANN-based tools can represent a generic approach for monitoring the LIPSS treatment operations. These tools can map the resulting areal parameters of processed surfaces to any disturbances present during the process, and consequently also to their desired functional performance.

In the previous Chapter available ANN methods were used to pre- and post- process areal surface roughness parameters obtained from LIPSS-covered surfaces. The results showed that high accuracy was achieved in both, classifying samples based on their processing conditions, and in predicting their functional response, i.e. wettability. For the first time an approach of linking surface topography data from LIPSS through ANNs techniques, was proposed.

CHAPTER 8: CONCLUSIONS, CONTRIBUTIONS AND FUTURE RESEARCH

The aim of the research presented in this thesis was to address four of current barriers preventing the LIPSS treatments to be used on a broader scale, which are specifically associated with their generation on thin films, their modelling on freeform surfaces and two related to their process monitoring. An approach for a synergistic use of two surface engineering technologies, i.e. LIPSS and DLC treatments, for producing durable replication masters was reported in Chapter 4 thus enabling, as a potential application, the serial manufacture of polymer parts with functional surfaces. In Chapter 5**,** an ultrafast laser irradiation model was proposed to simulate the varying processing conditions on freeform surfaces and predict key characteristics of generated LIPSS. A simple optical setup for tracking the changes of LIPSS characteristics was presented in Chapter 6 and its potential as an inline monitoring solution was discussed. Then, use of ANNs tools for pre- and post-processing areal surface parameters of LIPSS topographies were presented in Chapter 7 as a way to map them to their functional responses. A pilot implementation of these tools was also reported and their capabilities were discussed.

The sections below present the main conclusions and contributions to knowledge of the complete research and also suggest directions for future investigations.

8.1. Conclusions

A research on femtosecond laser processing of DLC treated substrates was presented in Chapter 4**.** The objective was to investigate the effects of femtosecond laser processing parameters for generating LIPSS on DLC coating. Additionally, it was to consider this synergistic approach as a potential application for injection moulding technology since the DLC coating is known for its superior surface properties due to its low friction coefficients and high wear resistance, as explained in Section 2.4.2.1. Hence, the LIPSS treatment of DLC coated steel substrate was studied for achieving functional and, at the same time, durable replication master. Conclusions were made against the considerations for the injection moulding technology, especially to judge whether the LIPSS generation on DLC is still suitable for this application. Even if the mechanical properties became inferior to the as-received DLC, the analysis showed that they were still higher than a conventional material for the moulds, e.g. mild or stainless steels.

The following main conclusions could be drawn:

- Uniform LIPSS were generated on DLC without any visible cracks, excessive ablation or delamination which was evaluated optically when the pulse fluence used was in the range from 0.07 to 0.13 J/cm^2 and the number of pulses per spot was between 28 and 39. All ranges of tested parameters in this study (detailed in Section 3.2) were from 0.06 to 0.48 J/cm^2 of pulse fluence and from 13 to 53 of total number of pulses per spot.
- The microstructure analysis confirmed the presence of thin, graphitized surface layer formed on laser-treated DLC surfaces that did not show any long-range

ordering (crystallisation) as a result of the femtosecond laser processing (which is a non-thermal process). However, the samples did not show differences in Raman spectra or no differences were indicated by GAXRD analysis even if the samples tested were produced with different laser processing parameters.

- Nano-indentations revealed a significant reduction in hardness from 22 to 9 GPa for as-received and the laser-treated samples with relatively low fluence, respectively. A further hardness decrease to 4 GPa was observed on the sample that was produced with a higher fluence and number of pulses, while it was still higher value when compared to the stainless steel substrate of 2.5 GPa which is a conventional material used for the moulds in injection moulding technology.
- The friction coefficient of laser structured DLC only marginally increased from 0.12 to 0.15, which can still be considered low in the injection moulding process when compared, for example, to CoF between steel and the same counterpart material (which is 0.35 [234]), and to similar CoF values between steel surface and polymers [235]. The increase was attributed to the increase of the contact area between the sample and the ball due to LIPSS profiles flattening after a small number of cycles.

The study in Chapter 4 targeted one application area, i.e. injection moulding technology, where the aim was to produce functional and durable master for the polymer replication process. The discussion was carried out with this as a potential application but the applicability can be extended to any area where ultrafast laser structuring of DLC is required. On top of that, the industrial need for broader use of the approach will require, for example, that the laser textured master to be also produced on more complex geometries and that brings out more open challenges in the LIPSS generation as a structuring process.

In the next Chapter 5, the second research question, introduced in Chapter 2, was addressed. The aim was to develop analytical modelling approach for predicting key LIPSS characteristics on freeform surfaces to help defining processing limits that also can be potentially used for identifying the limits on their functional responses. This approach can support the process of efficient strategy development for laser structuring off such surfaces. The material on which LIPSS were generated was stainless steel which was more representative to metals with similar optical properties and it can broaden the use of LIPSS applications, for instance of the ones mentioned in Section 2.4.1.

The analytical model was developed based on the ultrafast laser irradiation model but taking into account the actual spatial beam intensity distribution and local fluence threshold changes. Before, such LIPSS modelling approaches were used to predict the optimal laser processing parameters but here, for the first time, it was adapted and developed specifically for freeform surfaces. It accounted for the changes in laser processing conditions while the 3D disturbances affect the surface, that is FOD and BIA, as it is in the case for laser structuring of freeform surfaces.

The research on modelling laser structuring/texturing of freeform surfaces (Chapter 5) led to the following main findings:

- The actual beam spatial intensity was formally defined as a simple astigmatic Gaussian beam with elliptical cross-sections.

- The beam waist became more elliptical on the surface with the increase of BIA. The difference was less pronounced for angles up to 40 deg. However, the beam spot size rapidly increased for higher BIAs up to 80 deg when compared to the size of the beam in focus and normal to the surface.
- The interdependence of LIPSS characteristics to the accumulated fluence, F_{acc}, was determined by generating LIPSS on stainless steel without any disturbances and only with a varying peak fluence, F_0. LIPSS reached their optimum characteristics when F_0 varied in the range from 0.11 J/cm^2, the fluence threshold, to a value of 0.25 J/cm^2. The periodicity remained unchanged throughout the investigated F_0 range.
- Simulating the effects of F_{acc} when processing fields with a characterised beam led to a reduction of LIPSS amplitudes, and consequently to their disappearance with the increase of processing disturbances influence. The modelling and experimental results were in line with the validation samples produced when both BIA and FOD affected the processing conditions. However, the model could not foresee precisely the LIPSS amplitudes (average error of 20%) along sampling length however the moment where LIPSS started disappearing, until no longer generated on the surface, was captured (error of 4%). This information can be used for the proposed application of the model, i.e. defining the limits of LIPSS processing strategies on freeform surfaces.
- The decrease of F_{acc} led to a transition of the dominant periodicity Λ_{p-} to Λ_{p+} below F_{acc} values of 6 J/cm^2 and 2 J/cm^2 for initial F_{02} = 0.44 J/cm^2 and F_{01} = 0.25 J/cm^2, respectively, which were identified from the modelling of the processing conditions and measured PSDF values. These numbers are

important as they define another constraint for the LIPSS limits. The change in LIPSS periodicity behaviour was captured and that can influence LIPSS functional performances.

After defining the limits of the LIPSS generation based on the processing conditions prediction through ultrafast irradiation model, another barrier for successful application of LIPSS treatments into industrial manufacturing process would be the process monitoring which is often not a prime focus for LIPSS development areas. Developing monitoring methods is key in ensuring that any shifts and/or deviations in LIPSS features are detected because that can ultimately affect the LIPSS functional surface response. In Chapter 6 a concept was developed based on a simple light-scattering method and was judged to be suitable for inline monitoring method of the ripples.

The research on monitoring the LIPSS generation by analysing their light diffraction and reflectance (Chapter 6) led to following conclusions:

- The relative changes in optical response of LIPSS samples, produced with and without processing disturbances, were effectively detected by implementing a simple optical setup. Especially, this was achieved by measuring the first-order light diffraction and the zero-order reflectance while the measurements were calibrated by using reference SEM images.
- Changes of LIPSS amplitudes due to FOD variations were detected with the used experimental setup. Especially, the detectable changes within the depth of focus were 0.5% and 4% per 100 μm when performing diffraction angle and reflectance measurements, respectively.

- The BIA effects on LIPSS periodicity were quantified by performing light diffraction measurements and the detectable changes for p- and s-polarizations were 2% and 0.25% per 1 deg, correspondingly. The accuracy of the rotary stage of the laser micro processing platform used in the study was 29.1 μrad according to the specification [236] which correspond to $1.67*10^{-3}$ deg hence the detectable changes of diffraction measurement were caused by LIPSS periodicity changes as a consequence of BIA presence. Normally during manufacturing process the impact on LIPSS generation process could arise also from other process disturbances, such as insufficient laser beam calibration or type of focusing lens used. It is worth mentioning that the employed setup was placed in a laboratory environment however, by deploying commercially available sensors, the sensitivity could be greatly improved.
- The proposed simple and fast measurement method that offer sufficient sensitivity could be deployed as a cost-effective solution for inline monitoring of LIPSS generation. In this way, it will be possible to minimise and even avoid the necessity for time consuming and not practical SEM/AFM assessments/measurements.

The proposed inline monitoring method targeted detecting relative changes in LIPSS characteristics when 3D processing disturbances were present during the generation process. This can be indication that also the LIPSS functional performance may be changed however it is difficult to quantify it as every application can have different requirements for the structuring process tolerances and consequently the LIPSS spatial characteristics. Typically, separate experimental studies need to be carried out to establish a relation between LIPSS topography data and their functional response.

In Chapter 7 use of ANN tools was proposed for the identification of the processing conditions, present during the LIPSS generation process, based on the surface topography data, i.e. areal surface roughness parameters, as well as demonstrating that also surface functionality could be predicted. Employing ANNs tools for the aforementioned purpose in Chapter 7 led to the following main findings:

- Developed ANN-based tools represented a generic solution for monitoring the LIPSS treatment operations by identifying the processing disturbances during their treatments and by mapping the resulting areal parameters on processed surfaces with their functional performance, i.e. wettability.
- The use of GAN-based data augmentation technique for generating artificial LIPSS topographies proved to be a reliable tool for generating data sets for MLP training. By employing this technique, it was possible to minimise the experimental data necessary, i.e. AFM measurements, to create a MLP classifier.
- The performed feature selection analysis showed that the full range of standardized areal surface roughness parameters can be narrowed down to a group of 6 or 8 most informative ones to achieve high MLP accuracy in laser processing disturbances classification and when mapping LIPSS to their specific functional response, that is the static water contact angle values of LIPSS treated stainless steel.
- Validation of the MLP model performed on a large dataset identified with accuracy of 85% if the processing disturbances were present during LIPSS

generation process while the LIPSS wetting property could have been determined within the CA measurement uncertainty of around 10 degrees.

To conclude, in this thesis four topics related to addressing the use LIPSS on broader scale were explored. Figure 8.1 shows a schematic portraying how each Chapters fits within the overall LIPSS developments areas. Applications for LIPSS are developed because of the flexibility of the technology and the relatively simple and robust processing setups. To this day, novel applications are being developed for LIPSS and the search for new functionalities is continuing. Chapter 4 focused on only one application area through studying the LIPSS treatments on thin film, i.e. DLC, because it is proven to have low friction and wear resistant properties hence it has the potential to be applied in the injection moulding technology where this properties are important for process efficiency and tooling life. As a result, laser structured replication masters coated with DLC have the potential to reduce the demoulding forces as well as to improve replication fidelity. At the same time, a functionalized surface is produced that can be transferred to polymer replicas. Next Chapters focused more on addressing industrial challenges towards successful transfer of LIPSS technology, including modelling and monitoring, while considering complex geometries which can be linked to any functionality or application. The material used in those studies was stainless steel because it can be representative of metals with similar optical properties but the approach has the potential to be also applied to a broader range of materials, although further studies would be required. The developed analytical model in Chapter 5 can be used as a tool for determining the processing constraints for a laser parameter’s domain reducing the empirical studies in order to achieve the required LIPSS homogeneity and consistency in the functional response when structured on freeform surface. Then, a concept for inline monitoring method of LIPSS was developed in Chapter 6 to track changes in LIPSS when disturbances occur during the structuring process. Additionally, use of ANNs, as detailed in Chapter 7, also can be employed as a monitoring tool for LIPSS treatments operations because it allows fast and robust data analysis. It was possible to achieve, with high accuracy, detection of laser processing disturbances and prediction of LIPSS functional response, with wettability as an example, solely based on areal surface roughness parameters.

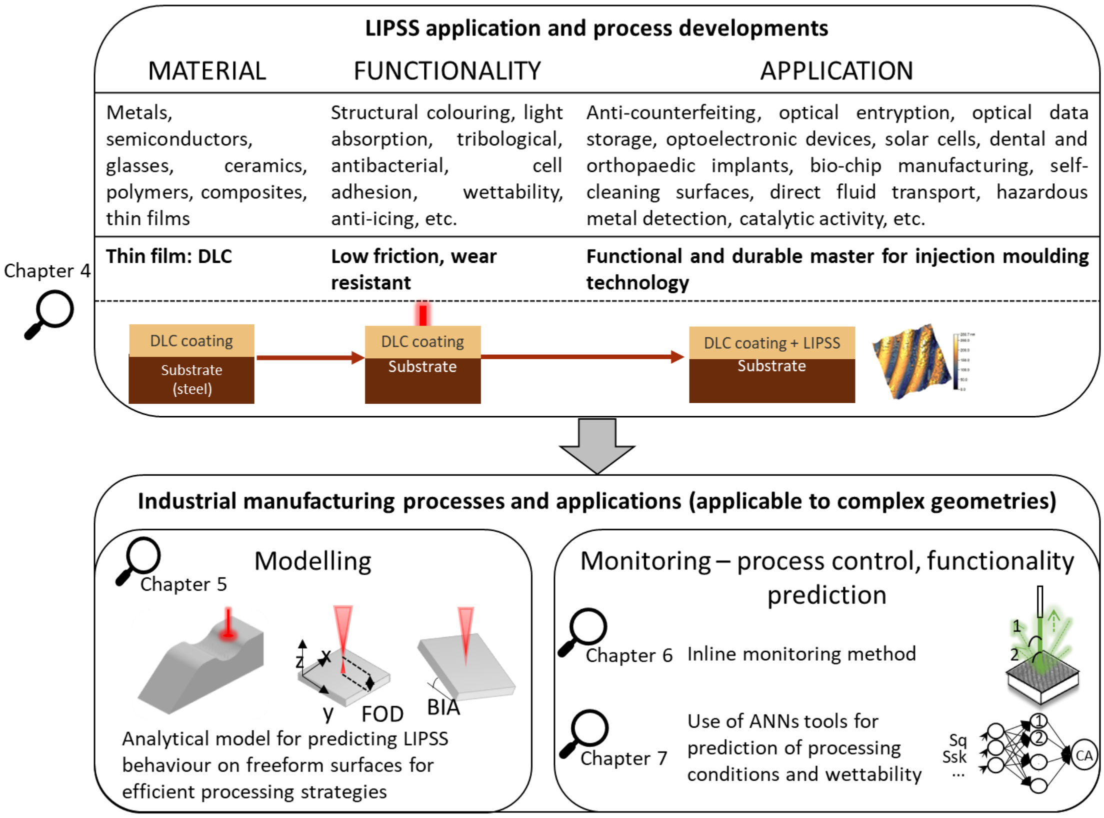

Figure 8.1 Schematic showing the links between the research Chapters 4, 5, 6 and 7 in this thesis on the LIPSS development areas.

8.2. Contributions to knowledge

The objectives of the research were achieved and the contributions to knowledge claimed in this thesis can be summarised as follows:

I. The ultrafast laser structuring/texturing of DLC treated surfaces led to two types of LIPSS, i.e. HSFL and LSFL, after a single spot irradiation when the pulse fluence and the number of pulses per spot were varied. A range of processing parameters, i.e. pulse fluence and number of pulses per spot, were established for generating uniform LIPSS on relatively large surfaces without any DLC delamination or visible cracks. This was accomplished by controlling precisely the accumulated fluence, i.e. pulse fluence and total number of pulses per spot. The mechanical and microstructural analysis of laser treated DLC revealed that the surface properties for laser treated DLC still can be considered as appropriate for producing replication masters. The hardness was significantly reduced from 22 GPa to 9 GPa from as-received DLC to laser structured samples but the value was still higher when compared to the substrate steel of hardness of 2.5 GPa that is conventional material used for the injection moulding technology. The small increase in tribological performance, from CoF of 0.12 for as-received DLC to 0.15 can still be considered low, because the typical values for CoF for the mould’s material are 0.35 [234], [235], and hence will contribute to lower adhesive nature of laser treated DLC substrates. For comparison the average demoulding forces in micro-injection moulding with DLC coated tool can be decreased up to 37% when compared to uncoated surface [95]. Thus, ultrafast laser treatments of DLC on replication masters can offer an improved wear resistance and demoulding performance and thus enable the manufacture of functionalised polymer replicas with sub-micron surface structures. A wider implication of this synergistic approach is contributing to the process efficiency improvement of polymers manufacturing as well as adding to producing polymer replicas with functionalised surfaces that can be, for instance, employed in food packaging or medical fields.

II. An ultrafast irradiation model was developed to investigate the effects of processing disturbances on LIPSS treated freeform surfaces. Compared to other modelling approaches, the proposed method for calculating the accumulated fluence, for the first time, takes into account the actual spatial pulse intensity while assuming a simple astigmatic Gaussian beam. Additionally, the effects of fluence distribution in processing inclined or curved surface, while BIA varies, are also accounted for in the model. It was demonstrated that the processing disturbances, i.e. FOD and BIA, modified the laser processing conditions, particularly by affecting the pulse fluence distribution. The beam spot size varies and this leads to changes of local fluence thresholds. A good agreement between the simulation and experimental results was achieved and thus the model can be used to identify processing conditions leading to LIPSS disappearance and transformations. The percentage error estimated between modelled and measured LIPSS amplitudes values was around 20.2% but the location where ripples were no longer generated on the surface was estimated to have the error of 4%. Also, the modelling results can be used to drive/constrain software tools used for partitioning freeform surfaces into fields/patches prior to their LIPSS treatments. In this way, the transformations of LIPSS topographies can be kept within acceptable limits and thus indirectly to maintain their respective functional responses within predefined ranges throughout the processed area. This is relevant to any LIPSS application area, as discussed in Chapter 2, where the ripples generation is required to be produced on freeform surfaces. The solution contributes to developing efficient processing strategy hence reducing the lead time and improving productivity from industrial perspective. For example, in tessellation algorithm of a sphere, setting the correct processing disturbances tolerances can reduce the number of fields to process by 10% when FOD limit is increased by 0.07 mm [126].

III. A method for monitoring the LIPSS generation was proposed based on tracking the relative changes of light diffraction and reflectance on processed surfaces. The concept was validated by using LIPSS produced on planar surfaces with set processing disturbances together with a reference one structured in focus with normal beam and optimised parameters. It was demonstrated that the LIPSS periodicities calculated by analysing the light diffraction were in good agreement with those obtained with other methods, such as 2D FFT performed on SEM and AFM images. In addition, the influences of processing disturbances on ripples' periodicities and amplitudes were analysed and the corresponding changes in their optical response were determined, too. BIA impacted mostly the LIPSS spatial frequencies that were detected through changes in diffraction angle, while, FOD affected the average peak-to-valley distance and as a consequence increased the LIPSS reflectance. The sensitivity of the implemented setup was judged sufficient to detect even small changes in LIPSS key characteristics. Detected changes were 4% per 100 µm for reflectance measurement for FOD variations and up to 2% per 1 deg for the BIA effects. The proposed method proved to be a very promising solution for inline monitoring/inspection of LIPSS treated surfaces. It would potentially contribute to the process control of the LIPSS fabrication process thus ensuring the quality in process control. It can be paired with commercially available sensors that have measurement time below 1s and sensitivity root mean square below 0.5 nm [237].

IV. For the first time use of artificial intelligence tools into predicting LIPSS functional response was combined together. Areal surface roughness parameters of ultrafast laser structured/textured surfaces were pre- and post-processed, fed into the already known ANN tools and used for prediction of functional responses and for classifying the laser processing parameters. High accuracy could have been achieved in classifying the laser processing disturbances and predicting the wetting properties of LIPSS treated stainless steel surfaces based on their respective areal parameters. It was demonstrated that a small number (from 6 to 8) of areal surface roughness parameters would be sufficient to identify disturbances affecting the LIPSS generation process with 85% accuracy, as well as predicting LIPSS surface contact angle within the measurement uncertainty of 10 deg. The input data, i.e. standardised surface areal parameters, can be obtained with any surface characterisation method or measurement instrument. Thus, using them with ANN tools can be deployed as a solution for monitoring the LIPSS generation and also to judge indirectly about their functional response. This contributes to process control of LIPSS fabrications but offers a direct connection between laser structured topographies and their functional performance. It is worth mentioning that trained ANN is well suited for real time systems because it gives fast responses, potentially within seconds [210].

8.3. Future research

Based on the work presented in the thesis, some directions for further research have been identified, i.e.:

- Investigation of mechanical properties and microstructural modifications of laser-processed DLCs showed that DLC and LIPSS treatments can be considered appropriate for synergistic use for the potential application of producing replication masters that are more durable than conventional uncoated tooling and at the same time functional sub-micron topographies are produced. Further studies should be focused on conducting actual injection moulding tests to assess the replication fidelity and the wear resistance of laser structured DLC treatments and also to measure demoulding forces and see if they are reduced. In this way, quantitative data about the improvements that such a synergistic use of these two surface engineering technologies could offer will be obtained. In addition, the LIPSS treated DLC masters should be analysed to see if the surface cleaning routes between the injection moulding cycles can be reduced and thus to increase both the replication fidelity and throughput.
- The theoretical model presented in Chapter 5 has accounted for variations in beam intensity distribution of each pulse in presence of processing disturbances, i.e. FOD and BIA. Also, the same modelling approach can be utilised for assessing the ablation efficiency achievable in ultrafast laser

machining of complex geometries and thus to optimise the processing parameters. However, the resulting crater profiles after each pulse may need to be considered while modelling the processing conditions.

- The effects of two processing disturbances, i.e. FOD and BIA, on LIPSS generation were considered in modelling the laser structuring of freeform surface and also in validating the proposed in-line monitoring method. The influences of these disturbances were studied separately or simultaneously on flat and inclined samples. However, other factors can affect the LIPSS treatments of complex geometries and therefore they should be considered, too. Specifically, beam positioning errors as a result of some calibration inaccuracies may become more prominent and also some other inconsistencies may occur depending on the type of focusing lenses used, i.e. telecentric or f-theta. So, identifying and studying the influence of those factors on functional performance of LIPSS on freeform surfaces can become essential in modelling the process. Also, if these factors are accounted for, this may bring some further insights into processing conditions when treating freeform surfaces and thus to set with a higher confidence the limits and requirements in executing different surface partitioning strategies.
- The simple setup used to investigate and validate the in-line LIPSS monitoring solution demonstrated its potential for tracking LIPSS changes based on their light diffraction and reflectance characteristics. Thus, the next steps should be focused on designing and implementing a compact sensor for analysing the optical response of LIPSS on both planar and freeform surfaces. The data analysis should include real-time measurement of diffraction angle and

efficiency together with the specular reflection intensity. This would facilitate the better understanding of interdependences between topographical characteristics of the ripples and their functional response, especially when processing disturbances are present. Consequently, the sensitivity of the method would increase significantly and this together with a faster analysis of the acquired data could create the necessary prerequisites for its deployment in laser manufacturing systems. Also, such sensor can offer capabilities for an instant detection of out-of-control conditions in the LIPSS generation process even on complex freeform surfaces.

- The use of ANN tools offered capabilities for mapping the areal surface parameters of LIPSS treated surfaces to their respective functional responses. The approach can be extended onto the creation of a database that can include more materials, e.g. polymers, and thus to link the areal surface parameters of different types of laser surface structures/textures (e.g. hierarchical LIPSS, dimples, trenches, pillars etc.) to their targeted functional property. With the help of ANNs, such data repository could be employed also as a guide for quality assessment, as an inspection tool or just as an aid in developing and implementing laser structuring/texturing technologies for new novel applications.

References

[1] J. Bonse, S. Hohm, S. V. Kirner, A. Rosenfeld, and J. Kruger, “Laser-Induced Periodic Surface Structures-A Scientific Evergreen,” *IEEE J. Sel. Top. Quantum Electron.*, vol. 23, no. 3, pp. 109–123, 2017, doi: 10.1109/JSTQE.2016.2614183.

[2] C. Florian, S. V. Kirner, J. Krüger, and J. Bonse, “Surface functionalization by laser-induced periodic surface structures,” *J. Laser Appl.*, vol. 32, no. 2, p. 022063, 2020, doi: 10.2351/7.0000103.

[3] T. H. Maiman, “Stimulated Optical Radiation in Ruby,” *Nature*, vol. 4736, no. 187, pp. 493–494, 1960.

[4] C. K. N. Patel, “Continuous-Wave Laser Action on Vibrational-Rotational Transitions of CO2,” *Phys. Rev.*, vol. 136, no. 5A, 1964, doi: 10.1103/PhysRev.136.A1187.

[5] A. Javan, W. R. Bennett, and D. R. Herriott, “Population inversion and continuous optical maser oscillation in a gas discharge containing a He-Ne mixture,” *Phys. Rev. Lett.*, vol. 6, no. 3, pp. 106–110, 1961, doi: 10.1103/PhysRevLett.6.106.

[6] J. E. Geusic, H. M. Marcos, and L. G. Van Uitert, “Laser oscillations in nd-doped yttrium aluminum, yttrium gallium and gadolinium garnets,” *Appl. Phys. Lett.*, vol. 4, no. 10, pp. 182–184, 1964, doi: 10.1063/1.1753928.

[7] A. H. Garrido, R. González, M. Cadenas, C. P. Wang, and F. Sadeghi, “Lasers in Surface Engineering,” *Lasers Manuf.*, pp. 247–291, 2013, doi: 10.1002/9781118562857.ch7.

[8] O. Svelto *et al.*, “Lasers and coherent light sources,” *Springer Handb. Lasers Opt.*, pp. 641–1046, 2012, doi: 10.1007/978-3-642-19409-2_11.

[9] J. C. Ion, “Lasers,” in *Laser Processing of Engineering Materials*, Elsevier, 2005, pp. 41–103.

[10] G. Chryssolouris, “Basics of Laser Machining,” in *Laser Machining. Mechanical Engineering Series*, New York: Springer, 1991, pp. 47–91.

[11] A. N. Samant and N. B. Dahotre, “Laser machining of structural ceramics-A review,” *J. Eur. Ceram. Soc.*, vol. 29, no. 6, pp. 969–993, 2009, doi: 10.1016/j.jeurceramsoc.2008.11.010.

[12] R. Le Harzic *et al.*, “Comparison of heat-affected zones due to nanosecond and femtosecond laser pulses using transmission electronic microscopy,” *Appl. Phys. Lett.*, vol. 80, no. 21, 2002, doi: https://doi.org/10.1063/1.1481195.

[13] G. Amoako, “Femtosecond Laser Structuring of Materials: A Review,” *Appl. Phys. Res.*, vol. 11, no. 3, p. 1, 2019, doi: 10.5539/apr.v11n3p1.

[14] W. M. Steen and J. Mazumder, “Background to Laser Design and General Applications,” in *Laser Material Processing*, London: Springer London, 2010, pp. 11–78.

[15] K. Takahashi, M. Tsukamoto, S. Masuno, and Y. Sato, “Heat conduction

analysis of laser CFRP processing with IR and UV laser light," *Compos. Part A Appl. Sci. Manuf.*, vol. 84, pp. 114–122, 2016, doi: 10.1016/j.compositesa.2015.12.009.

[16] A. Gisario, M. Mehrpouya, and E. Pizzi, "Dissimilar joining of transparent Poly(ethylene terephthalate) to aluminum 7075 sheets using a diode laser," *J. Laser Appl.*, vol. 29, no. 2, p. 022418, 2017, doi: 10.2351/1.4983268.

[17] S. Katayama, *Understanding and Improving Process Control in Pulsed and Continuous Wave Laser Welding*, Second Edi. Elsevier Ltd., 2018.

[18] M. S. Brown and C. B. Arnold, "Laser Precision Microfabrication," vol. 135, pp. 91–120, 2010, doi: 10.1007/978-3-642-10523-4.

[19] B. Hüttner, "Femtosecond laser pulse interactions with metals," *Springer Ser. Mater. Sci.*, vol. 119, pp. 341–361, 2017, doi: 10.1007/978-3-319-56711-2_11.

[20] A. Aristeidou *et al.*, "The evolution of corneal and refractive surgery with the femtosecond laser," *Eye Vis.*, vol. 2, no. 1, pp. 1–14, 2015, doi: 10.1186/s40662-015-0022-6.

[21] K. Sugioka, "Hybrid femtosecond laser three-dimensional micro-and nanoprocessing: A review," *Int. J. Extrem. Manuf.*, vol. 1, no. 1, 2019, doi: 10.1088/2631-7990/ab0eda.

[22] K. H. Leitz, B. Redlingshöer, Y. Reg, A. Otto, and M. Schmidt, "Metal ablation with short and ultrashort laser pulses," *Phys. Procedia*, vol. 12, no. PART 2, pp. 230–238, 2011, doi: 10.1016/j.phpro.2011.03.128.

[23] M. M. Mathew, R. N. Bathe, G. Padmanabham, R. Padmanaban, and S. Thirumalini, "A study on the micromachining of molybdenum using nanosecond and femtosecond lasers," *Int. J. Adv. Manuf. Technol.*, vol. 104, no. 9–12, pp. 3239–3249, 2019, doi: 10.1007/s00170-017-1454-z.

[24] R. Weber *et al.*, "Effects of radial and tangential polarization in laser material processing," *Phys. Procedia*, vol. 12, no. PART 1, pp. 21–30, 2011, doi: 10.1016/j.phpro.2011.03.004.

[25] J. C. Ion, "Systems for Material Processing," in *Laser Processing of Engineering Materials*, Elsevier, 2005, pp. 104–138.

[26] A. San-Blas *et al.*, "Femtosecond laser fabrication of LIPSS-based waveplates on metallic surfaces," *Appl. Surf. Sci.*, vol. 520, no. January, p. 146328, 2020, doi: 10.1016/j.apsusc.2020.146328.

[27] S. Zhang, G. Neil, and M. Shinn, "Single-element laser beam shaper for uniform flat-top profiles," *Opt. Express*, vol. 11, no. 16, p. 1942, 2003, doi: 10.1364/oe.11.001942.

[28] H. Qi *et al.*, "Development of high-power laser coatings," *High Power Laser Sci. Eng.*, vol. 1, no. 1, pp. 36–43, 2013, doi: 10.1017/hpl.2013.6.

[29] R.-C. Tyan *et al.*, "Design, fabrication, and characterization of form-birefringent multilayer polarizing beam splitter," *J. Opt. Soc. Am. A*, vol. 14, no. 7, p. 1627, 1997, doi: 10.1364/josaa.14.001627.

[30] Scanlab, "varioSCAN II dynamic and precise laser focussing Brochure," 2021.

https://www.scanlab.de/en/downloads/product-brochures (accessed May 08, 2022).

[31] P. Penchev, S. Dimov, and D. Bhaduri, “Experimental investigation of 3D scanheads for laser micro-processing,” *Opt. Laser Technol.*, vol. 81, pp. 55–59, 2016, doi: 10.1016/j.optlastec.2016.01.035.

[32] B. Jaeggi, B. Neuenschwander, M. Zimmermann, M. Zecherle, and E. W. Boeckler, “Time-optimized laser micro machining by using a new high dynamic and high precision galvo scanner,” *Laser Appl. Microelectron. Optoelectron. Manuf. XXI*, vol. 9735, no. 1, p. 973513, 2016, doi: 10.1117/12.2210791.

[33] R. De Loor, “Polygon scanner system for ultra short pulsed laser micro-machining applications,” *Phys. Procedia*, vol. 41, pp. 544–551, 2013, doi: 10.1016/j.phpro.2013.03.114.

[34] A. Streek and M. Lee, “Ultrafast Material Processing with High-Brightness Fiber Lasers,” *Laser Tech. J.*, vol. 14, no. 4, pp. 22–25, 2017, doi: 10.1002/latj.201700022.

[35] C. Ozga, “Unseen Possibilities of F-Theta Lenses,” *Opt. Photonik*, vol. 13, no. 2, pp. 48–51, 2018, doi: 10.1002/opph.201800015.

[36] D. Bruneel, L. Cangueiro, P. Hervier, X. Bollen, P. Jacques, and J. A. Ramos de Campos, “3D Femtosecond machining and simulation: Ablation of biomedical materials and new advances (Conference Presentation),” in *Laser-based Micro- and Nanoprocessing XIII*, Mar. 2019, p. 25, doi: 10.1117/12.2510139.

[37] R. Schmitt, T. Pfeifer, and G. Mallmann, “Machine integrated telecentric surface metrology in laser structuring systems,” *20th IMEKO World Congr. 2012*, vol. 1, no. 2, pp. 559–563, 2012, doi: 10.21014/acta_imeko.v2i2.106.

[38] S. Rung *et al.*, “Possibilities of Dry and Lubricated Friction Modification Enabled by Different Ultrashort Laser-Based Surface Structuring Methods,” 2019, doi: 10.3390/lubricants7050043.

[39] M. Birnbaum, “Semiconductor surface damage produced by Ruby lasers,” *J. Appl. Phys.*, vol. 36, no. 11, pp. 3688–3689, 1965, doi: 10.1063/1.1703071.

[40] P. Gecys, A. Vinciunas, M. Gedvilas, A. Kasparaitis, R. Lazdinas, and G. Raciukaitis, “Ripple Formation by Femtosecond Laser Pulses for Enhanced Absorptance of Stainless Steel,” *JLMN-Journal of Laser Micro/Nanoengineering*, vol. 10, no. 2, pp. 124–128, 2015, doi: 10.2961/jlmn.2015.0.

[41] J. G. A. B. Simões, R. Riva, and W. Miyakawa, “High-speed Laser-Induced Periodic Surface Structures (LIPSS) generation on stainless steel surface using a nanosecond pulsed laser,” *Surf. Coat. Technol.*, vol. 344, no. March, pp. 423–432, 2018, doi: 10.1016/j.surfcoat.2018.03.052.

[42] M. Mozetic, “Surface Modification to Improve Properties of Materials,” *Materials (Basel).*, vol. 12, no. 441, 2019, doi: 10.3390/ma12030441.

[43] J. Gspann, “Microstructuring by nanoparticle impact lithography,” *Sensors Actuators A Phys.*, vol. 51, no. 1, pp. 37–39, 1995, doi:

https://doi.org/10.1016/0924-4247(95)01067-X.

[44] Y. Su *et al.*, “Bioinspired surface functionalization of metallic biomaterials,” *J. Mech. Behav. Biomed. Mater.*, vol. 77, no. January 2017, pp. 90–105, 2018, doi: 10.1016/j.jmbbm.2017.08.035.

[45] S. Maragkaki, C. A. Skaradzinski, R. Nett, and E. L. Gurevich, “Influence of defects on structural colours generated by laser-induced ripples,” *Sci. Rep.*, vol. 10, no. 1, pp. 1–9, 2020, doi: 10.1038/s41598-019-56638-x.

[46] J. Li *et al.*, “Selective display of multiple patterns encoded with different oriented ripples using femtosecond laser,” *Opt. Laser Technol.*, vol. 71, pp. 85–88, 2015, doi: 10.1016/j.optlastec.2015.02.014.

[47] B. Dusser *et al.*, “Controlled nanostructrures formation by ultra fast laser pulses for color marking,” *Opt. Express*, vol. 18, no. 3, p. 2913, 2010, doi: 10.1364/OE.18.002913.

[48] M. H. Dar, R. Kuladeep, V. Saikiran, and N. D. Rao, “Femtosecond laser nanostructuring of titanium metal towards fabrication of low-reflective surfaces over broad wavelength range,” *Appl. Surf. Sci.*, vol. 371, pp. 479–487, 2016, doi: 10.1016/j.apsusc.2016.03.008.

[49] A. Dostovalov *et al.*, “Hierarchical anti-reflective laser-induced periodic surface structures (LIPSSs) on amorphous Si films for sensing applications,” *Nanoscale*, vol. 12, no. 25, pp. 13431–13441, 2020, doi: 10.1039/d0nr02182b.

[50] A. Y. Vorobyev and C. Guo, “Enhanced absorptance of gold following multipulse femtosecond laser ablation,” *Phys. Rev. B - Condens. Matter Mater. Phys.*, vol. 72, no. 19, pp. 1–5, 2005, doi: 10.1103/PhysRevB.72.195422.

[51] V. Parmar and Y. C. Shin, “Wideband anti-reflective silicon surface structures fabricated by femtosecond laser texturing,” *Appl. Surf. Sci.*, vol. 459, no. April, pp. 86–91, 2018, doi: 10.1016/j.apsusc.2018.07.189.

[52] C. Kunz *et al.*, “Tribological performance of metal-reinforced ceramic composites selectively structured with femtosecond laser-induced periodic surface structures,” *Appl. Surf. Sci.*, vol. 499, no. July 2019, p. 143917, 2020, doi: 10.1016/j.apsusc.2019.143917.

[53] J. Bonse *et al.*, “Femtosecond laser-induced periodic surface structures on steel and titanium alloy for tribological applications,” *Appl. Phys. A Mater. Sci. Process.*, vol. 117, no. 1, pp. 103–110, 2014, doi: 10.1007/s00339-014-8229-2.

[54] J. Bonse *et al.*, “Tribological performance of femtosecond laser-induced periodic surface structures on titanium and a high toughness bearing steel,” *Appl. Surf. Sci.*, vol. 336, pp. 21–27, 2015, doi: 10.1016/j.apsusc.2014.08.111.

[55] J. Schille *et al.*, “High-Rate laser surface texturing for advanced tribological functionality,” *Lubricants*, vol. 8, no. 3, pp. 1–20, 2020, doi: 10.3390/lubricants8030033.

[56] J. Bonse, S. V. Kirner, M. Griepentrog, D. Spaltmann, and J. Krüger, “Femtosecond laser texturing of surfaces for tribological applications,” *Materials (Basel).*, vol. 11, no. 5, pp. 1–19, 2018, doi: 10.3390/ma11050801.

[57] S. A. Jalil *et al.*, “Creating superhydrophobic and antibacterial surfaces on gold by femtosecond laser pulses,” *Appl. Surf. Sci.*, vol. 506, no. October 2019, pp. 0–6, 2020, doi: 10.1016/j.apsusc.2019.144952.

[58] N. Epperlein *et al.*, “Influence of femtosecond laser produced nanostructures on biofilm growth on steel,” *Appl. Surf. Sci.*, vol. 418, pp. 420–424, 2017, doi: 10.1016/j.apsusc.2017.02.174.

[59] A. Cunha *et al.*, “Femtosecond laser surface texturing of titanium as a method to reduce the adhesion of Staphylococcus aureus and biofilm formation,” *Appl. Surf. Sci.*, vol. 360, pp. 485–493, 2016, doi: 10.1016/j.apsusc.2015.10.102.

[60] E. Rebollar *et al.*, “Proliferation of aligned mammalian cells on laser-nanostructured polystyrene,” *Biomaterials*, vol. 29, no. 12, pp. 1796–1806, 2008, doi: 10.1016/j.biomaterials.2007.12.039.

[61] A. Batal, R. Sammons, and S. Dimov, “Response of Saos-2 osteoblast-like cells to laser surface texturing, sandblasting and hydroxyapatite coating on CoCrMo alloy surfaces,” *Mater. Sci. Eng. C*, vol. 98, no. May 2018, pp. 1005–1013, 2019, doi: 10.1016/j.msec.2019.01.067.

[62] C. Sciancalepore, L. Gemini, L. Romoli, and F. Bondioli, “Study of the wettability behavior of stainless steel surfaces after ultrafast laser texturing,” *Surf. Coatings Technol.*, vol. 352, no. April, pp. 370–377, 2018, doi: 10.1016/j.surfcoat.2018.08.030.

[63] C. Florian *et al.*, “Controlling the Wettability of Steel Surfaces Processed with Femtosecond Laser Pulses,” *ACS Appl. Mater. Interfaces*, vol. 10, no. 42, pp. 36564–36571, 2018, doi: 10.1021/acsami.8b13908.

[64] S. V. Kirner *et al.*, “Mimicking bug-like surface structures and their fluid transport produced by ultrashort laser pulse irradiation of steel,” *Appl. Phys. A Mater. Sci. Process.*, vol. 123, no. 12, pp. 1–13, 2017, doi: 10.1007/s00339-017-1317-3.

[65] R. Buividas, P. R. Stoddart, and S. Juodkazis, “Laser fabricated ripple substrates for surface-enhanced Raman scattering,” *Ann. Phys.*, vol. 524, no. 11, pp. 5–10, 2012, doi: 10.1002/andp.201200140.

[66] H. W. Chang, Y. C. Tsai, C. W. Cheng, C. Y. Lin, Y. W. Lin, and T. M. Wu, “Nanostructured Ag surface fabricated by femtosecond laser for surface-enhanced Raman scattering,” *J. Colloid Interface Sci.*, vol. 360, no. 1, pp. 305–308, 2011, doi: 10.1016/j.jcis.2011.04.005.

[67] S. Gräf, C. Kunz, A. Undisz, R. Wonneberger, M. Rettenmayr, and F. A. Müller, “Mechano-responsive colour change of laser-induced periodic surface structures,” *Appl. Surf. Sci.*, vol. 471, no. December 2018, pp. 645–651, 2019, doi: 10.1016/j.apsusc.2018.12.051.

[68] K. Lange, M. Schulz-Ruhtenberg, and J. Caro, “Platinum Electrodes for Oxygen Reduction Catalysis Designed by Ultrashort Pulse Laser Structuring,” *ChemElectroChem*, vol. 4, no. 3, pp. 570–576, 2017, doi: 10.1002/celc.201600630.

[69] C. Huang, R. Bell, A. Tsubaki, C. A. Zuhlke, and D. R. Alexander,

“Condensation and subsequent freezing delays as a result of using femtosecond laser functionalized surfaces,” *J. Laser Appl.*, vol. 30, no. 1, p. 011501, 2018, doi: 10.2351/1.4986058.

[70] P. A. Sørensen, S. Kiil, K. Dam-Johansen, and C. E. Weinell, “Anticorrosive coatings: A review,” *J. Coatings Technol. Res.*, vol. 6, no. 2, pp. 135–176, 2009, doi: 10.1007/s11998-008-9144-2.

[71] M. Lindenmo, A. Coombs, and D. Snell, “Advantages, properties and types of coatings on non-oriented electrical steels,” *J. Magn. Magn. Mater.*, vol. 215, pp. 79–82, 2000, doi: 10.1016/S0304-8853(00)00071-8.

[72] N. M. Renevier, J. Hamphire, V. C. Fox, J. Witts, T. Allen, and D. G. Teer, “Advantages of using self-lubricating, hard, wear-resistant MoS2-based coatings,” *Surf. Coatings Technol.*, vol. 142–144, pp. 67–77, 2001, doi: 10.1016/S0257-8972(01)01108-2.

[73] N. Yasumaru, K. Miyazaki, and J. Kiuchi, “Control of tribological properties of diamond-like carbon films with femtosecond-laser-induced nanostructuring,” *Appl. Surf. Sci.*, vol. 254, pp. 2364–2368, 2008, doi: 10.1016/j.apsusc.2007.09.037.

[74] A. Talbi *et al.*, “Femtosecond laser irradiation of titanium oxide thin films: accumulation effect under IR beam,” *Appl. Phys. A Mater. Sci. Process.*, vol. 126, no. 5, pp. 1–9, 2020, doi: 10.1007/s00339-020-03568-5.

[75] A. Rodríguez, M. C. Morant-Miñana, A. Dias-Ponte, M. Martínez-Calderón, M. Gómez-Aranzadi, and S. M. Olaizola, “Femtosecond laser-induced periodic surface nanostructuring of sputtered platinum thin films,” *Appl. Surf. Sci.*, vol. 351, pp. 135–139, 2015, doi: 10.1016/j.apsusc.2015.05.117.

[76] Y. Xing, Z. Wu, J. Yang, X. Wang, and L. Liu, “LIPSS combined with ALD MoS2 nano-coatings for enhancing surface friction and hydrophobic performances,” *Surf. Coatings Technol.*, vol. 385, no. October 2019, 2020, doi: 10.1016/j.surfcoat.2020.125396.

[77] J. Bonse, S. V. Kirner, R. Koter, S. Pentzien, D. Spaltmann, and J. Krüger, “Femtosecond laser-induced periodic surface structures on titanium nitride coatings for tribological applications,” *Appl. Surf. Sci.*, vol. 418, pp. 572–579, 2017, doi: 10.1016/j.apsusc.2016.10.132.

[78] R. B. Jackman and L. H. Chua, “Diamond-like carbon within microelectronics: Dielectric properties on silicon and GaAs,” *Diam. Relat. Mater.*, vol. 1, no. 8, pp. 895–899, 1992, doi: 10.1016/0925-9635(92)90131-7.

[79] T. Roch, V. Weihnacht, H. J. Scheibe, A. Roch, and A. F. Lasagni, “Direct Laser Interference Patterning of tetrahedral amorphous carbon films for tribological applications,” *Diam. Relat. Mater.*, vol. 33, pp. 20–26, 2013, doi: 10.1016/j.diamond.2012.12.002.

[80] B. Saha, E. Liu, S. B. Tor, N. W. Khun, D. E. Hardt, and J. H. Chun, “Anti-sticking behavior of DLC-coated silicon micro-molds,” *J. Micromechanics Microengineering*, vol. 19, no. 10, 2009, doi: 10.1088/0960-1317/19/10/105025.

[81] K. Czyz *et al.*, “Selected laser methods for surface structuring of biocompatible

diamond-like carbon layers,” *Diam. Relat. Mater.*, vol. 67, pp. 26–40, 2016, doi: 10.1016/j.diamond.2016.01.013.

[82] A. C. Ferrari and J. Robertson, “Interpretation of Raman spectra of disordered and amorphous carbon,” *Phys. Rev. B*, vol. 61, no. 20, pp. 95–107, 2000.

[83] S. F. Ahmed, M. W. Moon, and K. R. Lee, “Effect of silver doping on optical property of diamond like carbon films,” *Thin Solid Films*, vol. 517, no. 14, pp. 4035–4038, 2009, doi: 10.1016/j.tsf.2009.01.135.

[84] D. R. Tallant, J. E. Parmeter, M. P. Siegal, and R. L. Simpson, “The thermal stability of diamond-like carbon,” *Diam. Relat. Mater.*, vol. 4, no. 3, pp. 191–199, 1995, doi: 10.1016/0925-9635(94)00243-6.

[85] L. C. Nistor, J. Van Landuyt, V. G. Ralchenko, T. V. Kononenko, E. D. Obraztsova, and V. E. Strelnitsky, “Direct observation of laser-induced crystallization of a-C:H films,” *Appl. Phys. A Solids Surfaces*, vol. 58, no. 2, pp. 137–144, 1994, doi: 10.1007/BF00332170.

[86] T. V. Kononenko *et al.*, “Laser-induced spallation in diamond-like carbon films,” *Appl. Phys. A Mater. Sci. Process.*, vol. 79, no. 3, pp. 543–549, 2004, doi: 10.1007/s00339-003-2356-5.

[87] M. Pfeiffer *et al.*, “Ripple formation in various metals and super-hard tetrahedral amorphous carbon films in consequence of femtosecond laser irradiation,” *Appl. Phys. A Mater. Sci. Process.*, vol. 110, no. 3, pp. 655–659, 2013, doi: 10.1007/s00339-012-7146-5.

[88] L. Marcinauskas, A. Grigonis, G. Račiukaitis, M. Gedvilas, and V. Vinciunaite, “Irradiation of the amorphous carbon films by picosecond laser pulses,” *Thin Solid Films*, vol. 593, pp. 116–123, 2015, doi: 10.1016/j.tsf.2015.09.045.

[89] G. Miyaji and K. Miyazaki, “Origin of periodicity in nanostructuring on thin film surfaces ablated with femtosecond laser pulses,” *Opt. Express*, vol. 16, no. 20, p. 16265, 2008, doi: 10.1364/oe.16.016265.

[90] K. Miyazaki, N. Maekawa, W. Kobayashi, M. Kaku, N. Yasumaru, and J. Kiuchi, “Reflectivity in femtosecond-laser-induced structural changes of diamond-like carbon film,” *Appl. Phys. A Mater. Sci. Process.*, vol. 80, no. 1, pp. 17–21, 2005, doi: 10.1007/s00339-004-3008-0.

[91] G. Dumitru *et al.*, “Femtosecond laser ablation of diamond-like carbon films,” *Appl. Surf. Sci.*, vol. 222, no. 1–4, pp. 226–233, 2004, doi: 10.1016/j.apsusc.2003.08.031.

[92] E. V. Zavedeev *et al.*, “Femtosecond laser microstructuring of diamond-like nanocomposite films,” *Diam. Relat. Mater.*, vol. 74, pp. 45–52, 2017, doi: 10.1016/j.diamond.2017.02.003.

[93] N. Yasumaru, K. Miyazaki, and J. Kiuchi, “Glassy carbon layer formed in diamond-like carbon films with femtosecond laser pulses,” *Appl. Phys. A Mater. Sci. Process.*, vol. 79, no. 3, pp. 425–427, 2004, doi: 10.1007/s00339-004-2746-3.

[94] C. A. Griffiths *et al.*, “A novel texturing of micro injection moulding tools by applying an amorphous hydrogenated carbon coating,” *Surf. Coatings*

Technol., vol. 235, pp. 1–9, Nov. 2013, doi: 10.1016/j.surfcoat.2013.07.006.

[95] C. A. Griffiths, S. S. Dimov, E. B. Brousseau, C. Chouquet, J. Gavillet, and S. Bigot, “Investigation of surface treatment effects in micro-injection-moulding,” *Int. J. Adv. Manuf. Technol.*, vol. 47, no. 1–4, pp. 99–110, 2010, doi: 10.1007/s00170-009-2000-4.

[96] J. Bonse and S. Gräf, “Ten open questions about laser-induced periodic surface structures,” *Nanomaterials*, vol. 11, no. 12, pp. 1–21, 2021, doi: 10.3390/nano11123326.

[97] M. Csete, S. Hild, A. Plettl, P. Ziemann, Z. Bor, and O. Marti, “The role of original surface roughness in laser-induced periodic surface structure formation process on poly-carbonate films,” *Thin Solid Films*, vol. 453–454, pp. 114–120, 2004, doi: 10.1016/j.tsf.2003.11.086.

[98] M. Ardron, N. Weston, and D. Hand, “A practical technique for the generation of highly uniform LIPSS,” *Appl. Surf. Sci.*, vol. 313, pp. 123–131, 2014, doi: 10.1016/j.apsusc.2014.05.154.

[99] B. Bachy, R. Süß-Wolf, T. Kordass, and J. Franke, “Simulation and experimental investigation for the 2D and 3D laser direct structuring process,” *Int. J. Adv. Manuf. Technol.*, vol. 89, no. 5–8, pp. 1591–1602, 2017, doi: 10.1007/s00170-016-9173-4.

[100] L. Overmeyer, J. F. Duesing, O. Suttmann, and U. Stute, “Laser patterning of thin film sensors on 3-D surfaces,” *CIRP Ann. - Manuf. Technol.*, vol. 61, no. 1, pp. 215–218, 2012, doi: 10.1016/j.cirp.2012.03.087.

[101] J. F. Young, J. S. Preston, H. M. Van Driel, and J. E. Sipe, “Laser-induced periodic surface structure. II. Experiments on Ge, Si, Al, and brass,” *Phys. Rev. B*, vol. 27, no. 2, pp. 1155–1172, 1983, doi: 10.1103/PhysRevB.27.1155.

[102] Y. Fuentes-Edfuf *et al.*, “Tuning the period of femtosecond laser induced surface structures in steel: From angled incidence to quill writing,” *Appl. Surf. Sci.*, vol. 493, pp. 948–955, Nov. 2019, doi: 10.1016/j.apsusc.2019.07.106.

[103] Y. Liu, K. Kuo, and C. Cheng, “Femtosecond Laser-Induced Periodic Surface Structures on Different Tilted Metal Surfaces,” *Nanomaterials*, 2020, doi: 10.3390/nano10122540.

[104] T. Y. Hwang and C. Guo, “Angular effects of nanostructure-covered femtosecond laser induced periodic surface structures on metals,” *J. Appl. Phys.*, vol. 108, no. 4, pp. 354–359, 2010, doi: 10.1109/23.256579.

[105] T. Y. Hwang and C. Guo, “Femtosecond laser-induced blazed periodic grooves on metals,” vol. 36, no. 13, pp. 2575–2577, 2011.

[106] E. Kochkina, G. Wanner, D. Schmelzer, M. Tröbs, and G. Heinzel, “Modeling of the general astigmatic Gaussian beam and its propagation through 3D optical systems,” *Appl. Opt.*, vol. 52, no. 24, pp. 6030–6040, 2013, doi: 10.1364/AO.52.006030.

[107] M. Mezera and G. R. B. E. Römer, “Laser-induced periodic surface structures (LIPSS) manufacturing by defocused laser processing,” in *Proc. SPIE 10906, Laser-based Micro- and Nanoprocessing XIII*, 2019, doi:

https://doi.org/10.1117/12.2510004.

[108] U. Hermens, M. Pothen, K. Winands, K. Arntz, and F. Klocke, “Automated polarization control for the precise alignment of laser-induced self-organized nanostructures,” *Opt. Lasers Eng.*, vol. 101, no. September 2017, pp. 44–50, 2018, doi: 10.1016/j.optlaseng.2017.10.001.

[109] Z. H. W. Ang and Z. H. Y. Ao, “Functionalization of freeform curved surfaces by shaped femtosecond laser pulses in the propagation axis,” *Opt. Express*, vol. 29, no. 4, pp. 5487–5496, 2021.

[110] J. Bonse and S. Gräf, “Maxwell Meets Marangoni—A Review of Theories on Laser-Induced Periodic Surface Structures,” *Laser Photonics Rev.*, vol. 14, no. 10, pp. 1–25, 2020, doi: 10.1002/lpor.202000215.

[111] M. Mezera and G. R. B. E. Römer, “Model based optimization of process parameters to produce large homogeneous areas of laser-induced periodic surface structures,” *Opt. Express*, vol. 27, no. 5, p. 6012, 2019, doi: 10.1364/oe.27.006012.

[112] J. Eichstädt, G. R. B. E. Römer, and A. J. Huis In ’T Veld, “Determination of irradiation parameters for laser-induced periodic surface structures,” *Appl. Surf. Sci.*, vol. 264, pp. 79–87, 2013, doi: 10.1016/j.apsusc.2012.09.120.

[113] O. Varlamova and J. Reif, “Evolution of femtosecond laser induced surface structures at low number of pulses near the ablation threshold,” *J. Laser Micro Nanoeng.*, vol. 8, no. 3, pp. 300–303, 2013, doi: 10.2961/jlmn.2013.03.0019.

[114] I. Gnilitskyi, T. J. Y. Derrien, Y. Levy, N. M. Bulgakova, T. Mocek, and L. Orazi, “High-speed manufacturing of highly regular femtosecond laser-induced periodic surface structures: Physical origin of regularity,” *Sci. Rep.*, vol. 7, no. 1, pp. 1–11, 2017, doi: 10.1038/s41598-017-08788-z.

[115] J. E. Sipe, J. F. Young, J. S. Preston, and H. M. Van Driel, “Laser induced periodic surface structures. I. Theory,” *Phys. Rev. B*, vol. 96–98, no. 2, pp. 410–414, 1983, doi: 10.1016/0169-4332(95)00495-5.

[116] J. Bonse, M. Munz, and H. Sturm, “Structure formation on the surface of indium phosphide irradiated by femtosecond laser pulses,” *J. Appl. Phys.*, vol. 97, no. 1, 2005, doi: 10.1063/1.1827919.

[117] D. Dufft, A. Rosenfeld, S. K. Das, R. Grunwald, and J. Bonse, “Femtosecond laser-induced periodic surface structures revisited: A comparative study on ZnO,” *J. Appl. Phys.*, vol. 105, no. 3, 2009, doi: 10.1063/1.3074106.

[118] J. Z. P. Skolski, G. R. B. E. Römer, J. V. Obona, V. Ocelik, A. J. Huis In ’t Veld, and J. T. M. De Hosson, “Laser-induced periodic surface structures: Fingerprints of light localization,” *Phys. Rev. B - Condens. Matter Mater. Phys.*, vol. 85, no. 7, pp. 1–9, 2012, doi: 10.1103/PhysRevB.85.075320.

[119] J.-L. Déziel, J. Dumont, D. Gagnon, L. J. Dubé, S. H. Messaddeq, and Y. Messaddeq, “Constructive feedback for the growth of laser-induced periodic surface structures,” *Phys. status solidi*, vol. 13, no. 2–3, pp. 121–124, Mar. 2016, doi: 10.1002/pssc.201510146.

[120] J. Liang, W. Liu, Y. Li, Z. Luo, and D. Pang, “A model to predict the ablation

width and calculate the ablation threshold of femtosecond laser," *Appl. Surf. Sci.*, vol. 456, no. June, pp. 482–486, 2018, doi: 10.1016/j.apsusc.2018.06.093.

[121] L. Cangueiro *et al.*, "Model for ultrafast laser micromachining," vol. 1052010, no. February, p. 38, 2018, doi: 10.1117/12.2286250.

[122] A. Žemaitis, M. Gaidys, M. Brikas, P. Gečys, G. Račiukaitis, and M. Gedvilas, "Advanced laser scanning for highly-efficient ablation and ultrafast surface structuring: experiment and model," *Sci. Rep.*, vol. 8, no. 1, Dec. 2018, doi: 10.1038/s41598-018-35604-z.

[123] J. Lehr and A. Kietzig, "Production of homogenous micro-structures by femtosecond laser micro-machining," *Opt. Lasers Eng.*, vol. 57, pp. 121–129, 2014, doi: 10.1016/j.optlaseng.2014.01.012.

[124] A. Aguilar, C. Mauclair, N. Faure, J. P. Colombier, and R. Stoian, "In-situ high-resolution visualization of laser-induced periodic nanostructures driven by optical feedback," *Sci. Rep.*, vol. 7, no. 1, pp. 1–10, 2017, doi: 10.1038/s41598-017-16646-1.

[125] X. Wang, J. Duan, M. Jiang, S. Ke, B. Wu, and X. Zeng, "Study of laser precision ablating texture patterns on large-scale freeform surface," *Int. J. Adv. Manuf. Technol.*, vol. 92, no. 9–12, pp. 4571–4581, 2017, doi: 10.1007/s00170-017-0413-z.

[126] A. Batal, A. Michalek, P. Penchev, A. Kupisiewicz, and S. Dimov, "Laser processing of freeform surfaces: A new approach based on an efficient workpiece partitioning strategy," *Int. J. Mach. Tools Manuf.*, p. 103593, 2020, doi: 10.1016/j.ijmachtools.2020.103593.

[127] T. Purtonen, A. Kalliosaari, and A. Salminen, "Monitoring and adaptive control of laser processes," *Phys. Procedia*, vol. 56, no. C, pp. 1218–1231, 2014, doi: 10.1016/j.phpro.2014.08.038.

[128] E. Rebollar *et al.*, "In situ monitoring of laser-induced periodic surface structures formation on polymer films by grazing incidence small-angle X-ray scattering," *Langmuir*, vol. 31, no. 13, pp. 3973–3981, 2015, doi: 10.1021/acs.langmuir.5b00285.

[129] A. Lübcke, Z. Pápa, and M. Schnürer, "Monitoring of evolving laser induced periodic surface structures," *Appl. Sci.*, vol. 9, no. 17, 2019, doi: 10.3390/app9173636.

[130] M. Kreuzer, G. L. Whitworth, A. Francone, J. Gomis-Bresco, N. Kehagias, and C. M. Sotomayor-Torres, "In-line metrology for roll-to-roll UV assisted nanoimprint lithography using diffractometry," *APL Mater.*, vol. 6, no. 5, 2018, doi: 10.1063/1.5011740.

[131] S. Teutoburg-Weiss, B. Voisiat, M. Soldera, and A. F. Lasagni, "Development of a monitoring strategy for laser-textured metallic surfaces using a diffractive approach," *Materials (Basel).*, vol. 13, no. 1, 2020, doi: 10.3390/ma13010053.

[132] Y. Kotsiuba, I. Hevko, S. Bellucci, and I. Gnilitskyi, "Bitmap and vectorial hologram recording by using femtosecond laser pulses," *Sci. Rep.*, vol. 11, no.

1, pp. 1–8, 2021, doi: 10.1038/s41598-021-95665-5.

[133] T. Y. Hwang, Y. D. Kim, J. Cho, H. J. Lee, H. S. Lee, and B. Lee, “Multi-angular colorimetric responses of uni-and omni-directional femtosecond laser-induced periodic surface structures on metals,” *Nanomaterials*, vol. 11, no. 8, 2021, doi: 10.3390/nano11082010.

[134] C. Alleaume, S. Alamri, T. Kunze, J. Ziegler, A. Wilson, and R. Bola, “Scatterometry and diffractometry techniques to monitor surfaces textured by rapid ultra-short pulse laser,” *JPhys Photonics*, vol. 2, no. 3, 2020, doi: 10.1088/2515-7647/ab92b0.

[135] M. R. G. Meireles, P. E. M. Almeida, and M. G. Simões, “A comprehensive review for industrial applicability of artificial neural networks,” *IEEE Trans. Ind. Electron.*, vol. 50, no. 3, pp. 585–601, 2003, doi: 10.1109/TIE.2003.812470.

[136] H. Luo, H. Zeng, L. Hu, X. Hu, and Z. Zhou, “Application of artificial neural network in laser welding defect diagnosis,” *J. Mater. Process. Technol.*, vol. 170, no. 1–2, pp. 403–411, 2005, doi: 10.1016/j.jmatprotec.2005.06.008.

[137] C. Gonzalez-Val, A. Pallas, V. Panadeiro, and A. Rodriguez, “A convolutional approach to quality monitoring for laser manufacturing,” *J. Intell. Manuf.*, vol. 31, no. 3, pp. 789–795, 2020, doi: 10.1007/s10845-019-01495-8.

[138] D. J. Heath *et al.*, “Machine learning for 3D simulated visualization of laser machining,” *Opt. Express*, vol. 26, no. 17, p. 21574, 2018, doi: 10.1364/oe.26.021574.

[139] M. D. T. McDonnell *et al.*, “Machine learning for multi-dimensional optimisation and predictive visualisation of laser machining,” *J. Intell. Manuf.*, 2021, doi: 10.1007/s10845-020-01717-4.

[140] S. K. Dhara, A. S. Kuar, and S. Mitra, “An artificial neural network approach on parametric optimization of laser micro-machining of die-steel,” *Int. J. Adv. Manuf. Technol.*, vol. 39, no. 1–2, pp. 39–46, 2008, doi: 10.1007/s00170-007-1199-1.

[141] M. M. Noor, K. Kadirgama, M. M. Rahman, R. A. Bakar, and C. H. C. Haron, “Response Surface Method and Neural Network to Determine Surface Roughness for Laser Cutting on Acrylic Sheets,” 2009.

[142] M. M. Noor, K. Kadirgama, M. R. M. Rejab, M. M. Rahman, R. A. Bakar, and H. Ismail, “Artificial Intelligent Model to Predict Surface Roughness in Laser Machining,” in *International Conference on Recent Advances in Materials, Minerals & Environment*, 2009.

[143] K. M. Tanvir Ahmmed, C. Grambow, and A. M. Kietzig, “Fabrication of micro/nano structures on metals by femtosecond laser micromachining,” *Micromachines*, vol. 5, no. 4, pp. 1219–1253, 2014, doi: 10.3390/mi5041219.

[144] T. Jwad, P. Penchev, V. Nasrollahi, and S. Dimov, “Laser induced ripples’ gratings with angular periodicity for fabrication of diffraction holograms,” *Appl. Surf. Sci.*, vol. 453, pp. 449–456, 2018, doi: 10.1016/j.apsusc.2018.04.277.

[145] J. Robertson, “Diamond-like amorphous carbon,” *Mater. Sci. Eng. R Reports*, vol. 37, no. 4–6, pp. 129–281, 2002, doi: 10.1016/S0927-796X(02)00005-0.

[146] A. C. Ferrari, “Diamond-like carbon for magnetic storage disks,” *Surf. Coatings Technol.*, vol. 180–181, pp. 190–206, 2004, doi: 10.1016/j.surfcoat.2003.10.146.

[147] C. A. Griffiths, A. Rees, R. M. Kerton, and O. V. Fonseca, “Temperature effects on DLC coated micro moulds,” *Surf. Coatings Technol.*, vol. 307, pp. 28–37, 2016, doi: 10.1016/j.surfcoat.2016.08.034.

[148] N. Yasumaru, K. Miyazaki, J. Kiuchi, and K. Komai, “Tribological Properties of Diamond-Like Carbon Films with Surface Nano-Structure Formed by Femtosecond Laser Pulses,” *J. Laser Micro Nanoeng.*, vol. 2, no. 2, pp. 162–165, 2007, doi: 10.2961/jlmn.2007.02.0011.

[149] N. Yasumaru, K. Miyazaki, J. Kiuchi, and E. Sentoku, “Frictional properties of diamond-like carbon, glassy carbon and nitrides with femtosecond-laser-induced nanostructure,” *Diam. Relat. Mater.*, vol. 20, no. 4, pp. 542–545, 2011, doi: 10.1016/j.diamond.2011.02.010.

[150] A. M. Prokhorov, A. S. Svakhin, V. A. Sychugov, A. V Tischenko, and A. A. Khakimov, “Excitation and resonant transformation of a surface electromagnetic wave during irradiation of a solid by high-power laser radiation,” *Sov. J. Quantum Electron.*, vol. 13, no. 568, 1983.

[151] S. Gräf and F. A. Müller, “Polarisation-dependent generation of fs-laser induced periodic surface structures,” *Appl. Surf. Sci.*, vol. 331, pp. 150–155, 2015, doi: 10.1016/j.apsusc.2015.01.056.

[152] T. V Kononenko *et al.*, “Effects of pulse duration in laser processing of diamond-like carbon films,” *Diam. Relat. Mater.*, vol. 14, no. 8, pp. 1368–1376, 2005, doi: 10.1016/j.diamond.2005.02.009.

[153] A. Dekanski, J. Stevanovic, R. Stevanovic, B. Z. Nikolic, and V. M. Jovanovic, “Glassy carbon electrodes I. Characterization and electrochemical activation,” *Carbon N. Y.*, vol. 39, no. 1, pp. 1195–1205, 2001, doi: 10.1016/0008-6223(94)90011-6.

[154] P. Gregorčič, M. Sedlaček, B. Podgornik, and J. Reif, “Formation of laser-induced periodic surface structures (LIPSS) on tool steel by multiple picosecond laser pulses of different polarizations,” *Appl. Surf. Sci.*, vol. 387, pp. 698–706, 2016, doi: 10.1016/j.apsusc.2016.06.174.

[155] M. S. Komlenok *et al.*, “Structure and friction properties of laser-patterned amorphous carbon films,” *Diam. Relat. Mater.*, vol. 65, pp. 69–74, 2016, doi: 10.1016/j.diamond.2016.02.006.

[156] H. O. Jeschke, M. E. Garcia, and K. H. Bennemann, “Theory for laser-induced ultrafast phase transitions in carbon,” *Appl. Phys. A Mater. Sci. Process.*, vol. 69, no. 7, 1999, doi: 10.1007/s003399900340.

[157] C. Z. Wang, K. M. Ho, M. D. Shirk, and P. A. Molian, “Laser-induced graphitization on a diamond (111) surface,” *Phys. Rev. Lett.*, vol. 85, no. 19, pp. 4092–4095, 2000, doi: 10.1103/PhysRevLett.85.4092.

[158] J. Csontos, Z. Pápa, A. Gárdián, M. Füle, J. Budai, and Z. Toth, “Spectroscopic ellipsometric and Raman spectroscopic investigations of pulsed laser treated

glassy carbon surfaces," *Appl. Surf. Sci.*, vol. 336, pp. 343–348, 2015, doi: 10.1016/j.apsusc.2014.12.133.

[159] H. Pang, X. Wang, G. Zhang, H. Chen, G. Lv, and S. Yang, "Characterization of diamond-like carbon films by SEM, XRD and Raman spectroscopy," *Appl. Surf. Sci.*, vol. 256, no. 21, pp. 6403–6407, 2010, doi: 10.1016/j.apsusc.2010.04.025.

[160] M. Hokao, S. Hironaka, Y. Suda, and Y. Yamamoto, "Friction and wear properties of graphite/glassy carbon composites," *Wear*, vol. 237, no. 1, pp. 54–62, 2000, doi: 10.1016/S0043-1648(99)00306-3.

[161] R. G. Budynas and K. Nisbeth, *Shigley's Mechanical Engineering Design*, 9th ed. NY: McGraw-Hill, 2011.

[162] V. Bellantone, R. Surace, G. Trotta, and I. Fassi, "Replication capability of micro injection moulding process for polymeric parts manufacturing," *Int. J. Adv. Manuf. Technol.*, vol. 67, no. 5–8, pp. 1407–1421, 2013, doi: 10.1007/s00170-012-4577-2.

[163] S. Höhm, A. Rosenfeld, J. Krüger, and J. Bonse, "Laser-induced periodic surface structures on titanium upon single- and two-color femtosecond double-pulse irradiation," *Opt. Express*, vol. 23, no. 20, p. 25959, 2015, doi: 10.1364/oe.23.025959.

[164] K. Okamuro, M. Hashida, Y. Miyasaka, Y. Ikuta, S. Tokita, and S. Sakabe, "Laser fluence dependence of periodic grating structures formed on metal surfaces under femtosecond laser pulse irradiation," *Phys. Rev. B - Condens. Matter Mater. Phys.*, vol. 82, no. 16, pp. 1–5, 2010, doi: 10.1103/PhysRevB.82.165417.

[165] G. Li *et al.*, "Evolution of aluminum surface irradiated by femtosecond laser pulses with different pulse overlaps," *Appl. Surf. Sci.*, vol. 276, pp. 203–209, 2013, doi: 10.1016/j.apsusc.2013.03.067.

[166] H. Hiraoka, "Pulsed laser processings of polymer and ceramic surfaces," *J. Photopolym. Sci. Technol.*, vol. 10, no. 2, pp. 205–210, 1997, doi: 10.2494/photopolymer.10.205.

[167] W. Zhang, G. Cheng, X. D. Hui, and Q. Feng, "Abnormal ripple patterns with enhanced regularity and continuity in a bulk metallic glass induced by femtosecond laser irradiation," *Appl. Phys. A Mater. Sci. Process.*, vol. 115, no. 4, pp. 1451–1455, 2014, doi: 10.1007/s00339-013-8062-z.

[168] S. Gräf, C. Kunz, and F. A. Müller, "Formation and properties of laser-induced periodic surface structures on different glasses," *Materials (Basel).*, vol. 10, no. 8, 2017, doi: 10.3390/ma10080933.

[169] A. Y. Vorobyev and C. Guo, "Multifunctional surfaces produced by femtosecond laser pulses," *J. Appl. Phys.*, vol. 117, no. 3, 2015, doi: 10.1063/1.4905616.

[170] G. W. Römer, D. A. Del Cerro, R. C. J. Sipkema, M. N. W. Groenendijk, and A. J. Huis In 't Veld, "Ultra short pulse laser generated surface textures for anti-ice applications in aviation," *ICALEO 2009 - 28th Int. Congr. Appl. Lasers Electro-*

Optics, Congr. Proc., vol. 102, no. 2009, pp. 30–37, 2009, doi: 10.2351/1.5061570.

[171] A. H. A. Lutey *et al.*, “Towards laser-textured antibacterial surfaces,” *Sci. Rep.*, vol. 8, no. 1, pp. 1–10, 2018, doi: 10.1038/s41598-018-28454-2.

[172] L. Orazi *et al.*, “Osteoblast cell response to LIPSS-modified Ti-implants,” *Key Eng. Mater.*, vol. 813 KEM, pp. 322–327, 2019, doi: 10.4028/www.scientific.net/KEM.813.322.

[173] Z. Wang, Q. Zhao, and C. Wang, “Reduction of friction of metals using laser-induced periodic surface nanostructures,” *Micromachines*, vol. 6, no. 11, pp. 1606–1616, 2015, doi: 10.3390/mi6111444.

[174] Z. Ou, M. Huang, and F. Zhao, “The fluence threshold of femtosecond laser blackening of metals: The effect of laser-induced ripples,” *Opt. Laser Technol.*, vol. 79, pp. 79–87, 2016, doi: 10.1016/j.optlastec.2015.11.018.

[175] C. Yao *et al.*, “Polarization and fluence effects in femtosecond laser induced micro/nano structures on stainless steel with antireflection property,” *Appl. Surf. Sci.*, vol. 425, pp. 1118–1124, 2017, doi: 10.1016/j.apsusc.2017.07.157.

[176] A. Michalek, T. Jwad, P. Penchev, T. L. See, and S. Dimov, “Inline LIPSS Monitoring Method Employing Light Diffraction,” *J. Micro Nano-Manufacturing*, vol. 8, no. 1, Mar. 2020, doi: 10.1115/1.4045681.

[177] A. Batal *et al.*, “Effects of laser processing conditions on wettability and proliferation of Saos-2 cells on CoCrMo alloy surfaces,” *Adv. Opt. Technol.*, vol. 9, no. 1–2, pp. 67–78, 2020, doi: 10.1515/aot-2019-0051.

[178] M. Jiang, X. Wang, S. Ke, F. Zhang, and X. Zeng, “Large scale layering laser surface texturing system based on high speed optical scanners and gantry machine tool,” *Robot. Comput. Integr. Manuf.*, vol. 48, no. 1037, pp. 113–120, 2017, doi: 10.1016/j.rcim.2017.03.005.

[179] G. Cuccolini, L. Orazi, and A. Fortunato, “5 Axes computer aided laser milling,” *Opt. Lasers Eng.*, vol. 51, no. 6, pp. 749–760, 2013, doi: 10.1016/j.optlaseng.2013.01.015.

[180] T. Tari and P. Richter, “Correction of astigmatism and ellipticity of an astigmatic Gaussian laser beam by symmetrical lenses,” *Opt. Quantum Electron.*, vol. 24, no. 9, pp. 865–872, 1992, doi: 10.1007/BF01588591.

[181] J. Eichstädt, G. R. B. E. Römer, and A. J. Huis In ’T Veld, “Determination of irradiation parameters for laser-induced periodic surface structures,” *Appl. Surf. Sci.*, vol. 264, pp. 79–87, 2013, doi: 10.1016/j.apsusc.2012.09.120.

[182] D. Bergström, “The absorption of laser light by rough metal surfaces,” Luleå University of Technology, 2008.

[183] G. Farin, “A - Quick Reference of Curve and Surface Terms,” in *Curves and Surfaces for CAGD*, 5th ed., San Francisco: Morgan Kaufmann, 2002, pp. 437–444.

[184] Y. Jee, M. F. Becker, and R. M. Walser, “Laser-induced damage on single-crystal metal surfaces,” *J. Opt. Soc. Am. B*, vol. 5, no. 3, p. 648, 1988, doi:

10.1364/josab.5.000648.

[185] P. B. Johnson and R. W. Christy, “Optical constants of transition metals: Ti, V, Cr, Mn, Fe, Co, Ni, and Pd,” *Phys. Rev. B*, vol. 9, no. 12, pp. 5056–5070, 1974, doi: 10.1103/PhysRevB.9.5056.

[186] J. F. Young, J. S. Preston, H. M. Van Oriel, and J. E. Sipe, “Laser-induced periodic surface structure. II. Experiments on Ge, Si, Al, and brass,” *Phys. Rev. B*, vol. 27, no. 2, 1983.

[187] M. A. Ordal, R. J. Bell, R. W. Alexander, L. A. Newquist, and M. R. Querry, “Optical properties of Al, Fe, Ti, Ta, W, and Mo at submillimeter wavelengths,” *Appl. Opt.*, vol. 27, no. 6, p. 1203, 1988, doi: 10.1364/ao.27.001203.

[188] F. Di Niso, C. Gaudiuso, T. Sibillano, F. P. Mezzapesa, A. Ancona, and P. M. Lugarà, “Role of heat accumulation on the incubation effect in multi-shot laser ablation of stainless steel at high repetition rates,” *Opt. Express*, vol. 22, no. 10, p. 12200, 2014, doi: 10.1364/oe.22.012200.

[189] F. Fraggelakis, G. Mincuzzi, J. Lopez, I. Manek-Hönninger, and R. Kling, “Controlling 2D laser nano structuring over large area with double femtosecond pulses,” *Appl. Surf. Sci.*, vol. 470, no. November 2018, pp. 677–686, 2019, doi: 10.1016/j.apsusc.2018.11.106.

[190] J. Bonse, S. Höhm, S. V. Kirner, A. Rosenfeld, and J. Krüger, “Laser-induced periodic surface structures – a scientific evergreen,” *IEEE J. Sel. Top. Quantum Electron.*, vol. 23, no. 3, p. 9000615, 2017, doi: 10.1109/jstqe.2016.2614183.

[191] L. Gemini, M. Faucon, L. Romoli, and R. Kling, “High throughput laser texturing of super-hydrophobic surfaces on steel,” *Laser-based Micro- and Nanoprocessing*, vol. 10092, p. 100921G, 2017, doi: 10.1117/12.2252649.

[192] J. Bonse, J. Krüger, S. Höhm, and A. Rosenfeld, “Femtosecond laser-induced periodic surface structures,” *J. Laser Appl.*, vol. 24, no. 4, p. 042006, 2012, doi: 10.2351/1.4712658.

[193] J. M. Guay *et al.*, “Laser-induced plasmonic colours on metals,” *Nat. Commun.*, vol. 8, no. May, 2017, doi: 10.1038/ncomms16095.

[194] G. Li *et al.*, “Femtosecond laser color marking stainless steel surface with different wavelengths,” *Appl. Phys. A Mater. Sci. Process.*, vol. 118, no. 4, pp. 1189–1196, 2014, doi: 10.1007/s00339-014-8868-3.

[195] J. Yao *et al.*, “Selective appearance of several laser-induced periodic surface structure patterns on a metal surface using structural colors produced by femtosecond laser pulses,” *Appl. Surf. Sci.*, vol. 258, no. 19, pp. 7625–7632, 2012, doi: 10.1016/j.apsusc.2012.04.105.

[196] J. C. Le Bosse, G. Hansali, J. Lopez, and T. Mathia, “Characterisation of surface roughness by laser light scattering: Specularly scattered intensity measurement,” *Wear*, vol. 209, no. 1–2, pp. 328–337, 1997, doi: 10.1016/S0043-1648(96)07497-2.

[197] S. Schröder, T. Herffurth, H. Blaschke, and A. Duparré, “Angle-resolved scattering: an effective method for characterizing thin-film coatings,” *Appl. Opt.*,

vol. 50, no. 9, p. C164, 2011, doi: 10.1364/AO.50.00C164.

[198] Y. P. Zhao, I. Wu, C. F. Cheng, U. Block, G. C. Wang, and T. M. Lu, "Characterization of random rough surfaces by in-plane light scattering," *J. Appl. Phys.*, vol. 84, no. 5, pp. 2571–2582, 1998, doi: 10.1063/1.368419.

[199] J. W. Goodman, *Introduction to Fourier Optics*. Roberts and Company Publishers, 2005.

[200] S. Schwarz, S. Rung, and R. Hellmann, "One-dimensional low spatial frequency LIPSS with rotating orientation on fused silica," *Appl. Surf. Sci.*, vol. 411, pp. 113–116, 2017.

[201] T. Kobayashi, H. Sera, T. Wakabayashi, H. Endo, Y. Takushima, and J. Yan, "Surface Flattening and Nanostructuring of Steel by Picosecond Pulsed Laser Irradiation," *Nanomanufacturing Metrol.*, vol. 3456789, 2018, doi: 10.1007/s41871-018-0023-x.

[202] J. M. Romano, A. Garcia-Giron, P. Penchev, and S. Dimov, "Triangular laser-induced submicron textures for functionalising stainless steel surfaces," *Appl. Surf. Sci.*, vol. 440, pp. 162–169, 2018, doi: 10.1016/j.apsusc.2018.01.086.

[203] T. Jwad, P. Penchev, V. Nasrollahi, and S. Dimov, "Laser induced ripples' gratings with angular periodicity for fabrication of diffraction holograms," *Appl. Surf. Sci.*, vol. 453, no. 1, pp. 449–456, 2018, doi: 10.1016/j.apsusc.2018.04.277.

[204] G. Li *et al.*, "Realization of diverse displays for multiple color patterns on metal surfaces," *Appl. Surf. Sci.*, vol. 316, no. 1, pp. 451–455, 2014, doi: 10.1016/j.apsusc.2014.08.030.

[205] S. Hou *et al.*, "Formation of long- and short-periodic nanoripples on stainless steel irradiated by femtosecond laser pulses," *J. Phys. D. Appl. Phys.*, vol. 44, no. 50, 2011, doi: 10.1088/0022-3727/44/50/505401.

[206] L. Qi, K. Nishii, and Y. Namba, "Regular subwavelength surface structures induced by femtosecond laser pulses on stainless steel.," *Opt. Lett.*, vol. 34, no. 12, pp. 1846–1848, 2009, doi: 10.1364/OL.34.001846.

[207] A. Y. Vorobyev, V. S. Makin, and C. Guo, "Periodic ordering of random surface nanostructures induced by femtosecond laser pulses on metals," *J. Appl. Phys.*, vol. 101, no. 3, 2007, doi: 10.1063/1.2432288.

[208] M. Milosevic, "Fresnel Equations," in *Internal Reflection and ATR Spectroscopy*, John Wiley & Sons, Incorporated, 2012, pp. 39–54.

[209] T. Herffurth, S. Schröder, M. Trost, A. Duparré, and A. Tünnermann, "Comprehensive nanostructure and defect analysis using a simple 3D light-scatter sensor.," *Appl. Opt.*, vol. 52, no. 14, pp. 3279–87, 2013, doi: 10.1364/AO.52.003279.

[210] K. Kumar and G. S. M. Thakur, "Advanced Applications of Neural Networks and Artificial Intelligence: A Review," *Int. J. Inf. Technol. Comput. Sci.*, vol. 4, no. 6, pp. 57–68, 2012, doi: 10.5815/ijitcs.2012.06.08.

[211] M. Paliwal and U. A. Kumar, "Neural networks and statistical techniques: A

review of applications," *Expert Syst. Appl.*, vol. 36, no. 1, pp. 2–17, 2009, doi: 10.1016/j.eswa.2007.10.005.

[212] C. K. Desai and A. Shaikh, "Prediction of depth of cut for single-pass laser micro-milling process using semi-analytical, ANN and GP approaches," *Int. J. Adv. Manuf. Technol.*, vol. 60, no. 9–12, pp. 865–882, 2012, doi: 10.1007/s00170-011-3677-8.

[213] S. M. Karazi, A. Issa, and D. Brabazon, "Comparison of ANN and DoE for the prediction of laser-machined micro-channel dimensions," *Opt. Lasers Eng.*, vol. 47, no. 9, pp. 956–964, 2009, doi: 10.1016/j.optlaseng.2009.04.009.

[214] S. L. Campanelli, G. Casalino, A. D. Ludovico, and C. Bonserio, "An artificial neural network approach for the control of the laser milling process," *Int. J. Adv. Manuf. Technol.*, vol. 66, no. 9–12, pp. 1777–1784, 2013, doi: 10.1007/s00170-012-4457-9.

[215] D. Teixidor, M. Grzenda, A. Bustillo, and J. Ciurana, "Modeling pulsed laser micromachining of micro geometries using machine-learning techniques," *J. Intell. Manuf.*, vol. 26, no. 4, pp. 801–814, 2015, doi: 10.1007/s10845-013-0835-x.

[216] V. Shashank, V. Pardha Saradhi, and T. Jagadesh, "Modeling of Laser assisted machining process using Artificial Neural Network," in *Journal of Physics: Conference Series*, 2019, vol. 1172, no. 1, doi: 10.1088/1742-6596/1172/1/012040.

[217] B. F. Yousef, G. K. Knopf, E. V. Bordatchev, and S. K. Nikumb, "Neural network modeling and analysis of the material removal process during laser machining," *Int. J. Adv. Manuf. Technol.*, vol. 22, no. 1–2, pp. 41–53, 2003, doi: 10.1007/s00170-002-1441-9.

[218] S. Tani, Y. Aoyagi, and Y. Kobayashi, "Neural-network-assisted in situ processing monitoring by speckle pattern observation," *Opt. Express*, vol. 28, no. 18, p. 26180, 2020, doi: 10.1364/oe.400785.

[219] S. Feng, H. Zhou, and H. Dong, "Using deep neural network with small dataset to predict material defects," *Mater. Des.*, vol. 162, pp. 300–310, 2019, doi: 10.1016/j.matdes.2018.11.060.

[220] P. Isola, J. Y. Zhu, T. Zhou, and A. A. Efros, "Image-to-image translation with conditional adversarial networks," *Proc. - 30th IEEE Conf. Comput. Vis. Pattern Recognition, CVPR 2017*, vol. 2017, pp. 5967–5976, 2017, doi: 10.1109/CVPR.2017.632.

[221] B. Mills, D. J. Heath, J. A. Grant-Jacob, and R. W. Eason, "Predictive capabilities for laser machining via a neural network," *Opt. Express*, vol. 26, no. 13, p. 17245, Jun. 2018, doi: 10.1364/OE.26.017245.

[222] A. Michalek *et al.*, "Modelling ultrafast laser structuring/texturing of freeform surfaces," *Appl. Surf. Sci. Adv.*, vol. 2, no. October, p. 100036, Dec. 2020, doi: 10.1016/j.apsadv.2020.100036.

[223] A. Garcia-Giron, J. M. Romano, A. Batal, A. Michałek, P. Penchev, and S. S. Dimov, "Experimental investigation of processing disturbances in laser surface

patterning," *Opt. Lasers Eng.*, vol. 126, no. October 2019, 2020, doi: 10.1016/j.optlaseng.2019.105900.

[224] A. K. S. B. Sunil, K. P. Jha, A. M. Kulwant, S. Vivekanand, and K. S. Sinha, "Surface micro-structuring of type 304 stainless steel by femtosecond pulsed laser : effect on surface wettability and corrosion resistance," *Appl. Phys. A*, vol. 124, no. 12, pp. 1–9, 2018, doi: 10.1007/s00339-018-2243-8.

[225] R. Podor *et al.*, "3D-SEM height maps series to monitor materials corrosion and dissolution To cite this version : HAL Id : hal-02064121," *Mater. Charact.*, vol. 150, pp. 220–228, 2019, doi: 10.1016/j.matchar.2019.02.017.

[226] D. Moore, G. McGabe, and O. Akman, *Introduction to the practice statistics*, 10th ed. NY: Macmillian, 2021.

[227] V. Bolón-Canedo, N. Sánchez-Maroño, and A. Alonso-Betanzos, "Feature selection for high-dimensional data," *Prog. Artif. Intell.*, vol. 5, no. 2, pp. 65–75, 2016, doi: 10.1007/s13748-015-0080-y.

[228] M. Castellani, "Evolutionary generation of neural network classifiers-An empirical comparison," *Neurocomputing*, vol. 99, pp. 214–229, 2013, doi: 10.1016/j.neucom.2012.07.010.

[229] M. Castellani, "ANNE - A new algorithm for evolution of artificial neural network classifier systems," *2006 IEEE Congr. Evol. Comput. CEC 2006*, pp. 3294–3301, 2006, doi: 10.1109/cec.2006.1688728.

[230] A. L. Blum and P. Langley, "Selection of relevant features and examples in machine," *Artif. Intell.*, vol. 97, no. 1–2, pp. 245–271, 1997.

[231] D. T. Pham, M. S. Packianather, and A. A. Afify, "Artificial Neural Networks," in *Computational Intelligence*, Boston, MA: Springer US, 2007, pp. 67–92.

[232] D. E. Rumelhart and J. L. McClelland, *Parallel distributed processing: Explorations in the microstructure of cognition*. The MIT Press, 1986.

[233] D. T. Pham and M. Castellani, "Adaptive selection routine for evolutionary algorithms," *Proc. Inst. Mech. Eng. Part I J. Syst. Control Eng.*, vol. 224, no. 6, pp. 623–633, 2010, doi: 10.1243/09596518JSCE942.

[234] A. Santos, E. Córdoba, Z. Ramirez, C. Sierra, and Y. Ortega, "Determination of the coefficient of dynamic friction between coatings of alumina and metallic materials," *J. Phys. Conf. Ser.*, vol. 935, no. 1, 2017, doi: 10.1088/1742-6596/935/1/012042.

[235] A. S. Pouzada, E. C. Ferreira, and A. J. Pontes, "Friction properties of moulding thermoplastics," *Polym. Test.*, vol. 25, no. 8, pp. 1017–1023, 2006, doi: 10.1016/j.polymertesting.2006.06.009.

[236] Aerotech, "PRO165LM Mechanical Bearing, Linear Motor Stage | Aerotech." https://www.aerotech.com/product/stages-actuators/pro165lm-mechanical-bearing-linear-motor-stage/ (accessed Jun. 15, 2022).

[237] Fraunhofer Institute for Applied Optics and Precision Engineering IOF, "Compact Optical Roughness Sensor, Process-Intergratable Test System - horos," 2019. https://www.iof.fraunhofer.de/en/business-fields/photonic-

sensors-and-measuring-systems/surface-coating-characterization/compact-optical-roughness-sensor-horos.html (accessed Mar. 01, 2019).